

Theory and simulation of the charging of dust in plasmas

Drew Mercos Thomas

dmt107@imperial.ac.uk

Submitted in partial fulfilment of the requirements for the degree of
Doctor of Philosophy of Imperial College London and for the Diploma of
Membership of Imperial College.

March 2016

Department of Physics
Imperial College London
London
SW7 2BZ

Abstract

This dissertation documents my mathematical and computational models of the charging of spherical dust grains in plasmas.

The mathematical models are stochastic models which predict the equilibrium probability distribution of a sphere's charge state q in a collisionless, flowing plasma with Debye length λ_D . I solve the models for the distribution's exact form and deduce closed-form Gaussian approximations to it. The approximations' mean and variance are of order Ω at large Ω , where the dimensionless quantity Ω equals $3N_D a / \lambda_D$, N_D being the plasma's Debye number and a the sphere's radius. Faster plasma flow increases q 's variance for spheres much smaller than λ_D , but does not affect the variance for large ($a \gg \lambda_D$) spheres.

My computational model is pot, a simulator of a sphere in a flowing, homogeneously magnetized plasma, and the first to be fully microscopic with non-interpolated fields. I describe pot's design, present test results confirming that pot produces sensible output, and detail pot-derived estimates of a sphere's normalized, equilibrium surface potential η_a as a function of the dimensionless magnetization β_i and plasma flow speed. pot's η_a values come within 5% of those predicted by the existing "SOML" theory of spheres in flowing plasmas, and q 's equilibrium fluctuations during pot simulations statistically match those predicted by my stochastic modelling. Another comparison, of pot's results against past simulations — only partially microscopic — and against an unmagnetized-ion theory, verifies the earlier simulations' implication that the unmagnetized-ion theory is incorrect when β_i is small but non-negligible. Contra the theory, gently magnetizing a proton-electron plasma by increasing its β_i from zero to 0.4 does not raise η_a by 0.4, but at most by 0.1.

Contents

Originality and copyright declarations	6
Acknowledgements	7
Publications arising from this PhD	9
List of tables	10
List of figures	11
1 Introduction	14
1.1 Plasmas, dust, and dust in plasmas	14
1.2 Dust in plasmas in the real world	15
1.2.1 The Moon's exosphere	15
1.2.2 Saturn's rings	17
1.2.3 Semiconductor processing	19
1.2.4 Tokamaks	21
1.3 Quantitative properties of dust and plasmas	23
1.4 Spherical dust grains	24
2 Existing theories and simulations of spherical grain charging	25
2.1 Basic lemmas	25
2.1.1 Fundamental law of charging	25
2.1.2 Boltzmann relation	27
2.1.3 Maxwell-Boltzmann velocity distribution	28
2.1.4 Maxwellian flux onto an absorbing sphere	31
2.1.5 Order-of-magnitude estimate of η_a	31
2.1.6 Debye-Hückel screening and potential function	32
2.1.7 Bohm criterion and Bohm speed	35
2.1.8 Quasi-neutrality	40
2.2 Charging theories	41
2.2.1 Allen, Boyd, & Reynolds (ABR)	42
2.2.2 Orbital-motion limited (OML)	46

2.2.3	Orbital motion (OM)	51
2.2.4	Extensions to OML theory	52
2.3	Past sphere-charging simulations	57
2.4	Conclusion	59
3	Equilibrium probability distribution of an equipotential sphere's charge in flowing, collisionless plasma	61
3.1	Constructing the stochastic models	62
3.2	Exact equilibrium charge distribution	65
3.3	The sphere's modal equilibrium charge and the stochastic models' validity	66
3.4	Approximate Gaussian solutions to the models' master equations	70
3.5	Skewness of the exact charge distribution	74
3.6	Conclusion	77
4	Design of a treecode simulator of a spherical grain in plasma	79
4.1	The sphere-in-plasma system simulated	79
4.2	pot as a parallel program	81
4.3	Overview of my simulator, pot, and its core algorithms	81
4.3.1	Barnes and Hut's treecode algorithm	82
4.3.2	Particle-motion integrators	88
4.3.3	Hutchinson's reinjection algorithm	91
4.4	Prerequisites for valid simulation results	93
4.5	Conclusion	97
5	Treecode simulation results	99
5.1	Tests of physical correctness	99
5.1.1	Circular Kepler orbits	99
5.1.2	Rutherford scattering	103
5.1.3	Gases of non-interacting electrons and protons	104
5.1.4	Pure plasma	114
5.1.5	Conclusion	116
5.2	Comparing sphere-charging results to SOML theory	119
5.3	Comparing sphere-charging results to my stochastic model	123
5.4	Equilibrium η_a as a function of magnetic field	127
5.5	Conclusion	129
6	Conclusion	131
6.1	Summary	131
6.2	What is to be done?	132
Bibliography		136
A Symbols and abbreviations		148

B Better boundary conditions for ABR theory from a linear-Laplacian approximation	155
C Proof of f_q's unimodality	159
D Curve-fitting analysis of the Kepler-orbit test simulations	161

Originality and copyright declarations

The College's submission checklist informs me that I "must include a short statement in [my] own words, that the work is [my] own and that all else is appropriately referenced", and that this statement "should appear at the beginning of the thesis" [1]. It adds that the copyright declaration should also appear at the beginning, presumably fighting for space next to the own-work statement, and the title page, which is meant to be the first page. You figure it out, but in any case I am glad to grab the opportunity (indeed the obligation) to write in something closer to my own voice.

All of the intellectual labour represented in this dissertation is mine, except for that which isn't. I distinguish the latter work by festooning it with citations keyed to references and hence its original source (or sources). I have sought to be punctilious about referencing to the point of pedantry; every direct quotation in the prose has, unless I nodded off for a moment while writing, a citation *and* a page or figure number attached to it. (Except for the epigraphs, which would be a bit much, and for the quotations from documents without page numbers.) Aside from quotations and paraphrases (and institutionally mandated chapter titles) I wrote this dissertation all on my lonesome, apart from §3, which was originally a published paper I co-authored with my supervisor. As I wrote the paper's entire first draft myself, and signed off on every edit my supervisor suggested, I count it as my own work for current purposes. Lastly, I reproduce a few isolated figures by other people, each figure referenced and used under the fair-dealing provisions of sections 29 and 30 of the Copyright, Designs and Patents Act 1988.

On the topic of copyright, there is another "statement to be included at the beginning" of this text [1].

The copyright of this thesis rests with the author and is made available under a Creative Commons Attribution Non-Commercial No Derivatives licence. Researchers are free to copy, distribute or transmit the thesis on the condition that they attribute it, that they do not use it for commercial purposes and that they do not alter, transform or build upon it. For any reuse or redistribution, researchers must make clear to others the licence terms of this work

Bold in the original [1].

Acknowledgements

Visit the building, take the
Highway, park and
Come up and see me, I'll be
Working, working, but
If you come visit I'll put
Down what I'm doing
My friends are important.

Talking Heads (1977),
“Don’t Worry About the Government”

Moj stari veruje
Možda preteruje
Kad kaže
Da sam bolji od svih

Rani Mraz (1979), “Drago mi je zbog mog starog”

I have quite a few people to thank for helping me on my way to writing this dissertation. I thank Michael Coppins for drawing my attention to the physics of dust in plasmas, for offering me a (fully funded!) opportunity to study it, and for supervising my PhD in a manner that was laid-back without being lax. Robert Kingham has also contributed by reviewing interim reports of my work with a disinterested, critical eye. Christos Stavrou, Martin Read, George Hicks, Jason Cole, Steven McNamara, and Hirotaka Nakamura deserve credit for brightening up my years in room 732 of the Blackett Laboratory.

From my research group’s dusty-plasma contingent I am indebted not just to Christos but also to Josh Holgate, Joe Gibson, Richard Cameron, Minas Bacharis, Nikoleta Rizopoulou, and Nopparit Somboonkittichai for their comments on my work, and I owe Josh a second debt for building on my research by extending the simulation software I wrote.

On the home front I thank my father Michel for his encouragement and review of what I wrote, and I thank my mother Marina for her love and support while I completed this PhD, and for charging me less rent than the typical London landlord.

Looking further afield, I thank John E. Allen of the University of Oxford, who has regularly visited the plasma-physics research group here at Imperial College. He not only inspired several projects but worked with me to write them up as conference posters and two papers. I am likewise glad to have been able to collaborate on papers with two other physicists despite meeting them only at conferences; those co-authors were the sharp raconteur Raoul Franklin, and Mikhail Benilov, who brought to bear his trademark mathematical tenacity and rigour.

On computing facilities, I did much of my data analysis and produced many figures with the R language and environment for statistical computing, and R's LambertW package, for which I thank the R Core Team and Georg M. Goerg respectively. I also thank Imperial College's High Performance Computing service for running the College's CX1 computing cluster, without which I would have been unable to obtain the treecode simulator results in this dissertation. The service asks that I cite its website, <http://www.imperial.ac.uk/ict/services/teachingandresearchservices/highperformancecomputing>.

Finally, I thank my examiners Roland Smith and Tony Arber for having the patience to scrutinize this text and make exhaustive critiques of it, which saved me from not a few foggy phrasings and outright mistakes.

Any remaining errors are, of course, not my fault, but I haven't decided whose fault they are.

Publications arising from this PhD

My dissertation is not the only product of my PhD. I have also contributed prose and numerical computations to the following four journal papers.

1. D. M. Thomas, M. Coppins (2013). Equilibrium probability distribution of a conductive sphere's floating charge in a collisionless, drifting Maxwellian plasma. *Physical Review E*, **88**(2), 023110.
2. R. N. Franklin, J. E. Allen, D. M. Thomas, M. S. Benilov (2013). Plasmas generated by ultra-violet light rather than electron impact. *Physics of Plasmas*, **20**(12), 123508.
3. M. S. Benilov, D. M. Thomas (2014). Asymptotic theory of double layer and shielding of electric field at the edge of illuminated plasma. *Physics of Plasmas*, **21**(4), 043501.
4. D. M. Thomas, J. E. Allen (2015). Cylindrical plasmas generated by an annular beam of ultraviolet light. *Physics of Plasmas*, **22**(7), 073507.

The last three papers overlap little with the content of this dissertation, so it is not a complete account of my work during my PhD studies. The first paper, however, is represented in this dissertation; an amended version incorporating the minor erratum (*PRE*, **89**(2), 029903(E)) constitutes chapter 3. It seems prudent to mention that I conceived the paper and wrote the first draft single-handedly, that Michael Coppins and I retain the copyright for the paper, and that Dr. Coppins has granted me permission to use it here.

In addition to standalone papers, I also prepared and carried out the numerical work for the two conference posters

1. D. M. Thomas, C. T. N. Willis, J. E. Allen, M. Coppins (2012). The Bohm criterion for flowing plasmas. Europhysics Conference on the Atomic and Molecular Physics of Ionized Gases, Viana do Castelo, Portugal, July 10–14.
2. D. M. Thomas, R. N. Franklin, J. E. Allen (2013). Plasmas generated by ultra-violet irradiation. XXXI International Conference on Phenomena in Ionized Gases, Granada, Spain, July 14–19.

with accompanying abstracts published in the relevant proceedings. (Because of an oversight the published abstract for the second poster credits only Allen.)

List of tables

2.1	Quantitative definitions of quasi-neutrality	41
4.1	Quantitative parameter requirements for physically valid pot simulations	94
5.1	Fits of eq. (5.1) to results of circular-Kepler-orbit pot tests	102
5.2	pot's default parameter values	106
5.3	q 's variance and its standard error at equilibrium during unmagnetized pot runs with $\Delta t \leq 1$ ps, compared to the small-sphere stochastic model's prediction of q 's variance	126

List of figures

1.1 Apollo 17 astronaut Eugene Cernan's sketch of lunar horizon glow, with NASA's coloured annotations	17
1.2 Saturn's B ring in differently scattered lights	18
1.3 Wafer-contamination sources in microchip manufacturing	20
1.4 Diameter distributions of dust collected from tokamaks	22
2.1 Results of numerically integrating eq. (2.45) with the DH solution as a boundary condition, assuming various a/λ_D and η_a	36
2.2 ABR predictions of η_a for a dust grain of radius a in an H^+ or in an Ar^{1+} plasma . .	45
2.3 Trajectories of ions approaching a negatively charged dust grain, all with speed v_∞ at infinity, but differing impact parameters	47
2.4 η_a at a sphere's surface in a singly ionized plasma, according to the OML model . . .	49
2.5 Trajectories illustrating a lack of absorption radius in an r^{-2} field, and an absorption radius in an r^{-4} field	49
2.6 Comparison of OML and MOML predictions of η_a for a sphere in a hydrogenic, singly ionized plasma	54
2.7 SOML theory's η_a predictions for a sphere in a hydrogenic, singly ionized plasma at various flow speeds	56
2.8 Comparison of SOML η_a estimates to SCEPTIC's	58
3.1 Illustration of a one-step process	62
3.2 Auxiliary functions $s_1(u)$, $s_2(u)$, and their ratio	68
3.3 f_q 's variance σ^2 for a small sphere in hydrogenic plasma with $k_B T_e = 1$ eV and $a = 10$ nm	73
3.4 Contour plots of f_q 's skewness for a small sphere in hydrogenic plasma with 1 eV electrons	74
3.5 f_q 's skewness as a function of μ for a small sphere in a stationary plasma with 1 eV electrons and $a = 10$ nm	75
3.6 f_q and its Gaussian approximation for a small sphere in hydrogenic plasma with $a = 10$ nm, $u = 0$, $\Theta = 0.001$ and 1 eV electrons	76
3.7 Contour plots of f_q 's skewness, as a function of γ , μ , a and u for a large sphere in a plasma with 1 eV electrons and ions	76

4.1	Example of estimating the net field at a charge in a 2-dimensional box of charges	82
4.2	Partitioning the simulation domain into a hierarchy of cells	83
4.3	Cell-based decomposition of the simulation domain as a tree	84
4.4	Estimating the field at a particle according to the treecode algorithm	85
5.1	Electron positions during circular-Kepler-orbit pot tests	101
5.2	Ion trajectories in circular-Kepler-orbit pot tests	102
5.3	$v_0^2 b$, $\theta_s/2$, and their relationship in Rutherford-scattering pot tests of different integrators	103
5.4	$v_0^2 b$, $\theta_s/2$, and their relationship for electrons with $b < (4/5)R$	105
5.5	Mean kinetic energy of electrons and protons during a pot run without a collecting sphere and without electric fields	106
5.6	Mean momentum components of electrons and protons during a pot run without a collecting sphere and without electric fields	108
5.7	Histograms of electrons' and protons' speed and velocity components at equilibrium in a pot test run without a collecting sphere and without electric fields	109
5.8	Mean kinetic and potential energies of electrons and protons during a pot run with a collecting sphere but no interactions among electrons and protons	110
5.9	Electron and proton number densities, and electron counts compared to the Boltzmann relation, at the end of a pot run with a collecting sphere but no interactions among electrons and protons	111
5.10	Mean momentum components of electrons and protons during a pot run with a collecting sphere but no interactions among electrons and protons	112
5.11	Histograms of electrons' and protons' speed and velocity components at equilibrium in a pot test run with a collecting sphere but no interactions among electrons and protons	113
5.12	In a pot test run with a collecting sphere but no interactions among electrons and protons, the CDF of the protons' standardized v_y at the run's end, and the sphere's q over time	113
5.13	Mean kinetic and potential energies of electrons and protons during a pure-plasma pot run	115
5.14	Early time evolution of mean electron potential energy in a pure-plasma pot run . .	116
5.15	Mean kinetic and potential energies of electrons and protons during pure-plasma runs with two versions of pot	117
5.16	Mean momentum components of electrons and protons during a pot run with inter-particle interactions but no collecting sphere	118
5.17	Histograms of electrons' and protons' speed and velocity components at equilibrium in a pot test run with inter-particle interactions but no collecting sphere	119
5.18	pot's median equilibrium η_a as a function of flow speed with $\Theta = 1$ and $\Theta = 0.1$, compared against SOML predictions	120
5.19	The ratio of pot's η_a estimates to η_{SOML} , the corresponding SOML η_a predictions .	121

5.20 pot's median equilibrium η_a as a function of flow speed compared against SOML-theory predictions, among runs with $\Delta t \leq 1$ ps	122
5.21 Comparing two means of estimating η_a from the same pot runs: median equilibrium η_a versus η_a obtained by fitting SOML charging curves	123
5.22 Fitted-SOML-curve η_a estimates from pot as a function of flow speed, versus SOML-theory predictions	124
5.23 q time series and autocorrelation function from a pot run, near and at equilibrium .	124
5.24 η_a as a function of β_i from pot, SCEPTIC, and an unmagnetized-ion theory	128

Chapter 1

Introduction

The subject may appear an insignificant one, but we shall see that it possesses some interest; and the maxim “de minimis lex non curat,” does not apply to science.

Charles Darwin (1881),
The Formation of Vegetable Mould Through the Action of Worms, with Observations on their Habits, p. 2

1.1 Plasmas, dust, and dust in plasmas

Plasmas are quasi-neutral gases ionized to such an extent that they exhibit collective behaviours [2]. By “quasi-neutral” I mean that a plasma’s total electric charge is negligible; on macroscopic scales, the positive charge borne by a plasma’s ions essentially cancels out the negative charge of the plasma’s electrons (and its negative ions, if present). By “collective behaviours” I mean phenomena such as Debye-Hückel screening [3] and the veritable zoo of plasma waves [4], which do not appear in neutral gases but may be realized in plasmas because plasmas contain mobile charges which push and pull each other.

Just as solids, liquids, and gases in the real world are routinely impure, many actually existing plasmas are contaminated with dust [5]. The word “dust” refers not only to literal dust in the lay sense, but to any solid bodies big enough to accumulate electric charge and small enough to be immersed in a larger plasma. This definition excludes bodies smaller than about a nanometre in size [6], like the individual electrons and ions comprising the plasma proper, but it includes macroscopic objects like the centimetre-sized spherical probes used to take measurements in laboratory plasmas [7, 8, 9, 10]. The definition is a pragmatic operational [11] one: since accumulating charge is the most salient thing the archetypal dust particle does in a plasma, it is practical to define “dust” in this context as something solid which accumulates charge in a plasma.

This dissertation develops quantitative models of dust in plasmas, models I solve by mathematical calculation and computer simulation. Like “dust” and “plasmas”, “dust in plasmas” is a term of art. It refers to dust-adulterated plasmas where the dust particles are far enough apart that they may be treated as non-interacting. This distinguishes “dust in plasmas” from “dusty plasmas” [12, §1] where the individual dust particles are close enough together to interact to a

non-negligible degree, whether through direct dust-dust forces or indirectly through perturbations of the surrounding plasma medium. This difference between the two types of dust-adulterated plasma is not a hard and fast one, and one review article has noted that “any plasma containing [...] charged dust grains is often loosely referred to as a dusty plasma” [12, p. 419]. Nonetheless, I try to observe the distinction in this dissertation’s theoretical chapters because the models in those chapters neglect interactions between dust particles in a plasma.

1.2 Dust in plasmas in the real world

Crafting a precise definition of dust in plasmas would be idle labour if there were no real-life examples of such. But there are many. Although the discovery of dark matter proves that plasma is not the universe’s dominant state of matter,* plasma nonetheless makes up about 4% of the universe’s matter [14], and dust “turns out to be ubiquitous in cosmic plasmas, planetary plasmas, plasmas near the earth and plasmas in the laboratory” [15, p. 74]. Examples of dust in plasmas [15, p. 75] are too numerous for this dissertation to elaborate on them all, but a few have captured the attention of physicists better than others, and those more-discussed cases are worth a closer look.

1.2.1 The Moon’s exosphere

Earth’s Moon does not have an atmosphere in the usual sense of a multi-layered system of collisional gases kept in place by gravity [16]. Part of the explanation for that is the Moon being too small for its gravity to hold on to gas particles. At a surface temperature of 400 K, a gravitational calculation indicates that “the lifetime of a hydrogen atom would be 1600 seconds, and of an oxygen atom 1.4 years” in a lunar atmosphere [17, p. 3065], time scales short enough to imply a dearth of hydrogen and oxygen on the Moon. However, performing the same calculation for denser elements like xenon and krypton suggests that the Moon would retain those heavier atoms for its entire lifetime [18]. How does one reconcile this result with the observed fact that the density of gas around the Moon is extremely low?

The answer is that gravity is not the sole determinant of an atom’s lunar lifetime. The Sun bathes the Moon in ultraviolet (UV) light which ionizes the lunar surface and any lingering gas, and many of the electrons liberated from the surface by this photoionization have enough kinetic energy to escape to space, leaving the surface positively charged. Eventually the Moon electrostatically ejects the positive gas ions left behind into space as well; this photoelectric expulsion sharply cuts the lifetime of heavy atoms near the Moon’s surface to a millennium or three, consigning them to the same astronautic fate as lighter atoms [17, pp. 3069–3070].

In spite of this, the space around the Moon is not quite devoid of gas. Escaping particles are replaced by particles from the solar wind, comet trails, and material sputtered, outgassed, vaporized, or thermally desorbed from the Moon itself [16, p. 475–479]. This supply of particles is

* Contra the occasional over-excited claim, found even in recent, reputable scientific publications (e.g. [13, p. 1]), that “99% of the universe” is plasma.

not rapid enough to furnish the Moon with a true atmosphere, but it does maintain an *exosphere*, a layer of gas so rarefied that its collision length is longer than its scale height [19, p. 102]. The exosphere is very superficial, with a typical surface number density no greater than 10^{12} m^{-3} , compared to Earth's 10^{25} m^{-3} [20].

Not all of the gas ionized by incoming radiation escapes the Moon. Some of the resulting ions and free electrons stay in the exosphere, and the exosphere is therefore a plasma. Also aloft in the lunar exosphere are fine dust grains, so the exosphere comprises dust in plasma. Signs of the exospheric dust, as well as information about its size and altitude, come from various unexpected observations made in situ by the Surveyor, Lunokhod, and Apollo missions in the 1960s and 1970s [21].

The Surveyor 5, 6, and 7 spacecraft landed on the Moon equipped with video cameras. The tenuous nature of the exosphere would seem to imply that “lunar sunsets should be completely deficient of the colourful visual effects which accompany terrestrial sunsets”, but in fact the Surveyor cameras saw glowing light above the horizon shortly after sunset [22, p. 121]. The otherwise mysterious glow can be explained as visible sunlight scattered by dust particles, with radii of 5–10 μm , levitated in a cloud up to a foot above the ground [22, pp. 121–130].

When Lunokhod-2 subsequently landed on the Moon in 1973, it recorded unusually high levels of visible and UV light at “twilight [...] after the Sun was 1° below the local horizon” [23, p. 124]. Evidence that the light was scattered into the craft’s astrophotometer by distant dust emerged by comparing the concurrent measurements of visible light and UV light. The albedo of putative dust need not be the same at all wavelengths; its albedo a_V for visible light may be greater than its albedo a_U for UV light. When Severny, Terez and Zvereva computed the ratio a_V/a_U consistent with the Lunokhod-2 measurements, they found it was 6, “agree[ing] quite well with the value of 7.0 for lunar dust”, consistent with Lunokhod-2 seeing light scattered by dust lifted from the lunar surface [23, p. 126].

Apollo 17’s three astronauts also witnessed a lunar horizon glow while in orbit. About three minutes before sunrise they saw a wide glowing “shoulder” (figure 1.1) augmenting the anticipated narrow hump of light from the Sun’s corona and the Solar System’s zodiacal cloud of interplanetary dust [24, 25]. Reflecting on the astronauts’ descriptions of the glow, Zook and McCoy deduced that it was unlikely to have come from gas, being far better explained as sunlight scattered from “sub-micron dust grains” suspended in the exosphere with a scale height of 5–20 km [25, p. 2117]. Surprise results from the mission’s Lunar Ejecta and Meteorite experiment — a box of dust impact sensors placed on the Moon’s surface — have also been interpreted as detections of levitated dust in flight near the ground [26, 27], but Brian O’Brien’s recent paper [28] has meticulously marshalled much circumstantial evidence for the apparent impact events being spurious bursts of interference from nearby electrical systems switching (possibly heaters turning on and off before sunsets and after sunrises).

Expeditions like these have firmly established the existence and most basic properties of lunar dust in plasma, but “there [remain] unsolved problems concerning its parameters and manifestations” [20]. While there is a good deal of post-1970s information about the lunar plasma

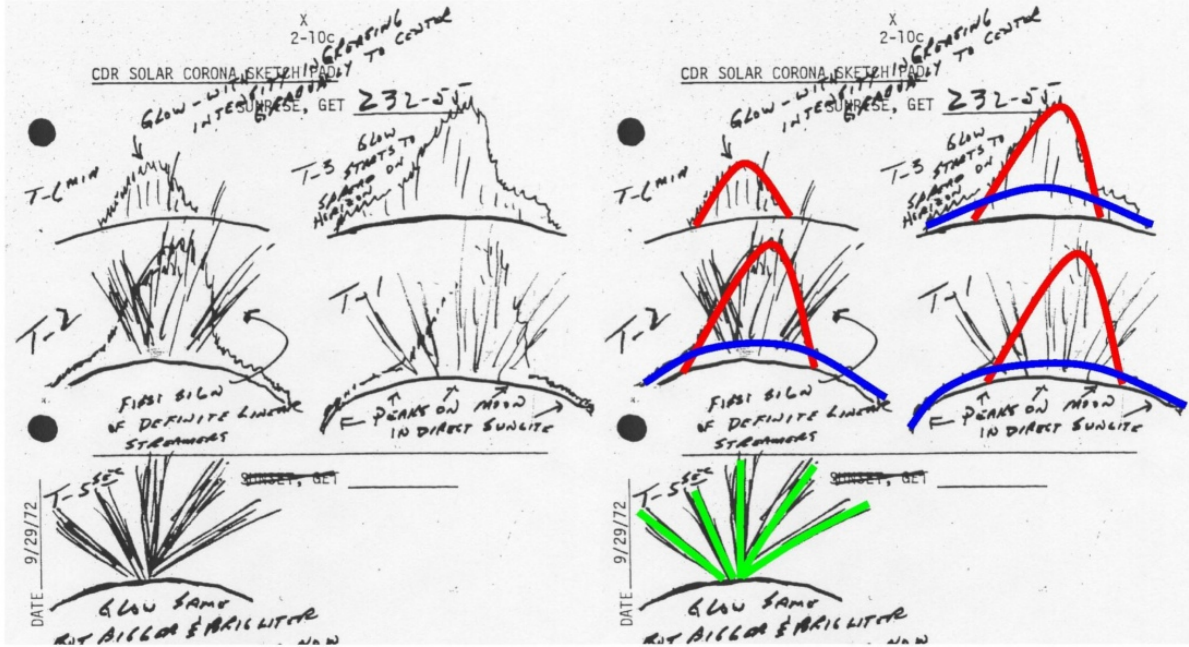


Figure 1.1: Apollo 17 astronaut Eugene Cernan’s sketch of lunar horizon glow, annotated in colour by NASA (http://www.nasa.gov/centers/goddard/images/content/455851main_Cernan_sketch_annotated.jpg via [29]). Red outlines the predicted coronal and zodiacal light; blue outlines the lunar horizon glow scattered by exospheric dust.

medium [30], there is rather less about the *dust* within it and the interaction between dust and plasma. Questions about the adhesive behaviour of Moon dust, and the dust’s electrophysical properties (quantum photoemission yield and work function), for example, remain unanswered, although NASA’s Lunar Atmosphere and Dust Environment Explorer spacecraft, which landed on the Moon in April 2014, promises to return informative detail about the physics of mobile lunar dust in plasma [31].

1.2.2 Saturn’s rings

Further from Earth are the rings of Saturn. The study of Saturn’s rings as a dust-in-plasma system began when observations from the Voyager space missions[†] “revealed that [the rings] are not smooth disks but show large radial variations of optical depth”, and photographs showed radial spokes within the rings, which appeared as brighter or darker patches depending on the viewing angle [33, p. 283]. The spokes were most visible in Saturn’s B ring (figure 1.2), the widest, middle ring of Saturn’s three clearest rings. The dependence of the spokes’ brightness on the direction of the scattered light implies the presence of dust grains on the order of a micron in size [33, 5]. Not only that, but the spokes “develop remarkably fast, with new spokes forming in as little as five minutes”, a time scale so short that electromagnetic forces must be part of the explanation for spoke formation, not just gravity [5, p. 32]. Further evidence for electromagnetic influence comes

[†]W.-H. Ip’s 1980 review [32] nicely summarizes the pre-Voyager state of knowledge of Saturn’s rings.

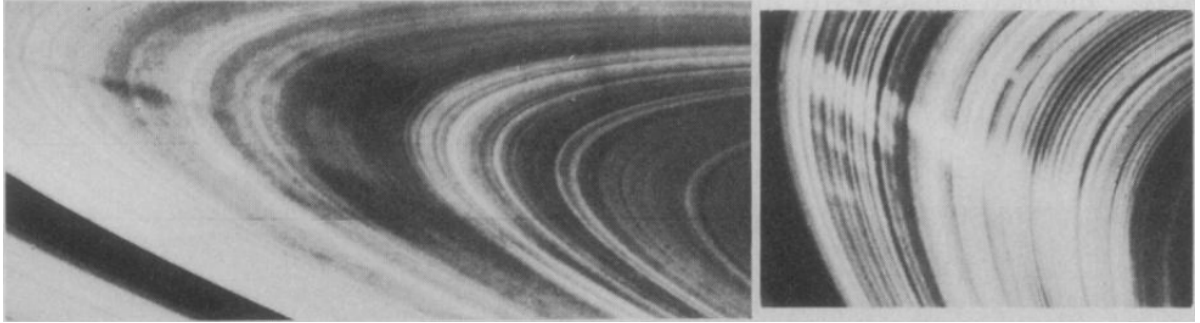


Figure 1.2: “Views of [Saturn’s] B ring in (left) backscattered and (right) forward-scattered light. The backscatter image shows several spoke features as dark regions. [...] In forward scattering, [...] the spokes appear as bright features.” Voyager 1 took these images [35, p. 190, fig. 44].

from the peaking of the spoke activity power spectrum every 621 ± 22 minutes, the same as the rotation period of Saturn’s magnetic field (639 minutes) to within statistical error [34].

As early as the first Voyager mission, researchers poring over the satellite’s images of Saturn guessed that the dust grains produced the rings’ spokes when the grains were “levitat[ed] [...] above the ring plane” [36, p. 160]. (And even at that early stage they noted that radio-frequency “discharges from the rings” hinted at “electrostatic charging effects in spoke formation and dynamics.”) A photograph taken near Saturn’s ring plane gave some idea of how far the grains were levitated by setting an upper bound of 15–80 kilometres on their height above the rings [37].

Although not “universally accepted” as an explanation for the ring spokes’ structure in the 1980s [33, p. 1989], levitated dust later became the default explanation for the spokes [12, 26]. The levitated dust hypothesis is both plausible and affirmed by light scattering observations, and there seems to be no alternative hypothesis which enjoys such support. However, explaining the rings’ spokes in terms of levitated dust calls for an explanation of the levitation. Gravitational explanations are unsupported by the facts, which point instead to electromagnetic forces acting on charge picked up by dust specks. For some years the standard explanation for dust charging has been dust grains harvesting charged particles from ambient plasma surrounding Saturn’s rings [38].

This invocation of an ambient ring plasma itself presents a puzzle, because macroscopic solid lumps in the optically thick B ring are powerful plasma sinks, so one might expect those lumps to mop up ambient plasma before the dust grains can do so. Into the 2000s, physicists accounted for this by positing that ambient plasma was replenished by meteors and meteoroids crashing into Saturn’s rings [39, 40, 38]. When a meteoroid collides with a body in orbit around Saturn, a backward-propagating shock through the meteoroid compresses and heats it, producing hot, partially ionized vapour [39]. This generation by collisions would replace plasma absorbed by the dust and other solid ring material. But a group of space physicists has controvorted this meteoroid impact hypothesis in favour of a proposal based on cosmic rays and thunderstorms, a proposal which has received recent support from plasma physicists [41]. Cosmic rays arriving at Saturn’s cloud tops during lightning-producing thunderstorms can trigger avalanches of electrons, which

“beam along magnetic field lines into space” [42, p. 1]. As these energetic electron beams curl away from the planet, some shoot into Saturn’s rings, where they immediately charge the ring matter negatively and ionize lingering gas. Once both the fine dust grains and the larger ring particles are negatively charged, they repel each other, lifting the fine dust out of the ring plane to cause spokes. According to the proponents of this model, it can directly explain various features of the spokes, such as their rapid (“practically instantaneous”) formation, more frequent occurrence of spokes “in the outer B ring’s morning sector”, and the “variety of spoke morphologies at formation” [42, p. 2]. This newer model could be verified by concurrent observation of Saturnian thunderstorms and “spokes at the footprint of magnetic filed [sic] lines mapping back to the[ir] regions in the atmosphere” [41, p. 878].

1.2.3 Semiconductor processing

Space is not the only place where dust infiltrates plasmas. Back on Earth, “the use of low-temperature, partially ionized plasmas in manufacturing and materials processing” has boomed since the end of the 1980s [43, p. 2164], and a particularly important application of plasmas in manufacturing is semiconductor fabrication, where plasmas are used to etch and deposit material onto substrates [44, p. 7]. Such fabrication must take place in extremely clean conditions, because even nanoscopic solid particles can cause short circuits or gaps in the sub-microscopic features of a semiconductor device [45]. Semiconductor manufacturers were therefore dismayed to discover that solid particle contamination continued to occur even after “modern clean-rooms [...] reduced the once appreciable contamination” from the ambient environment [46, p. 1876], because the processing plasmas themselves generate contaminating specks of dust [45].

Until the late 1980s this in-situ dust production was relatively unimportant, because processing plasmas were only one source of contamination among several, and a minority source at that (figure 1.3). But from 1985 to the mid-1990s, increasing automation, better training of staff, ever cleaner clean rooms, and increasingly pure input materials meant that people and clean rooms became virtually irrelevant as sources of contamination [47]. As processing plasmas came to produce more contaminant dust than any other manufacturing step, interest in characterizing the formation of that dust and its behaviour in the plasma mounted [48].

Dust formation proceeds in two main stages. The first, lasting only a few seconds when driven by homogeneous chemical reactions, is the agglomeration of nanoscopic clusters of atoms [49]. (I leave aside the much less understood case of dust formation by heterogeneous reactions [50].) In a low-pressure silane (SiH_4) discharge — a low-temperature plasma system routinely used in semiconductor fabrication — these initial clusters are silicon crystallites with a diameter $\approx 2 \text{ nm}$, and they themselves form within milliseconds of the discharge being switched on [49]. As the clusters link together the average solid particle size increases linearly [49, 51]. Ultimately the solid particles become large enough to collect individual plasma electrons and ions at a non-negligible rate, inaugurating the second phase, where the solid particles continue to grow either by simple collection of electrons and ions [52], or by colliding with each other and sticking together [50].

Although the newly formed dust particles capture both electrons and ions from the ambient

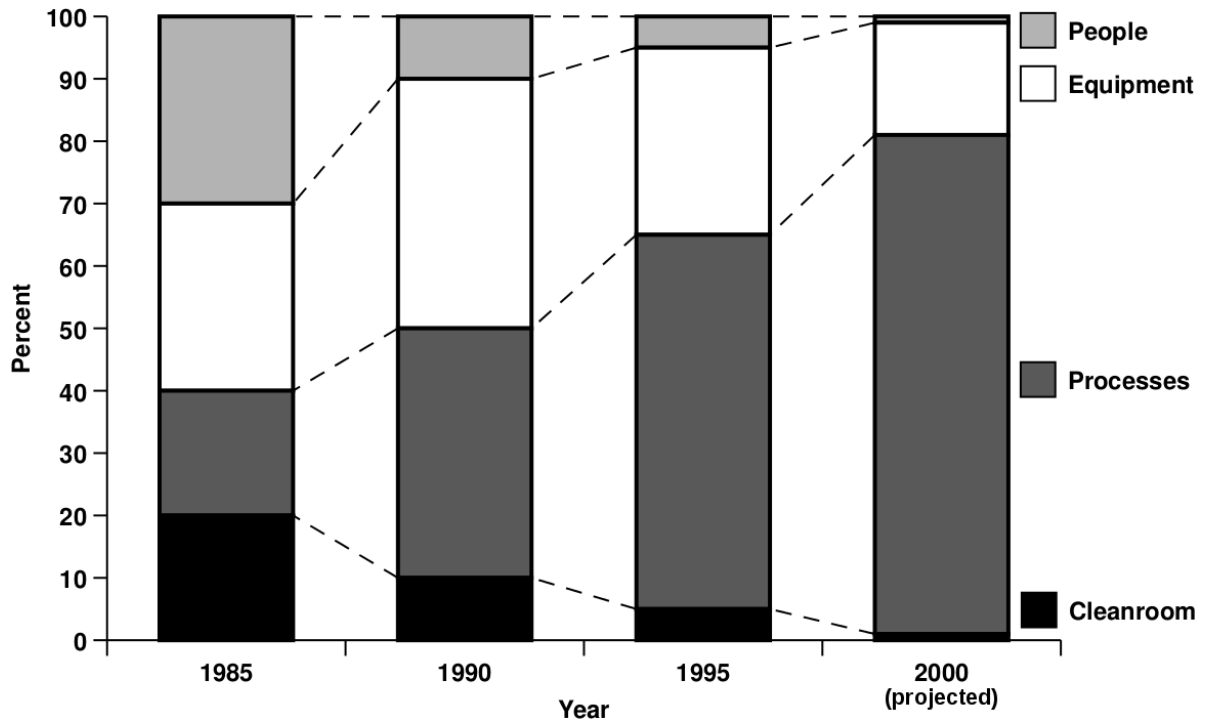


Figure 1.3: Wafer-contamination sources in microchip manufacturing, adapted from [47, p. 3-2, fig. 3-3].

plasma, they initially capture electrons at a faster rate than ions, because the electrons, being lighter than the ions, move more quickly. The dust therefore acquires a negative charge. The higher electron mobility likewise means that every other exposed surface in the plasma chamber charges to a negative electric potential, including the product being processed in the chamber. The chamber walls therefore repel the dust, blocking the dust from leaving the plasma and suspending the dust in the chamber as long as the plasma is present. Once the plasma process (whether etching, deposition, or vapour decomposition) is complete, however, the operator switches off the discharge and the plasma dissipates, as does the negative wall potential. The walls then cease to repel the dust, which falls from the middle of the chamber onto whatever semiconductor product (typically a silicon wafer) was being processed [48].

Ab initio nucleation in the plasma itself is not the sole dust source. Dust can also flake off the walls of the plasma chamber, especially in deposition processes, which have the side effect of coating the chamber walls, not just the intended product [48]. Temperature variation in a growing film on a chamber wall produces thermal-mechanical stresses which ultimately break the film, at which point the film's stored elastic energy ejects pieces of loosened material [53].

Having discovered that flaked-off and freshly nucleated dust particles were contaminating their devices, researchers sought means of reducing dust exposure and cleaning silicon products between processing stages. They had some success: dust contamination is no longer an overwhelmingly dominant source of defects in integrated circuits, though it is still an important one [54], and semiconductor manufacturers continue to spend “billions of dollars” a year attacking the

contamination problem [55, p. 98]. This may seem an exorbitant amount to spend on dust, but a back-of-the-envelope calculation suggests it is commensurate with the cost of dust contamination.[‡] A silicon wafer is divided into 50–1000 microchips [57], usually about 300 [58, p. xiv]. According to unusually detailed results from an IBM defect-reduction project at a Vermont fabrication facility, a typical wafer suffers ~ 1 foreign material defect (a number I derive by summing mean defect rates plotted for six fabrication processes in a conference report [59]). This implies a foreign material defect rate of about 1 in 300 microchips, or 0.3%. In 2014 the semiconductor industry had sales of \$336 billion [60], so under the simplifying assumptions that (1) all sales revenue comes from selling microchips and (2) the contamination defect rate is 0.3% across all product lines, the industry rejects $\sim \$1$ billion of contaminated microchips annually. If only because of the semiconductor industry’s sheer size, dust in semiconductor-processing plasmas endures as a billion-dollar-a-year problem.

1.2.4 Tokamaks

Thermonuclear fusion has been investigated as a prospective power source since the 1940s [61, 62, 63, 64]. The basic obstacle to generating power by thermonuclear fusion has been the need to trap the fusion fuel, and its heat, in a circumscribed region at extremely high temperature. Fusion, putting it crudely, amounts to banging light atomic nuclei into each other so hard that the nuclei merge exothermically into a heavier nucleus. This is easier said than done. Atomic nuclei repel each other because they are positively charged, so they must have atypically great kinetic energy (tens of thousands of electronvolts at the least [65, p. 16]) to collide and merge.

Scientists have proposed several technologies to master this obstacle and forge a route to exploiting fusion as a continuous energy source [66]. The most promising is the tokamak, invented in the USSR in 1950 [67]. Tokamaks are doughnut-shaped chambers which use strong magnetic fields to contain a plasma at a temperature $\sim 10^8$ K, the fields being necessary to hold the plasma’s hot core away from the chamber’s solid walls [68, p. 2]. The fuel undergoing fusion in a tokamak is a plasma simply because it is so hot — the fuel’s electrons have enough kinetic energy to pull free of their nuclei, rendering the fuel a soup of electrons and nuclei.

Plasma in a tokamak is not entirely pure [69]. Interactions between the tokamak’s interior surfaces and the plasma’s outer edge (as well as the products of the fusion reactions) make dust particles [70] which can survive between the cooler outer plasma and the tokamak’s interior walls. Tokamak plasmas can generate dust in several ways: triggering sputtering or arcing from the tokamak interior [69]; loosing flakes of material previously (re-)deposited on the interior; coagulation of individual atoms on interior surfaces or directly “from supersturated vapor”; “and possibly” by the same lower-temperature dust-formation mechanisms as “in reactive process

[‡]A back-of-the-envelope estimate is the most an outsider like myself can offer. Semiconductor manufacturers have never been keen to publish comprehensive quality-control data, and they have become more secretive still in the 21st century. Such information as is published tends to come from academia rather than industry, and more recent academic papers often turn out to be citing old data, or indeed nothing at all. One mischievous *Chinese Physics* paper [56, p. 1796] “suggests that particles are responsible for 75% of the yield loss in volume-manufacturing of very large-scale integration [sic] integrated circuits”, justifying its claim with citations to two earlier *CP* papers, one of which does not exist (volume 12, page 21 — the reference list of an unrelated paper on chaos) and another which mentions no “75%” statistic.

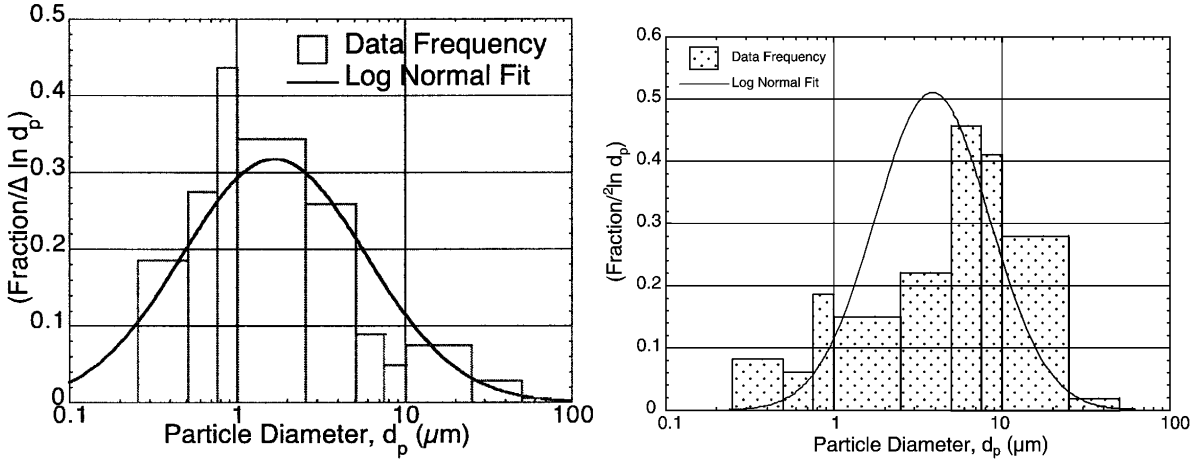


Figure 1.4: Diameter distributions of dust collected from tokamaks; solid curves represent fitted lognormal distributions. *Left*: distribution for dust from “the very bottom of the ASDEX-Upgrade vessel, behind the lower divertor structure” [71, p. 158, fig. 3]. *Right*: distribution for dust “from plasma-exposed surfaces in the upper divertor region of NSTX” [72, p. 1001, fig. 2].

plasmas” [70, pp. 3864 & 3866].

Tokamak operators have collected dust from tokamaks to estimate the size distributions of the dust grains tokamaks produce. Tabulating size data from seven tokamaks (DIII-D, TFTR, Alcator C-mod, JET, TEXTOR, Tore Supra, and ASDEX-Upgrade), Sharpe, Petti, & Bartels recorded median grain-diameter estimates between 0.6 and 27 μm , and geometric standard deviations of diameter ranging from 2.0 to 3.1 [71, p. 159]. Representing the dispersions of diameter with geometric standard deviations made particular sense because a “large majority of dust samples analyzed” by optical microscopy had lognormal size distributions [71, p. 158]. Sharpe et al. exhibited the specific example of the diameter distribution of dust from the base of the ASDEX-Upgrade tokamak, which appeared broadly lognormal (fig. 1.4, left). Not every observed distribution has proven lognormal. Among newer samples from the NSTX tokamak, most had “distributions that reasonably fit log-normal distributions” [72, p. 1001], but at least one deviated noticeably from a lognormal distribution (fig. 1.4, right).

At the time of Sharpe et al.’s review, researchers “generally” measured the sizes of collected grains by “[s]izing and counting” them “with the optical microscope” [71, p. 158]. This method has the disadvantage of missing grains of diameter $\lesssim 0.2 \mu\text{m}$, leaving the size distribution of those grains unknown. To investigate those small grains, physicists have occasionally used laser scattering instead [73]. The most revealing instance of this is Smirnov et al.’s application of Mie theory to laser scattering results from the DIII-D tokamak [74], because teams of researchers led by William Carmack had earlier used optical microscopy to estimate the average grain diameter in the same tokamak [75, 76]. Where Carmack et al. found median grain radii of 0.25–1.0 μm , Smirnov et al. obtained mean grain radii of 0.16–0.18 μm , highlighting the laser scattering technique’s insensitivity to micron-sized and larger grains, and optical microscopy’s inability to

detect much smaller grains.[§]

As in semiconductor-processing plasmas, dust in tokamaks is a nuisance. Dust which reaches the core plasma contaminates it and wastefully radiates energy out of the plasma, though the latter problem is not nearly as bad for low-atomic-mass dust [77]. At the same time, dust which avoids the core plasma by loitering on the tokamak’s walls can reduce efficiency (by absorbing tritium fuel which would otherwise be used in fusion) and alter the behaviour of interior surfaces by coating them or blocking “gaps and crevices” [71, p. 157]. Dust may even cool the plasma enough to destabilize it, initiating a disruption, an abrupt termination of the plasma [77, 78]. Finally, tokamak dust can be dangerous in its own right, because it can be toxic, radioactive, and chemically reactive [79, 71].

These hazards are of special concern for the ITER tokamak [71], still under construction but designed to be larger than any tokamak built to date [80, 81]. ITER’s main walls will include the toxic element beryllium [82], so dust eroded from the walls will itself be toxic. Some of the dust in ITER will also be radioactive, because of tritium absorption from the plasma and activation by high-energy particles [79]. Last of all, much of the dust will be chemically reactive because of its high surface-area-to-mass ratio. A particular worry is that the dust could prove adept at oxidizing in the presence of steam, ready to produce explosive hydrogen gas in the event of accidental coolant loss [79]. ITER’s engineers do not regard these safety risks as insuperable, as evidenced by the fact that building work on ITER continues (albeit at a glacial pace [83]), but it is another constraint they must take into account.

1.3 Quantitative properties of dust and plasmas

Though short and prefatory, the previous section’s tour of dust in plasmas teems with numbers. This is a fine illustration of the impossibility of rigorously discussing, let alone modelling, dust in plasmas without characterizing it quantitatively. Some of the most fundamental properties have appeared already, namely the number density and temperature of a plasma, and the size of the dust particles in a plasma. This dissertation uses the following notation for these quantities: n_e and n_i are respectively the electron number density (electrons per cubic metre) and ion number density (ions per cubic metre) in a plasma; T_e and T_i are the electron temperature and the ion temperature, both in Kelvin; and a is a dust grain’s size in metres. For simplicity of modelling and exposition I assume throughout that any plasma under discussion has only one ion species; this makes it unnecessary to account for different ion species having different temperatures or densities. Where I write about particle species in general, I drop the subscripts and write just “ n ” or “ T ”.

These are not the only relevant properties, of course. One can refer to a particle’s “charge state”, its net charge in units of the elementary charge $e = +1.6 \times 10^{-19}$ C. I write a dust grain’s

[§]This numerical comparison if anything understates the difference between the averages, because grain size distributions are positively skewed, and would usually have larger means than medians. Had Carmack et al. reported mean grain radii like Smirnov et al., rather than medians, Carmack et al.’s range of averages would likely be higher than the 0.25–1.0 μm I can quote here.

charge state as q , and an ion's as Z . In this dissertation Z is usually taken to be +1. Individual plasma particles each have a velocity \mathbf{v} , a speed $v = |\mathbf{v}|$, and a mass m (and as with n and T , “ e ” and “ i ” subscripts denote electrons and ions respectively). Electrostatic effects being important in plasmas, the electric potential ϕ also makes appearances.

As always in physics, some dimensionless combinations of variables turn out to have special importance, and I define these as variables in their own right. Θ is T_i/T_e , the ion-to-electron temperature ratio. The ion-to-electron mass ratio m_i/m_e is equally notable, so I define μ as its square root. (The square root proves a little more convenient than the ratio itself.) Finally, η is $e\phi/(k_B T_e)$, the electric potential relative to distant plasma, normalized by the ambient-electron thermal energy.

1.4 Spherical dust grains

Analyzing dust particles of arbitrary shape is a major challenge. My models simplify away this difficult aspect of reality by treating all dust particles as spheres, which allows the models to invoke results based on spherical symmetry. In keeping with this, a is always a dust grain's *radius* in the remainder of this dissertation.

The models further assume the dust grains to be *equipotential* spheres, i.e. spheres with the same electric potential ϕ everywhere on their surface. By the principle of superposition, that potential is the potential from the sphere's own charge qe plus the potential from charge separation in the plasma around the sphere. When the sphere is small enough, charge separation's contribution to ϕ is negligible compared to that of the sphere's qe , and one may define ϕ at the sphere's surface solely in terms of qe :

$$\phi \equiv \frac{qe}{4\pi\epsilon_0 a} \quad (1.1)$$

In this special case η 's value at a sphere's surface is

$$\eta_a \equiv \frac{e\phi}{k_B T_e} = \frac{e^2 q}{4\pi\epsilon_0 k_B T_e a} \quad (1.2)$$

which means, among other things, that η_a is always negative if q is negative.

η_a and q are the main dependent variables of interest in this dissertation, as they represent the most salient properties of a dust grain, namely its electric potential and electric charge. They are key variables because they determine the electrostatic forces on a grain in a plasma, and so the grain's motion. My models of η_a and q in later chapters could, therefore, serve as a basis for better understanding the motion of dust in actual plasma environments like those enumerated above. But before elucidating my models, it is sensible to review earlier lemmas and theories about plasmas, dust, and the charging of dust in plasmas.

Chapter 2

Existing theories and simulations of spherical grain charging

Everything is vague to a degree you do not realize till you have tried to make it precise

Bertrand Russell (1918),
“The Philosophy of Logical Atomism”, §1

Essentially, all models are wrong, but some are useful.

George E. P. Box and Norman R. Draper (1987),
Empirical Model-Building and Response Surfaces, p. 424

2.1 Basic lemmas

Models of dust grain charging need foundations. These foundations are a fundamental law of how a body charges in a plasma, and mathematical results which describe, for a particle species in a plasma at thermodynamic equilibrium, the probability distribution of velocity v for that species, and how n depends on ϕ .

2.1.1 Fundamental law of charging

A lot of computation is involved in predicting how a specific body charges up in a specific plasma, but one law of charging always applies as long as certain conditions hold. Because the law is general, no fine-grained knowledge of a specific system is necessary to deduce it; the law follows from rudimentary physical and mathematical considerations.

The fundamental law of charging is that at equilibrium, the charge of a body in a plasma is negative, assuming the body does not emit any negative charge. Section 1.2.3 has already alluded to the law’s basis: a plasma’s electrons moving more quickly than the plasma’s ions because electrons are far lighter than ions. Plasma physics being as complex as it is, there are some subtleties here, so prudence demands a more systematic justification for this law.

A body may charge by absorbing electrons, positive ions, and negative ions. I start by assuming negligible absorption of negative ions; the law turns out to hold regardless. The body's equilibrium charge $q_0 e$ is then the charge at which the average negative current from absorbing electrons cancels out the average positive current from absorbing positive ions.

Represent the body's charge as qe ; the average electron current onto the body as $I_e(q)$; and the average ion current onto the body $I_i(q)$. Physically, $|I_e(q)|$ is strictly increasing in q because a more positive charge on the body attracts electrons and a more negative charge on the body repels them. Likewise, $I_i(q)$ is strictly decreasing in q because the body repels more ions if it becomes more positively charged. It is then a theorem that any equilibrium charge q_0 satisfying $|I_e(q_0)| = I_i(q_0)$ is unique. A proof by contradiction: suppose multiple values of q satisfy the equilibrium equality, two of which values are q_1 and q_2 with $q_1 > q_2$; then $|I_e(q_1)| = I_i(q_1)$, $|I_e(q_2)| = I_i(q_2)$, and, from the strict monotonicity of $|I_e(q)|$ and $I_i(q)$, $|I_e(q_2)| < |I_e(q_1)| = I_i(q_1) < I_i(q_2)$, implying $|I_e(q_2)| < I_i(q_2)$ and contradicting the assumption that $|I_e(q_2)| = I_i(q_2)$.

I now observe that in general the electric current I of a plasma's particle species onto a body is

$$I = nA\langle v_{in} \rangle Ze \quad (2.1)$$

where n is the species' number density at the body's surface (and assumed constant over the body's surface); A the body's surface area; $\langle v_{in} \rangle$ the average inward, perpendicular velocity of particles impinging on the body; and Z the charge state of each particle. The only one of these quantities which depends on the body's charge qe is n , and A and e are the same for all particle species, so

$$\frac{I_i(q)}{|I_e(q)|} = \frac{n_i(q)\langle v_{in,i} \rangle Z}{n_e(q)\langle v_{in,e} \rangle} \quad (2.2)$$

where Z now just represents an ion's charge state. When $q = 0$ the body is uncharged and $n_i(q) = n_e(q)$ because the body neither attracts nor repels the plasma particles. Ergo

$$\frac{I_i(0)}{|I_e(0)|} = \frac{\langle v_{in,i} \rangle Z}{\langle v_{in,e} \rangle} \quad (2.3)$$

The next step is to invoke the equipartition theorem: that at thermal equilibrium, each degree of freedom associated with a particle's motion has an average energy of $k_B T/2$, T being the particle species' temperature. Equating this energy with a particle's translational motion along a given axis implies that a particle's typical speed v along a given axis is $\sqrt{k_B T/m}$. Applying this to the inward, perpendicular motion of electrons and ions,

$$\frac{I_i(0)}{|I_e(0)|} = \frac{Z\sqrt{k_B T_i/m_i}}{\sqrt{k_B T_e/m_e}} \equiv Z \frac{\sqrt{\Theta}}{\mu} \quad (2.4)$$

In almost all plasmas at equilibrium, the ions are protons or heavier particles, are singly or doubly charged, and are no hotter than the electrons. In these circumstances $Z \leq 2$, $\Theta \lesssim 1$ and

$m_i/m_e \geq m_p/m_e$, so

$$\frac{I_i(0)}{|I_e(0)|} \lesssim \frac{2}{\mu} \leq \frac{2}{\sqrt{m_p/m_e}} \ll 1 \quad (2.5)$$

That is, the ion current onto an uncharged body in a plasma is far smaller in magnitude than the electron current onto the body. Combined with the strict monotonicity of $I_i(q)$ and $|I_e(q)|$, it follows that the equilibrium charge q_0 is negative. Another proof by contradiction: suppose $q_0 \geq 0$; monotonicity would then have $|I_e(q_0)| \geq |I_e(0)|$ and $I_i(q_0) \leq I_i(0)$; inequality (2.5) shows that $I_i(0) < |I_e(0)|$; therefore $I_i(q_0) \leq I_i(0) < |I_e(0)| \leq |I_e(q_0)|$, inconsistent with the equilibrium requirement that $I_i(q_0) = |I_e(q_0)|$. It cannot be the case that $q_0 \geq 0$, so q_0 must be negative: the fundamental law.

Having put the law on a firm footing, one may easily explain why the law remains true when negative ions are present. One can represent the effect of negative ions by making $|I_e(q)|$ bigger for every q , while retaining that function's monotonicity (a more negative q implies repelling more negative ions, as well as repelling more electrons). Inequality (2.5) remains true, and thus the fundamental law must remain true.

The law need not remain true if the body emits enough negatively charged particles, because then there is a negative electric current *from* the body as well as one onto it, and the outgoing current may dominate the incoming current. The most common way for this to happen is thermionic emission: a body in a plasma being so hot that the electrons at its surface have enough kinetic energy to break free from the surface. If the body sloughs off electrons at a fast enough rate, it can maintain a positive charge.

2.1.2 Boltzmann relation

Charged particles experience a force where they encounter a change in ϕ . These forces attract or repel the particles, depending on the signs of ϕ and each particle's q , but either way the end result is to make n depend on ϕ for a charged particle species. How, precisely?

If there are no sources or sinks of particles, the relationship between n and ϕ turns out to be straightforward at thermodynamic equilibrium, and is known as the Boltzmann relation. The Boltzmann relation (BR) is so straightforward that some authors do not bother with a complete derivation [84, pp. 5 & 18] or indeed any at all [85, p. 7]. For reference I paraphrase a typical fluid-mechanical derivation from Bellan's textbook [86, pp. 8–9].

Represent the particle species as a continuous fluid of particles with well-defined $n(\mathbf{r})$ and velocity $\mathbf{v}(\mathbf{r})$, both functions of position, \mathbf{r} . This fluid has a pressure $P(\mathbf{r})$, spatial gradients in which imply a force on the fluid. The total force on the fluid is then the sum of any Lorentz force and the pressure gradient force, and neglecting magnetic fields and particle collisions, the fluid's equation of motion is

$$m \frac{d\mathbf{v}(\mathbf{r})}{dt} = qe\mathbf{E}(\mathbf{r}) - \frac{\nabla P(\mathbf{r})}{n(\mathbf{r})} \quad (2.6)$$

where q is the species' charge state. At thermodynamic equilibrium the equation's left-hand side is zero, and the species' temperature T does not change over time or space. Supposing now that

the particle species is an ideal gas, $P(\mathbf{r}) = n(\mathbf{r})k_B T$, and

$$0 = qe\mathbf{E}(\mathbf{r}) - \frac{\nabla(n(\mathbf{r})k_B T)}{n(\mathbf{r})} = qe\mathbf{E}(\mathbf{r}) - k_B T \frac{\nabla n(\mathbf{r})}{n(\mathbf{r})} \implies -qe\nabla\phi(\mathbf{r}) = k_B T \frac{\nabla n(\mathbf{r})}{n(\mathbf{r})} \quad (2.7)$$

integrating which over space gives

$$-qe\phi(\mathbf{r}) = k_B T \ln n(\mathbf{r}) + \text{constant} \quad (2.8)$$

Exponentiating,

$$n(\mathbf{r}) = n(\phi(\mathbf{r})) \propto \exp\left(-\frac{qe\phi(\mathbf{r})}{k_B T}\right) \quad (2.9)$$

Fixing the potential's zero point at the location where $n(\phi(\mathbf{r}))$ equals a reference density of n_0 ,

$$n(\phi(\mathbf{r})) = n_0 \exp\left(-\frac{qe\phi(\mathbf{r})}{k_B T}\right) \quad (2.10)$$

which is the BR. For electrons in particular $q = -1$ and the BR has the trivial expression

$$n_e(\eta) = n_0 \exp(\eta) \quad (2.11)$$

in terms of the normalized electric potential

$$\eta \equiv \frac{e\phi}{k_B T_e} \quad (2.12)$$

Notice that the BR only accounts for variation in n caused by variation in ϕ ; the effects of sources and sinks do not enter into the formula, and near a source or sink the BR is liable to incorrectly estimate the species' density.

2.1.3 Maxwell-Boltzmann velocity distribution

From eq. (2.10), the BR is indifferent to position per se; the BR can tell apart a particle's possible locations only by the particle's $\phi(\mathbf{r})$ at each location. At equilibrium the chance of finding a particle at a point in space is simply proportional to the exponential of the particle's normalized potential energy at that point.

One might ask whether this fact generalizes from real space to phase space, and from potential energy to the total energy. The answer would be that it does: Boltzmann's distribution law asserts that the probability of a system's state being occupied is proportional to $\exp(-E/(k_B T))$, "where T is the system's absolute temperature" and E is the state's energy [87, p. 2].

A particle's phase space is the six-dimensional space of the particle's possible position \mathbf{r} and velocity \mathbf{v} . A point in phase space is synonymous with a state, and Boltzmann's distribution law applies, though I must pay tribute to the continuity of the plasma particle's phase space by referring to "probability density" rather than "probability". The probability density of a particle

occupying a point in phase space is proportional to

$$\exp\left(-\frac{E}{k_B T}\right) = \exp\left(-\frac{qe\phi(\mathbf{r}) + K(\mathbf{v})}{k_B T}\right) = \exp\left(-\frac{qe\phi(\mathbf{r})}{k_B T}\right) \exp\left(-\frac{K(\mathbf{v})}{k_B T}\right) \quad (2.13)$$

where the energy E associated with the point in phase space is the sum of the potential energy $qe\phi(\mathbf{r})$ and the kinetic energy $K(\mathbf{v})$. Observing that $\phi(\mathbf{r})$ depends only on \mathbf{r} and $K(\mathbf{v})$ depends only on \mathbf{v} , I may treat the position and velocity subspaces, and their associated energies, separately and infer that the probability density $f(\mathbf{v})$ of a particle occupying a point in the velocity subspace has the proportionality

$$f(\mathbf{v}) \propto \exp\left(-\frac{K(\mathbf{v})}{k_B T}\right) \quad (2.14)$$

A particle with velocity \mathbf{v} has kinetic energy $K(\mathbf{v}) = m|\mathbf{v}|^2/2$, neglecting relativistic effects, and the probability density of the particle's location in the velocity phase space then has the form

$$f(\mathbf{v}) \propto \exp\left(-\frac{m|\mathbf{v}|^2}{2k_B T}\right) \quad (2.15)$$

Being a probability distribution over \mathbf{v} , $f(\mathbf{v})$ satisfies the normalization condition

$$\int_{\mathbf{v}} f(\mathbf{v}) d^3 \mathbf{v} = 1 \quad (2.16)$$

In Cartesian coordinates $\mathbf{v} = v_x \hat{\mathbf{x}} + v_y \hat{\mathbf{y}} + v_z \hat{\mathbf{z}}$ and the normalization condition is

$$\int_{-\infty}^{+\infty} \int_{-\infty}^{+\infty} \int_{-\infty}^{+\infty} C \exp\left(-\frac{m|\mathbf{v}|^2}{2k_B T}\right) dv_x dv_y dv_z = 1 \quad (2.17)$$

where C is a normalization constant to be deduced. Writing the triple integral as a product of single integrals,

$$\int_{-\infty}^{+\infty} \exp\left(-\frac{mv_x^2}{2k_B T}\right) dv_x \int_{-\infty}^{+\infty} \exp\left(-\frac{mv_y^2}{2k_B T}\right) dv_y \int_{-\infty}^{+\infty} \exp\left(-\frac{mv_z^2}{2k_B T}\right) dv_z = \frac{1}{C} \quad (2.18)$$

evaluating which gives

$$\left(\frac{2\pi k_B T}{m}\right)^{3/2} = \frac{1}{C} \quad (2.19)$$

thus $C = (m/(2\pi k_B T))^{3/2}$ and the velocity distribution is

$$f(\mathbf{v}) = \left(\frac{m}{2\pi k_B T}\right)^{3/2} \exp\left(-\frac{m|\mathbf{v}|^2}{2k_B T}\right) \equiv \left(\frac{m}{2\pi k_B T}\right)^{3/2} \exp\left(-\frac{m(v_x^2 + v_y^2 + v_z^2)}{2k_B T}\right) \quad (2.20)$$

which is the Maxwell-Boltzmann velocity distribution, the standard velocity distribution for particles in a rarefied gas or plasma at thermodynamic equilibrium [88, p. 168]. The distribution

is isotropic: any component v_j of the velocity has the probability distribution

$$f(v_j) = \sqrt{\frac{m}{2\pi k_B T}} \exp\left(-\frac{mv_j^2}{2k_B T}\right) \quad (2.21)$$

which one can deduce by marginalizing* the full distribution in eq. (2.20) over each possible pair of components, and observing that the marginal distributions of v_x , of v_y , and of v_z are identical. (A more expeditious if less rigorous route to the same conclusion is to rewrite $f(\mathbf{v})$ as a product of three functions, each dependent on a distinct velocity component orthogonal to the others, then observe that the functions are otherwise identical.)

The Maxwell-Boltzmann velocity distribution implies a corresponding probability distribution for the speed $v = |\mathbf{v}|$. It is imperative to resist the temptation to try deriving the speed distribution by taking eq. (2.15) and overwriting $f(\mathbf{v})$ with $f(v)$. In isolation that is an illegitimate step because $f(\mathbf{v})$ is expressly a probability distribution over \mathbf{v} , and to transform it into a probability distribution over v one must account for the accompanying transformation of the variable space too. This warrants not the equation of $f(\mathbf{v})$ and $f(v)$ but the equation

$$f(\mathbf{v}) d^3 \mathbf{v} = f(v) dv \implies f(\mathbf{v}) \frac{d^3 \mathbf{v}}{dv} = f(v) \quad (2.22)$$

and to deduce $f(v)$ I must compute the ratio of the differentials in the two different spaces. The easiest means of computing it is to rewrite $d^3 \mathbf{v}$ once more, this time explicitly in terms of v . Transforming the differential into spherical coordinates achieves that:

$$d^3 \mathbf{v} = v^2 (\sin \theta) dv d\psi d\theta \implies \frac{d^3 \mathbf{v}}{dv} = v^2 (\sin \theta) d\psi d\theta \quad (2.23)$$

where ψ and θ are \mathbf{v} 's azimuthal and zenith angles respectively [89]. Substituting into eq. (2.22),

$$f(v) = f(\mathbf{v}) v^2 (\sin \theta) d\psi d\theta \quad (2.24)$$

Substituting in eq. (2.20),

$$f(v) = f(v; \psi, \theta) = \left(\frac{m}{2\pi k_B T} \right)^{3/2} \exp\left(-\frac{mv^2}{2k_B T}\right) v^2 (\sin \theta) d\psi d\theta \quad (2.25)$$

where the transformation of $f(\mathbf{v})$ into $f(v)$ brings along the unwanted angles ψ and θ . I do not want v 's joint distribution with ψ and θ , only v 's unconditional distribution. To quash the nuisance

*Translating from statisticial jargon to physicist-friendly jargon: “marginalizing” a multivariate probability distribution is integrating out all but one random variable to obtain that variable’s unconditional (“marginal”) distribution.

variables and extract the unconditional distribution I marginalize:

$$\begin{aligned}
f(v) &= \int_0^{2\pi} \int_0^\pi f(v; \psi, \theta) d\theta d\psi \\
&= \left(\frac{m}{2\pi k_B T} \right)^{3/2} v^2 \exp\left(-\frac{mv^2}{2k_B T}\right) \int_0^{2\pi} \int_0^\pi (\sin \theta) d\theta d\psi \\
&= 4\pi \left(\frac{m}{2\pi k_B T} \right)^{3/2} v^2 \exp\left(-\frac{mv^2}{2k_B T}\right)
\end{aligned} \tag{2.26}$$

the Maxwell-Boltzmann speed distribution.

2.1.4 Maxwellian flux onto an absorbing sphere

A sphere's absorption of charged particles from a plasma constitutes an electric current onto the sphere. For a given charged particle species this current is the product

$$I = 4\pi a^2 q e n \langle v_{\text{in}} \rangle \tag{2.27}$$

where $\langle v_{\text{in}} \rangle$ is the particles' mean velocity in the inward direction perpendicular to the sphere's surface.

Assuming the particles have a Maxwell-Boltzmann velocity distribution, isotropy allows me to employ eq. (2.21) to compute $\langle v_{\text{in}} \rangle$ as

$$\langle v_{\text{in}} \rangle = \int_0^{+\infty} v_{\text{in}} f(v_{\text{in}}) dv_{\text{in}} = \int_0^{+\infty} \sqrt{\frac{m}{2\pi k_B T}} \exp\left(-\frac{mv_{\text{in}}^2}{2k_B T}\right) v_{\text{in}} dv_{\text{in}} = \sqrt{\frac{k_B T}{2\pi m}} \tag{2.28}$$

where the lower integration limit is 0 and not $-\infty$ because at the sphere's surface there are no outward-moving particles (since they would have had to emerge from the absorbing surface). Substituting into the formula for I ,

$$I = 4\pi a^2 q e n \times \sqrt{\frac{k_B T}{2\pi m}} \tag{2.29}$$

Often this expression is most useful when its dependence on the sphere's surface potential ϕ_a is made most explicit by incorporating the Boltzmann relation:

$$I = 4\pi a^2 q e n_0 \exp\left(-\frac{qe\phi_a}{k_B T}\right) \sqrt{\frac{k_B T}{2\pi m}} \tag{2.30}$$

2.1.5 Order-of-magnitude estimate of η_a

The physics presented in the preceding subsections is enough for an order-of-magnitude estimate of an absorbing sphere's equilibrium η_a , η_a being the normalized electric potential on the sphere's surface. If there are no negative ions in the plasma around the sphere, equilibrium obtains when the ion current I_i onto the sphere cancels out the electron current I_e onto the sphere. From eq.

(2.30),

$$I_e = -4\pi a^2 e n_0 \times \sqrt{\frac{k_B T_e}{2\pi m_e}} \exp(\eta_a) \quad (2.31)$$

Eq. (2.30) does not give I_i , however, because the Boltzmann relation is inapplicable to ions in this situation. The fundamental charging law means that $\eta_a < 0$, so the sphere actively attracts ions and substantially depletes the ion distribution function in the surrounding space. This invalidates the Boltzmann relation, which requires that there be no (non-negligible) particle sinks in the region of interest.

Barred from using the more sophisticated eq. (2.30), I make the simplifying approximation that I may neglect η_a 's effect on n_i , and substitute $n = n_i = n_0$ (and $q = Z$) into eq. (2.29) to get

$$I_i = 4\pi a^2 Z n_0 \times \sqrt{\frac{k_B T_i}{2\pi m_i}} \quad (2.32)$$

Equating I_i and $-I_e$,

$$\sqrt{\frac{k_B T_i}{2\pi m_i}} Z = \sqrt{\frac{k_B T_e}{2\pi m_e}} \exp(\eta_a) \quad (2.33)$$

which has the solution

$$\eta_a = \ln \frac{Z \sqrt{\Theta}}{\mu} \quad (2.34)$$

Although primitive, this order-of-magnitude estimate of the equilibrium η_a elegantly isolates the plasma parameters most relevant to grain charging: the ion charge state Z and the square roots of the ion-to-electron mass ratio and temperature ratio. One could also use eq. (2.34) to check the plausibility of more complex models, because, as long as there is no reason to expect η_a to alter I_i by orders of magnitude, any workable model should give an η_a of similar magnitude to eq. (2.34).

It may be helpful to apply eq. (2.34) to two specific cases which recur in the rest of this section. Both cases assume a singly charged ($Z = 1$) plasma with ions at the same temperature as electrons ($\Theta = 1$), reducing eq. (2.34) to $\eta_a = -\ln \mu$. The two cases are of a plasma with H^+ ions ($\mu = 43$), for which the formula predicts $\eta_a = -3.76$, and a plasma with Ar^{1+} ions ($\mu = 271$), where the formula predicts $\eta_a = -5.60$. Generalizing from these numbers suggests the heuristic that $|\eta_a| \sim 4$ in a singly ionized plasma with $\Theta = 1$. This vindicates a posteriori the starting assumption of eq. (2.31); the heuristic suggests that η_a would generally be negative enough to repel almost all approaching electrons, legitimating the application of the Boltzmann relation to the electrons.

2.1.6 Debye-Hückel screening and potential function

Knowing the Boltzmann relation opens up a route to estimating $\phi(r)$ precisely in a plasma outside an equipotential sphere. The most popular model for deriving $\phi(r)$'s functional form in plasma physics is that inspired by Peter Debye and Erich Hückel. Debye and Hückel originally built their model [90] to estimate $\phi(r)$ around an ion in an electrolyte medium, but the essence of their model is equally applicable to charged spheres in a plasma medium, because plasmas and electrolytes have in common the property most relevant to the model: they both contain electrons which are

free to move in response to electric fields. The Debye-Hückel (DH) model, as adapted to plasma physics [85, §1.4], hinges on the observation that these electrons move away from regions where ϕ is more negative and towards regions where ϕ is more positive, an effect known as “screening” or “shielding” because it means that electrons rearrange themselves to help cancel out — that is, screen out or shield — spatial variations in ϕ in a plasma. In concrete terms, a negatively charged body in a plasma pushes away nearby electrons, ensconcing itself in a sheath region where ions outnumber electrons.

The DH model quantifies this effect with the Boltzmann relation and deduces $\phi(r)$ from it as follows. Assume a plasma, within which is an equipotential sphere with r the distance from its centre. Spherical symmetry obtains, and Poisson’s electrostatic equation in spherical coordinates has the form

$$\nabla^2 \phi(r) = \frac{1}{r^2} \frac{d}{dr} (r^2 \phi'(r)) \equiv \phi''(r) + \frac{2\phi'(r)}{r} = \frac{e}{\epsilon_0} (n_e(r) - Zn_i(r)) \quad (2.35)$$

Making the simplifying assumption that screening arises from the electrons’ behaviour alone and not the slower response of the ions, I take $n_i(r)$ to be n_0/Z everywhere, n_0 being the electron density infinitely far from the sphere where $\phi(r) \rightarrow 0$. Thus

$$\phi''(r) + \frac{2\phi'(r)}{r} \approx \frac{e}{\epsilon_0} (n_e(r) - n_0) \quad (2.36)$$

By the fundamental law of charging, the sphere has a negative equilibrium $\phi(a)$, in which case it repels electrons at equilibrium. Assuming equilibrium, and that the sphere keeps away enough electrons that I may neglect its absorption of impinging electrons, the Boltzmann relation approximates $n_e(r)$ well, and

$$\phi''(r) + \frac{2\phi'(r)}{r} \approx \frac{en_0}{\epsilon_0} \left(\exp\left(\frac{e\phi(r)}{k_B T_e}\right) - 1 \right) \quad (2.37)$$

which is a nonlinear differential equation similar to the Poisson-Boltzmann equation. To render it soluble, I suppose that $\phi(r) \ll k_B T_e/e$, so I may approximate the exponential term as a linear one:

$$\phi''(r) + \frac{2\phi'(r)}{r} \approx \frac{en_0}{\epsilon_0} \left(1 + \frac{e\phi(r)}{k_B T_e} - 1 \right) \equiv \frac{e^2 n_0}{\epsilon_0 k_B T_e} \phi(r) \quad (2.38)$$

At this stage textbook derivations[†] often reveal the final solution with, at most, a hand-waving reference to boundary conditions, much as a magician might wave their hands when pulling a rabbit from a hat. I propose to motivate the solution less mysteriously. Observe that near a small, charged sphere in a plasma, the main determinant of $\phi(r)$ is the charge Q on the sphere rather than the more diffuse sheath region of space charge around the sphere. Neglecting that sheath’s effect, $\phi(r)$ is essentially the sphere’s vacuum potential function:

$$\lim_{\substack{r \rightarrow a \\ a \rightarrow 0}} \phi(r) = \frac{Q}{4\pi\epsilon_0 r} \propto \frac{1}{r} \quad (2.39)$$

[†]Those of Bellan [86, p. 10], Boyd & Sanderson [85, p. 8], Chen [91, p. 10], and Hutchinson [92, p. 58], to take four examples.

Mimicking the form of that limit suggests the ansatz $\phi(r) = f(r)/r$. Putting the ansatz into eq. (2.38) gives

$$\frac{f''(r)}{r} \approx \frac{e^2 n_0}{\epsilon_0 k_B T_e} \frac{f(r)}{r} \quad (2.40)$$

which amounts to $f''(r) \propto f(r)$. This family of differential equations may be solved by the characteristic-equation method, which in this case produces the general solution

$$f(r) = C_1 \exp\left(\frac{r}{\lambda_D}\right) + C_2 \exp\left(-\frac{r}{\lambda_D}\right) \quad (2.41)$$

where C_1 and C_2 are arbitrary constants and

$$\lambda_D \equiv \sqrt{\frac{\epsilon_0 k_B T_e}{e^2 n_0}} \quad (2.42)$$

is the plasma parameter known as the electron Debye length or electron Debye distance, which is the sheath's characteristic size in this model. Assuming again that $\phi(r) \rightarrow 0$ infinitely far away,

$$\lim_{r \rightarrow \infty} \phi(r) = 0 \quad (2.43)$$

a boundary condition which requires $C_1 = 0$. The boundary condition represented by eq. (2.39) then implies $C_2 = Q/(4\pi\epsilon_0)$ and hence the complete DH solution

$$\phi(r) = \frac{Q}{4\pi\epsilon_0 r} \exp\left(-\frac{r}{\lambda_D}\right) \quad (2.44)$$

which is the vacuum potential function multiplied by an extra term which decays exponentially with distance. The sheath around a negatively charged sphere therefore attenuates the electric potential (and field) due to the sphere, on a length scale of λ_D . (This does not mean that $\phi(r)$ and $\phi'(r)$ always decay over distances $\sim \lambda_D$. If the sphere is much smaller than λ_D then the $1/r$ aspect of the DH solution can cause the potential and field to decay on a scale of $a \ll \lambda_D$.)

Particularly attentive readers may notice that this derivation contradicts itself. At one step it assumes the sphere repels enough electrons for the Boltzmann relation to hold, which requires $|\phi_a| \gtrsim k_B T_e/e$. But the very next step assumes $|\phi(r)| \ll k_B T_e/e$ at all r . The two assumptions cannot both be true, so the derivation is internally inconsistent.

No plasma-physics textbook seems to parry this objection. Fortunately, one paper [93] confronts it by acknowledging that linearizing $\phi(r)$ implies an unphysical negative density of repelled particles (ions in that paper's case, electrons here) where $\phi(r) < -k_B T/e$. The expedient of defining a “hole” around the sphere where the repelled-particle density is assumed zero eliminates the issue, and the resulting Debye-Hückel-hole theory reduces to the original DH theory arbitrarily far from the grain or if $n_0/T_e^3 \rightarrow 0$. There is also T. H. Gronwall et al.'s more rigorous mathematical treatment of the Debye-Hückel problem, which generates the DH $\phi(r)$ as a first-order approximation [94, 95]. These papers corroborate eq. (2.44) despite its dubious origins.

A more accessible means of testing the DH solution's robustness is to solve the Poisson-

Boltzmann-like equation without linearizing it, and compare that non-linearized equation's solution to the DH solution obtained by linearization. To maximize the comparison's generality one may solve the dimensionless version of eq. (2.37),

$$\eta''(\xi) + \frac{2}{\xi} \eta'(\xi) \approx \exp(\eta(\xi)) - 1 \quad (2.45)$$

obtained by defining $\xi \equiv r/\lambda_D$. Linearizing the dimensionless equation implies the dimensionless DH solution for $\eta(\xi)$,

$$\eta(\xi) = \eta_a \frac{a/\lambda_D}{\xi} \exp\left(\frac{a}{\lambda_D} - \xi\right) \quad (2.46)$$

where η_a denotes $\eta(a/\lambda_D)$, the normalized electric potential on the sphere's surface. Because this DH solution is a good approximate solution to eq. (2.45) where $|\eta(\xi)| \ll 1$, one may use eq. (2.46) and its spatial derivative as the boundary conditions for numerically solving eq. (2.45), as long as those conditions are applied at a ξ where $\eta(\xi)$ is tiny.

The resulting system of equations is closed but has a circularity: the boundary conditions are defined in terms of η_a , but η_a 's value is undefined until the boundary conditions are fully defined. This does not mean there is no solution — for a given a/λ_D , one and only one η_a value is consistent with the system of equations — but it does mean an accurate numerical solution can be found only by iteratively converging on the η_a value that produces an internally consistent result.

This, it transpires, is convenient for the purpose of testing eq. (2.46)'s validity. Consider the extreme case where the DH solution is virtually perfect, perhaps because η_a is so small that $|\eta(\xi)| \ll 1$ for all ξ and the linearization is everywhere an exceptionally good approximation. In that extreme situation, using eq. (2.46) as a boundary condition introduces negligible error, and numerically integrating eq. (2.45) inwards to $\xi = a/\lambda_D$ would give an $\eta(a/\lambda_D)$ value nearly identical to the η_a value chosen for eq. (2.46), whatever the latter value was. By contrast, when the DH solution is invalid, eq. (2.46) and its derivative are incorrect boundary conditions, and using them as boundary conditions for a numerical integration would lead to an $\eta(a/\lambda_D)$ value different to the η_a value substituted into eq. (2.46). The disparity between the η_a value put into eq. (2.46) and the $\eta(a/\lambda_D)$ obtained by numerical integration is therefore an index of the DH solution's internal inconsistency.

Figure 2.1 uses this to illustrate the DH solution's self-consistency as a function of a/λ_D and the assumed η_a . It is apparent that the DH solution becomes self-consistent in the $a/\lambda_D \rightarrow 0$ limit, and that self-consistency improves as the normalized surface potential $\eta_a \rightarrow 0$. Even when both quantities are non-negligible, the DH solution is impressively robust given its crude origins. Supposing $|\eta_a| \sim 4$ (the heuristic from §2.1.5), the DH solution is grossly wrong only when $a/\lambda_D \gtrsim 0.2$.

2.1.7 Bohm criterion and Bohm speed

The previous section models the ion sheath around a negatively charged sphere by considering the electrons alone. In practice the ions are not unresponsive to the sphere's attractive $\phi(r)$ and the electrons' flight, and at equilibrium the sphere continually attracts ions from afar. To

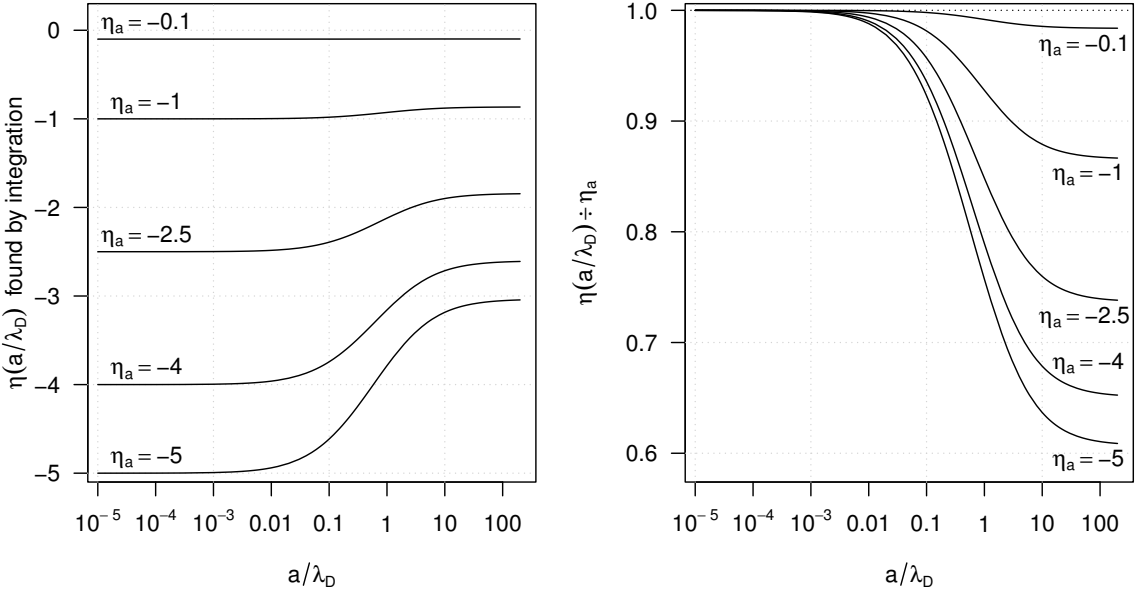


Figure 2.1: Results of numerically integrating eq. (2.45) with the DH solution as a boundary condition, assuming various values of a/λ_D and η_a . *Left:* $\eta(a/\lambda_D)$ as obtained by integration; the numerical solution is self-consistent when $\eta(a/\lambda_D)$ matches the assumed η_a . *Right:* $\eta(a/\lambda_D)/\eta_a$, an index of the numerical solutions' self-consistency; the closer the ratio to 1, the greater the self-consistency.

investigate this ion motion one has to relax the assumption that n_i remains constant, and bring in the continuity and energy conservation equations for the ions, which I now proceed to do. However, since one cannot solve the resulting system of equations in spherical geometry without appealing to extra ad hoc assumptions, I solve the equations instead in planar geometry, combining elements of David Bohm's original 1949 derivation [96] and Karl-Ulrich Riemann's beautifully pedantic treatment [97]. After arriving at the relevant solution in planar geometry I give the more assumption-heavy path to the analogous result in spherical geometry.

Because a planar surface amounts to a spherical surface with an infinite radius of curvature, the solution of the planar system serves as a substitute for the spherical system's solution in the large-sphere limit ($a/\lambda_D \rightarrow \infty$). In planar geometry the analogue of a negative $\phi(r)$ around an infinitely large sphere is a negative $\phi(x)$ in front of an infinitely large plane, with x the (perpendicular) distance from the plane. As in the spherical case, the motion due to the potential is the only motion of interest here, so I neglect both collisions and the random thermal motion of the ions, and suppose that the ions are stationary at infinity. The ions' motion is therefore exclusively in the \hat{x} direction and solely a function of $\phi(x)$.

Defining the sheath edge as the locus $x = x_0$ where the ion density approximately returns to normal, I take $n_i(x_0) = n_0/Z$ and the potential as zero, so $\phi(x_0) = 0$. Writing the ion speed and ion number density there as v_0 and n_0 respectively, the ion continuity equation and energy

conservation equation are

$$n_i(x_0)v_0 = \frac{n_0}{Z}v_0 = n_i(x)v \iff \frac{n_i(x)}{n_0} = \frac{v_0}{Zv} \quad (2.47)$$

$$\frac{m_i v_0^2}{2} = \frac{m_i v^2}{2} + Ze\phi(x) \iff v = \sqrt{v_0^2 - \frac{2Ze\phi(x)}{m_i}} \quad (2.48)$$

Combining the two equations,

$$\frac{n_i(x)}{n_0} = \frac{v_0}{Z} \left(v_0^2 - \frac{2Ze\phi(x)}{m_i} \right)^{-1/2} \quad (2.49)$$

Writing this result in terms of the dimensionless electric potential η ,

$$\frac{n_i(x)}{n_0} = \frac{v_0}{Z} \left(v_0^2 - \frac{2Zk_B T_e \eta(x)}{m_i} \right)^{-1/2} \equiv \frac{1}{Z} \left(1 - \frac{2Zk_B T_e \eta(x)}{m_i v_0^2} \right)^{-1/2} \quad (2.50)$$

Next I reprise the Boltzmann relation and Poisson's electrostatic equation, this time in Cartesian coordinates:

$$\nabla^2 \phi(x) = \phi''(x) = \frac{e}{\epsilon_0} \left(n_0 \exp\left(\frac{e\phi(x)}{k_B T_e}\right) - Z n_i(x) \right) \quad (2.51)$$

Reexpressing the equation in terms of η and the dimensionless distance $\zeta \equiv x/\lambda_D$, with λ_D the electron Debye length,

$$\eta''(\zeta) = \exp(\eta(\zeta)) - \frac{Z n_i(\zeta)}{n_0} \quad (2.52)$$

Translating eq. (2.50) to normalized coordinates and substituting it in,

$$\eta''(\zeta) = \exp(\eta(\zeta)) - \left(1 - \frac{2Zk_B T_e \eta(\zeta)}{m_i v_0^2} \right)^{-1/2} \quad (2.53)$$

Multiplying through by $\eta'(\zeta)$,

$$\eta''(\zeta) \eta'(\zeta) \equiv \frac{1}{2} \frac{d((\eta'(\zeta))^2)}{d\zeta} = \exp(\eta(\zeta)) \eta'(\zeta) - \left(1 - \frac{2Zk_B T_e \eta(\zeta)}{m_i v_0^2} \right)^{-1/2} \eta'(\zeta) \quad (2.54)$$

Integrating both sides with respect to ζ ,

$$\frac{(\eta'(\zeta))^2}{2} = \exp(\eta(\zeta)) + \frac{m_i v_0^2}{Z k_B T_e} \left(\sqrt{1 - \frac{2Zk_B T_e \eta(\zeta)}{m_i v_0^2}} \right) + \text{arbitrary constant} \quad (2.55)$$

Invoking the requirement that $\eta'(\zeta)$ vanishes where $\eta(\zeta)$ vanishes (i.e. as $\zeta \rightarrow \infty$) eliminates the arbitrary constant:

$$\frac{(\eta'(\zeta))^2}{2} = (\exp(\eta(\zeta)) - 1) + \frac{m_i v_0^2}{Z k_B T_e} \left(\sqrt{1 - \frac{2Zk_B T_e \eta(\zeta)}{m_i v_0^2}} - 1 \right) \quad (2.56)$$

This equation cannot be integrated again analytically. Fortunately another integration is unnecessary because the equation's most important corollary emerges if one expands the equation in powers of $\eta(\zeta)$:

$$\frac{(\eta'(\zeta))^2}{2} = \left(\eta(\zeta) + \frac{\eta^2(\zeta)}{2} + \mathcal{O}(\eta^3(\zeta)) \right) + \frac{m_i v_0^2}{Z k_B T_e} \left(-\frac{Z k_B T_e}{m_i v_0^2} \eta(\zeta) - \left(\frac{Z k_B T_e}{m_i v_0^2} \right)^2 \frac{\eta^2(\zeta)}{2} + \mathcal{O}(\eta^3(\zeta)) \right) \quad (2.57)$$

Near the sheath's edge, $\eta \approx 0$, only the lowest-order terms matter and the equation simplifies to

$$(\eta'(\zeta))^2 \approx \left(1 - \frac{Z k_B T_e}{m_i v_0^2} \right) \frac{\eta^2(\zeta)}{2} \quad (2.58)$$

η being everywhere real, η^2 and the left-hand side must both be non-negative. According to eq. (2.58) that requirement is satisfiable only if $Z k_B T_e / (m_i v_0^2) \leq 1$. The ion velocity v_0 at the sheath edge must therefore satisfy

$$v_0 \geq c_s \equiv \sqrt{\frac{Z k_B T_e}{m_i}} \quad (2.59)$$

where c_s is the ion sound speed, also known in this context as the Bohm velocity or Bohm speed, and inequality (2.59) is known as the Bohm criterion [97].

Put into words, the final inequality shows that ions must enter the sheath in front of a plane at at least the sound speed. Bohm himself characterized the inequality as a requirement for the existence of a “stable” sheath [96, p. 82], but the criterion’s physical meaning is simpler and clearer than that: it is a criterion for whether an ion sheath begins at $x = x_0$ at all. According to the model, the normalized net charge density ρ_f/n_0 may be written as a function of the normalized electric potential alone:

$$\frac{\rho_f}{n_0} = \left(1 - 2 \frac{c_s^2}{v_0^2} \eta \right)^{-1/2} - \exp(\eta) = \left(\frac{c_s^2}{v_0^2} - 1 \right) \eta + \mathcal{O}(\eta^2) \quad (2.60)$$

An ion sheath is a region of net-positive space charge, i.e. a region where $\rho_f/n_0 > 0$. Just inside the sheath, $|\eta| \ll 1$, and presumably $\eta < 0$ because the sheath is in front of a negatively charged plane. Eq. (2.60) then means that v_0 must be at least c_s , for otherwise ρ_f/n_0 would be negative just inside the sheath, contradicting the starting assumption that the sheath be a region of net-positive space charge.

It is easy and useful to expand on this verbal explanation of the Bohm speed. Were one to consider the electrons alone, as in the adapted Debye-Hückel model of §2.1.6, no special criterion or explanation would be needed; one could note that a negatively charged surface repels electrons, and immediately infer that this electron depletion would leave behind a zone of net-positive space charge. But the Bohm model accounts for acceleration of ions towards the surface, and the continuity equation implies that this acceleration lowers the ions’ number density. It is then no longer obvious that a positive sheath forms. Conceivably the decline in ion density due to acceleration outweighs the decline in electron density due to repulsion. Pursuing that point, eq. (2.60) indicates that the ion density *would* in fact become less than the electron density were the ions moving too slowly [97]. The Bohm criterion merely quantifies this physical fact.

The criterion has a further implication. With the ions assumed stationary at infinity, they must accelerate on their journey towards the sheath to satisfy the Bohm criterion, and so the model implies the existence of a *pre-sheath*, a quasi-neutral region of plasma where an electric field accelerates ions to at least the Bohm speed on the approach to the sheath.

Switching to spherical geometry, the equations for the Bohm model become less tractable. In spherical geometry the Laplacian operator has a more complicated definition and the normalized ion density becomes

$$\frac{n_i(r)}{n_0} = \frac{r_0^2 v_0}{r^2 v} = \frac{r_0^2}{r^2} \left(1 - \frac{2Ze}{m_i v_0^2} \phi(r) \right)^{-1/2} \quad (2.61)$$

producing the normalized electrostatic Poisson equation

$$\frac{1}{\xi^2} \frac{d}{d\xi} (\xi^2 \eta'(\xi)) \equiv \eta''(\xi) + \frac{2}{\xi} \eta'(\xi) = \exp(\eta(\xi)) - \frac{\xi_0^2}{\xi^2} \left(1 - \frac{2Zk_B T_e}{m_i v_0^2} \eta(\xi) \right)^{-1/2} \quad (2.62)$$

where $\xi \equiv r/\lambda_D$, and $\xi_0 \equiv r_0/\lambda_D$ denotes the sheath edge in normalized radii. As opposed to the planar eq. (2.53), eq. (2.62) is burdened with extra powers of the spatial coordinate. These cannot be readily eliminated and they prevent one from integrating after multiplying the equation through by $\eta'(\xi)$.

To reproduce the Bohm criterion in spherical geometry, one has to use a different tactic, such as assuming that the sheath edge may also be defined as the locus where the plasma ceases to be quasi-neutral [98]. Subject to this assumption, quasi-neutrality obtains for all $\xi > \xi_0$ and one may take $Zn_i(\xi)/n_0 \approx \exp(\eta(\xi))$ there. Thus

$$\frac{Zn_i(\xi)}{n_0} = \frac{\xi_0^2}{\xi^2} \left(1 - \frac{2Zk_B T_e}{m_i v_0^2} \eta(\xi) \right)^{-1/2} \approx \exp(\eta(\xi)) \quad (2.63)$$

i.e.

$$\frac{\xi^2}{\xi_0^2} \left(1 - 2 \frac{c_s}{v_0^2} \eta(\xi) \right)^{1/2} \exp(\eta(\xi)) \approx 1 \quad (2.64)$$

Differentiating with respect to ξ and rearranging for $\eta'(\xi)$ gives the quasi-neutral estimate of $\eta'(\xi)$

$$\eta'(\xi) \approx \frac{2}{\xi} \left(\frac{1}{2\eta(\xi) + 1 - v_0^2/c_s^2} - 1 \right) \quad (2.65)$$

Supposing that the breakdown of quasi-neutrality manifests mathematically as a singularity in the quasi-neutral $\eta(\xi)$ solution where its $\eta'(\xi)$ becomes infinite, quasi-neutrality fails where

$$\frac{2}{\xi} \left(\frac{1}{2\eta(\xi) + 1 - v_0^2/c_s^2} - 1 \right) \rightarrow \infty \quad (2.66)$$

This model applies to the space outside a sphere of nonzero size, so $\xi > 0$ and the singularity therefore occurs where

$$2\eta(\xi) + 1 - \frac{v_0^2}{c_s^2} = 0 \quad (2.67)$$

and since I selected the sheath edge as my locus of zero electric potential, the singularity — hence the breakdown of quasi-neutrality, hence the sheath edge — occurs where

$$1 - \frac{v_0^2}{c_s^2} = 0 \iff v_0 = c_s \quad (2.68)$$

which is the equality form of the Bohm criterion. There is therefore a basis for expecting ions to enter sheaths at the Bohm speed in both spherical and planar geometries, assuming negligible ion collisionality.

2.1.8 Quasi-neutrality

It is time to put some quantitative flesh on the bones of the terms “quasi-neutral” and “quasi-neutrality”, not least because physicists use the concept of quasi-neutrality to refer, confusingly, to two intimately related but distinct ideas.

The first is the *physical observation* that in most regions of a plasma much larger than λ_D , the magnitude of the plasma’s net charge density is much smaller than the charge-density magnitude of the plasma’s negative or positive species. In algebraic terms,

$$|Zn_i - n_e| \ll n_e \approx Zn_i \quad (2.69)$$

The physical reason for eq. (2.69) is that the charged particles of a plasma are free to move, so a plasma region with net charge of one sign tends to draw in charge of the opposite sign until it ceases to be a region with net charge.

The second is the mathematical approximation of assuming the positive charge density exactly cancels the negative charge density, i.e. that $Zn_i = n_e$. This exact equality is an assumption one makes to expedite the solution of mathematical models of plasmas. If the original models included Poisson’s equation, one discards Poisson’s equation when making the $Zn_i = n_e$ assumption.

Table 2.1 documents the two different kinds of meaning that physicists have given quasi-neutrality in their writing. My survey leaves out less general definitions which apply only in more exotic settings, such as Boyd & Sanderson’s defining quasi-neutrality as “ $\omega|\Omega_e|/\omega_p^2 \ll 1$ ” in the context of resistive magnetohydrodynamics [85, p. 60] and collisionless magnetohydrodynamics [85, p. 71]. My goal is not to make an all-inclusive list but to sample broadly the variation in definitions of quasi-neutrality.

The literature has also the phrase “plasma approximation”, which seems as if it should help clear up the muddle, because “plasma approximation” usually refers only to the mathematical $Zn_i = n_e$ assumption. In practice, dishearteningly, the phrase brings its own danger of ambiguity for two reasons. One reason is that some authors write about the plasma approximation as if it were an exact synonym for quasi-neutrality: Lieberman & Lichtenberg do so in their book’s main text [99, p. 40] and index [99, p. 755], Pécseli clarifies four times in *Waves and Oscillations in Plasmas* that quasi-neutrality is also called the “plasma approximation” [102, pp. 251, 281, 311, & 387], and Franklin’s *Plasma Phenomena in Gas Discharges* calls $n_e = n_i$ “the approximation of

Author(s)	Definition	Reference
Lieberman & Lichtenberg	“ $ Zn_i - n_e \ll n_e$ ” “ $n_e \approx n_i$ ”	[99, p. 40] [99, p. 405]
Boyd & Sanderson	“ $n_e \approx Zn_i$ ” and “ $Zn_i \approx n_e$ ” “ $Zn_i(r) = n_e(r)$ ” and “ $Zn_i = n_e$ ”	[85, pp. 57 & 64] [85, pp. 87 & 413]
Hutchinson	“ $n_e \approx Zn_i$ ” “ $n_e - n_i \ll n_e$ ” “ $n_i = n_e$ ”	[92, p. 5] [92, p. 63] [92, p. 327]
Chen	“ $n_i \approx n_e \approx n$ ”	[43, p. 10]
Somov	“ $\frac{Z_i n_i - n_e}{n_e} \ll 1$ ”	[100, p. 189]
Lifshitz & Pitaevskii	“ $\left \frac{z\delta N_i - \delta N_e}{\delta N_e} \right \sim \frac{a_e^2}{L^2} \ll 1$ ” “ $N_e = zN_i$ ”	[84, p. 150] [84, p. 150]
Franklin	“ $n_e = n_i$ ”	[101, p. 26]
Pécseli	“ $n_e = n_i$ ” “ $\varepsilon_0 \rightarrow 0 [\dots] n_e \approx n_i$ ”	[102, p. 251] [102, p. 252]

Table 2.1: Quantitative definitions of quasi-neutrality.

quasi-neutrality [101, p. 26] in chapter 2 before rechristening it “the plasma approximation” [101, p. 58] in chapter 4.[‡] The other reason is that calling the $Zn_i = n_e$ approximation the “plasma” approximation wrongly suggests that plasmas themselves satisfy $Zn_i = n_e$ exactly, which they do not. The whole point is that plasmas are *quasi-neutral*, “that is, neutral enough so that one can take $n_i \approx n_e \approx n [\dots]$ but not so neutral that all interesting electromagnetic forces vanish” [43, p. 10].

I have considered using “quasi-neutrality” myself to refer to only the approximate neutrality of real-world plasmas, and using a different phrase such as “neutral approximation” to refer to the $Zn_i = n_e$ assumption. In the final analysis, however, I think the gain in clarity from doing so would be cancelled out by the loss from introducing a new term, so I follow other physicists in using “quasi-neutral” and “quasi-neutrality” to represent both eq. (2.69) and $Zn_i = n_e$, especially because I think my uses of the words are clear enough in context. As penance I write this subsection to warn readers of the potential ambiguity.

2.2 Charging theories

Having established the key results of the previous section, I can use them to describe the standard theories of how a sphere charges in a plasma. The models predict the equilibrium η for an isolated

[‡]Franklin later arrived at another definition of quasi-neutrality, writing to me by email that “In my book, and I mean in my book quasi-neutrality is defined as equality of normalized densities to order ($\lambda dA/L$)**2 i.e. one does not employ Poisson’s equation. Few textbooks even use the term but my statement is in Lieberman and Lichtenberg” [103]. I did not find this more specific definition in Franklin’s book, and Lieberman and Lichtenberg assume it only to immediately obtain $|Zn_i - n_e| \ll n_e$, their explicit quasi-neutrality criterion [99, p. 40].

spherical grain in a plasma.

2.2.1 Allen, Boyd, & Reynolds (ABR)

ABR charging theory is a radial motion theory. It assumes the plasma ions are collisionless and cold, so that ions initially far from the grain simply fall in straight radial lines onto the grain through its attractive electric field. Allen, Boyd, and Reynolds's original paper [104] adumbrates the model but my description takes after the more recent and systematic treatment of Kennedy and Allen [8].

The basic strategy for computing η here is to derive an ordinary differential equation (ODE) which one can solve numerically for η . The ODE comes from Poisson's electrostatic equation, which is

$$\nabla^2 \phi = -\frac{\rho_f}{\epsilon_0} \quad (2.70)$$

where ρ_f is the space density of free charge. In a plasma ρ_f is the sum of the charge densities due to electrons and due to ions. Incorporating this fact, and employing the system's spherical symmetry,

$$\nabla^2 \phi = \frac{1}{r^2} \frac{d}{dr} \left(r^2 \frac{d\phi}{dr} \right) = \frac{e(n_e - Zn_i)}{\epsilon_0} \quad (2.71)$$

where r is the distance from a spherical dust grain's centre. The next stage is nondimensionalizing the equation by rewriting it in terms of the dimensionless electric potential η and the dimensionless radius $\xi \equiv r/\lambda_D$, with

$$\lambda_D \equiv \sqrt{\frac{\epsilon_0 k_B T_e}{n_0 e^2}} \quad (2.72)$$

being the electron Debye length and n_0 the electron number density infinitely far from the sphere, where $\eta \rightarrow 0$. Taking $Z = 1$, Poisson's equation becomes

$$\frac{1}{\xi^2} \frac{d}{d\xi} \left(\xi^2 \frac{d\eta}{d\xi} \right) = \frac{n_e}{n_0} - \frac{n_i}{n_0} \quad (2.73)$$

To make the equation meaningful in this situation, the right-hand ratios must be written in terms of η and ξ . The Boltzmann relation makes light work of rewriting n_e/n_0 :

$$n_e = n_0 \exp(\eta) \implies \frac{n_e}{n_0} = \exp(\eta) \quad (2.74)$$

Rewriting n_i/n_0 is more involved. One alternative expression for it comes from the inward current I_i of ions at radius $r \geq a$,

$$I_i = 4\pi r^2 e n_i v_{in} \quad (2.75)$$

where v_{in} is the inward radial ion velocity. Hence

$$\frac{n_i}{n_0} = \frac{I_i}{4\pi e n_0 r^2 v_{in}} \quad (2.76)$$

setting now the task of finding I_i and v_{in} . I turn to the electron current onto the sphere,

$$I_e = -4\pi a^2 e n_0 \times \sqrt{\frac{k_B T_e}{2\pi m_e}} \exp(\eta_a) \quad (2.77)$$

from eq. (2.30), where η_a is $\eta|_{r=a}$, the normalized surface potential. At equilibrium, I_e must exactly negate I_i at $r = a$, the sphere's surface:

$$I_i|_{r=a} = 4\pi a^2 e (n_i v_{\text{in}}|_{r=a}) = 4\pi a^2 e n_0 \times \sqrt{\frac{k_B T_e}{2\pi m_e}} \exp(\eta_a) \quad (2.78)$$

Because the ions are collisionless, conservation of particles guarantees that I_i is independent of r , assuming no ionization. Therefore I may substitute $I_i|_{r=a}$ into eq. (2.76) as I_i to get

$$\frac{n_i}{n_0} = \frac{4\pi a^2 e n_0 \times \sqrt{\frac{k_B T_e}{2\pi m_e}} \exp(\eta_a)}{4\pi e n_0 r^2 v_{\text{in}}} \equiv \frac{a^2 \times \sqrt{\frac{k_B T_e}{2\pi m_e}} \exp(\eta_a)}{r^2 v_{\text{in}}} \quad (2.79)$$

To find v_{in} I bring in the assumption that every ion has negligible kinetic energy infinitely far from the grain. Then an ion's kinetic energy is merely that acquired from the grain's attractive potential:

$$\frac{m_i v_{\text{in}}^2}{2} = -Ze\phi = -e\phi \quad (2.80)$$

a trivial rearrangement of which is

$$v_{\text{in}} = \sqrt{\frac{-2e\phi}{m_i}} = \sqrt{\frac{-2k_B T_e}{m_i}} \eta \quad (2.81)$$

Substituting into eq. (2.79) and simplifying,

$$\frac{n_i}{n_0} = \frac{a^2}{r^2} \sqrt{\frac{m_i}{4\pi m_e}} \frac{\exp(\eta_a)}{\sqrt{-\eta}} = \frac{v \exp(\eta_a)}{\xi^2 \sqrt{-\eta}} \quad (2.82)$$

where I wrap up the relevant dust and plasma properties in the parameter

$$v \equiv \left(\frac{a}{\lambda_D} \right)^2 \frac{\mu}{\sqrt{4\pi}} > 0 \quad (2.83)$$

recalling that $\mu \equiv \sqrt{m_i/m_e}$, representing the plasma's ion species. Substituting eqs. (2.74) and (2.82) into the dimensionless version of Poisson's equation,

$$\frac{d}{d\xi} \left(\xi^2 \frac{d\eta}{d\xi} \right) = \xi^2 \exp(\eta) - \frac{v \exp(\eta_a)}{\sqrt{-\eta}} \quad (2.84)$$

This final form of Poisson's equation is entirely in terms of ξ and η , except for the unknown surface potential η_a . However, computing η with the ODE requires two boundary conditions.

One boundary condition comes from observing that far away from the sphere, the plasma is

quasi-neutral, meaning that the left-hand side of eq. (2.84) is far smaller than $\xi^2 n_e/n_0$ and $\xi^2 n_i/n_0$. In algebraic terms,

$$\left| \frac{d}{d\xi} \left(\xi^2 \frac{d\eta}{d\xi} \right) \right| \ll \xi^2 \frac{n_e}{n_0} \approx \xi^2 \frac{n_i}{n_0} \iff \left| \frac{d}{d\xi} \left(\xi^2 \frac{d\eta}{d\xi} \right) \right| \ll \xi^2 \exp(\eta) \quad (2.85)$$

and for such large ξ , I take the left-hand side of Poisson's equation to be negligible, leading to

$$0 \approx \xi^2 \exp(\eta) - \frac{\nu \exp(\eta_a)}{\sqrt{-\eta}} \quad (2.86)$$

which has the implicit solution

$$\xi^2 \approx \frac{\nu \exp(\eta_a)}{\sqrt{-\eta} \exp(\eta)} \quad (2.87)$$

or, equivalently, the more cumbersome explicit solution

$$\eta \approx \frac{1}{2} W_0 \left(-\frac{2\nu^2 \exp(2\eta_a)}{\xi^4} \right) \quad (2.88)$$

where $W_0(z)$ is the principal branch of the [Lambert W function of \$z\$](#) [105, 106]. This constitutes one boundary condition for solving the ODE. A second may be found by differentiating the explicit solution:

$$\frac{d\eta}{d\xi} \approx \frac{-2W_0(-2\nu^2 \exp(2\eta_a)/\xi^4)}{(1 + W_0(-2\nu^2 \exp(2\eta_a)/\xi^4))\xi} \approx \frac{-4\eta}{(1 + 2\eta)\xi} \quad (2.89)$$

To choose a ξ at which to apply the boundary conditions, one must know where quasi-neutrality holds, because the boundary conditions assume quasi-neutrality. To estimate where quasi-neutrality obtains, I substitute the solution's derivative into eq. (2.85), the quantitative definition of quasi-neutrality:

$$\left| \frac{d}{d\xi} \left(\frac{-4\xi\eta}{1+2\eta} \right) \right| \equiv \left| \frac{-4\left(\eta + 2\eta^2 + \xi \frac{d\eta}{d\xi}\right)}{(1+2\eta)^2} \right| \ll \xi^2 \exp(\eta) \quad (2.90)$$

Re-applying eq. (2.89), the quasi-neutrality criterion becomes

$$\frac{-4\eta}{(1+2\eta)^2} \left| 1 - \frac{4}{1+2\eta} + 2\eta \right| \ll \xi^2 \exp(\eta) \quad (2.91)$$

Imposing the strategically chosen condition that $\xi > 2\sqrt{\nu} \exp(1/32 + \eta_a/2)$, eq. (2.88) then implies $\eta \gtrsim -1/16$ and

$$\left| 1 - \frac{4}{1+2\eta} + 2\eta \right| \lesssim \frac{207}{56} \quad (2.92)$$

and hence

$$\frac{-(207/14)\eta}{(1+2\eta)^2} \lesssim \frac{414}{343} \ll \xi^2 \exp\left(-\frac{1}{16}\right) \quad (2.93)$$

suffices to ensure quasi-neutrality, though for brevity I replace this with the more stringent requirement that $\xi \gg 2$. The conjunction of this $\xi \gg 2$ requirement and the earlier condition that $\xi > 2\sqrt{\nu} \exp(1/32 + \eta_a/2)$ therefore ensures quasi-neutrality.

For a given η_a , an algorithm can therefore solve for η as a function of ξ by defining a boundary

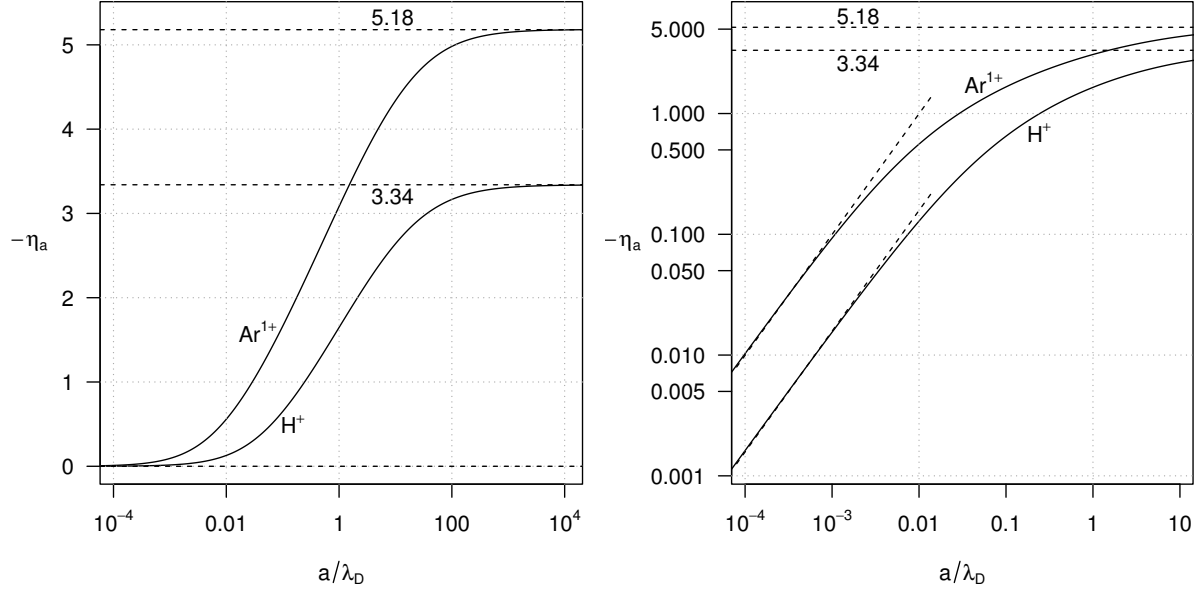


Figure 2.2: The ABR model’s predictions of η_a for an isolated dust grain of radius a in an H^+ plasma ($\mu = 43$) or in an Ar^{1+} plasma ($\mu = 271$). *Left:* log-linear axes; compare Kennedy and Allen’s figure 4 [8, p. 247]. *Right:* log-log axes; the sloping dashed lines plot $\exp(-1)\mu a/\lambda_D$.

at $\xi = \xi_b$ satisfying the conjunction; computing η and $d\eta/d\xi$ at $\xi = \xi_b$ with eqs. (2.88) and (2.89); then numerically integrating eq. (2.84) inwards to $\xi = a/\lambda_D$, the grain’s surface. The system might seem underspecified because there is no explicit expression for η_a , which might appear to prevent evaluation of eq. (2.84). But for a particular dust-in-plasma system with a particular ν , only one value of η_a gives a self-consistent solution; in general, substituting an arbitrary η_a into eq. (2.84) and the quasi-neutrality condition, and then integrating the ODE inwards leads to a value of η at $r = a$ different to the assumed η_a : a contradiction.

Practically, this system is a boundary value problem which a shooting method can solve; a computer can iteratively solve the system by assuming various η_a until it converges on the correct η_a for a particular ν . I wrote a computer program to solve the ABR model in this way, and had it compute η_a as a function of a/λ_D for an isolated sphere in a cold-ion plasma (figure 2.2). Writing the program meant resolving interesting numerical stability problems, but since they are irrelevant to the physics I banish them to appendix B.

I replicate Kennedy and Allen’s report [8] that in the model vanishingly small ($a/\lambda_D \rightarrow 0$) spheres have vanishingly small potentials, and that η_a converges on a finite asymptote as $a/\lambda_D \rightarrow \infty$. I extend the former finding by observing that, for hydrogen-based plasmas and singly-ionized argon plasmas, η_a is roughly proportional to $\mu a/\lambda_D$ when the latter is small, and I extend the latter finding by observing that

$$\lim_{a/\lambda_D \rightarrow \infty} \eta_a \approx 0.4189 - \ln \mu \quad (2.94)$$

an expression I discovered by computing η_a for many $(\mu, a/\lambda_D)$ pairs, estimating the $a/\lambda_D \rightarrow \infty$ limit of η_a for each μ , observing a nearly straight line when I plotted these estimated limits against

μ when μ had a logarithmic scale, and then regressing the estimated limits against $\ln \mu$. On the basis of unrigorous, post hoc algebra inspired by eq. (2.94) I conjecture that the limit has the closed-form expression

$$\lim_{a/\lambda_D \rightarrow \infty} \eta_a = \frac{(\ln 2\pi) - 1}{2} - \ln \mu \quad (2.95)$$

despite having no derivation from first principles to justify it.

2.2.2 Orbital-motion limited (OML)

ABR theory models the charging of a sphere in a plasma with cold ions, leaving aside the question of how a sphere charges in a plasma with ions of non-negligible kinetic energy. To answer the latter, I now turn to the most popular sphere-charging model, the OML theory of Harold M. Mott-Smith and Irving Langmuir [107]. My description of OML theory takes after those of Kennedy and Allen [9] and Willis [108], Willis's itself being adapted from Shukla and Mamun's [109, pp. 37–40].

Begin with an ion with charge Ze and initial speed v_∞ approaching a spherical grain from afar. The ion's impact parameter is b , the perpendicular distance between the sphere's centre and the ion's initial bearing. Neglecting collisions, whether the sphere absorbs the ion depends on the ion's v_∞ and b . Suppose there is an ion with some particular v_∞ and $b = b_{\text{crit}}$ such that the ion just grazes the grain's surface tangentially (figure 2.3). Suppose also that all ions with the same v_∞ but smaller b are collected and that all ions with the same v_∞ but larger b escape. Then the grain has an effective cross-section $\sigma = \pi b_{\text{crit}}^2$ to ions with a particular v_∞ . If nothing else this explains OML theory's name: the theory assumes that the tangential motion of approaching ions constrains the capturing cross-section the grain presents to them, so the grain's collection current is limited by the ions' orbital motion.

Conservation of angular momentum holds for approaching ions because the sphere exerts a central force by symmetry, and collisions are negligible by assumption. Equating a distant ion's angular momentum with the angular momentum as the same ion brushes against the sphere, $m_i v_\infty b_{\text{crit}} = m_i v_a a$, where v_a is the ion's speed as it grazes the grain tangentially. Therefore $b_{\text{crit}} = v_a a / v_\infty$, implying $\sigma = \pi v_a^2 a^2 / v_\infty^2$.

In the absence of collisions it is also easy to find the grazing ion's kinetic energy at infinity and its kinetic energy as it brushes the sphere. The ion's initial kinetic energy is $m_i v_\infty^2 / 2$ and its final kinetic energy is the initial energy plus the energy garnered by falling towards the grain:

$$\frac{m_i v_a^2}{2} = \frac{m_i v_\infty^2}{2} - Ze\phi_a \quad (2.96)$$

where ϕ_a is the grain's surface potential. It immediately follows that

$$v_a^2 = v_\infty^2 - \frac{2Ze\phi_a}{m_i} \quad (2.97)$$

and so

$$\sigma = \frac{\pi a^2}{v_\infty^2} \left(v_\infty^2 - \frac{2Ze\phi_a}{m_i} \right) = \pi a^2 \left(1 - \frac{2Ze\phi_a}{m_i v_\infty^2} \right) \quad (2.98)$$

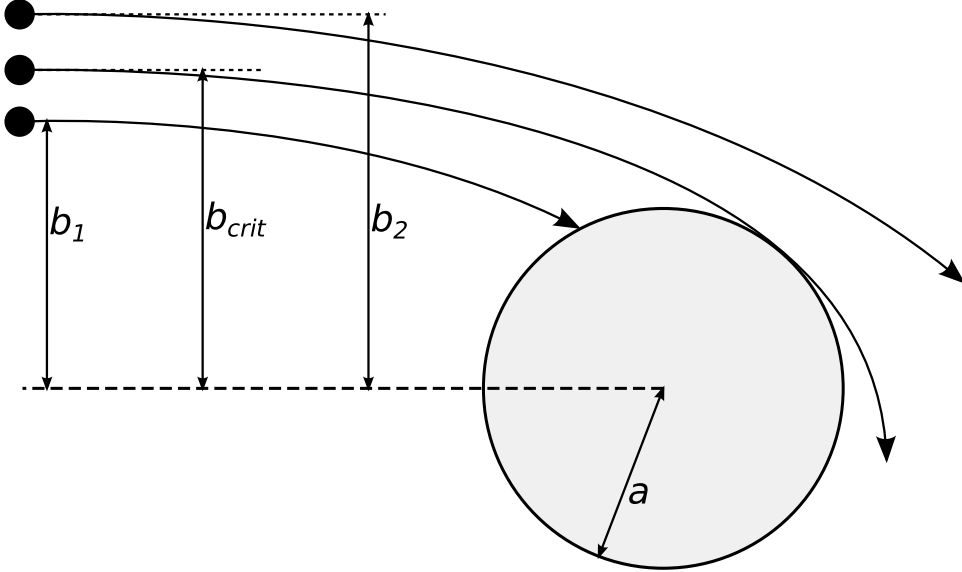


Figure 2.3: Trajectories of ions approaching a negatively charged dust grain, all with speed v_∞ at infinity, but differing impact parameters. The ion with impact parameter b_{crit} just grazes the grain tangentially, whereas an ion with impact parameter $b_1 < b_{\text{crit}}$ is absorbed and an ion with impact parameter $b_2 > b_{\text{crit}}$ escapes.

Given that the grain presents an effective cross-section of $\sigma(v_\infty)$ to ions at infinity with speed v_∞ , it will absorb such ions at a rate of $v_\infty n_i f(v_\infty) \sigma(v_\infty)$ where $f(v_\infty)$ is the probability distribution of the ions' v_∞ values and n_i is the faraway ion density. Integrating this absorption rate over all possible v_∞ values and multiplying by the ion charge Ze gives the total ion current onto the grain

$$I_i = Ze \int_0^\infty v_\infty n_i f(v_\infty) \sigma(v_\infty) dv_\infty \quad (2.99)$$

Far from the grain the ions presumably have a Maxwell-Boltzmann speed distribution (eq. (2.26)), so their v_∞ has the distribution

$$f(v_\infty) = 4\pi \left(\frac{m_i}{2\pi k_B T_i} \right)^{3/2} v_\infty^2 \exp\left(\frac{-m_i v_\infty^2}{2k_B T_i} \right) \quad (2.100)$$

and therefore

$$I_i = 4\pi^2 a^2 n_i Z e \left(\frac{m_i}{2\pi k_B T_i} \right)^{3/2} \int_0^\infty v_\infty^3 \left(1 - \frac{2Z e \phi_a}{m_i v_\infty^2} \right) \exp\left(\frac{-m_i v_\infty^2}{2k_B T_i} \right) dv_\infty \quad (2.101)$$

$$= 4\pi a^2 n_i Z e \times \sqrt{\frac{k_B T_i}{2\pi m_i}} \left(1 - \frac{Z e \phi_a}{k_B T_i} \right) \quad (2.102)$$

Now I have an expression for I_i all that is left is to equate it with I_e and solve that equation. I may assume the grain charges negatively (the law of charging), and repels most approaching electrons at equilibrium (§2.1.5). The electrons therefore, unlike the ions, approximately obey the

Boltzmann relation and I may approximate I_e with eq. (2.30):

$$I_e \approx -4\pi a^2 e n_0 \exp\left(\frac{e\phi_a}{k_B T_e}\right) \sqrt{\frac{k_B T_e}{2\pi m_e}} \quad (2.103)$$

At equilibrium $I_i + I_e = 0$. Substituting in eqs. (2.102) and (2.103), and cancelling out the identical factors on both sides,

$$Zn_i \times \sqrt{\frac{T_i}{m_i}} \left(1 - \frac{Ze\phi_a}{k_B T_i}\right) \approx n_0 \exp\left(\frac{e\phi_a}{k_B T_e}\right) \sqrt{\frac{T_e}{m_e}} \quad (2.104)$$

Plasmas being quasi-neutral, $Zn_i = n_0$, and

$$\sqrt{\frac{T_i}{m_i}} \left(1 - \frac{Ze\phi_a}{k_B T_i}\right) \approx \exp\left(\frac{e\phi_a}{k_B T_e}\right) \sqrt{\frac{T_e}{m_e}} \quad (2.105)$$

Rewriting the equation to use the dimensionless surface potential η_a , and the dimensionless plasma properties Θ and μ ,

$$\frac{\sqrt{\Theta}}{\mu} \left(1 - \frac{Z}{\Theta} \eta_a\right) \approx \exp(\eta_a) \quad (2.106)$$

Boiled down to this core, one can solve the OML potential equation for η_a . Allegedly the equation “must be solved numerically” [110, p. 1223] but it has the solution

$$\eta_a \approx \frac{\Theta}{Z} - W_0\left(\frac{\mu\sqrt{\Theta}}{Z} \exp\left(\frac{\Theta}{Z}\right)\right) \quad (2.107)$$

where W_0 is again the principal branch of the Lambert W special function. Figure 2.4 plots η_a as a function of Θ and μ for singly ionized plasmas ($Z = 1$). With $\Theta \sim 1$, the grain’s equilibrium surface potential is negative and usually 2–5 times $k_B T_e/e$ in magnitude. For the canonical case of a hydrogen-based plasma with $\Theta = 1$, $\eta_a = -2.504$ at a sphere’s surface.

It is worth returning attention to the model’s assumption that for every possible v_∞ there exists a critical impact parameter b_{crit} for which an ion grazes the sphere tangentially, and that this b_{crit} separates the range of impact parameters for which an ion hits the grain ($0 \leq b < b_{\text{crit}}$) from those for which an approaching ion avoids the grain ($b > b_{\text{crit}}$). This assumption, intuitive as it may be, need not be true. For a particular v_∞ there might instead be an “absorption radius” $r_A > a$ such that any ion coming within r_A of the grain’s centre is sure to be absorbed. If such an absorption radius exists for an ion with $b = b_0$, then if “all functions are smoothly varying”, ions with the same v_∞ but $b < b_0$ “would strike the [grain] with finite radial velocity” [9, p. 489]. Were $b_0 > b_{\text{crit}}$, the absorption radius would make a nonsense of b_{crit} ’s physical definition, because there would be no ion with the relevant v_∞ which could graze the grain tangentially; every ion with the relevant v_∞ would either hit the grain with some inward velocity, or miss the grain outright by a nonzero distance. Where absorption radii existed, OML theory’s prediction for η_a (eq. (2.107)) would then only be correct if b_{crit} happened to be at least b_0 for all absorption radii.

My description of absorption radii may sound quite abstract. To make the idea more concrete,

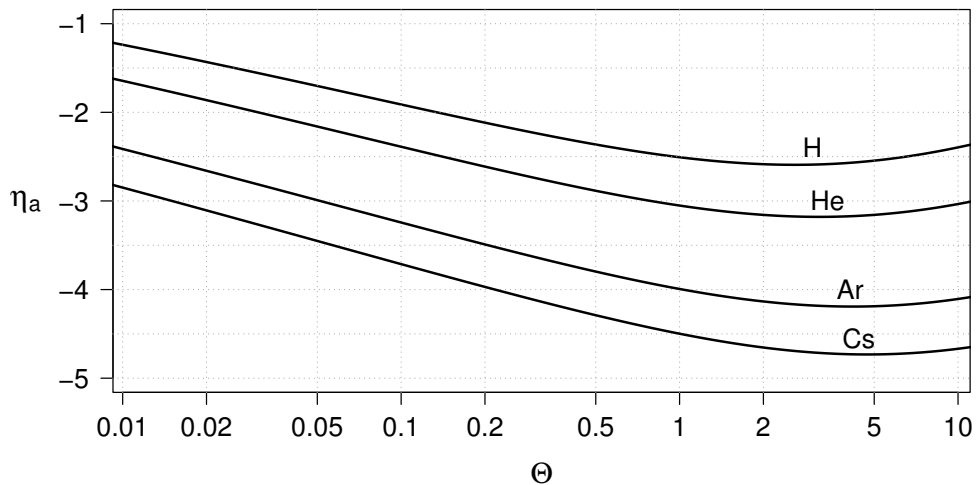


Figure 2.4: The normalized electric potential η_a at the surface of a sphere in a singly ionized ($Z = 1$) plasma, according to the OML model. As the ion species becomes heavier (caesium here chosen as a particularly heavy example) the sphere's equilibrium charge becomes ever more negative.

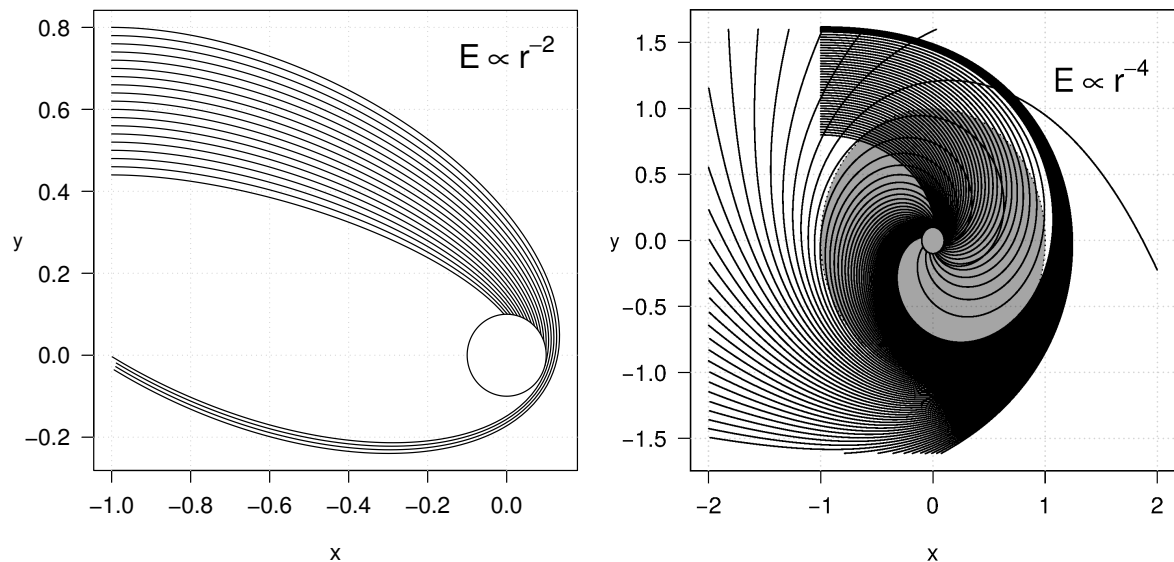


Figure 2.5: Illustrative trajectories, in the \hat{x} - \hat{y} plane, of ions in a sphere's attractive electric field, the field being proportional to r^{-2} (left) or proportional to r^{-4} (right). The former case has no absorption radius. The latter case does, highlighted as the translucent, grey region bordered by a dotted ellipse; trajectories coming closer than the absorption radius always end on the sphere.

figure 2.5 presents a graphical example, showing how ions with identical initial velocities follow different trajectories around (and onto) a spherical grain, depending on their initial position and the attractive electric field's dependence on the distance r from the grain's centre. When the field is proportional to r^{-2} the ions follow elliptical Kepler orbits which may come arbitrarily close to the grain without landing on it. Assuming a different field proportional to r^{-4} produces an absorption radius, represented in the figure's right panel as a translucent ellipse. Every trajectory which comes closer to the grain's centre than the absorption radius ends on the grain, and because the absorption radius is larger than a , there is no grazing orbit which makes contact with the grain with zero radial velocity.

One example gives little information about the incidence of absorption radii in practice. To deduce whether absorption radii are a practical defect in OML theory, or are so rare that they may be ignored, necessitates further algebra. Suppose an ion with speed v is at a distance r from the sphere's centre. From Pythagoras' theorem, v^2 has the decomposition

$$v^2 = v_r^2 + v_t^2 \quad (2.108)$$

where v_r is the radial velocity component and v_t is the velocity component tangential to the imagined sphere of radius r centred on the actual sphere. The ion's angular momentum about the grain is then $m_i v_t r$, and conservation of this momentum implies

$$m_i v_\infty b = m_i v_t r \quad (2.109)$$

Applying now energy conservation,

$$\frac{m_i v^2}{2} = \frac{m_i v_\infty^2}{2} - Z e \phi(r) \quad (2.110)$$

which simply generalizes eq. (2.96). Together these equations imply

$$v_r^2 = v_\infty^2 \left(1 - \frac{b^2}{r^2} \right) - \frac{2 Z e \phi(r)}{m_i} \quad (2.111)$$

If there is a grazing ion with $b = b_{\text{crit}} = v_a a / v_\infty$, as OML theory assumes,

$$v_r^2 = v_\infty^2 \left(1 - \frac{v_a^2 a^2 / v_\infty^2}{r^2} \right) - \frac{2 Z e \phi(r)}{m_i} \quad (2.112)$$

along all of that ion's trajectory, which is possible only if the right-hand side is non-negative for all $r \geq a$, i.e. if

$$\frac{2 Z e \phi(r)}{m_i} \leq v_\infty^2 \left(1 - \frac{v_a^2 a^2 / v_\infty^2}{r^2} \right) \quad (2.113)$$

for all $r \geq a$. Employing eq. (2.97) gives

$$\frac{2 Z e \phi(r)}{m_i} \leq \frac{v_\infty^2}{r^2} \left(r^2 - \frac{a^2}{v_\infty^2} \left(v_\infty^2 - \frac{2 Z e \phi_a}{m_i} \right) \right) \equiv \frac{v_\infty^2}{r^2} (r^2 - a^2) + \frac{2 Z e \phi_a a^2}{m_i r^2} \quad (2.114)$$

which holds in the $v_\infty^2 \rightarrow 0$ limit only if

$$\frac{\phi(r)}{\phi_a} \geq \frac{a^2}{r^2} \quad (2.115)$$

Hence if $\phi(r)$ shrinks more rapidly than r^{-2} , ions which move slowly far from the grain cannot end up grazing the grain; at small v_∞ absorption radii greater than a exist.

Inconveniently it is likely that $\phi(r)$ does shrink more rapidly. Substituting in the $\phi(r)$ and ϕ_a given by the standard Debye-Hückel model (eq. (2.44)), the no-absorption-radius condition is

$$\frac{a \exp(a/\lambda_D)}{r \exp(r/\lambda_D)} > \frac{a^2}{r^2} \quad (2.116)$$

which is never satisfied for sufficiently large r because there $\exp(r/\lambda_D)$ grows faster than r . One could argue that using the DH model to invalidate the OML model is invalid because the two models make different assumptions in the first place. However, the pessimistic conclusion that OML theory is always afflicted with absorption radii re-emerges in more rigorous treatments [111, 9] which do not assume $\phi(r)$ is of DH form. They find that when distant ions have a Maxwell-Boltzmann velocity distribution and $\Theta \leq 1$, OML theory is internally inconsistent because it assumes no absorption radius exists while its other assumptions guarantee an absorption radius exists [111, 9].

Nonetheless, the more sophisticated self-consistent computations of R. V. Kennedy and J. E. Allen give ϕ_a estimates similar to the OML estimates of ϕ_a as long as $a/\lambda_D \ll \Theta$, and they recover the OML ϕ_a as the $a/\lambda_D \rightarrow 0$ limit of their results [9, p. 499]. Martin Lampe likewise finds that limit and that if $a/\lambda_D \ll \Theta/0.03$ the distorting effect of absorption radii on OML theory is minor [112]. For the purpose of finding ϕ_a for small spheres, OML theory is therefore a reasonable choice despite its self-inconsistency.

2.2.3 Orbital motion (OM)

The self-consistent computations just mentioned [111, 9] use the orbital motion theory of charging, which generalizes OML theory by describing “ion motion at all distances from the [sphere’s] surface” [9, p. 491]. By modelling what happens in the space between the sphere’s surface and infinity, OM theory has the power to account for absorption radii and to generate expressions for η_a and the ion density as a function of r [113, 114]. Inevitably this greater power comes hand-in-hand with a greater cost. The algebra and calculus of the OM model are more involved and less tractable than those of the OML model, and the OM model does not produce any closed-form expressions for $\eta(r)$, nor even η_a .

Because of this complexity and intractability, OM theory might be called a Sunday-best theory: for everyday dusty-plasma physics it goes unused, left hanging in the wardrobe of models, taken out only now and then to rigorously check the sloppier but more convenient workaday models. This dissertation upholds that tradition by forgoing elaboration of the OM model’s definition and solution. The sphere-in-plasma systems to which the current dissertation devotes the most analysis are small spheres in warm plasmas ($0 < a/\lambda_D \lesssim \Theta$), and for those systems OML theory is adequate

and OM theory is overkill.

2.2.4 Extensions to OML theory

For systems which fit neither OML theory nor ABR theory, a physicist may resort to OM theory, but that is often unnecessary. An attractive alternative is to extend OML theory to accommodate these systems, since even extended OML theories can be easier to handle than OM theory.

Modified OML (MOML)

With ABR theory on hand to model spheres in cold-ion plasmas, and OML theory able to model small spheres in warm-ion plasmas, the obvious case left uncovered is that of large spheres in warm-ion plasmas. In this light it is no surprise that a modified OML theory has recently been developed to handle this case [115, 108, 116], based on the work of Stangeby [117], who in turn used a generalization of the Bohm model (§2.1.7).

MOML theory's innovation is to apply OML theory not to the sphere's surface directly, but to the spherical boundary between the pre-sheath and the sheath around the spherical grain. Making this change ameliorates the original OML model's absorption radius problem, because for large a/λ_D most absorption radii occur within the sheath, so applying the OML assumptions only at and beyond the sheath edge cuts out most of the inaccuracies induced by absorption radii [108].

Applying this insight means substituting the sheath-edge potential ϕ_s for ϕ_a in the OML model's formula for I_i . Physically, this amounts to the assumption that as $a/\lambda_D \rightarrow \infty$, every ion which enters the sheath eventually lands on the sphere. (This limit is therefore also known as the “thin sheath” limit [108, pp. 50, 67–70, 73, 76, & passim].) Retaining the original formula for I_e and equating it to the modified I_i formula gives the new equilibrium equation

$$\frac{\sqrt{\Theta}}{\mu} \left(1 - \frac{\eta_s}{\Theta}\right) \approx \exp(\eta_a) \quad (2.117)$$

which differs from the original OML equilibrium equation (eq. (2.106)) in having the normalized sheath-edge potential η_s in place of η_a on the left-hand side. (I have also taken $Z = 1$ here to streamline the derivation.) Regrettably the new equation, unlike the original, is not closed, because of the new unknown η_s . To obtain η_a it is necessary to simultaneously add a new equation relating η_s to η_a .

The MOML theory produces that second equation from two more assumptions which asymptotically hold as $a/\lambda_D \rightarrow \infty$. Beginning with general expressions for the electron and ion currents onto a sphere of radius a ,

$$I_e = -4\pi a^2 e n_0 \exp(\eta_a) \times \sqrt{\frac{k_B T_e}{2\pi m_e}} \quad (2.118)$$

and

$$I_i = 4\pi a^2 e n_i(a) \langle v_i \rangle(a) \quad (2.119)$$

respectively, the sphere has its equilibrium charge when these currents cancel to zero. Alge-

braically, $I_i = -I_e$ at equilibrium, i.e.

$$n_i(a)\langle v_i \rangle(a) = n_0 \exp(\eta_a) \times \sqrt{\frac{k_B T_e}{2\pi m_e}} \quad (2.120)$$

With the existing large-sphere assumption that the sphere collects every ion which enters the sheath,

$$n_i(r_0)\langle v_i \rangle(r_0) \approx n_i(a)\langle v_i \rangle(a) = n_0 \exp(\eta_a) \times \sqrt{\frac{k_B T_e}{2\pi m_e}} \quad (2.121)$$

at equilibrium, where $r = r_0$ is the sheath's edge as before. The next assumption is that screening from the sheath means that quasi-neutrality obtains at the sheath's edge, so the ion and electron densities are approximately equal there:

$$n_i(r_0) \approx n_0 \exp(\eta_s) \quad (2.122)$$

Combining eqs. (2.121) and (2.122),

$$n_0 \exp(\eta_s)\langle v_i \rangle(r_0) \approx n_i(r_0)\langle v_i \rangle(r_0) \approx n_0 \exp(\eta_a) \times \sqrt{\frac{k_B T_e}{2\pi m_e}} \quad (2.123)$$

Rearranging,

$$\eta_s \approx \eta_a + \ln \left(\sqrt{\frac{k_B T_e}{2\pi m_e}} / (\langle v_i \rangle(r_0)) \right) \quad (2.124)$$

The final MOML assumption is that in the large-sphere limit, the surfaces of the sphere and its sheath are locally virtually planar, so Bohm's result (§2.1.7) that ions enter the sheath with velocity c_s is applicable here. Thus $\langle v_i \rangle(r_0) \approx c_s$ and

$$\eta_s \approx \eta_a + \ln \left(\sqrt{\frac{k_B T_e}{2\pi m_e}} / c_s \right) \equiv \eta_a + \frac{1}{2} \ln \left(\frac{k_B T_e}{2\pi m_e} / c_s^2 \right) \quad (2.125)$$

Bohm's derivation implies $c_s^2 = k_B T_e / m_i$, in which case

$$\eta_s \approx \eta_a + \ln \frac{\mu}{\sqrt{2\pi}} \quad (2.126)$$

However, Bohm's derivation assumes away the ions' thermal motion, making it a cold-ion theory. It is therefore inappropriate to substitute that derivation's value of c_s^2 into MOML theory, because MOML theory is intended for warm-ion plasmas. To avoid this problem, MOML theory uses a warm-ion expression for the Bohm speed [115, 116],

$$c_s = \sqrt{\frac{k_B(T_e + \gamma T_i)}{m_i}} \quad (2.127)$$

where γ is the heat capacity ratio, also known as the adiabatic index [116, 118]. Typical values for γ are 1, 5/3, and 3, which correspond to "isothermal flow", "adiabatic flow with isotropic pressure",

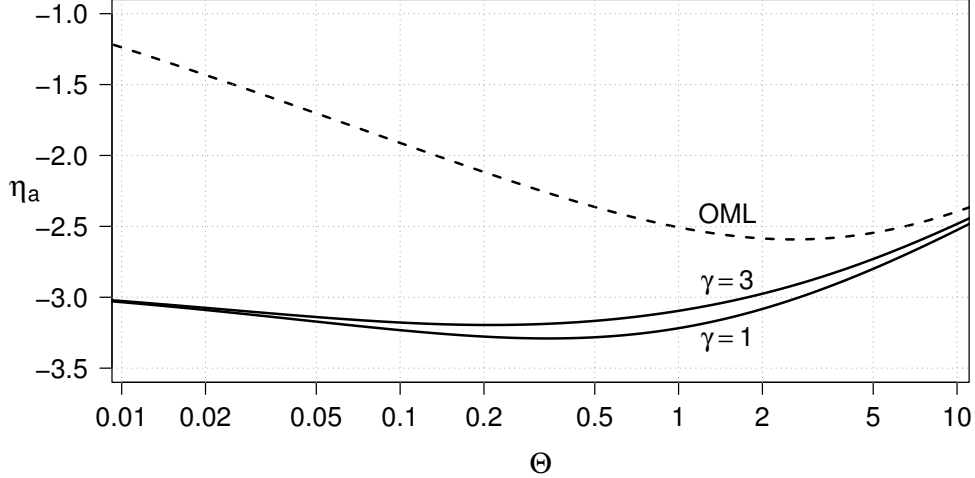


Figure 2.6: Comparison of the OML (dashed curve) and MOML (solid curves) predictions of η_a for a sphere in a hydrogenic ($\mu = 43$) and singly ionized ($Z = 1$) plasma, given two possible values for the heat capacity ratio γ .

and “1D adiabatic flow” respectively [115, p. 2]. To maintain generality I do not choose a specific number but proceed with a generic γ . The η_s formula is then

$$\eta_s \approx \eta_a - \frac{1}{2} \ln \left(\frac{2\pi}{\mu^2} (1 + \gamma \Theta) \right) \quad (2.128)$$

Slotting that expression into eq. (2.117),

$$\frac{\sqrt{\Theta}}{\mu} \left(1 - \frac{1}{\Theta} \left(\eta_a - \frac{1}{2} \ln \frac{2\pi}{\mu^2} (1 + \gamma \Theta) \right) \right) \approx \exp(\eta_a) \quad (2.129)$$

an ugly equation but a solvable one:

$$\eta_a \approx \Theta - W \left(\sqrt{2\pi\Theta(1 + \gamma\Theta)} \exp(\Theta) \right) + \frac{1}{2} \ln \left(\frac{2\pi}{\mu^2} (1 + \gamma\Theta) \right) \quad (2.130)$$

For realistic parameter values ($\Theta \lesssim 10$, $\mu \gtrsim 40$, and $1 \leq \gamma \leq 3$) this MOML solution consistently gives a more negative η_a estimate than the original OML solution (fig. 2.6 illustrates this for hydrogenic plasmas). γ has some impact on the η_a prediction, but not much, and its influence is negligible for extreme Θ values ($\Theta \ll 1$ or $\Theta \gg 1$).

Shifted OML (SOML)

A completely different extension of OML theory is SOML theory, the shifted-OML theory [116]. SOML theory generalizes OML theory by invoking a shifted (or “drifting”) Maxwell-Boltzmann velocity distribution for ions far from the sphere. The shifted distribution represents the distant ions’ equilibrium velocity distribution, and it is the original Maxwell-Boltzmann velocity distribution

(eq. (2.20)) augmented with the plasma's flow velocity \mathbf{v}_d to translate the distribution in \mathbf{v} space:

$$f(\mathbf{v}) = \left(\frac{m}{2\pi k_B T} \right)^{3/2} \exp \left(-\frac{m |\mathbf{v} - \mathbf{v}_d|^2}{2k_B T} \right) \quad (2.131)$$

The shifted distribution allows the theory to model the charging of small spheres in a flowing plasma. In the special case where the speed of flow is zero, SOML theory reduces to OML theory.

Because the SOML model is otherwise the same as the OML model, and §2.2.2 walks through a derivation of the OML model, I omit a comprehensive treatment of SOML theory. The important result is that the SOML model expresses the singly-charged ion current onto a sphere as

$$I_i = 4\pi a^2 n_0 e \times \sqrt{\frac{k_B T_i}{2\pi m_i}} \left(s_1(u) - s_2(u) \frac{e\phi_a}{k_B T_i} \right) \quad (2.132)$$

where

$$s_1(u) \equiv \sqrt{\pi} \frac{(1+2u^2)\text{erf}(u)}{4u} + \frac{\exp(-u^2)}{2} \quad (2.133)$$

$$s_2(u) \equiv \sqrt{\pi} \frac{\text{erf}(u)}{2u} \quad (2.134)$$

$$\text{erf}(u) \equiv \frac{2}{\sqrt{\pi}} \int_0^u \exp(-x^2) dx \quad (2.135)$$

and u is the plasma's flow speed divided by $\sqrt{2k_B T_i/m_i}$ [119, 116]. (Including a factor of 2 under the square root in u 's definition makes the formulae for $s_1(u)$ and $s_2(u)$ simpler.) Because

$$\lim_{u \rightarrow 0} s_1(u) = \lim_{u \rightarrow 0} s_2(u) = 1 \quad (2.136)$$

the SOML ion current (eq. (2.132)) reduces to the OML ion current (eq. (2.102)) with $Z = 1$ in the limit of zero flow speed.

Equating the SOML I_i with I_e (which is the same as the OML I_e on the assumption that the flow speed is invariably negligible compared to the electron thermal velocity) gives the equilibrium equation

$$\frac{\sqrt{\Theta}}{\mu} \left(s_1(u) - \frac{s_2(u)}{\Theta} \eta_a \right) \approx \exp(\eta_a) \quad (2.137)$$

which, like the OML equilibrium equation, has an analytic solution in terms of the Lambert W function:

$$\eta_a \approx \frac{\Theta s_1(u)}{s_2(u)} - W \left(\frac{\mu \sqrt{\Theta}}{s_2(u)} \exp \left(\frac{\Theta s_1(u)}{s_2(u)} \right) \right) \quad (2.138)$$

which reduces to the OML equilibrium η_a (eq. (2.107)) with $Z = 1$ in the $u \rightarrow 0$ limit. Indeed, even far from that limit the SOML solution qualitatively resembles the OML solution: the relationship between η_a and $\ln \Theta$ remains V-shaped regardless of u (figure 2.7).

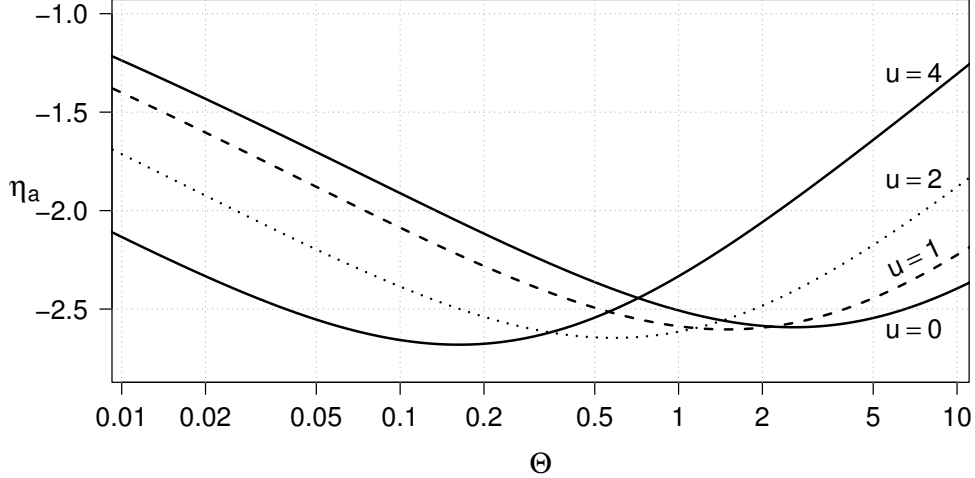


Figure 2.7: SOML theory's predictions of η_a for a sphere in a hydrogenic ($\mu = 43$) and singly ionized ($Z = 1$) plasma with various flow speeds. $u = 0$ corresponds to the special case of no flow, where SOML theory reduces to OML theory.

Shifted, modified OML (SMOML)

One can simultaneously make the SOML generalization (allowing arbitrary flow speed) and MOMP modification (taking the large-sphere limit) to OML theory to obtain SMOML theory, which predicts η_a for large spheres in flowing plasmas. With the heavy lifting already done in the two previous subsections, deducing the SMOML equilibrium equation is as simple as taking eq. (2.137), the SOML equilibrium equation, replacing η_a on its left-hand side with η_s , and then substituting in eq. (2.128), MOMP's η_s formula. The result is

$$\frac{\sqrt{\Theta}}{\mu} \left(s_1(u) - \frac{s_2(u)}{\Theta} \left(\eta_a - \frac{1}{2} \ln \frac{2\pi}{\mu^2} (1 + \gamma\Theta) \right) \right) \approx \exp(\eta_a) \quad (2.139)$$

and its obligatory solution in terms of the Lambert W function is

$$\eta_a \approx \frac{\Theta s_1(u)}{s_2(u)} - W \left(\exp \left(\frac{\Theta s_1(u)}{s_2(u)} \right) \frac{\sqrt{2\pi\Theta(1+\gamma\Theta)}}{s_2(u)} \right) + \frac{1}{2} \ln \frac{2\pi}{\mu^2} (1 + \gamma\Theta) \quad (2.140)$$

which encompasses the MOMP, SOML, and plain OML solutions as special cases, as one should expect. Replacing $s_1(u)$ and $s_2(u)$ with 1 gives the MOMP solution; replacing $(1 + \gamma\Theta)$ with $\mu^2/(2\pi)$ gives the SOML solution; and executing both replacements gives the OML solution for singly-charged-ion plasmas ($Z = 1$).

I have not plotted a comparison of this solution against the solutions of the other models in the OML family, because the dimensions of the SMOML parameter space (Θ, μ, γ and u) are too many. Disappointed readers who feel they have yet to hear enough about the SMOML model may be heartened to know that it plays a starring role in the next chapter, which extends the model in yet another direction.

2.3 Past sphere-charging simulations

The models set out in the previous section, complicated as they may be to solve, are all relatively easy to define. Each consists of a few equations which necessarily abstract away most features of the plasma. This raises the concern that these theories are inadequate representations of reality which risk giving spurious estimates of η_a and any other quantities of interest.

An obvious way to tackle this concern is to build a higher-fidelity model of a plasma which captures more of the real physics than a handful of variables and equations. Maximum fidelity comes from simulating the motion of individual plasma particles around an absorbing sphere, and a few plasma physicists have exploited the ever-increasing processing power of computers to do just that.

The first of those physicists appears to be Giovanni Lapenta, who compared [120, p. 1444] his equilibrium charge results to what he called “OML” theory, though his actual benchmark must have been SOML theory (because he simulated flowing plasmas, and OML theory sensu stricto describes only stationary plasmas). Unfortunately, Lapenta’s simulation results were too noisy to be a demanding test of SOML theory; his results were consistent with the theory, but that does not mean much because he attached large error bars to those results.

More successful was Ian H. Hutchinson, who in 2002 introduced his “specialized-coordinate electrostatic particle and thermals in cell” computer program, or SCEPTIC, which used the particle-in-cell (PIC) method[§] to simulate the behaviour of individual ions in a flowing plasma, with vanishing Debye length, around an absorbing sphere [123, p. 1954]. Rather than relying solely on blunt, *a priori* equations to deduce a plasma’s macroscopic properties, the program computed those properties from the specific behaviour of the individual ions. In this way SCEPTIC relaxed assumptions made by simple charging theories, like OML theory’s assumption that no absorption radii exist anywhere. This is not to say that SCEPTIC did away with *every* familiar simplifying assumption. While it simulated the motion of individual ions, SCEPTIC did not simulate individual electrons; it modelled them instead as a continuous medium obeying the Boltzmann relation.

Over the next few years Hutchinson extended SCEPTIC and his results to flowing plasmas with non-negligible Debye length [125, 124], and he and his students have cultivated a research programme which uses SCEPTIC and successors to SCEPTIC to study absorbing spheres in plasmas in increasing depth [126, 127, 128, 129]. Some of the results from this programme are directly comparable to the predictions of the SOML model. Figure 2.8 reproduces Hutchinson’s graphical comparison of SCEPTIC’s η_a estimates to predictions from SOML theory, and it makes plain that SCEPTIC and the SOML model broadly agree under most conditions for $a \leq \lambda_D$ [124, p. 75].

Hutchinson reckoned that SCEPTIC’s estimates had an “uncertainty of perhaps 2% judged by

[§]I do not discuss the PIC method here because it is not the subject of this section, and because an ample literature about the method already exists, including the original report on the technique [121], Birdsall and Langdon’s venerable textbook treatment [122], and Christopher Willis’s dissertation chapter about SCEPTIC’s use of the PIC method [108, pp. 52–64]. The ultimate documentation of that last is the SCEPTIC source code itself, made available by Hutchinson at <https://github.com/ihutch/sceptic>.

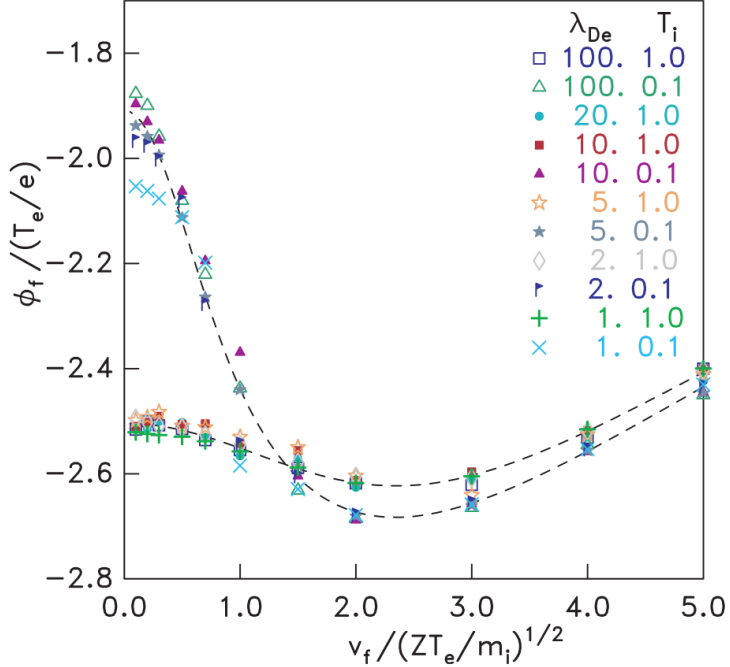


Figure 2.8: Comparison of normalized, surface electric-potential estimates from SCEPTIC (individual points) and from SOML theory (dashed curves), reproduced from [124, fig. 2]. Hutchinson’s λ_{De} and T_i quantities have units of a and T_e respectively. In my notation, the graph plots η_a against $\sqrt{2\Theta/Z}u$ (or, equivalently, the flow speed divided by c_s) for different λ_D/a and Θ .

the scatter” [124, p. 74], which translates to an absolute uncertainty of about 0.05 since the η_a estimates lie between -1.8 and -2.7 . One might therefore assume that the SOML model’s fit to SCEPTIC’s estimates is basically perfect, since all of the SCEPTIC estimates were within 0.05 of the SOML predictions. However, inspecting the plot closely suggests that Hutchinson mistakenly conflated *random* statistical error with *systematic* differences between the simulation results and the model’s predictions, interpreting them both as random “scatter” and “uncertainty” [124, p. 74].

SCEPTIC’s deviations from the SOML predictions, although small, are visibly mostly systematic. With $\Theta = 0.1$, $\lambda_D \geq 10a$, and $u < 1/2$, for example, SCEPTIC’s results are consistently less negative than the SOML predictions by about 0.03, and while that deviation is small it is always positive, suggesting that the deviation is not a random one of fluctuating sign, but a systematic disagreement with SOML predictions. To interpret the deviation as mere “scatter” is to overestimate the random error in SCEPTIC’s results and underestimate the systematic difference.

In an important respect this is encouraging news: Hutchinson’s overestimation of his results’ noisiness implies that those results are even better than he recognized. It is only because the random error is so small (a percent or less, from my inspection of the point-to-point variation of the noisiest data series, the unfilled maize-coloured stars) that one can discern the small systematic differences between simulation and theory. As such, although those differences are genuine, they are mostly subtle enough to avoid overshadowing the broad agreement between SCEPTIC and SOML theory, and this substantial agreement lends mutual credibility to both.

The main exception to this conclusion was noted by Hutchinson himself: “at low velocity and temperature, when $\lambda_{De} \sim 1$, the potential is dropping, indicating a gradual breakdown of the OML assumptions” [124, p. 75]. Specifically, with $\Theta = 0.1$, $\lambda_D = a$, and minuscule flow ($u \approx 0.07$), SCEPTIC gave an η_a estimate about 0.12 less than the SOML prediction. Hutchinson’s interpretation of this discrepancy is very plausible given that, as mentioned in §2.2.2, OML theory, and hence SOML theory, can be expected to fail when $a/\lambda_D \gg \Theta$.

Christopher Willis, focusing on the special case of a stationary plasma, ran further SCEPTIC simulations over wider ranges of Θ and a/λ_D values, obtaining similar results [108, pp. 63–73]. Willis’s plot quantifying discrepancies between SCEPTIC and OML theory shows that for sufficiently large a/λ_D , SCEPTIC always gave an η_a more negative than the OML value, but that this effect shrank greatly at higher Θ [108, fig. 4.2]. When choosing $\Theta = 10$, Willis found that SCEPTIC’s η_a was only about 4% more negative than OML’s prediction even when $a/\lambda_D = 100$; by contrast, with $\Theta = 0.1$, SCEPTIC’s η_a was 65%–70% more negative with $a/\lambda_D = 100$.

Willis also found that, regardless of temperature, SCEPTIC’s η_a moved towards the OML prediction with declining a/λ_D [108, p. 66]. SCEPTIC’s η_a actually became *less* negative than the OML prediction for $a/\lambda_D \leq 0.1$ and $\Theta \leq 1$, which may be partly due to a low- Θ self-heating instability in SCEPTIC which Willis noticed [108, pp. 59 & 64]. A further sequence of plots in Willis’s dissertation gives an idea of how SCEPTIC’s η_a estimates vary when a/λ_D , Θ and μ change simultaneously [108, pp. 70–73]. As long as Θ was large enough ($\gtrsim 0.1$) to avoid numerical instability, then for all μ SCEPTIC’s η_a tended towards the OML value as $a/\lambda_D \rightarrow 0.01$, and tended towards a finite, more negative asymptote as $a/\lambda_D \rightarrow 100$.

Summarizing his findings, Willis found that OML theory predicted η_a well for a/λ_D up to $1.25\Theta^{0.4}$ [108, p. 69], and he concluded from a plot of results for flowing plasmas that “SOML adequately describes the floating potential of small grains” [108, p. 94]. Along with Hutchinson’s results, where SCEPTIC agreed with SOML theory given $a/\lambda_D \lesssim \Theta$, these PIC-derived results amplify the theoretical demonstrations (q.v. §2.2.2) that OML-based models are valid as long as a/λ_D is small.

2.4 Conclusion

This chapter reviews the most popular theories of the charging of dust in plasmas, as well as the more fundamental lemmas on which those theories build. It is informative to have a summary of how dusty-plasma physicists quantitatively think about dust charging, and to collect in one place the theories I draw on throughout the rest of this dissertation. Although plasma-physics textbooks contain many of the results in this chapter, they do not have all of them, and the textbooks often present or derive results in a needlessly clipped fashion which elides flaws or steps of reasoning, a pitfall I have tried to fill in by providing more comprehensive derivations.

Several theories in this chapter — ABR, OML, OM, MOML, SOML, and SMOML — predict the equilibrium value of η_a for an absorbing, equipotential sphere in a plasma. SOML theory is of particular interest here because, in chapter 5, I present results from simulations I have run of small spheres charging in flowing plasmas with warm ions, and SOML theory is the simplest

theory applicable to such spheres. To the extent that SOML theory is valid, I can therefore rely on it as a benchmark against which to check η_a results from my trial simulations. Reassuringly, existing simulations of small spheres in flowing plasmas have come close to matching the η_a predictions of SOML theory, giving independent evidence for the validity of SOML theory in the small-sphere regime, and giving warrant to my planned use of SOML theory as a benchmark.

Chapter 3

Equilibrium probability distribution of an equipotential sphere's charge in flowing, collisionless plasma*

P. I think that I can remember a Latin proverb about that.
Natura non facit saltus. Nature makes no jumps.

M. Yes, but it's only a half-truth. Nature does make jumps; but then all magnitudes which are connected with each other make jumps at the same time.

Wilhelm Ostwald and Elizabeth C. Ramsay (1906),
*Conversations on Chemistry:
First Steps in Chemistry*, p. 202

The charging models reviewed so far predict an equipotential sphere's η_a , and hence its net charge qe , at equilibrium. A notable simplifying assumption of these models is that the sphere's net charge is continuous and changes continuously. Under this assumption q converges smoothly and monotonically to its unique equilibrium value q_0 .

But this is unrealistic, because in reality the sphere's charge, and the electron and ion currents, are discrete. The currents are made up of individual electrons and ions landing on a collecting sphere one at a time, and because those electrons and ions arrive at random intervals, the sphere's q may be pushed *away* from q_0 by a chance fluctuation in the currents, and one is not guaranteed to observe q as q_0 even if the plasma is at thermodynamic equilibrium and q was recently q_0 .

A natural way to address q 's discreteness is to consciously put it at the heart of a charging model. In this chapter I do exactly that, building stochastic models of sphere charging step by step. The models predict not only q 's equilibrium average, but the *probability distribution* of q at equilibrium. This allows a more precise comparison of the model's results to results from simulation or experiment. Deriving probability distributions instead of a single average also avoids the continuous models' conceptual problem of giving non-integer point predictions for the equilibrium q .

*The work in this chapter was previously published in 2013 as *Physical Review E*, **88**(2), 023110.

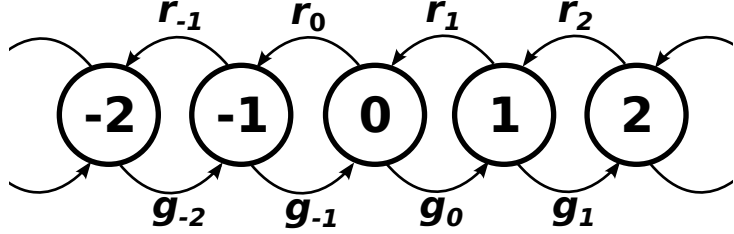


Figure 3.1: Illustration of a one-step process, where circles denote states, arrows denote transitions between states, and arrow labels give transition probabilities per unit time [135, p. 134].

The idea of concocting and solving stochastic models for the charging of dust grains in plasmas is not new, and several authors have solved special cases of the sphere-in-plasma system [130, 131, 132, 133, 134]. The models they solved, however, had two major limitations: they assumed a stationary plasma, and the models depended on the OML theory of the currents onto a sphere, thereby assuming spheres small relative to the Debye length.

My work in this chapter goes beyond the earlier work by eliminating those limitations. I use the SOML and SMOML generalizations of OML theory to allow for plasma flow and circumvent OML theory's small-sphere requirement. Ultimately I obtain two sets of results which, between them, speak to spheres of all sizes, excepting spheres so tiny that their average charge is of order e . A further advantage of my work is that it produces formulae for q 's equilibrium probability distribution which are exact up to a normalizing constant.

3.1 Constructing the stochastic models

I retain the usual modelling assumption that the electron current I_e and ion current I_i characterize the time evolution of a sphere's q , and that I_e and I_i are, for a given sphere in a given plasma, functions of q and q alone. Modelled in this way, fluctuations in q are a random process parametrized exclusively by q , and the charging process is a Markov process: the state variable q jumps between different values over time, with transition probabilities dependent solely on q 's current value.

For a plasma with only one ion species, a singly-charged ion species, q changes only in increments of ± 1 , and q 's fluctuations are a particularly tractable kind of Markov process known as a one-step process [135, p. 134]. As figure 3.1 illustrates, a one-step process is characterized by a state variable, in this case the charge state q , and two sets of rate coefficients r_q and g_q , where r_q denotes the probability per unit time of a shift from state q to $q - 1$ and g_q denotes the probability per unit time of a shift from state q to $q + 1$ [135, p. 134].

For a collecting sphere in a singly ionized plasma the rate coefficients correspond to the electron-collection rate $I_e/(-e)$ and ion-collection rate I_i/e . Defining a neutral sphere's electron-collection rate as the convenience variable

$$\aleph \equiv 4\pi a^2 n_0 \times \sqrt{\frac{k_B T_e}{2\pi m_e}} \quad (3.1)$$

the electron-collection rate is, from eq. (2.30),

$$\frac{I_e}{-e} = 4\pi a^2 n_0 \exp(\eta_a) \times \sqrt{\frac{k_B T_e}{2\pi m_e}} = \aleph \exp(\eta_a) \quad (3.2)$$

This expression neglects the effect of the plasma's flow, because in practice the flow speed is usually much slower than the electron thermal speed and so the flow has minimal impact on the electron current.

The choice of expression for I_i , meanwhile, depends on the collecting sphere's radius a relative to λ_D , the Debye length. SOML theory defines a formula for I_i but, as §2.2.2 and §2.3 explain, the OML and SOML models are valid only at certain a/λ_D . Throughout this chapter I therefore define small spheres as spheres with a/λ_D small enough for SOML theory to apply, and define large spheres as spheres with a/λ_D so large that the SMOML model is more appropriate. To represent these definitions as a crisp quantitative expression which separates small spheres from large, I use Willis's criterion for the failure of OML theory, $a/\lambda_D \gtrsim 1.25\Theta^{0.4}$ [108, p. 69]. Spheres satisfying the inequality are large; spheres violating the inequality are small.

For small spheres the SOML equations (2.132), (2.133) and (2.134) give I_i , while for large spheres the SMOML ion current is more accurate. Accommodating both options, I write the ion-collection rate as

$$\frac{I_i}{e} = \aleph \frac{\sqrt{\Theta}}{\mu} \left(s_1(u) - s_2(u) \frac{\eta^*}{\Theta} \right) \quad (3.3)$$

where η^* is η_a , if the sphere is small, or the sheath-edge potential η_s if the sphere is large. This bifurcates the stochastic model into a stochastic model for small spheres and another stochastic model for large ones. u , $s_1(u)$, and $s_2(u)$ retain their definitions from the previous chapter: u is the plasma's flow speed divided by $\sqrt{2k_B T_i/m_i}$, and eqs. (2.133) and (2.134) define $s_1(u)$ and $s_2(u)$.

For both models the rate coefficients are

$$r_q = \frac{I_e}{-e} = \aleph \exp(\eta_a) \quad (3.4)$$

and

$$g_q = \frac{I_i}{e} = \aleph \frac{\sqrt{\Theta}}{\mu} \left(s_1(u) - s_2(u) \frac{\eta^*}{\Theta} \right) \quad (3.5)$$

Except for η^* , every variable and function on eq. (3.5)'s right-hand side is non-negative; because of that, if η^* is positive it may make g_q negative, which would not be meaningful because g_q is a rate coefficient. To preempt this potential problem, I supplement the models with the requirements that $\eta^* \leq 0$ and $q \leq 0$ (which the fundamental charging law implies are not onerous restrictions).

To close the equations defining the stochastic models, I must define η_a in terms of q . Assuming an equipotential sphere, and neglecting charge separation in the plasma around the sphere,

$$\eta_a = \frac{e\phi_a}{k_B T_e} = \frac{e^2}{4\pi\epsilon_0 a k_B T_e} q = \frac{q}{\Omega} \quad (3.6)$$

where

$$\Omega \equiv \frac{4\pi\epsilon_0 k_B T_e a}{e^2} \quad (3.7)$$

is a dimensionless characteristic parameter which proves key to the results that follow, with many of the approximations to come relying on its being large ($\Omega \gg 1$ or $\Omega \gg 1/\Theta \gtrsim 1$).

Ω has close connections to standard plasma parameters. It is a complement to the Coulomb coupling parameter Γ_C for a singly-ionized simple plasma; writing the average distance between plasma electrons as \bar{r} , $\Omega = (a/\bar{r})/\Gamma_C$. An even more similar plasma parameter is the Debye number N_D , sometimes called just the “plasma parameter” [136, p. 40]. N_D is the average number of electrons in a sphere of unperturbed plasma of radius λ_D [2, p. 8],

$$N_D \equiv \frac{4}{3}\pi\lambda_D^3 n_0 \quad (3.8)$$

From eqs. (2.42) and (3.7),

$$\Omega = 4\pi a \frac{\epsilon_0 k_B T_e}{e^2 n_0} = 4\pi a \lambda_D^2 n_0 \quad (3.9)$$

and hence

$$\Omega = 3 \frac{a}{\lambda_D} N_D \sim \frac{a}{\lambda_D} N_D \quad (3.10)$$

underscoring that Ω directly represents the sphere’s relative size and the plasma’s Debye number.

In terms of Ω , eq. (3.4) is simply

$$r_q = \aleph \exp\left(\frac{q}{\Omega}\right) \quad (3.11)$$

For small spheres, I likewise have

$$g_q = \aleph \frac{\sqrt{\Theta}}{\mu} \left(s_1(u) - \frac{s_2(u)}{\Theta} \frac{q}{\Omega} \right) \quad (3.12)$$

which I rewrite as

$$g_q = \aleph \frac{s_2(u)}{\Omega \mu \sqrt{\Theta}} (\alpha \Omega - q) \quad (3.13)$$

to streamline forthcoming algebra, with

$$\alpha \equiv \Theta \frac{s_1(u)}{s_2(u)} \quad (3.14)$$

For large spheres, $\eta^* = \eta_s$ and is not even dependent on q , being the SMOML sheath-edge potential [137]

$$\eta_s = \alpha - W \left(\frac{\sqrt{2\pi} \alpha \exp(\alpha)}{s_1(u)} \sqrt{\gamma + \frac{1}{\Theta} \exp(\Theta)} \right) \quad (3.15)$$

The large-sphere g_q is then

$$g_q = g \equiv \aleph \frac{s_2(u)}{\mu \sqrt{\Theta}} W \left(\frac{\sqrt{2\pi} \alpha \exp(\alpha)}{s_1(u)} \sqrt{\gamma + \frac{1}{\Theta}} \right) \quad (3.16)$$

where I drop g_q ’s q subscript to emphasize the independence from q for large spheres.

I now have a complete stochastic model — eqs. (3.11) and (3.13) — for small spheres, and a complete stochastic model — eqs. (3.11) and (3.16) — for large spheres. The next step is solving them for q 's probability distribution f_q . Normally one would solve each model's master equation [135, *passim*], but these models' master equations are not exactly solvable. For an exact solution I use a more direct approach.

3.2 Exact equilibrium charge distribution

At equilibrium detailed balance holds [135, p. 142]. That is, in an infinitely large ensemble of sphere-in-plasma systems at equilibrium, just as many should be going from charge state q to $q - 1$ as are going from charge state $q - 1$ to q (on average). As such

$$r_q f_q = g_{q-1} f_{q-1} \quad (3.17)$$

which is a recurrence relation that has the equilibrium f_q as its solution.

I solve it for small spheres first. Substituting eqs. (3.11) and (3.13) into eq. (3.17),

$$\frac{f_{q-1}}{f_q} = \frac{\Omega\mu\sqrt{\Theta}}{s_2(u)} \frac{\exp(q/\Omega)}{\alpha\Omega + 1 - q} \quad (3.18)$$

for $q \leq 0$. To solve this equation, note that it implies

$$\frac{f_q}{f_0} \equiv \frac{f_{-1}}{f_0} \frac{f_{-2}}{f_{-1}} \cdots \frac{f_q}{f_{q+1}} = \frac{\Omega\mu\sqrt{\Theta}}{s_2(u)} \frac{\exp(\frac{0}{\Omega})}{\alpha\Omega + 1} \times \frac{\Omega\mu\sqrt{\Theta}}{s_2(u)} \frac{\exp(\frac{-1}{\Omega})}{\alpha\Omega + 2} \times \cdots \times \frac{\Omega\mu\sqrt{\Theta}}{s_2(u)} \frac{\exp(\frac{q+1}{\Omega})}{\alpha\Omega - q} \quad (3.19)$$

and hence

$$f_q = f_0 \left(\prod_{q^*=q+1}^0 \frac{\Omega\mu\sqrt{\Theta}}{s_2(u)} \exp\left(\frac{q^*}{\Omega}\right) \right) \Bigg/ \prod_{q^*=q+1}^0 \alpha\Omega + 1 - q^* \quad (3.20)$$

for $q < 0$. (For $q = 0$, f_0 is just equal to itself.) By inspection the first product is

$$\left(\frac{s_2(u)}{\Omega\mu\sqrt{\Theta}} \right)^q \exp\left(-\frac{q(q+1)}{2\Omega}\right) \quad (3.21)$$

and the second is equivalent to

$$\left(\prod_{q^*=0}^{-q-1} 1 + \alpha\Omega + q^* \right) \equiv (1 + \alpha\Omega)_-^q \quad (3.22)$$

where $(x)_n^+$ is the rising factorial (or “Pochhammer symbol”), defined as

$$(x)_n^+ \equiv x(x+1)(x+2)\cdots(x+n-1) \quad (3.23)$$

Putting together expressions (3.20), (3.21) and (3.22),

$$f_q = f_0 \left(\frac{s_2(u)}{\Omega \mu \sqrt{\Theta}} \right)^q \frac{\exp\left(-\frac{q(q+1)}{2\Omega}\right)}{(1 + \alpha\Omega)_-^q} \quad (3.24)$$

where f_0 is determined by the normalization condition

$$\sum_{q=-\infty}^0 f_q = 1 \quad (3.25)$$

which is not analytically solvable. However, eq. (3.24) permits numerical calculation of q 's probability distribution; one can compute $\sum f_q/f_0$ for those q where f_q/f_0 is non-negligible, and set eq. (3.24)'s f_0 to that sum's reciprocal.

As one may rewrite $(x)_n^+$ as a ratio of gamma functions (unless x or $x+n$ is a negative integer), eq. (3.24) constitutes an analytic definition of f_q in terms of elementary functions and the gamma function, lacking only f_0 's value:

$$f_q = f_0 \exp\left(q \ln\left(\frac{s_2(u)}{\Omega \mu \sqrt{\Theta}}\right) - \frac{q(q+1)}{2\Omega}\right) \frac{\Gamma(1 + \alpha\Omega)}{\Gamma(1 + \alpha\Omega - q)} \quad (3.26)$$

I now turn to the large-sphere model. Substituting eqs. (3.11) and (3.16) into eq. (3.17),

$$\frac{f_{q-1}}{f_q} = \frac{\exp(q/\Omega)}{g^*} \quad (3.27)$$

where $g^* \equiv g/\aleph$ is a more convenient form of g . The implied product of exponentials is solvable by inspection:

$$f_q = f_0 g^{*q} \exp\left(-\frac{q(q+1)}{2\Omega}\right) \quad (3.28)$$

The normalization condition does not appear to be analytically solvable for this distribution, either.

3.3 The sphere's modal equilibrium charge and the stochastic models' validity

Deriving a closed form expression for f_q 's mode is conceptually straightforward. Calling the mode M , $f_{q-1}/f_q \leq 1$ for $q < M$, and $f_{q-1}/f_q \geq 1$ for $q > M$. Therefore, because f_{q-1}/f_q is monotonic for small and large spheres, the mode M is located where $f_{M-1}/f_M \approx 1$. (I may safely refer to “the” mode because f_q is unimodal in the sense of Medgyessy [138], a proof of which I defer to appendix C to preserve this chapter's readability.)

I derive M for small spheres first. Setting eq. (3.18)'s left-hand side to 1, substituting M for q , and solving,

$$M \approx 1 + \Omega \left(\alpha - W \left(\frac{\mu \sqrt{\Theta}}{s_2(u)} \exp\left(\alpha + \frac{1}{\Omega}\right) \right) \right) \quad (3.29)$$

For large Ω (i.e. sufficiently large $T_e a$), M 's dependence on the Lambert W term is weak and M 's

dependence on Ω goes approximately as $\mathcal{O}(\Omega)$.

Equation (3.29) leads to an obvious precondition for the stochastic model's validity. As the model assumes the sphere never has a positive charge, a positive value of M indicates that the model has broken down and become self-inconsistent. Therefore $M \leq 0$ is a necessary condition for model validity.

When is $M \leq 0$? Rearranging eq. (3.29), $M \leq 0$ when

$$\frac{1}{\Omega} \lesssim W\left(\frac{\mu\sqrt{\Theta}}{s_2(u)} \exp\left(\alpha + \frac{1}{\Omega}\right)\right) - \alpha \quad (3.30)$$

By exploiting $W(x)$'s definition, monotonicity and positivity for positive arguments, one can rewrite the inequality to remove the right-hand side's dependence on Ω :

$$\frac{1}{\Omega} \lesssim \frac{\mu\sqrt{\Theta}}{s_2(u)} - \alpha \quad (3.31)$$

This sets a lower bound on Ω , below which the inequality is unsatisfied and the model fails. This is unsurprising because the model assumes the sphere is not very tiny, which implies a substantial $\Omega \propto T_e a$. Substituting in eq. (3.14),

$$\frac{1}{\Omega} \lesssim \frac{\mu\sqrt{\Theta} - \Theta s_1(u)}{s_2(u)} \quad (3.32)$$

Evidently, in the cold-ion limit ($\Theta \rightarrow 0$), the inequality reduces to $1/\Omega \lesssim 0$ and is never satisfied, indicating model failure. This is also unsurprising, as a vanishing Θ requires either an infinite T_e (and hence an infinite \aleph and I_e) or a zero T_i (and hence an infinite ion current whenever $\eta_a < 0$). Inversely, for vanishing T_e ($\Theta \rightarrow +\infty$), the inequality's right-hand side tends to $-\infty$, in which case the inequality is again never fulfilled and the model fails.

The inequality also shows that flow affects the model's validity. Because $\Theta > 0$ and $s_1(u)$ increases with u (figure 3.2), eq. (3.32)'s right-hand side becomes negative for large u , and the model eventually fails. Fortunately this only occurs at huge flow speeds, as shown by solving the sub-inequality

$$\mu\sqrt{\Theta} - \Theta s_1(u) < 0 \quad \Rightarrow \quad s_1(u) > \frac{\mu}{\sqrt{\Theta}} \quad (3.33)$$

Because ions are rarely hotter than electrons, and the lightest ions are protons, $\mu/\sqrt{\Theta} \gtrsim \sqrt{m_p/m_e} = 43$, which is always more than $s_1(u)$ for $u < 48$.

More sedate flow speeds have the effect of *increasing* eq. (3.32)'s right-hand side, as shown by calculating that

$$\frac{1}{s_2(u)} = 1 + \frac{1}{3}u^2 + \mathcal{O}(u^4) \quad (3.34)$$

$$\frac{s_1(u)}{s_2(u)} = 1 + \frac{2}{3}u^2 + \mathcal{O}(u^4) \quad (3.35)$$

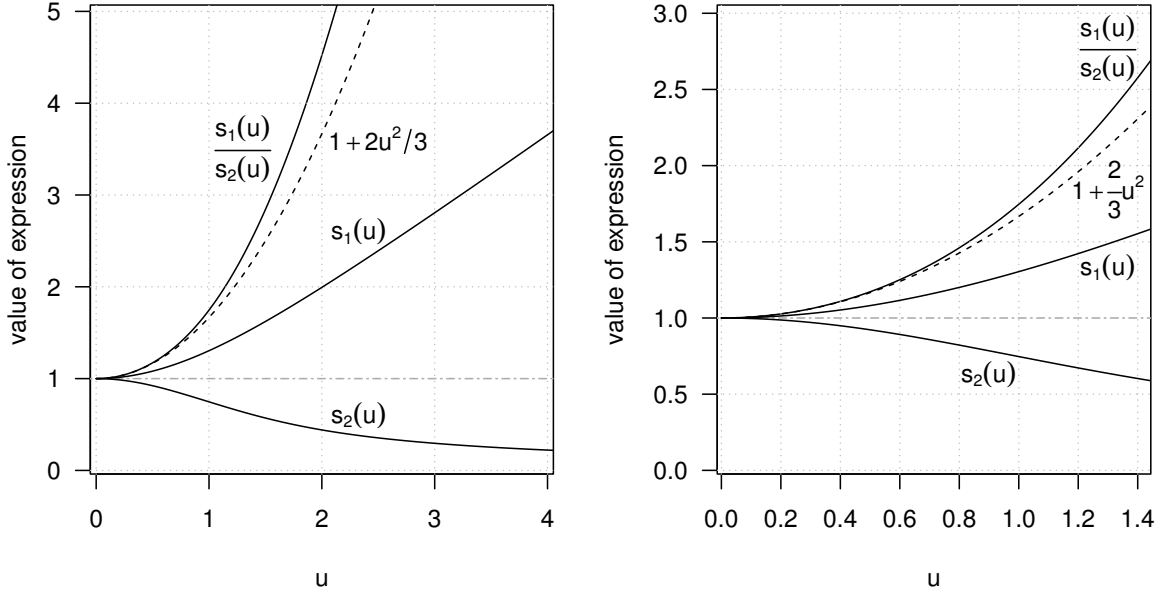


Figure 3.2: The auxiliary functions $s_1(u)$ and $s_2(u)$, and their ratio, as functions of u , the plasma drift velocity normalized by $(2k_B T_i/m_i)^{1/2}$. The black dashed curves are the second-order Maclaurin expansion of $s_1(u)/s_2(u)$ (cf. eq. (3.35)).

and substituting into equation (3.32):

$$\frac{1}{\Omega} \lesssim (\mu\sqrt{\Theta} - \Theta) + \frac{1}{3}(\mu\sqrt{\Theta} - 2\Theta)u^2 \quad (3.36)$$

Invariably $\mu\sqrt{\Theta} > 2\Theta$, so flow's effect (to second order) is to increase the right-hand side, loosening the validity constraint. The second-order effect can also compensate for a low Θ ; as Θ shrinks, $\mu\sqrt{\Theta}$ gets greater relative to the negative $\mathcal{O}(\Theta)$ terms, enhancing flow's beneficial effect on the model's validity.

Deriving M for large spheres is trivial. Setting eq. (3.27)'s left-hand side to 1 entails

$$M \approx \Omega \ln g^* \quad (3.37)$$

The proportionality to Ω dovetails with eq. (3.29)'s approximate $\mathcal{O}(\Omega)$ dependence for large Ω .

The same $M \leq 0$ validity condition applies here. From eq. (3.37), $M \leq 0$ only if $g^* \leq 1$, i.e. if

$$\frac{s_2(u)}{\sqrt{\Theta}} W \left(\frac{\sqrt{2\pi}\Theta}{s_2(u)} \sqrt{\gamma + \frac{1}{\Theta}} \exp(\alpha) \right) \lesssim \mu \quad (3.38)$$

To get insight from this knotty expression I consider limiting cases. For example, I can expand about $\Theta = 0$ to obtain a validity inequality for a cold-ion plasma:

$$\sqrt{2\pi} - \frac{2\pi\sqrt{\Theta}}{s_2(u)} + \mathcal{O}(\Theta) \lesssim \mu \quad (3.39)$$

Neglecting higher order terms, this inequality is always true, since the LHS is always less than $\sqrt{2\pi}$, and $\sqrt{2\pi} < \mu$. With a large sphere and cold ions the stochastic model is always self-consistent, regardless of flow.

Another limiting case is that where $u \rightarrow 0$. With $u = 0$, $s_1(u) = s_2(u) = 1$, and eq. (3.38) becomes

$$W\left(\sqrt{2\pi\left(\gamma + \frac{1}{\Theta}\right)}\Theta \exp(\Theta)\right) \lesssim \mu\sqrt{\Theta} \quad (3.40)$$

By exploiting $W(x)$'s definition, monotonicity and positivity for positive arguments once again,

$$\sqrt{2\pi(\gamma\Theta + 1)} \exp(\Theta) \lesssim \mu \exp(\mu\sqrt{\Theta}) \quad (3.41)$$

For ease of solution, I replace this with a more stringent validity condition. Specifically, when

$$\sqrt{2\pi(\gamma\Theta + 1)} < \mu \quad (3.42)$$

the inequality

$$\exp(\Theta) \lesssim \exp(\mu\sqrt{\Theta}) \quad (3.43)$$

is clearly an even tighter bound on Θ than eq. (3.41). This tighter condition soon reduces to $\Theta \lesssim \mu^2$ and with eq. (3.42) it implies the condition

$$\Theta \lesssim \frac{1}{\gamma} \left(\frac{\mu^2}{2\pi} - 1 \right) \quad (3.44)$$

when $\gamma \geq 1/(2\pi)$, which is always true because γ is between 1 and 3 [115]. Even when μ^2 is as small as realistically possible ($m_p/m_e = 1836$) and γ as large as realistically possible (3), Θ must be at least 97 to violate even this conservative validity condition.

Thus the large-sphere model always satisfies the $M \leq 0$ validity requirement when at least one of Θ or u is small. To find a regime where the model must break down, I now approach the large- u limit, where

$$s_2(u) \rightarrow \frac{\sqrt{\pi}}{2u} \quad (3.45)$$

$$\frac{s_1(u)}{s_2(u)} = u^2 + \frac{1}{2} + \frac{u \exp(-u^2)}{\sqrt{\pi} \operatorname{erf}(u)} \rightarrow u^2 + \frac{1}{2} \quad (3.46)$$

and eq. (3.38) becomes

$$W\left(2\sqrt{2}\Theta u \times \sqrt{\gamma + \frac{1}{\Theta}} \exp\left(\Theta u^2 + \frac{\Theta}{2}\right)\right) \lesssim \frac{2\mu\sqrt{\Theta}u}{\sqrt{\pi}} \quad (3.47)$$

Taking the inverse Lambert W function of both sides and cancelling common terms,

$$\sqrt{2(\Theta\gamma + 1)} \exp\left(\Theta u^2 + \frac{\Theta}{2}\right) \lesssim \frac{\mu}{\sqrt{\pi}} \exp\left(\frac{2\mu\sqrt{\Theta}u}{\sqrt{\pi}}\right) \quad (3.48)$$

Taking logarithms and rearranging,

$$\Theta u^2 - \frac{2\mu\sqrt{\Theta}u}{\sqrt{\pi}} \lesssim \left(\ln \frac{\mu}{\sqrt{2\pi(\Theta\gamma+1)}} \right) - \frac{\Theta}{2} \quad (3.49)$$

The right-hand side is smallest when μ is smallest and γ and Θ are largest. Realistically, $\mu \geq 43$, $\gamma \leq 3$ and $\Theta \lesssim 1$, so the RHS is at least 1.6. As such, setting the RHS to zero gives the tighter inequality

$$\Theta u^2 - \frac{2\mu\sqrt{\Theta}u}{\sqrt{\pi}} \lesssim 0 \quad (3.50)$$

which implies the conservative velocity limit

$$u \lesssim \frac{2\mu}{\sqrt{\pi\Theta}} \quad (3.51)$$

As with the small-sphere model, assuming ions are not much hotter than electrons, flow only forces the large-sphere model to break down at exceptional speeds ($u \gtrsim 49$).

3.4 Approximate Gaussian solutions to the models' master equations

Although the stochastic models' master equations have no exact, analytic solution, I can follow Matsoukas, Russell, & Smith [139, 131, 132] in finding approximate solutions by approximating f_q as a differentiable function of q and, temporarily, t . A one-step process has the master equation [135, p. 134]

$$\frac{\partial f_q(t)}{\partial t} = r_{q+1}f_{q+1}(t) + g_{q-1}f_{q-1}(t) - (r_q + g_q)f_q(t) \quad (3.52)$$

This one-step master equation is approximated well by the following Fokker-Planck equation when r_q and g_q are smooth, slowly varying functions of q [135, pp. 197–198 & 207–208]:

$$\frac{\partial f_q(t)}{\partial t} = -\frac{\partial}{\partial q}(g_q - r_q)f_q(t) + \frac{1}{2}\frac{\partial^2}{\partial q^2}(r_q + g_q)f_q(t) \quad (3.53)$$

For this chapter's models, the FP approximation's conditions are satisfied when q 's equilibrium average is large. Unless the sphere is so tiny that $q \sim 1$, q is almost always relatively close to M , and hence the FP approximation is valid when M is large. M is of order Ω for small spheres satisfying $\Omega \gg 1$ and of order $\Omega \ln g^*$ for large spheres. Thus the FP approximation is a good one for small spheres when $\Omega \gg 1$, and for large spheres when $\Omega \gg -1/\ln g^*$.

At equilibrium, eq. (3.53)'s left-hand side is nil. This banishes $f_q(t)$'s time dependence, so I write the equilibrium probability distribution as f_q as before. Integrating both sides with respect to q ,

$$s = -(g_q - r_q)f_q + \frac{1}{2}\frac{d}{dq}(r_q + g_q)f_q \quad (3.54)$$

where s is a constant of integration corresponding to the relative probability current between

charge states [140, p. 72]. At equilibrium this current is a constant, and for this system must be zero because q is bounded [140, p. 98]. Applying the boundary condition $s = 0$ and then the product rule,

$$0 = (r_q - g_q)f_q + \frac{1}{2} \left((r_q + g_q)f'_q + f_q \frac{d(r_q + g_q)}{dq} \right) \quad (3.55)$$

where $f'_q \equiv df/dq$. Rearranging,

$$\frac{f'_q}{f_q} = \frac{d \ln f_q}{dq} = y(q) \quad (3.56)$$

where

$$y(q) \equiv \frac{2g_q - 2r_q - \frac{d}{dq}(g_q + r_q)}{g_q + r_q} \quad (3.57)$$

Then

$$f_q = \exp \left(\int y(q) dq \right) \quad (3.58)$$

The integral is insoluble for both models, but approximate solutions are possible by linearizing $y(q)$ about a q where most of f_q 's probability density is concentrated. I could use the mode M but the algebra is tidier if I use the value q_0 satisfying $y(q_0) = 0$. (q_0 is the continuous analogue of M , being where f_q is maximized, from $y(q)$'s definition.) Then

$$y(q) \approx y(q_0) + (q - q_0)y'(q_0) = (q - q_0)y'(q_0) \quad (3.59)$$

Substituting into eq. (3.58),

$$f_q \approx \exp \left(-y'_0 q_0 q + \frac{y'_0}{2} q^2 \right) \propto \exp \left(-\frac{(q - q_0)^2}{2/-y'_0} \right) \quad (3.60)$$

where $y'_0 \equiv y'(q_0)$ for brevity. This is a Gaussian probability distribution with mean q_0 and variance $-1/y'_0$, so the final approximate probability distribution is

$$f_q = \sqrt{\frac{-y'_0}{2\pi}} \exp \left(-\frac{(q - q_0)^2}{2/-y'_0} \right) \quad (3.61)$$

Because $y(q_0) = 0$, eq. (3.57) implicitly defines the mean q_0 as the q_0 satisfying

$$2(g_{q_0} - r_{q_0}) = \frac{d}{dq} \Big|_{q=q_0} (g_q + r_q) \quad (3.62)$$

Inserting r_q and g_q for small spheres from eqs. (3.11) and (3.13),

$$\frac{s_2(u)}{\Omega \mu \sqrt{\Theta}} (1 + 2(\alpha \Omega - q_0)) = \left(2 + \frac{1}{\Omega} \right) \exp \left(\frac{q_0}{\Omega} \right) \quad (3.63)$$

This has the solution

$$q_0 = \frac{1}{2} + \Omega \left(\alpha - W \left(\frac{\mu \sqrt{\Theta}}{s_2(u)} \left(1 + \frac{1}{2\Omega} \right) \exp \left(\alpha + \frac{1}{2\Omega} \right) \right) \right) \quad (3.64)$$

which is of similar form to eq. (3.29), the expression for M , and again of order Ω for large Ω . For a Gaussian distribution the mean equals the mode, so it makes sense that $q_0 \approx M$ algebraically.

Substituting the large-sphere r_q and g_q (eqs. (3.11) and (3.16)) into eq. (3.62) gives

$$2g^* = \left(2 + \frac{1}{\Omega}\right) \exp\left(\frac{q_0}{\Omega}\right) \quad (3.65)$$

which has the solution

$$q_0 = \Omega \ln \frac{2g^*}{2 + 1/\Omega} \quad (3.66)$$

similar to the large-sphere formula for M (eq. (3.37)).

Still simpler expressions for q_0 arise when the derivatives in eq. (3.62) are small compared to g_{q_0} and r_{q_0} , which occurs when $1/\Omega \ll \Theta \lesssim 1$. In that regime eq. (3.62) reduces to

$$2(g_{q_0} - r_{q_0}) \approx 0 \quad (3.67)$$

giving the solutions

$$q_0 \approx \Omega \left(\alpha - W \left(\frac{\mu\sqrt{\Theta}}{s_2(u)} \exp(\alpha) \right) \right) \quad (3.68)$$

for small spheres (becoming close to eq. (3.29) for very large Ω) and

$$q_0 \approx \Omega \ln g^* \quad (3.69)$$

for large spheres, which matches M (eq. (3.37)) and makes the asymptotic $\mathcal{O}(\Omega)$ dependence very explicit. Eq. (3.67) amounts to equating I_i and I_e , so eq. (3.68) implies the same normalized electric potential as eq. (2.137), the SOML equation, which comes from explicitly taking $I_i = I_e$. The more exact q_0 given by eq. (3.64) implies a more negative electric potential.

The same simplification allows a concise approximation for y'_0 and so the distribution's variance σ^2 . Neglecting derivatives,

$$y(q) \approx \frac{2(g_q - r_q)}{g_q + r_q} \quad (3.70)$$

and so, applying the quotient rule and simplifying,

$$y'(q) \approx \frac{4}{(g_q + r_q)^2} \left(r_q \frac{dg_q}{dq} - g_q \frac{dr_q}{dq} \right) \quad (3.71)$$

Solving for y'_0 for small spheres is tedious but feasible. Substituting in r_q and g_q , and applying eq. (3.68) eventually gives

$$y'_0 \approx -\frac{1}{\Omega} \left(1 + \frac{1}{W \left(\frac{\mu\sqrt{\Theta}}{s_2(u)} \exp(\alpha) \right)} \right) \quad (3.72)$$

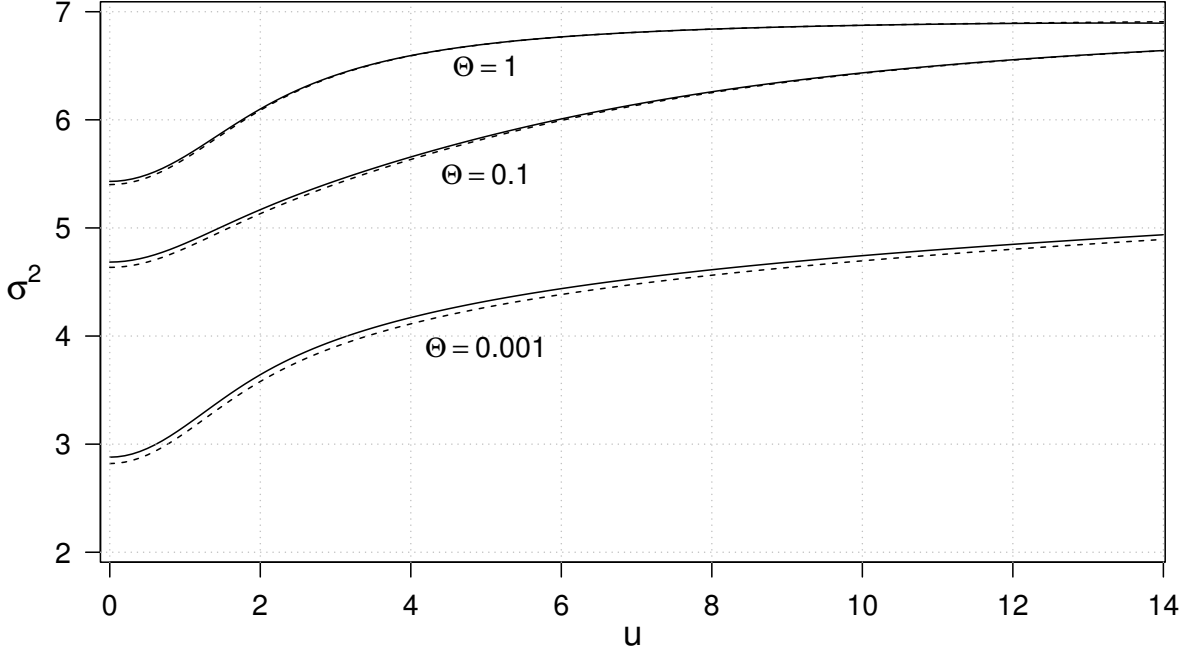


Figure 3.3: The variance σ^2 of f_q for a small sphere in a hydrogenic plasma with $k_B T_e = 1$ eV and $a = 10$ nm, calculated numerically from f_q (solid lines) and from eq. (3.73) (dashed lines).

The variance is then

$$\sigma^2 = \frac{1}{-y'_0} \approx \Omega \left/ \left(1 + \frac{1}{W\left(\frac{\mu\sqrt{\Theta}}{s_2(u)} \exp(\alpha)\right)} \right) \right. \approx \frac{\Omega}{1 + \frac{\Omega}{a\Omega - q_0}} \quad (3.73)$$

for $1/\Omega \ll \Theta$, so $\sigma^2 \propto \Omega \propto T_e a$ in this regime, consistent with Matsoukas & Russell's finding that $\sigma^2 \propto a$ [131, p. 4288]. Also consistent is the implication that the coefficient of variation $\sigma/|q_0| \propto 1/\sqrt{\Omega} \propto 1/\sqrt{a}$.

While the dependence of σ^2 on Ω tends to $\mathcal{O}(\Omega)$, the dependence on u is more complicated. Figure 3.3 shows how σ^2 nonlinearly increases with u , and how eq. (3.73) slightly underestimates σ^2 . Gentle flows ($u \ll 1$) have a minimal effect on σ^2 , but as the flow speed exceeds the ion thermal speed ($u \sim 1$), σ^2 rises appreciably with u , plateauing at a higher value for very rapid flow. For still faster flows ($u \gtrsim 2\mu/\sqrt{\Theta}$) the model breaks down as M becomes positive and the sphere's chance of acquiring a positive charge becomes non-negligible.

For large spheres,

$$y'_0 \approx \frac{-4g}{(g + r_{q_0})^2} \left. \frac{dr_q}{dq} \right|_{q=q_0} = \frac{-4g^* \exp(q_0/\Omega)/\Omega}{(g^* + \exp(q_0/\Omega))^2} \quad (3.74)$$

Applying eq. (3.69), the variance is

$$\sigma^2 = \frac{1}{-y'_0} \approx \frac{(g^* + \exp(q_0/\Omega))^2}{4g^* \exp(q_0/\Omega)/\Omega} \approx \Omega \quad (3.75)$$

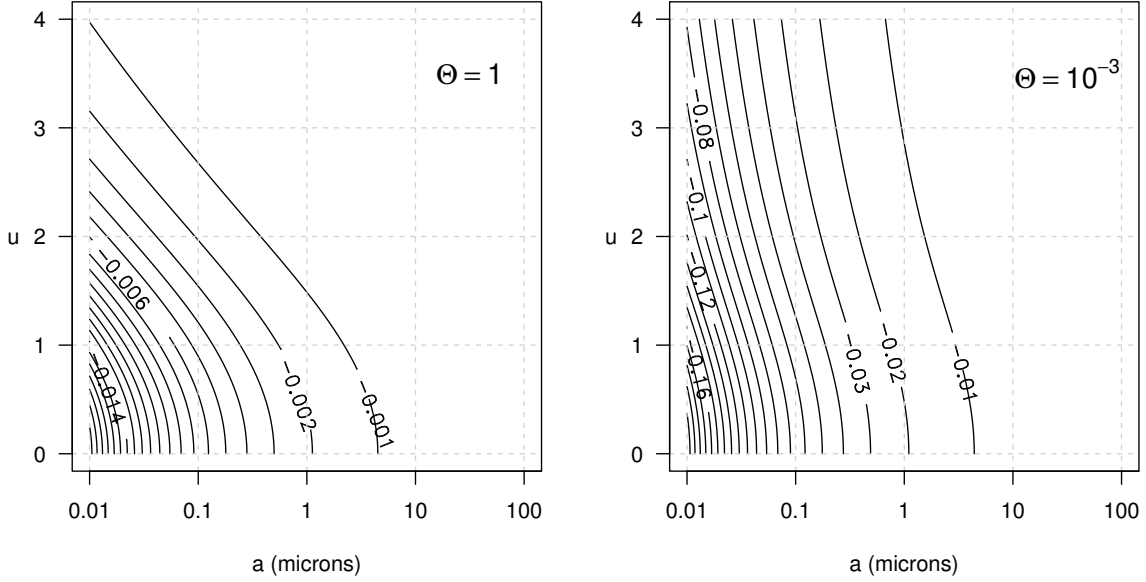


Figure 3.4: Contour plots of f_q 's skewness for a small sphere in a hydrogenic plasma with 1 eV electrons. *Top:* $\Theta = 1$. *Bottom:* $\Theta = 10^{-3}$.

which aligns with the asymptotic Ω dependence for small spheres. Notice that for large spheres σ^2 depends only on Ω . This remains the case if I use the more exact value of q_0 given by eq. (3.66):

$$\sigma^2 \approx \frac{(g^* + \exp(q_0/\Omega))^2}{4g^* \exp(q_0/\Omega)/\Omega} = \Omega \left(1 + \frac{1}{16\Omega^2 + 8\Omega} \right) \equiv \Omega + \frac{1}{8(2\Omega + 1)} \quad (3.76)$$

Using the more exact q_0 has the sole effect of making σ^2 slightly greater than Ω ; it reveals no dependence on μ , Θ , or u . I therefore reach the interesting conclusion that for a given large sphere, the mean charge is sensitive to the values of the plasma parameters μ , Θ , u , and γ , but the charge's *variance* is not. The variance depends on only $T_e a$.

3.5 Skewness of the exact charge distribution

The Gaussian approximation to f_q roughly matches f_q 's mean and variance, but ignores f_q 's higher-order moments. This may be problematic if f_q has appreciable skew, which is likely if it deviates a lot from a Gaussian distribution. The Gaussian approximation hinges on several assumptions, namely that the charging process is virtually continuous, with r_q and g_q being smooth and only weakly dependent on q (so I may represent the master equation as a Fokker-Planck equation), and that f_q 's probability mass is concentrated around its mode (to justify the linearization embodied in eq. (3.59)). These assumptions never hold perfectly, so I expect a little non-Gaussianity and so a little skew. However, the skewness may be negligible for realistic parameter values.

I explore this possibility for small spheres first. To assess f_q 's skewness I compute it numerically, for a hydrogenic plasma with 1 eV electrons, as a function of u and the sphere radius

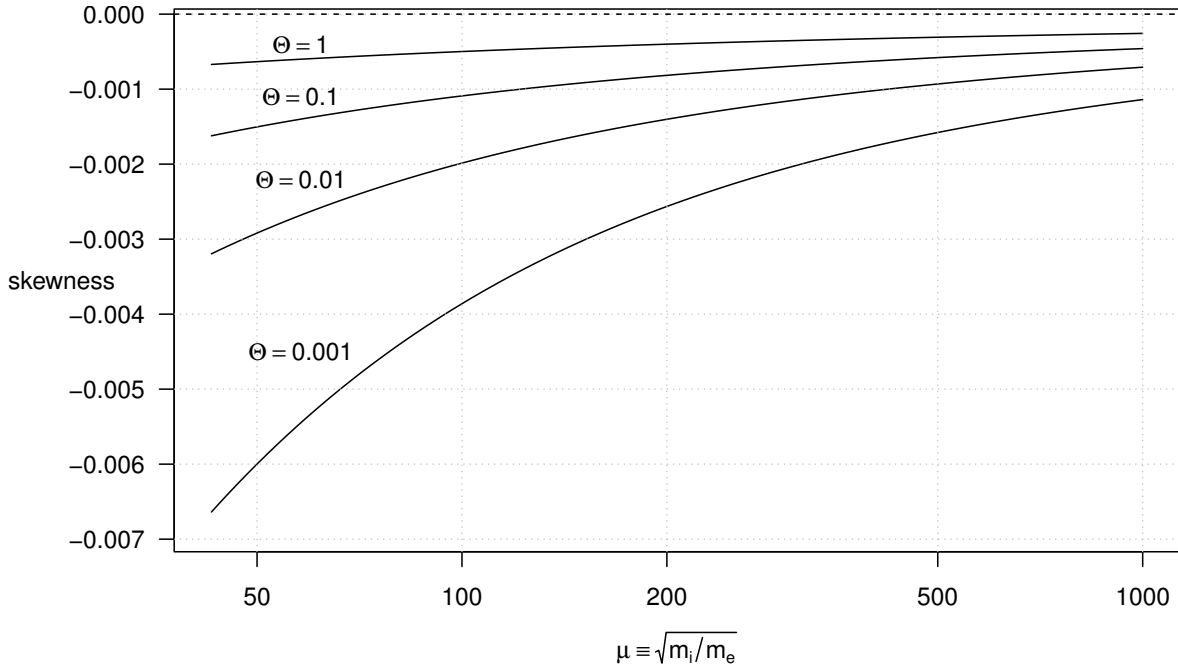


Figure 3.5: f_q 's skewness as a function of μ for a small sphere in a stationary plasma with 1 eV electrons and $a = 10$ nm.

a (fig. 3.4). To calculate f_q 's skewness for each chosen set of parameter values, I evaluate f_q numerically from eq. (3.26) or eq. (3.28), and hence calculate f_q 's first three moments directly from the standard mathematical definitions of a probability distribution's first three moments. The numerical calculations reveal that the skewness is less with heavier ions (fig. 3.5), so the hydrogenic plasma results in figure 3.4 are a worst-case scenario.

Figure 3.4 shows decreasing skewness with increasing radius and flow speed. With equal ion and electron temperatures ($\Theta = 1$) skewness is consistently small, except in the limit of negligible sphere radius, but in that limit the model becomes invalid anyway because $\Omega \ll 1$. With cooler ions, skewness is greater and less affected by flow.

All in all, figures 3.4 and 3.5 document that for small spheres f_q is most skewed when u , a , μ , and Θ are smallest. Playing adversary to the model by picking very small values for those four parameters, a 10 nm sphere in a stationary hydrogenic plasma with 1 eV electrons and $\Theta = 0.001$ has an f_q distribution with a skewness of -0.206 . (This corresponds to the bottom left corner of the lower plot in figure 3.4.) This is a non-negligible but modest degree of skew, and the Gaussian approximation holds up well (figure 3.6). That it does so even for these inconvenient parameter values suggests that the Gaussian approximation is robust.

The large-sphere model's f_q is still less skewed for realistic parameter values. For large spheres the skewness depends on the four parameters Ω , Θ , u and γ , but figure 3.7's left panel illustrates that the increase in skewness with γ is scarcely visible over the range $1 \leq \gamma \leq 3$, and that, as in the small-sphere model, the skewness decreases to negligibility as μ grows.

Unlike the small-sphere model, the large-sphere model's skewness *decreases* with Θ (except

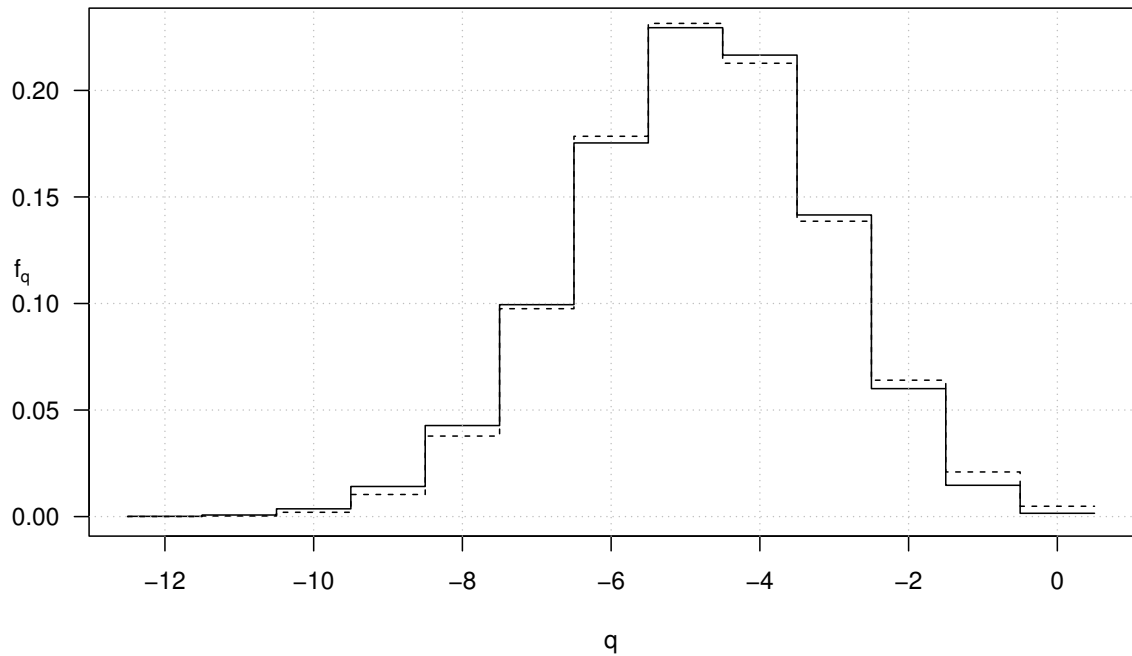


Figure 3.6: f_q (solid line) and its Gaussian approximation (dashed line) for a small sphere in a hydrogenic plasma with $a = 10 \text{ nm}$, $u = 0$, $\Theta = 0.001$, and 1 eV electrons.

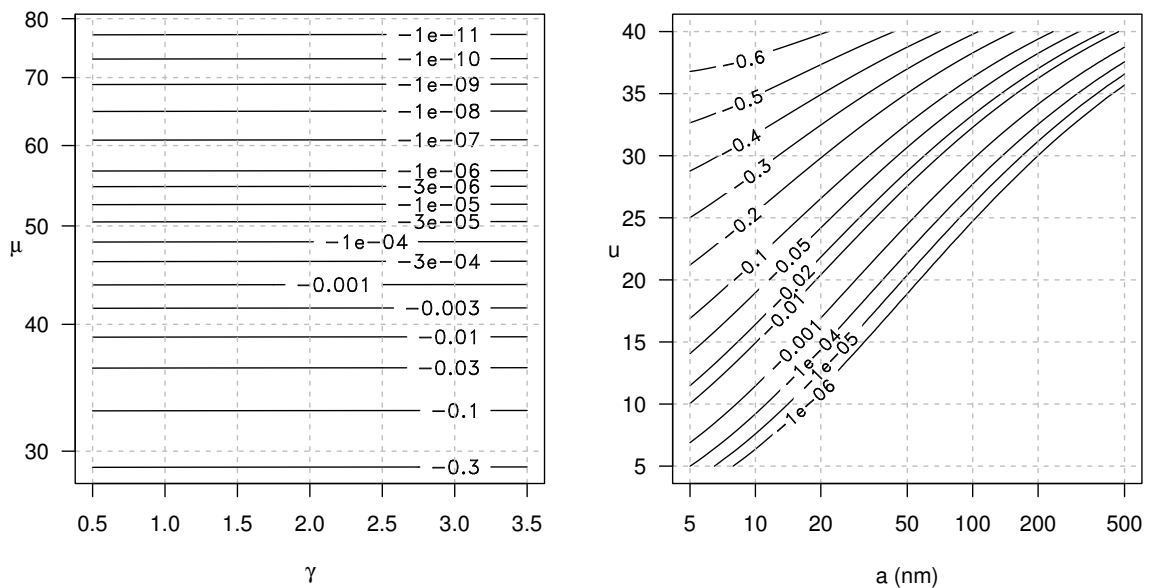


Figure 3.7: Contour plots of f_q 's skewness for a large sphere in a plasma. *Left:* skewness as a function of γ and μ in plasmas with $u = 25$, 1 eV electrons and ions, and $a = 50 \text{ nm}$. *Right:* skewness as a function of a and u in hydrogenic plasmas with $\gamma = 3$ and 1 eV electrons and ions.

when $\Omega \sim 1$, u is huge, and Θ is already very small). This fits the finding above that for cold ions the small-sphere model breaks down, while the large-sphere model improves its self-consistency.

The foregoing means that f_q 's skewness is highest for large spheres when γ , Θ and u are high, and when Ω (or $T_e a$) is low. The right panel in figure 3.7 presents numerical calculations of f_q 's skewness where Θ and γ take on their highest realistic values (1 and 3 respectively). Even in this most pessimistic case, appreciable skewness is only a risk when u is enormous or the sphere's radius tends towards the nanometre scale, and is merely a symptom of the large-sphere model failing as its validity conditions are progressively violated. When those conditions are instead satisfied, the skewness of the predicted charge distribution is negligible, and the large-sphere model's Gaussian approximation appears to be even more robust than the small-sphere model's.

3.6 Conclusion

I have derived equilibrium probability distributions of an equipotential sphere's charge in a flowing, collisionless plasma, using stochastic models based on the SOML and SMOML charging theories. These distributions are expressible in closed form in terms of exponential and gamma functions. The modal charge M is proportional to $T_e a$ for large spheres, and remains approximately proportional to $T_e a$ for small spheres with large Ω .

When a sphere is large enough (and the ions are no hotter than the electrons, which is usually true) Gaussian distributions approximate the exact distributions well, affirming Matsoukas et al.'s demonstration that sphere charge "fluctuations are Gaussian, regardless of the detailed form of the charging currents" if $\Omega \gg 1$ [132, p. 630]. In that regime the Gaussian approximation is sound and the Gaussian distribution's mean is near M for both small and large spheres. For small spheres, the Gaussian distribution's variance σ^2 increases with the normalized flow velocity u , with the dependence on u strongest for $u \approx 1$. For large spheres σ^2 has no relationship to u , only to Ω (which relationship effectively becomes an equality when $\Omega \gg 1$).

My results in this chapter give me theories which predict not only the mean charge on a sphere in a plasma, but also the higher-order moments of the probability distribution of the sphere's charge at equilibrium. Having these more predictive theories means that when I present results from computer simulations of sphere charging in chapter 5, I will be able to make tighter comparisons between those simulation results and theory.

There are many directions in which this chapter's results might be extended. For example, the models here assume a sphere with an equipotential surface, but that assumption is imperfect for non-conducting spheres, while conducting spheres would polarize in the face of approaching electrons and ions and so eq. (3.6) could become a poor approximation. In effect my models here assume spheres which are conducting yet not polarizable. Physically this is a contradiction in terms, but it simplifies the derivations and has a substantial effect only on nanoscopic spheres ($a \lesssim 10$ nm) in plasmas with cool electrons ($k_B T_e \lesssim 1$ eV) [132]. It might nonetheless be useful to incorporate electrical polarization into the models. The models might also be generalizable to magnetized plasmas, collisional plasmas, sphere-in-plasma systems out of equilibrium, non-spherical dust grains, plasmas with non-Maxwellian electron-velocity distributions, spheres in a

sheath, and spheres that emit electrons (whether by photoelectric, thermionic, or field emission). As my models stand, however, they should be applicable to a broad range of close-to-spherical grains in typical flowing plasmas.

Chapter 4

Design of a treecode simulator of a spherical grain in plasma

L. J. Henderson liked to remind his more attentive students that “it’s a good thing to know what you are doing.”

Robert K. Merton (1975),
“Thematic Analysis in Science: Notes on Holton’s Concept”

Systems built without requirements cannot fail;
they merely offer surprises

Robert Morris (date unknown)

In section 2.3 I compared published results from sphere-charging simulations to predictions from sphere-charging theories, and found that the simulations tended to agree with the theories in the parameter regime where they ought to agree. That conclusion, though encouraging, did not decisively prove the validity of the theories and simulations. The simulations incorporated only some of the microscopic detail of an actual plasma, and the theories dispensed with it entirely. A sceptic could use this fact to argue that the simulations and theories agreed only because they suffered common systematic biases arising from the details they both omitted.

To preempt that critique one could maximize the faithfulness of the simulations by programming them to calculate the motion of every single plasma particle in the simulated plasma. A simulation which successfully approximated the behaviour of every electron and every ion in a plasma would necessarily produce results like those of a real plasma. The rest of this chapter outlines the design of a computer program I wrote to run such simulations.

4.1 The sphere-in-plasma system simulated

My program, pot, simulates a lone collecting sphere in a spherical or cubic region of wholly ionized plasma, with the user able to choose the size of both the collecting sphere and the simulation region. The plasma consists solely of $[N/2]$ electrons and $[N/2]$ ions of one pre-defined species, where N is

a user-supplied argument to pot. The program simulates the plasma by approximately solving for the trajectory of every particle through the particle's full six-dimensional (x, y, z, v_x, v_y, v_z) phase space. pot models the electrons and ions as classical, non-relativistic point charges of constant mass which interact with each other through their electric fields. Changes in the net electric field due to the charges' movement propagate instantly throughout the simulation domain; pot does not calculate retarded fields or potentials.

As the preceding paragraph implies, there are no neutral particles (except the collecting sphere, if it is uncharged) in pot simulations, and hence no collisions between plasma particles and neutral particles. The only collisions which take place are the Coulomb collisions engendered by the charged particles' interactions through their electric fields. pot is therefore a collisional simulation, but it does not impose the collisions artificially on the particles in the simulation; the collisions it simulates are those which would naturally obtain because of Coulomb forces.

The user determines the values of the plasma parameters. pot accepts T_e and T_i as command-line arguments. Z , m_i , and m_e may also be adjusted by changing compile-time constants in pot's source code. n_i and n_e cannot be set directly, but their values are implied by the user's choice of N and the simulation domain's size.

To save processing time, pot assumes away the time-varying magnetic field generated by the particles' motion but allows the user to impose an arbitrary space- and time-independent magnetic field \mathbf{B} on the plasma. Each simulated particle experiences the usual Lorentz force of $qe(\mathbf{E} + \mathbf{v} \times \mathbf{B})$ from the user-imposed \mathbf{B} and the time-varying electric field \mathbf{E} from the system's charge distribution. The \mathbf{E} field from a charge in the simulation is analogous to, but not quite the same as, the usual Coulomb (or vacuum) field. Given an electron, ion, or sphere with charge Q , pot defines the \mathbf{E} field at a displacement \mathbf{r} from the body's centre as

$$\mathbf{E} = \frac{Q}{4\pi\epsilon_0(|\mathbf{r}|^2 + \epsilon^2)} \hat{\mathbf{r}} \quad (4.1)$$

where ϵ is a short softening distance, set by the user, to prevent \mathbf{E} from becoming arbitrarily large if particles happen to approach each other very closely. The simulator uses this expression for the sphere's electric field as well as the plasma particles', thereby assuming no polarization of the charge on the sphere.

Each simulation begins with electrons and ions randomly uniformly distributed throughout the domain with velocities randomly sampled from a drifting Maxwell-Boltzmann distribution. The user may specify the velocity distribution's flow speed in the $\hat{\mathbf{x}}$ direction (there is no flow in the $\hat{\mathbf{y}}$ or $\hat{\mathbf{z}}$ directions). The sphere begins with no charge and initially collects no charge, because the simulation starts with a short settling time during which the plasma particles travel through the sphere as if it were not there. This settling time ensures the plasma relaxes fully to equilibrium. Once the settling period elapses the sphere rapidly acquires charge by absorbing electrons and ions which collide with it, or which are within the sphere's volume when the settling period finishes.

pot reinjects every absorbed electron and ion at a random point on the simulation domain's boundary, assigning those particles new, randomly chosen velocities. pot also reinjects particles with new, random velocities if they travel past the simulation region's boundary. (Alternatively,

`pot` can be recompiled to bounce departing particles back into the simulation domain, but I did not use that mode of operation when running my final simulations.)

Although I always intended `pot` to sample particles' initial positions uniformly in space, `pot`'s original particle-initializing code had a bug: where it should have sampled particles' initial distances from the centre by taking cube roots of uniformly distributed variates, it took square roots. The bug's practical effect was that simulations began with a lower particle density near the domain edge, and thus out of equilibrium. This effect was the motivation for my using an initial settling time to let the plasma restore equilibrium.

I have fixed the bug by rewriting the relevant code to use the correct cube-root transformation, but because I diagnosed the bug only after running the simulations I present in §5, those simulations, except where I write otherwise, began with equilibrating oscillations. I lacked the processor time to repeat every simulation, and the bug affected only the initial states of the simulated plasmas, not the final equilibria of interest, so I have not re-run all of the §5 simulations with the corrected version of `pot`.

4.2 `pot` as a parallel program

`pot` uses the Message Passing Interface (MPI) to divide each simulation's computational work across multiple processes. The specific MPI implementation I used to develop the program was Open MPI 1.6, but `pot` is not tied to that MPI implementation, and the program is readily recompileable on platforms with different MPI libraries. I have repeatedly compiled and run the program on Imperial College's CX1 computer cluster, which employs version 3.1 of Intel's MPI library, without having to change the code to suit the different library. Inquisitive readers hoping to discover whether `pot` works on any other systems can download the program's source code from its Github site, <https://github.com/drewthomas/pot>, and see for themselves.

Each process in a `pot` run generates its (pseudo)random numbers with a WELL512 pseudo-random number generator [141, 142], and each process uses its own seed for the generator. By default the seed is 64 bytes read from `/dev/urandom` (a special file provided by many Unix-like operating systems which produces an arbitrarily long sequence of pseudorandom bytes) before the simulation starts, but if it fails to read `/dev/urandom` the process falls back on using its MPI rank (an integer process ID) as the seed and warns the user.

4.3 Overview of my simulator, `pot`, and its core algorithms

Like a lot of computer programs, `pot` is a conglomerate of interlocking parts which handle different tasks. `pot` could not operate without linking several algorithms together to compute approximations to the motion of the simulated plasma's particles.

Each of the algorithms addresses a distinct aspect of that physical problem. The treecode algorithm of Barnes and Hut [143] approximately computes the \mathbf{E} field experienced by each of N plasma particles in $\mathcal{O}(N \log N)$ time, instead of the $\mathcal{O}(N^2)$ runtime necessary for an exact computation, which makes it feasible to run large- N particle-by-particle plasma simulations on current

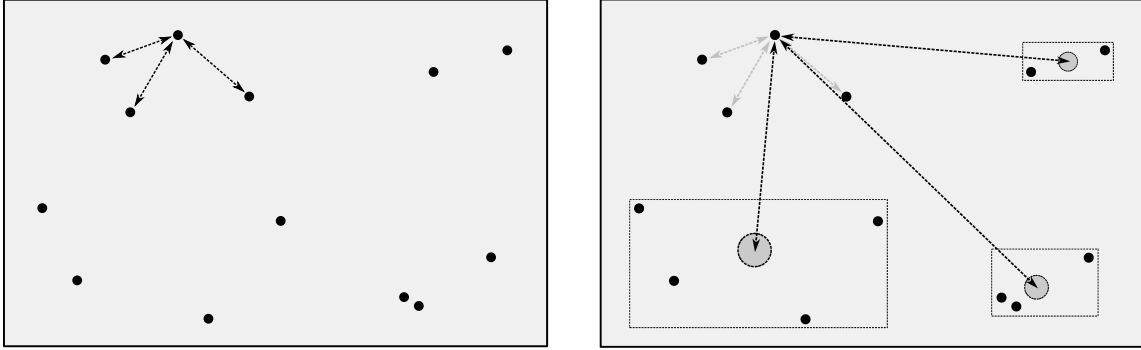


Figure 4.1: An example of estimating the net field at a charge (here, the uppermost one) in a 2-dimensional box of charges. *Left:* modelling interactions with nearby charges individually with full precision. *Right:* grouping distant particles into clusters to approximate their total field as the fields from the clusters' centres of charge. Summing the short-range particle fields and long-range cluster fields gives, roughly, the net field at the uppermost particle.

commodity computer hardware. Particle-motion integrator algorithms use E -field estimates to extrapolate the particles' future positions and velocities from their current positions and velocities — pot implements several integrators which have different advantages and disadvantages. Together the treecode algorithm and a particle-motion integrator tell pot how to work out the particles' motion through the simulation domain, but both algorithms are silent on the question of how to reintroduce particles if they leave the domain. A third algorithm, namely the reinjection algorithm [125] Hutchinson implemented in SCEPTIC, answers that question by defining how to randomly sample a particle's new position and velocity when reinjecting the particle into the simulation region. Because these algorithms are so vital to pot, and because it can be inconvenient to locate lucid, precise specifications of these algorithms, I give self-contained descriptions of these algorithms as implemented in pot.

4.3.1 Barnes and Hut's treecode algorithm

If one has a system of N particles which interact through their fields, the time taken to compute the total field at each particle is of order N^2 . Computing the field at one particle requires iteration over the other $N - 1$ particles, and doing that for each of N particles introduces a factor of N , for a computation time proportional to $(N - 1)N \equiv N^2 - N$, which has order N^2 . With runtime quadratic in N , one needs an uneconomical amount of computing time to simulate large- N systems.

A physicist can avoid this formidable runtime cost by computing approximate estimates of the net field in lieu of exact values. The treecode algorithm is a method for carrying out this approximate calculation, trading off accuracy to gain speed.

To motivate and illustrate the treecode algorithm, consider a box of charged point particles. Someone wanting to approximate the net field at a particle would have to sum the individual fields from the particle's close neighbours with high precision; because those fields may be large,

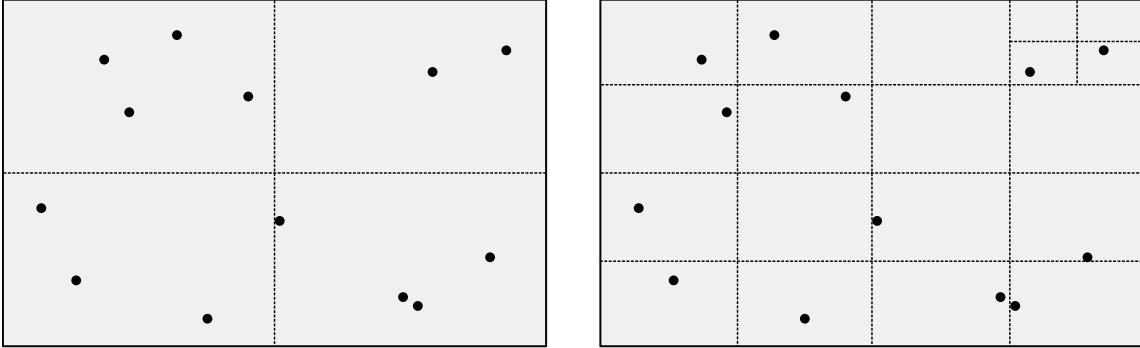


Figure 4.2: Partitioning the simulation domain into a hierarchy of cells. *Left*: dividing the entire domain into 4 cells. *Right*: the final decomposition of the domain into cells, sub-cells, and a sub-sub-cell, so that each contiguous region contains at most one particle.

even a small relative error could translate into a big, spurious effect on the particle's velocity. So the nearby-neighbour fields would be a poor candidate for approximation, and it would be wise to treat them exactly as direct particle-particle interactions (fig. 4.1, left). On the other hand, the fields from distant charges would tend to be smaller, and would indeed average out to near zero in a plasma because of screening and quasi-neutrality. Therefore those long-range fields could safely be approximated, and an intuitive way to do so is to group distant particles into disjoint clusters, compute the clusters' centres of charge, and calculate the fields from those charge centres (fig. 4.1, right). As there are fewer clusters than particles, the clustering reduces the number of interactions to treat, accelerating the simulation.

This is a worthwhile line of thinking but to fructify it two issues must be squared away. The first is defining an automated and fast method of detecting and defining clusters. I recognize the clusters in figure 4.1 by sight and define them by hand, but that tactic is slow and not available to most computers. The second issue is the fact that which charges constitute distant ones is position-dependent. In the top left corner of a square simulation, it would probably be safe to treat the charges in the bottom right corner as a distant cluster. However, in the bottom right corner the situation is reversed: the charges in the bottom right corner are no longer “distant” and have to be treated in finer detail. This means that as a simulation estimates the field at each particle in turn, it has to repeatedly redefine the clusters because each particle is in a different place — but if the simulation spends too long redefining clusters it nullifies the efficiency gain from using clusters in the first place.

The treecode algorithm addresses the two issues by formally defining distant clusters and specifying how to partially pre-compute these clusters so that they needn't be rederived wholesale for every particle. The algorithm begins by checking whether the simulation domain as a whole contains multiple particles. If so, the algorithm divides the domain into 2^D cells by splitting it (typically in half) along each of its D dimensions (fig. 4.2, left). The algorithm then checks which of these cells contain multiple particles. Cells with no particles or one particle are left as they

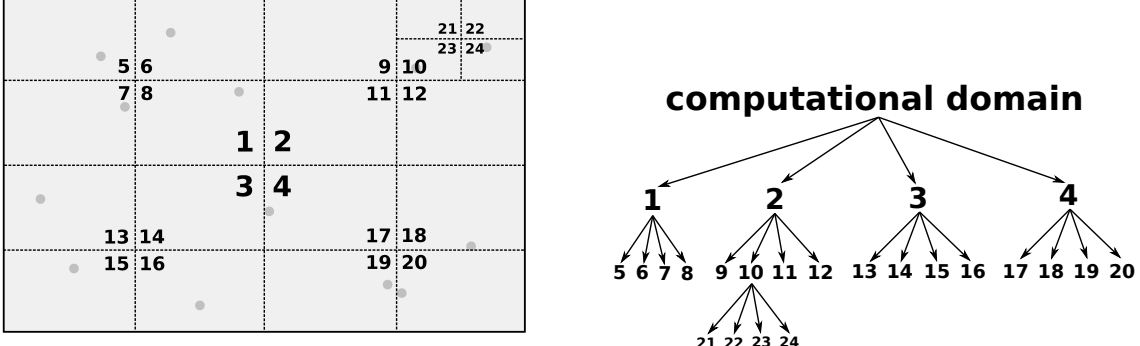


Figure 4.3: The cell-based decomposition of the simulation domain as a tree.

are, and cells with multiple particles are themselves divided into 2^D new, smaller cells. Each of the new cells is checked to see whether it too contains multiple particles — each such cell is divided into 2^D yet smaller cells. This check-and-divide process goes on with each round of newer, tinier cells, until every contiguous region of the simulation domain contains at most one particle, at which point further divisions are otiose (fig. 4.2, right). The resulting hierarchy of cells has a natural representation as a tree (fig. 4.3), whence the treecode method’s name.

Having decomposed the domain into a tree of nested cells, the simulator visits every cell of every size, recording each cell’s total charge and centre of charge, the centre of charge being the position

$$\frac{\sum_{j: \text{particles in cell}} |Q_j| \mathbf{r}_j}{\sum_{j: \text{particles in cell}} |Q_j|}$$

when the denominator is nonzero, and Q_j and \mathbf{r}_j the charge and position respectively of particle j .

Once the simulation program builds the tree of cells, it refers to the tree to rapidly define clusters for calculating fields at each particle. To illustrate that process, I now re-estimate the field at the uppermost particle shown in figure 4.1. This time I define the clusters using the tree in the way the treecode method stipulates, rather than defining clusters by eye.

I begin with the centres of charge of the largest cells (fig. 4.4, top left). Taking the top left cell first, I calculate two quantities: d , the distance between the particle and the cell’s centre of charge, and l , the cell’s size (fig. 4.4, top right). As the cell contains multiple particles, I apply an “opening angle criterion”, which decides whether the cell is far enough away that I can disregard the precise charge distribution within it by modelling its contents as the cell’s total charge located at its charge centre. This criterion is simply whether $l/d < \theta$, where $\theta > 0$ is a fixed “opening angle” parameter. θ sets how enthusiastically the treecode algorithm approximates cells by their total charges. With a small θ a treecode defines more, smaller clusters that better represent individual charges, and with a large θ a treecode is more ruthless about bundling charges into fewer, larger clusters to cut runtime. The choice of θ determines how the algorithm trades off accuracy against speed.

For simplicity I define $\theta = 1$ here. Given that θ value, the top left cell plainly fails to satisfy

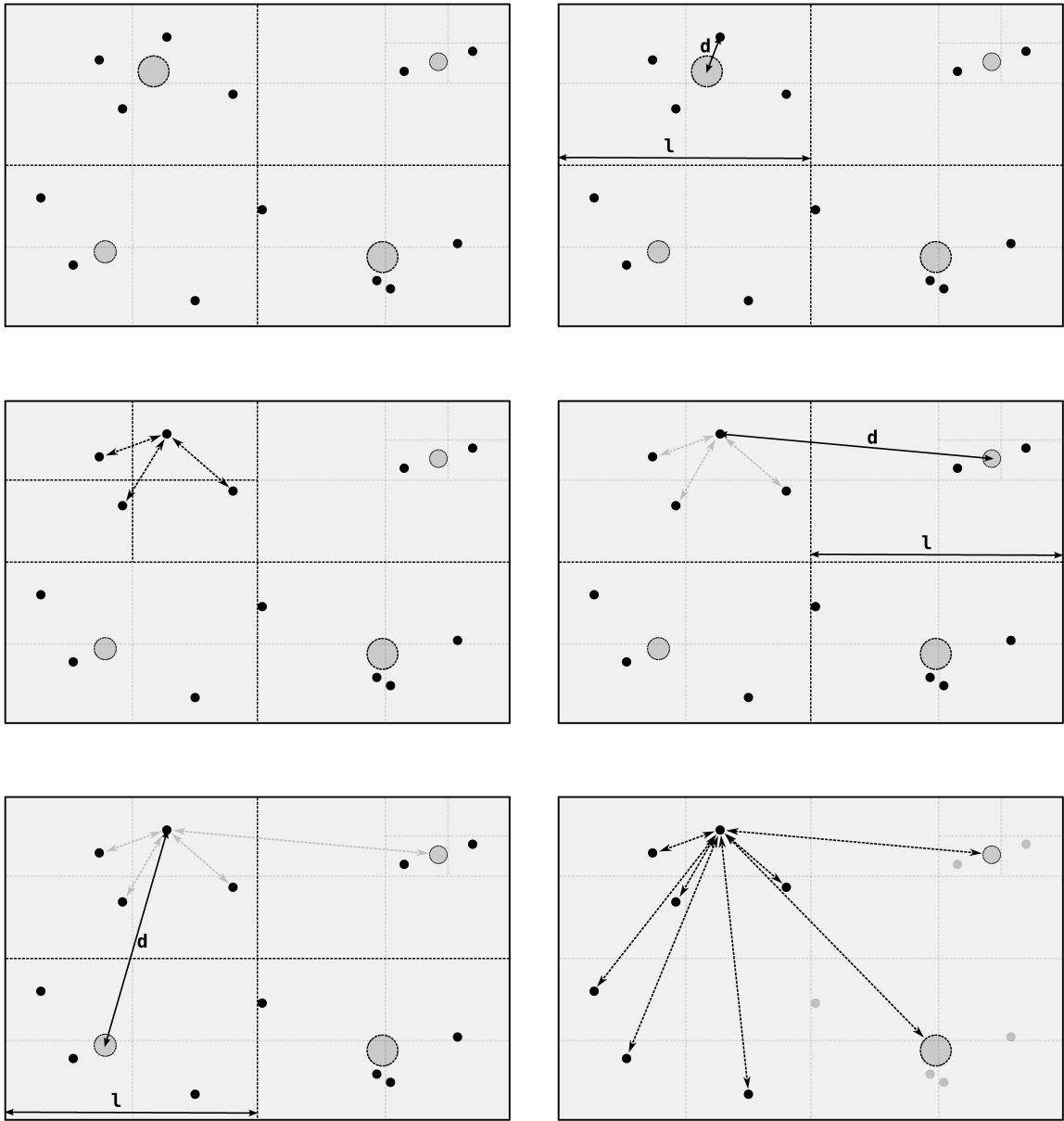


Figure 4.4: Estimating the field at the uppermost particle according to the treecode algorithm. *Left, top:* the four highest-level cells, and their charge centres (dark grey circles with dotted borders). *Right, top:* testing whether the top left cell satisfies the opening angle criterion $l/d < \theta$. *Left, middle:* the top left cell fails the $l/d < \theta$ test, so I evaluate the fields from the individual particles in its sub-cells. *Right, middle:* applying the $l/d < \theta$ test to the top right cell, which passes. *Left, bottom:* applying the $l/d < \theta$ test to the bottom left cell, which fails. *Right, bottom:* the final set of fields evaluated by the algorithm.

$l/d < \theta$, so the cell fails the opening angle criterion — it is too close to safely approximate as a cluster.* Therefore I turn to the cell’s four sub-cells. Unlike their parent cell, the sub-cells each have only one particle, so they cannot be approximated as clusters; I have to take them as they come, adding up the individual particle fields (fig. 4.4, middle left).

This exhausts the top left cell, so I move on to the top right cell. This too contains multiple particles and so I again apply the $l/d < \theta$ criterion (fig. 4.4, middle right). The top right cell has $l < d$ and so satisfies the criterion. Because it satisfies the criterion I approximate the entire cell as its total charge, located at the cell’s charge centre, without regard for the cell’s individual particles. Moving on to the bottom left cell (fig. 4.4, bottom left), it fails the $l/d < \theta$ criterion, and so I consider its four sub-cells. Each of these is either empty and therefore contributes nothing (the top right sub-cell) or has just one particle (in which case I add that particle’s individual field contribution). This completes my handling of the bottom left cell. Finally, the bottom right cell is far enough away to satisfy the $l/d < \theta$ criterion, and so I only add the field from its total charge and am done with it. At this point I have handled the entirety of the simulation domain, and the job of deciding which fields to calculate is complete (fig. 4.4, bottom right).

Stepping through a concrete example demonstrates how the treecode algorithm solves the first problem mentioned above of having a consistent, automated means of defining clusters. What may remain non-obvious is how it solves the other problem of minimizing the time spent defining clusters. I alluded above to the treecode accomplishing this by partially pre-computing the clusters used to approximate the field at a particle. I can now be more specific: a treecode pre-computes the hierarchical cell tree, and reuses this tree as it estimates fields on each particle. For any given particle, the algorithm builds clusters by depth-first traversal[†] of the tree, choosing different nodes based on the properties of the cells they represent. The number of cells visited to estimate the field at a particle is typically of order $\log N$, implying a time of order $N \log N$ to estimate the field at all N particles [143]. Building the tree also usually requires $\mathcal{O}(N \log N)$ time, but since tree-building time is amortized over all N particles [143] it does not affect the total runtime’s asymptotic N dependence.

My example illustrates that the treecode algorithm is simple enough for a (very patient) person to understand and execute it. In spite of that, the algorithm was not invented until the mid-1980s, when the computational astrophysicists Josh Barnes and Piet Hut developed it to simulate interacting galaxies with an efficient but easy-to-understand algorithm [143]. Barnes and Hut did not originate the innovation of using trees to hierarchically cluster particles in gravitational simulations; Andrew Appel had done that a few years earlier as an undergraduate

*The eagle-eyed reader might glimpse a potential flaw here. If a particle is in one corner of a cell, with the cell’s centre of charge in the opposite corner, the distance d between them may be bigger than l . Under these circumstances, if θ is too great, the treecode may apply the centre-of-charge approximation in spite of the charge centre including the particle’s own charge! This would lead to a spurious self-interaction. Mercifully, in practice, when $\theta \lesssim 1.2$ this effect appears to be negligible [144, p. 725].

[†]The term “depth-first traversal” originates in computer science, and refers to visiting every node of the tree by descending down the tree’s hierarchy as far as possible before proceeding sideways through nodes at the same level. An example depth-first traversal of the tree in fig. 4.3 begins 5, 6, 7, 8, 1, 9, 21, 22, 23, 24, 10, 11, 12, 2. Compare breadth-first traversal, which refers to visiting every node in order of their level of the tree: the root node, then the root nodes’ immediate descendants, then those nodes’ immediate descendants, and so on. Visiting the nodes of fig. 4.3’s tree in ascending order of their numbering would be a breadth-first traversal.

student [145, 146]. Unfortunately, Appel's method of updating the tree across simulation steps required complex algorithmic footwork, making his method harder to implement and analyze in terms of errors [143, p. 446].

The unadorned treecode algorithm as I describe it here has many variations. One alteration, which Barnes and Hut identified in their original paper, is to represent clusters not only by their monopole moments (total charge and charge centre) but by their higher-order moments: dipole moments, quadropole moments, and so on [143, p. 448]. This improves the approximation of a cell's particles as a cluster without imposing onerous extra runtime costs.

Embracing that improvement, pot's implementation of the treecode algorithm offers the compile-time option of using cells' dipole moments to compute particle-cluster interactions. When that option is chosen, pot recursively calculates each cell's electric dipole moment \mathbf{p} as well as its total charge and centre of charge. The recursive \mathbf{p} calculation exploits the theorem that a charge distribution's dipole moment, evaluated about one point, is trivially reevaluable about another point. Given point charges labelled by an index j , with charges Q_j and positions \mathbf{r}_j , the charges' dipole moment about a point \mathbf{s} is

$$\mathbf{p}(\mathbf{s}) \equiv \sum_j Q_j (\mathbf{r}_j - \mathbf{s}) \quad (4.2)$$

Hence the charges' dipole moment about the point $\mathbf{s}' \equiv \mathbf{s} + \boldsymbol{\delta}$ is

$$\begin{aligned} \mathbf{p}(\mathbf{s}') &= \sum_j Q_j (\mathbf{r}_j - \mathbf{s}') = \sum_j Q_j (\mathbf{r}_j - \mathbf{s} - \boldsymbol{\delta}) \equiv \left(\sum_j Q_j (\mathbf{r}_j - \mathbf{s}) \right) - \sum_j Q_j \boldsymbol{\delta} \\ &= \mathbf{p}(\mathbf{s}) - \boldsymbol{\delta} \sum_j Q_j \end{aligned} \quad (4.3)$$

a practical formula for quickly calculating a cell's \mathbf{p} from the cell's total charge and sub-cells' \mathbf{p} moments.

pot then computes the electric potential $\phi(\mathbf{R})$ and electric field $\mathbf{E}(\mathbf{R})$ from a cluster as

$$\phi(\mathbf{R}) = \frac{1}{4\pi\epsilon_0} \left(\frac{\sum_j Q_j}{|\mathbf{R}|} + \frac{\mathbf{R} \cdot \mathbf{p}}{|\mathbf{R}|^3} \right) \quad (4.4)$$

a result easily found in electromagnetism textbooks (e.g. [147, pp. 35–36] and [148, pp. 2–4]), and

$$\mathbf{E}(\mathbf{R}) = -\nabla\phi(\mathbf{R}) = \frac{1}{4\pi\epsilon_0 |\mathbf{R}|^3} \left(\left(\sum_j Q_j \right) \mathbf{R} - \mathbf{p} + \frac{3\mathbf{R} \cdot \mathbf{p}}{|\mathbf{R}|^2} \mathbf{R} \right) \quad (4.5)$$

to dipole order, a result less easily found in electromagnetism textbooks. Both the position \mathbf{R} and dipole moment \mathbf{p} must be taken relative to the same point; as their origin pot uses the cluster's centre of charge. Notice that unlike eq. (4.1), eq. (4.5) does not use the softening length ϵ . Softening the field from a cluster is unnecessary, because a cluster's field is evaluated only at particles far from the cluster's centre of charge, where there is no risk of a negligible \mathbf{R} implying an arbitrarily large \mathbf{E} field. The same applies when pot computes clusters' \mathbf{E} fields without dipole moments; it does a calculation equivalent to eq. (4.5) with $\mathbf{p} = \mathbf{0}$.

4.3.2 Particle-motion integrators

The equation of motion for a plasma particle is Newton's second law with the Lorentz force law substituted into it:

$$\frac{d}{dt} \begin{pmatrix} \mathbf{r}(t) \\ \mathbf{v}(t) \end{pmatrix} = \begin{pmatrix} \mathbf{v}(t) \\ qe(\mathbf{E}(\mathbf{r}(t), t) + \mathbf{v}(t) \times \mathbf{B})/m \end{pmatrix} \quad (4.6)$$

pot must solve this equation for each particle's $\mathbf{r}(t)$ and $\mathbf{v}(t)$. In the N -body plasmas pot simulates it is utterly impossible to solve eq. (4.6) analytically, so pot cannot deduce any particle's exact $\mathbf{r}(t)$ or $\mathbf{v}(t)$ over a continuous range of t . Instead, as is common in computational physics when solving equations of motion like eq. (4.6), pot aims to estimate $\mathbf{r}(t)$ and $\mathbf{v}(t)$ only at specific t values separated by a short, pre-defined time step Δt . The algorithms pot uses to accomplish this, known as "integrators" because they integrate eq. (4.6), define methods for estimating $\mathbf{r}(t_0 + \Delta t)$ and $\mathbf{v}(t_0 + \Delta t)$ from $\mathbf{r}(t_0)$, $\mathbf{v}(t_0)$, and the right-hand side of eq. (4.6). Executing these algorithms iteratively gives $\mathbf{r}(t_0 + 2\Delta t)$ and $\mathbf{v}(t_0 + 2\Delta t)$, $\mathbf{r}(t_0 + 3\Delta t)$ and $\mathbf{v}(t_0 + 3\Delta t)$, and so on, and hence eventually an approximation of a particle's trajectory through phase space over time.

For that approximation to be adequate, Δt must be short enough for the integrator to follow the changes in the particle's motion as they occur, a constraint which is tighter for electrons than ions, because electrons in a plasma are faster and lighter than ions. Because of the electrons' greater speed, a typical electron's \mathbf{r} changes on shorter time scales than a typical ion's, and because of electrons' relative lightness, a typical electron's \mathbf{v} changes on shorter time scales than a typical ion's. pot exploits this fact by using a longer de facto time step to integrate the ions' motion than it uses for the electron motion. The program updates the electrons' \mathbf{r} and \mathbf{v} on every time step, but updates the ions' only every $\sqrt{T_e m_i / (T_i m_e)}$ time steps (rounding down the square root to ensure it is an integer), so the ion motion is integrated with an effective time step of $[\mu/\sqrt{\Theta}] \Delta t$.

The requirement that pot tracks changes in the particles' motion is not the only factor enforcing an upper bound on Δt . The quality of the integrator also has an effect; one integrator might have difficulty with a particular Δt that another integrator can employ without trouble. For this reason, among others, it is useful to have several integrators available for pot to use. The program implements three integrators, any of which may be chosen at compile time: the velocity Verlet integrator, the Euler-Richardson integrator, and the Boris integrator.

Velocity Verlet integrator

A popular integrator is the leapfrog integrator, but it has the disadvantage of not giving a particle's position and velocity at the same t . It instead gives $\mathbf{v}(t_0 + \Delta t/2)$ and $\mathbf{r}(t_0 + \Delta t)$, which means the integrator never precisely locates a particle in phase space at time t ; it instead switches rapidly between locating the particle in the velocity subspace and then in the position subspace, which switching gives the integrator its name [149, p. 451].

The velocity Verlet (VV) integrator is a variant of the leapfrog integrator modified to give

$\mathbf{v}(t_0 + \Delta t)$ and $\mathbf{r}(t_0 + \Delta t)$ in a three-stage calculation [149, p. 452]:

$$\mathbf{v}(t_0 + \Delta t/2) = \mathbf{v}(t_0) + \frac{\Delta t}{2} \frac{\mathbf{F}(\mathbf{r}(t_0), t_0)}{m} \quad (4.7)$$

$$\mathbf{r}(t_0 + \Delta t) = \mathbf{r}(t_0) + (\Delta t) \mathbf{v}(t_0 + \Delta t/2) \quad (4.8)$$

$$\mathbf{v}(t_0 + \Delta t) = \mathbf{v}(t_0 + \Delta t/2) + \frac{\Delta t}{2} \frac{\mathbf{F}(\mathbf{r}(t_0 + \Delta t), t_0 + \Delta t)}{m} \quad (4.9)$$

where \mathbf{F} is the Lorentz force on the particle. Notice that \mathbf{F} must be evaluated twice, once at the particle's initial time and position, and then again after the time step and the particle's move to its next position. This means that the treecode algorithm has to run twice on each time step to supply the VV integrator with the necessary input.

In the form of eqs. (4.7)–(4.9), the VV integrator has a wonderful combination of features: it is time-reversible, energy-conserving, accurate to second order, and explicit [150]. But those equations are no good for simulating a magnetized plasma: in a magnetic field \mathbf{F} is velocity-dependent, eq. (4.9) then defines $\mathbf{v}(t_0 + \Delta t)$ in terms of itself, and the VV algorithm ceases to be explicit. One can restore the algorithm's explicit character by evaluating \mathbf{F} in eq. (4.9) using $\mathbf{v}(t_0 + \Delta t/2)$ instead of $\mathbf{v}(t_0 + \Delta t)$, and pot takes this approach. But this crude fix exacts the punishing toll of destroying the integrator's time-reversibility, ability to conserve energy, and second-order accuracy [150]. After implementing it in pot, I found that with $\mathbf{B} \neq \mathbf{0}$ the modified integrator, which worked adequately in the absence of a magnetic field, broke down: the simulated electrons moved in spirals with exponentially growing Larmor radii and field-perpendicular speeds. The time constant of the exponential growth increased as \mathbf{B} 's magnitude shrank, so the instability became more subtle with weaker \mathbf{B} , but there was nothing to suggest that the instability would disappear for any finite \mathbf{B} . It remained detectable even when the electron-Larmor-orbit period was as long as $2000\Delta t$.

Euler-Richardson integrator

Seeking a ready-made integrator compatible with nonzero \mathbf{B} , I discovered the Euler-Richardson (ER) integrator, the integrator one obtains by applying Richardson extrapolation to the basic Euler method [151]. A second-order Runge-Kutta method [152, p. 82], the ER integrator incorporates velocity-dependent forces without needing modification and without losing its stability [151]. An ER calculation has four stages:

$$\mathbf{r}(t_0 + \Delta t/2) = \mathbf{r}(t_0) + \frac{\Delta t}{2} \mathbf{v}(t_0) \quad (4.10)$$

$$\mathbf{v}(t_0 + \Delta t/2) = \mathbf{v}(t_0) + \frac{\Delta t}{2} \frac{\mathbf{F}(\mathbf{r}(t_0), \mathbf{v}(t_0), t_0)}{m} \quad (4.11)$$

$$\mathbf{r}(t_0 + \Delta t) = \mathbf{r}(t_0) + (\Delta t) \mathbf{v}(t_0 + \Delta t/2) \quad (4.12)$$

$$\mathbf{v}(t_0 + \Delta t) = \mathbf{v}(t_0) + (\Delta t) \frac{\mathbf{F}(\mathbf{r}(t_0 + \Delta t/2), \mathbf{v}(t_0 + \Delta t/2), t_0 + \Delta t/2)}{m} \quad (4.13)$$

With this integrator pot remained stable when \mathbf{B} was nonzero (and even when \mathbf{B} was multiple

tesla in magnitude) as long as Δt was sufficiently short.

Boris integrator

“Due to its excellent long term accuracy”, the Boris integrator “is the *de facto* standard” for solving for the motion of charged particles in magnetized plasmas [153, p. 084503-1]. I implemented it according to the concise specification of Patacchini and Hutchinson [154] rather than that in Boris’s original paper [155]:

$$\mathbf{r}(t_0 + \Delta t/2) = \mathbf{r}(t_0) + \frac{\Delta t}{2} \mathbf{v}(t_0) \quad (4.14)$$

$$\mathbf{v}(t_0 + \Delta t) = \left(\mathbf{R}_{\Delta\phi} \left(\mathbf{v}(t_0) + \frac{\Delta t}{2} \frac{qe\mathbf{E}(\mathbf{r}(t_0 + \Delta t/2), t_0 + \Delta t/2)}{2m} \right) \right) + \frac{\Delta t}{2} \frac{qe\mathbf{E}(\mathbf{r}(t_0 + \Delta t/2), t_0 + \Delta t/2)}{2m} \quad (4.15)$$

$$\mathbf{r}(t_0 + \Delta t) = \mathbf{r}(t_0 + \Delta t/2) + \frac{\Delta t}{2} \mathbf{v}(t_0 + \Delta t) \quad (4.16)$$

where $\mathbf{R}_{\Delta\phi}$ is an operator representing a rotation of characteristic vector [154]

$$\Delta\phi \equiv 2 \arctan \left(\frac{\Delta t}{2} \omega_L \right) \frac{\mathbf{B}}{|\mathbf{B}|} \quad (4.17)$$

and $\omega_L \equiv qe|\mathbf{B}|/m$ is the Larmor angular frequency, the angular frequency at which the particle would orbit a magnetic field line in the absence of \mathbf{E} . Geometrically speaking, $\mathbf{R}_{\Delta\phi}$ rotates its operand vector about \mathbf{B} through an angle of $2 \arctan(\omega_L \Delta t/2)$.

As this integrator’s algebraic description is more convoluted than the others’, I translate it into a physical description. Equations (4.14), (4.15), and (4.16) represent a “Drift”, a “Kick”, and a second “Drift” operation respectively, where a “Drift” updates the particle’s position according to a half-step of free (i.e. constant velocity) motion, and a “Kick” accelerates the particle’s velocity in response to \mathbf{E} and \mathbf{B} [154, p. 2605]. The “Kick” itself has three parts: the first is a half-step of acceleration by \mathbf{E} , the second is a full step of Larmor orbit around \mathbf{B} , and the third is another half-step of acceleration by \mathbf{E} .

A shrewd feature of this algorithm is that it computes \mathbf{E} (and \mathbf{B}) only once, in the middle of a time step. Because computing \mathbf{E} costs a relatively large amount of runtime, this means that the Boris integrator saves a lot of time relative to the VV and ER integrators, both of which must compute \mathbf{E} twice. Better still, the Boris integrator maintains second-order accuracy in spite of computing \mathbf{E} only once [154], because it uses \mathbf{E} ’s mid-time-step value rather than $\mathbf{E}(t_0)$.

Computing \mathbf{E} and \mathbf{B} only at the middle of a time step makes possible another artful aspect of the Boris algorithm, its time reversibility. The Boris algorithm is time-reversible because its steps are individually time-reversible, and those steps are arranged so as to be symmetric in time about $t = t_0 + (\Delta t/2)$. The “Drift”-“Kick”-“Drift” sequence is the same whether run forwards or backwards; the central “Kick” step is the same whether run forwards or backwards (either way, it carries out an \mathbf{E} - \mathbf{B} - \mathbf{E} sequence of accelerations); and, as mentioned, the \mathbf{E} and \mathbf{B} fields are evaluated halfway through a time step, not at the step’s start or finish. Courtesy of its time reversibility, the Boris

integrator avoids generating unbounded error in a particle’s energy over arbitrarily many time steps, as long as $\omega_L \Delta t \ll \pi$ [154, 153].

4.3.3 Hutchinson’s reinjection algorithm

When a particle in a pot simulation is collected by the sphere, or breaches the simulation’s outer boundary, pot (by default) reinjects the particle into the simulation domain to begin a new trajectory and conserve the plasma’s particle number. To set a particle on a new trajectory, pot must sample a new \mathbf{r} and a new \mathbf{v} for the particle from appropriate probability distributions.

Naively one might expect that to be a trivial process: select a point on the simulation’s boundary uniformly at random, then sample the three velocity components independently from Gaussian distributions to produce a Maxwell-Boltzmann distribution. But implementing this naive sampling method reveals that it doesn’t work: the equilibrium velocity distribution it produces for a plasma species in the domain is *nearly* Maxwell-Boltzmann, but not quite (the velocity components’ distributions appear slightly more leptokurtic), and that equilibrium distribution has a temperature about a third lower than the injection distributions’ temperature.

The naive reinjection method fails to take into account the geometry of the simulation domain. Any small, smooth, contiguous region of the simulation’s boundary faces in a particular direction, and because of this anisotropy the velocity distribution of particles entering the domain through that region differs from (the inbound part of) a Maxwell-Boltzmann distribution. A reinjection method must account for that effect, as well as the distortion in the velocity distribution from any electric potential beyond the simulation domain.

When designing SCEPTIC, Hutchinson had to solve this problem for a spherical domain, and in pot I implemented his solution from his published description of it [125, §3.2]. Hutchinson’s exposition is not comprehensive, so as well as paraphrasing it I fill some of its gaps for the convenience of anyone wishing to understand how I implemented the method for pot. (My discussion may also be useful for understanding SCEPTIC, though there is no guarantee of this because pot’s implementation of Hutchinson’s general method differs from SCEPTIC’s.) To ease comparison of my discussion with Hutchinson’s, I mimic Hutchinson’s notation in the rest of this subsection by writing a particle’s velocity at infinity as \mathbf{u} , the plasma’s flow velocity at infinity as \mathbf{U} , their speeds as u and U respectively, and the cosine of the angle between \mathbf{u} and \mathbf{U} as c . This notation clashes with the notation in the rest of this dissertation, but I judge that preferable to replacing Hutchinson’s notation with my own (especially as I use Hutchinson’s notation in the relevant sections of pot’s source code).

Making the assumptions that outside the domain $\phi(r)$ is spherically symmetric, ions move collisionlessly, and $\phi(r)$ obeys the OML validity condition, Hutchinson writes a formula for the flux into the spherical simulation domain “in the velocity element du from a distant solid angle element” [125, p. 1482]. With the only anisotropy in the distant velocity distribution being that introduced by flow, that differential flux may be written in terms of u , U , and c .

From his expression for the differential flux, Hutchinson deduces the cumulative distribution functions (CDFs) of the probability distributions of c and u for a particle entering the simulation

domain [125, p. 1483]. c 's CDF depends only on c , u , and U , and once u has been sampled it is trivial to generate c variates by inverse transform sampling.[‡] u 's CDF is more complicated, depending also on $\chi_b \equiv qe\phi(r_b)/(k_B T)$, Hutchinson's notation for the normalized electric potential at the simulation boundary $r = r_b$. Nonetheless, that CDF too may be inverted numerically by interpolation (as SCEPTIC does) or by Newton-Raphson iteration (as pot does), and it is feasible to generate u variates by inverse transform sampling.

The first stage in reinjecting a particle is therefore to sample u and then c . The next is to sample a value for the particle's distant impact parameter b . Under Hutchinson's assumptions, a particle which enters the simulation domain with a given u and c must have had a b between 0 and $b_{\max} = r_b \sqrt{1 - \chi_b/u^2}$, so Hutchinson's method dictates sampling b^2 uniformly from the range $[0, b_{\max}^2]$.

Having sampled u and b , Hutchinson's algorithm then defines a partial solution to the problem of deducing where the particle enters the domain: calculating "the angle α in the plane of impact between the position of impact [where the particle reaches the simulation's boundary] and the direction [...] at infinity" by evaluating the orbit integral

$$\alpha \equiv \int_0^1 \left(\frac{r_b^2}{b^2} \left(1 - \frac{\chi(r_b/r)}{u^2} \right) - \left(\frac{r_b}{r} \right)^2 \right)^{-\frac{1}{2}} d\left(\frac{r_b}{r}\right) \quad (4.18)$$

with $\chi(r_b/r)$ denoting the normalized electric potential profile $qe\phi(r)/(k_B T)$ [125, p. 1484]. Solving this integral requires knowledge of $\chi(r_b/r)$ for $0 \leq r_b/r \leq 1$, which describes the normalized potential's spatial variation outside the simulation domain. Because, by definition, the simulation does not extend that far out, it is not possible to calculate $\chi(r_b/r)$ directly from the simulation's microscopic state; one must instead impose an assumption about how χ varies in the distant plasma outside the simulation. pot uses the electron-only version of the Debye-Hückel potential profile (q.v. eqs. (2.44) & (2.46)), and evaluates the integral with an adaptive Simpson's[§] rule. SCEPTIC uses a more elaborate version of the Debye-Hückel profile which incorporates the depletion of ions caused by the sphere's ion absorption, and evaluates the integral with the trapezium rule [125, p. 1481 & 1484].

These calculations do not precisely specify where on the simulation boundary a particle should be reinjected, nor the particle's reinjection velocity. c defines (the cosine of) the angle between \mathbf{U} and \mathbf{u} , and α the angle between \mathbf{u} and the position vector where the particle enters the domain, but they are only relative angles which leave the absolute orientation of the reinjection position and velocity vectors unspecified. To decide the absolute orientation, an implementation of Hutchinson's algorithm must "[c]choose the ignorable angles of the position and impact parameter from 0 to 2π ", in Hutchinson's words, thereby "specif[ying] the reinjection at infinity" [125, p. 1484]. Hutchinson's paper does not give a concrete procedure to accomplish this, so I give mine.

[‡]The main subtlety here is that programming Hutchinson's formula for c 's CDF directly into a program fails if $U = 0$, because the program then tries to divide zero by zero. But if $U = 0$ it is easy to deduce — whether from the spherical symmetry that obtains without flow, or by applying l'Hôpital's rule to the CDF — that c has a uniform distribution over $[-1, 1]$, its range of possible values.

[§]Actually earlier invented by Bonaventura Cavalieri and published by James Gregory [156], according to the historian of mathematics Herman H. Goldstine [157, p. 77].

To generate a random \mathbf{u} variate consistent with the already generated u and c , set \mathbf{u} to the vector $(0, 0, u)$ in Cartesian coordinates, rotate it about $\hat{\mathbf{y}}$ through $(\pi/2) - \arccos c$ radians, then rotate the result about $\hat{\mathbf{x}}$ through a uniformly randomly chosen angle between 0 and 2π radians. Setting \mathbf{u} to $(0, 0, u)$ gives \mathbf{u} the necessary magnitude; the first rotation forces \mathbf{u} to lie on the conical locus of position vectors at an angle of $\arccos c$ from $\hat{\mathbf{x}}$, $\hat{\mathbf{x}}$ being the plasma's flow direction in pot; and the second rotation then selects a random position vector on that conical locus.

With \mathbf{u} now fully specified it becomes possible to sample a reinjection position \mathbf{r} for the particle and hence its reinjection velocity \mathbf{v} . To sample \mathbf{r} pot recycles the stratagem of treating \mathbf{u} as if parallel to $\hat{\mathbf{z}}$ and then applying a rotation. On the pretence that \mathbf{u} and $\hat{\mathbf{z}}$ are parallel, pot generates a random \mathbf{r} in spherical coordinates as the vector of length r_b , zenith angle α and a uniformly randomly chosen azimuthal angle ψ . Of course in general \mathbf{u} is not parallel to $\hat{\mathbf{z}}$, so pot deduces the rotation which transforms a vector from $\hat{\mathbf{z}}$ to $\hat{\mathbf{u}}$, then applies that rotation to the newly generated \mathbf{r} variate — this produces the same result as if pot had directly sampled \mathbf{r} from the conical locus of position vectors at an angle α from \mathbf{u} . pot applies rudimentary vector algebra and trigonometry to compute the appropriate rotation. Because a rotation's axis is perpendicular to the pre-rotation and post-rotation position vectors, the necessary rotation axis is $\mathbf{u} \times \hat{\mathbf{z}}$. The rotation's angle about that axis is $\arccos((\mathbf{u} \cdot \hat{\mathbf{z}})/u)$, which follows from the angle's cosine being the ratio of \mathbf{u} 's $\hat{\mathbf{z}}$ component to \mathbf{u} 's length. In short, pot obtains \mathbf{r} by sampling $\psi \sim U(0, 2\pi)$ and rotating the position vector with spherical coordinates (r_b, ψ, α) about the characteristic vector $\zeta \equiv \mathbf{u} \times \hat{\mathbf{z}} \arccos(\hat{\mathbf{u}} \cdot \hat{\mathbf{z}})/|\mathbf{u} \times \hat{\mathbf{z}}|$.

Finally pot computes the velocity \mathbf{v} with which the particle must enter the domain if it enters at \mathbf{r} and has distant velocity \mathbf{u} . Mimicking Hutchinson's normalization by having \mathbf{u} and \mathbf{v} represent velocities normalized by $\sqrt{2k_B T/m}$, conservation of energy gives $|\mathbf{v}|^2$ directly as $u^2 - \chi_b$, the square root of which is the particle's reinjection speed v . Breaking \mathbf{v} into its components in spherical coordinates,

$$v^2 = v_r^2 + v_t^2 = v_r^2 + (v_\phi^2 + v_\theta^2) \quad (4.19)$$

by Pythagoras' theorem, where v_ϕ and v_θ are \mathbf{v} 's azimuthal and zenith components respectively. Angular momentum conservation means $ub = v_t r_b$, so $v_t^2 = (ub/r_b)^2$, determining v_t and v_r . Momentarily reinstating the pretence that $\mathbf{u} \propto \hat{\mathbf{z}}$, angular momentum conservation also implies that $v_\phi = 0$, because if $\mathbf{u} \propto \hat{\mathbf{z}}$ the particle has no angular momentum in the $\hat{\mathbf{z}}$ direction. pot therefore initially computes \mathbf{v} 's components v_r , v_ϕ and v_θ as $-(u^2(1 - b^2/r_b^2) - \chi_b)^{1/2}$, zero, and ub/r_b respectively, before rotating \mathbf{v} about the characteristic vector ζ to account for the fact that \mathbf{u} is generally *not* parallel to $\hat{\mathbf{z}}$.

4.4 Prerequisites for valid simulation results

pot affords a lot of flexibility in its parameters, and it is perfectly possible to run the program with parameter values that produce physically unrealistic results. An obvious example would be running pot with a Δt far longer than any of the characteristic time scales of the sphere-in-plasma system. Such a simulation's output could be realistic only by sheer luck.

Prerequisite for validity of pot results	Requirement
resolution of particle motion	$\Delta t \ll a/v_{\text{the}}$ $\Delta t \ll \lambda_D/v_{\text{the}} = \omega_{pe}^{-1}$ $\Delta t \ll 2\pi m_e/(Be)$
accurate inter-particle force estimation	$\theta \lesssim 1$ $\epsilon \ll \bar{r}$ $\epsilon \lesssim Z^2 e^2 / (6\pi \epsilon_0 k_B T)$
weakly coupled, ideal plasma	$\Gamma_C \gg 1$ $N_D \ll 1$
realistic sphere charging	$\epsilon \ll a \ll L/2$ $\tau_c \gg \nu_{pe}^{-1}$ ($a \ll L/2$ or $\lambda_D \ll L/2$)

Table 4.1: Quantitative requirements for the physical realism and validity of pot simulations. (The parenthetical criterion applies only if pot is compiled without Hutchinson’s reinjection algorithm.)

Table 4.1 summarizes that constraint and the other constraints which pot simulations must satisfy if those simulations are to be physically realistic. The rest of this section describes those constraints less tersely and explains their physical bases.

§4.3.2 has already mentioned the most basic constraint, the constraint that Δt is short enough for the integrator to follow the particles’ motion through phase space. This Δt constraint is set by the electrons alone because they move and accelerate more abruptly than ions, so it suffices to require that Δt is shorter than the time scales over which electrons move and accelerate. The canonical electron-motion time scale in a plasma is the inverse of the electron oscillation frequency

$$\nu_{pe} \equiv \frac{1}{2\pi} \sqrt{\frac{n_0 e^2}{\epsilon_0 m_e}} \quad (4.20)$$

which is the oscillation frequency of a cold plasma region with a surfeit of electrons [158].

Realism therefore requires $\Delta t \ll \nu_{pe}^{-1}$. Joining this constraint are Δt constraints based on the *distances* over which there are substantial differences in ϕ , because these are the distances over which electrons (and ions) accelerate. For the relatively simple and symmetric sphere-in-plasma systems pot simulates, the main sustained variation in ϕ is that around the sphere due to the sphere’s charge. Assuming the sphere’s ϕ decays roughly as a Debye-Hückel function (q.v. §2.1.6), the two distances over which the sphere’s ϕ may vary are a and λ_D . To ensure that electrons are unlikely to traverse those distances in a shorter time than Δt , pot should run with $\Delta t \ll a/v_{\text{the}}$ and $\Delta t \ll \lambda_D/v_{\text{the}}$, where v_{the} is the electron thermal speed.

The $\Delta t \ll \lambda_D/v_{\text{the}}$ constraint in fact makes the $\Delta t \ll \nu_{pe}^{-1}$ constraint redundant, because

$$\frac{\lambda_D}{v_{\text{the}}} = \sqrt{\frac{\epsilon_0 k_B T_e / (n_0 e^2)}{k_B T_e / m_e}} \equiv \sqrt{\frac{\epsilon_0 m_e}{n_0 e^2}} = (2\pi \nu_{pe})^{-1} = \omega_{pe}^{-1} < \nu_{pe}^{-1} \quad (4.21)$$

where ω_{pe} is the angular electron-oscillation frequency, which is v_{pe} rescaled into units of $\text{rad}\cdot\text{s}^{-1}$ instead of s^{-1} (or hertz). λ_D/v_{the} being less than v_{pe}^{-1} , the $\Delta t \ll v_{pe}^{-1}$ constraint is always satisfied if the $\Delta t \ll \lambda_D/v_{\text{the}}$ constraint is satisfied, so table 4.1 demands only the latter constraint.

If pot runs a simulation with a static magnetic field, there is one more Δt bound. Δt should be much shorter than the time a particle takes to execute a Larmor orbit around a magnetic field line. The Larmor orbital period of a particle with charge Q is $2\pi m/(B|Q|)$ in a magnetic field of magnitude B , so the typical electron's orbit period again decides the upper bound on Δt : $2\pi m_e/(Be)$. The bound's $B \rightarrow 0$ limiting behaviour is as one should expect — the bound tends to infinity, becoming no constraint at all.

After the hurdles which Δt must clear are the hurdles that risk thwarting the calculation of forces and fields. Firstly, θ must be small enough for the treecode algorithm to produce reasonable \mathbf{E} estimates. The algorithm's inventors proposed [143] using any $\theta \sim 1$, and observed that they obtained accurate results with $\theta = 1$, leading me to formalize the θ bound as $\theta \lesssim 1$.

Secondly, pot's softening distance ϵ must satisfy two constraints. The first is that the average distance \bar{r} between nearest-neighbour electrons is much longer than ϵ . Otherwise, particles in a simulation would spend a lot of their time travelling in a significantly softened potential, which could distort the macroscopic properties of the simulated plasma. The second ϵ constraint comes from the need to accurately simulate large-angle collisions between mutually repelling particles. Small-angle collisions are less of a worry; if two electrons would have deflected each other by 8° in real life but deflect each other by 7° in a simulation, that is unlikely to be a meaningful problem. But if two particles undergo a nearly head-on collision in a simulation, they might well pass by (or through) each other if ϵ is too large, turning a nearly total deflection into a deflection with a spuriously small angle. This would be a much more serious failure than slightly underestimating a small-angle collision.

Failure to model large-angle collisions can occur if the particles have enough kinetic energy to overcome the softened potential barrier between them. Consider a pair of particles, each with charge qe , separated by a distance r . Their joint softened potential energy is

$$U(r) = 2 \frac{q^2 e^2}{4\pi\epsilon_0 \sqrt{r^2 + \epsilon^2}} \quad (4.22)$$

In the worst-case scenario where the two particles are on course to collide head-on, the particles pass through each other if their total kinetic energy is more than $U(0)$. On average both particles have a kinetic energy of $(3/2)k_B T$ each, so in a head-on collision the net kinetic energy is typically $\sim 3k_B T$. Hence in a head-on collision, the particles are likely to pass through each other if

$$3k_B T \gtrsim U(0) = \frac{q^2 e^2}{2\pi\epsilon_0 \epsilon} \quad (4.23)$$

and so to prevent this eventuality the simulation must have

$$3k_B T \ll \frac{q^2 e^2}{2\pi\epsilon_0 \epsilon} \iff \epsilon \ll \frac{q^2 e^2}{6\pi\epsilon_0 k_B T} \quad (4.24)$$

The worst-case scenario of a head-on collision happens relatively infrequently, so eq. (4.24) is more stringent than is necessary in general. Weakening the much-less-than relation accordingly produces the constraint that $\epsilon \lesssim Z^2 e^2 / (6\pi\epsilon_0 k_B T)$, the relevant T being the larger of T_e and T_i , and the relevant q being Z because the magnitude of an ion's charge is always at least the magnitude of an electron's charge.

The constraints reviewed so far are those pot must satisfy to simulate the plasma particles' motion sensibly. A further desideratum of pot simulations is that the particles simulated do, in fact, represent a plasma: a quasi-neutral ionized gas which exhibits collective behaviours. To be gaseous, the collection of particles must have an average kinetic energy at least as large as the average electrostatic potential energy, and to behave collectively the particles must be “weakly coupled”—there must be a high enough density of charged particles for them to exhibit behaviours like Debye screening [136, pp. 34 & 40]. The Coulomb coupling parameter Γ_C encapsulates the gaseousness criterion [2, p. 6] as

$$\Gamma_C \equiv \frac{e^2}{4\pi\epsilon_0 \bar{r} k_B T} \ll 1 \quad (4.25)$$

for a singly ionized plasma, and the requirement for collective behaviours like Debye screening is that

$$N_D \equiv \frac{4}{3}\pi\lambda_D^3 n_0 \gg 1 \quad (4.26)$$

where N_D is the Debye number or “plasma parameter” [136, p. 40], which is the average number of electrons in a “Debye sphere”, a sphere of unperturbed plasma of radius λ_D [2, p. 8]. For either species in a singly ionized plasma, $\bar{r} = \sqrt[3]{3/(4\pi n_0)}$ and $N_D = (\lambda_D/\bar{r})^3$ [2, p. 8]. Combining these facts with basic algebra and the definition of λ_D ,

$$\Gamma_C N_D = \frac{\lambda_D}{3\bar{r}} = \frac{1}{3} \sqrt[3]{N_D} \iff \Gamma_C = \frac{1}{3} N_D^{-2/3} \quad (4.27)$$

and thus the $\Gamma_C \ll 1$ and $N_D \gg 1$ criteria, despite their distinct physical justifications, prove essentially equivalent in practice.

The final set of constraints pot must satisfy a priori are those relating to the collecting sphere and its charging. To prevent softening from noticeably distorting plasma particles' trajectories near the sphere, ϵ should be much less than a , and, to guarantee a thick layer of plasma between the sphere's surface and the domain's boundary, a itself should be much less than $L/2$, the half-length or radius of the simulation domain.

Redirecting attention from length scales to a time scale, the collecting sphere's charging time τ_c should be appreciably longer than the electron oscillation period v_{pe}^{-1} , lending plasma electrons time to react to the sphere's charging as it takes place. This minimizes the risk of a hysteresis effect where, as soon as the simulation begins, the sphere's charging drives the bulk plasma out of equilibrium faster than the plasma electrons can restore equilibrium, which could lead to the sphere converging to a different η_a to that predicted by models which assume equilibrium of the bulk plasma.

One extra constraint applies if pot is compiled to use the naive reinjection method of reinjecting particles uniformly randomly on the simulation boundary with a Maxwell-Boltzmann velocity

distribution, instead of using Hutchinson’s reinjection algorithm. The naive method does not account for a nonzero ϕ at the simulation boundary, so the naive method requires that at least one of a and λ_D is much less than $L/2$ to make the sphere’s electric potential negligible at the boundary, whether because of the Coulombic term in the potential decaying on a scale of a , or because of the plasma screening out the potential over several Debye lengths.

To the extent that Hutchinson’s reinjection algorithm is correct to assume a Debye-Hückel-like $\phi(r)$ outside the simulation domain, pot simulations using Hutchinson’s algorithm are not bound by the constraint that $\max(a, \lambda_D) \ll L/2$. If $\phi(r)$ is approximately a DH function beyond the simulation domain, Hutchinson’s reinjection method accounts for $\phi(r)$ by design, and ϕ need not be negligible at the simulation boundary for the algorithm to give approximately correct results.

I believe this exempts the simulations I present in the next chapter from the $\max(a, \lambda_D) \ll L/2$ requirement, but to reassure readers doubtful of that surmise, I add that those simulations all had $a \ll L/2$ and hence a tiny normalized boundary potential χ_b regardless of their λ_D . A tiny χ_b renders moot the question of how χ varies with r outside a simulation domain, because any reasonable assumption about that variation would have at most a small absolute error, limiting the error introduced by Hutchinson’s reinjection algorithm.

4.5 Conclusion

During my doctoral studies I have written pot, a program to simulate a (small) region of plasma centred on a collecting sphere. This chapter is an overview of the sphere-in-plasma systems pot can simulate, the constraints pot’s parameters must satisfy for pot to simulate a sphere in a plasma properly, and the algorithms pot uses in its simulations. There is more to pot than those algorithms; their implementations occupy only a quarter of pot’s 5,600 lines of C code. This chapter prioritizes the algorithms regardless, because the other three quarters of the code are relatively mundane and easy to interpret, being mostly comments, definitions of data structures, initialization code, graphics-related code, code linking one algorithm to a second, or input/output-related code. Gleaning insight by inspecting those parts of pot is a less arduous task than trying to understand the algorithmic code by inspection, so I do not dissect those parts here.

There are two further reasons to focus on the algorithms when summarizing the program. Firstly, they are the most relevant aspects of pot from a physicist’s perspective, defining the physical behaviour of the plasma represented in the program’s memory. Secondly, my discussion of the algorithms’ implementations marks a starting point for improving the program. A future programmer could take advantage of pot’s modular design by replacing pot’s current implementations of the core algorithms with superior ones.

pot’s version of the treecode algorithm, for instance, could use a different opening angle criterion, which might improve the fidelity of the algorithm’s results (albeit by incurring a higher runtime). pot’s implementation of the VV integrator accounts for magnetic fields with an ad hoc modification which does not work, a modification I experimented with because the usual formulae defining the VV integrator (eqs. (4.7)–(4.9)) give only an *implicit* integration method if $\mathbf{B} \neq \mathbf{0}$. However, for the special case pot simulates, where \mathbf{B} is constant over time and space, one could

rearrange eq. (4.9) into an explicit expression for $\mathbf{v}(t_0 + \Delta t)$, producing a true, explicit VV integrator that accommodates nonzero \mathbf{B} . Implementing that form of VV integrator might give better results when \mathbf{B} is nonzero than my modified-ad-hoc version. As for pot’s implementation of the Boris integrator, it could be made to run slightly faster by applying the small-angle approximation to evaluate $\arctan(\omega_L \Delta t / 2)$ in $\Delta\phi$ ’s definition. The integrator could even be replaced by Patacchini and Hutchinson’s newer “cyclotronic” integrator [154].

By dint of the limited time frame of my PhD, I have not been able to justify implementing and testing these changes myself, because pot functions adequately as it stands. The next chapter summarizes the evidence verifying that pot works, before moving on to the novel results that have emerged from running pot.

Chapter 5

Treecode simulation results

I'm
Counting out time
Got the whole thing down by numbers,
All those numbers
Give me guidance

Genesis (1974), "Counting out Time"

5.1 Tests of physical correctness

It is not enough to have a computer program to simulate a plasma; one has to have some grounds for trusting its output. To check that pot had no glaring faults and was producing sensible results, I tested pot by having it simulate tractable test systems where I could compare its results against analytic solutions.

I began with two-body systems, the most basic. I had pot simulate an electron orbiting an extremely heavy ion, and electrons scattering around an extremely heavy ion. Afterwards I progressed to having pot simulate many-body systems: a pure gas of non-interacting masses, a collecting sphere surrounded by a gas of particles which interacted only with the sphere, and a pure proton-electron plasma without a collecting sphere.

5.1.1 Circular Kepler orbits

In my first scenario an electron orbited a virtually stationary positive ion in a simulation domain with a radius R of 2×10^{-4} m. I repeatedly had pot simulate this system for two billion time steps, changing the integrator and the time-step duration Δt across runs to assess how the choice of integrator and Δt affected the quality of pot's results.

Every run had the same initial conditions. Both particles began with identical x and y coordinates, but were separated by $(R/2)\hat{z}$. The electron's initial velocity was $(e/\sqrt{4\pi\varepsilon_0 m_e R/2})\hat{y}$, the speed (1591 m·s $^{-1}$) being that corresponding to a circular orbit. To give the combined electron-ion system zero net linear momentum I set the ion's initial velocity to the electron's initial velocity

multiplied by $-m_e/m_i$, but I also made the ion exceptionally massive ($m_i/m_e = 10^{15}$) so that it was essentially stationary during the electron's orbits.

The ideal ($m_i/m_e \rightarrow \infty$) version of this system has a two-dimensional phase space: the ion is forever stationary, and the electron always stays in the same orbit and the same orbital plane, so the only two degrees of freedom are the electron-ion distance r and the electron's position in its orbit θ_e (the electron's polar angle in the orbital plane). The system's solution is then

$$\frac{1}{r} = \frac{\mu}{h^2} (1 + e_K \cos(\theta_e - \theta_0)) \quad (5.1)$$

where μ/h^2 sets the orbital radius, e_K is the eccentricity, and θ_0 is a constant phase factor [159, pp. 28–29]. I fitted this solution to the electron trajectories pot generated to see whether e_K was negligible and μ/h^2 was 10^4 m^{-1} , as the system's initial conditions should've dictated. I also inspected plots of $1/r$ against θ_e to see whether the result was a flat line, as it should be when $e_K = 0$.

Figure 5.1 exhibits a sample of the plots I examined, and table 5.1 collects the statistical curve-fitting results. (There were some statistical subtleties to account for in the curve fitting, on which consult appendix D.) The integrators worked about equally well for $\Delta t \leq 10 \text{ ps}$, as shown by the integrators having statistically equivalent estimates of μ/h^2 and e_K when $\Delta t = 4 \text{ ps}$ or $\Delta t = 10 \text{ ps}$ (table 5.1). For the longer Δt values of 40 ps and 100 ps , the VV and Boris integrators performed very similarly, and both produced more faithful trajectories than the ER integrator. At the longest Δt of 400 ps , the VV integrator clearly dominated the other two integrators, and the Boris integrator outperformed the ER integrator (although the Boris and ER integrators' e_K values were statistically equal because of the ER e_K 's large standard error).

In general, the choice of integrator was unimportant when the time step was small ($\Delta t \leq 10 \text{ ps}$) but at longer time steps the ER integrator was the worst and the VV integrator ultimately the best. Most importantly, whatever the integrator, the electron's deviation from its analytic solution was tiny, and statistically indistinguishable from zero, at the shortest time step employed (4 ps).

As for the ion, the simulations' exaggerated m_i/m_e ratio of 10^{15} implies that the ion should have been virtually immobile, a prediction easy to check: plotting the ion's simulated trajectories in the $\hat{\mathbf{y}}\text{-}\hat{\mathbf{z}}$ plane directly illustrates how far the ion spuriously drifted from its origin (fig. 5.2). It suffices to check the simulated ion's trajectories in the $\hat{\mathbf{y}}\text{-}\hat{\mathbf{z}}$ plane because the ion never moved to a detectable extent in the $\hat{\mathbf{x}}$ direction.

The ion trajectory was nearly the same for all three integrators when Δt was sufficiently short, but the ER integrator's performance degenerated more with longer Δt . In the worst case (ER with $\Delta t = 100 \text{ ps}$ — curiously, the drift in y and z was negligible for every integrator with $\Delta t = 400 \text{ ps}$, perhaps because of the proportional reduction in the number of steps making up the 8 ms test period) the ion drifted by 495 picometres during 8 ms of in-simulation time, or a normalized drift of 2.4×10^{-10} electron orbital radii per electron orbital period, a reassuringly small rate of drift.

Shrinking the time step slowed the ion's drift. For $\Delta t = 10 \text{ ps}$ the ion drifted 192 pm in 8 ms with both integrators, for a normalized drift of 9.5×10^{-10} orbital radii per period. This is more than acceptable for the purpose of simulating a plasma, and it is encouraging that even with the

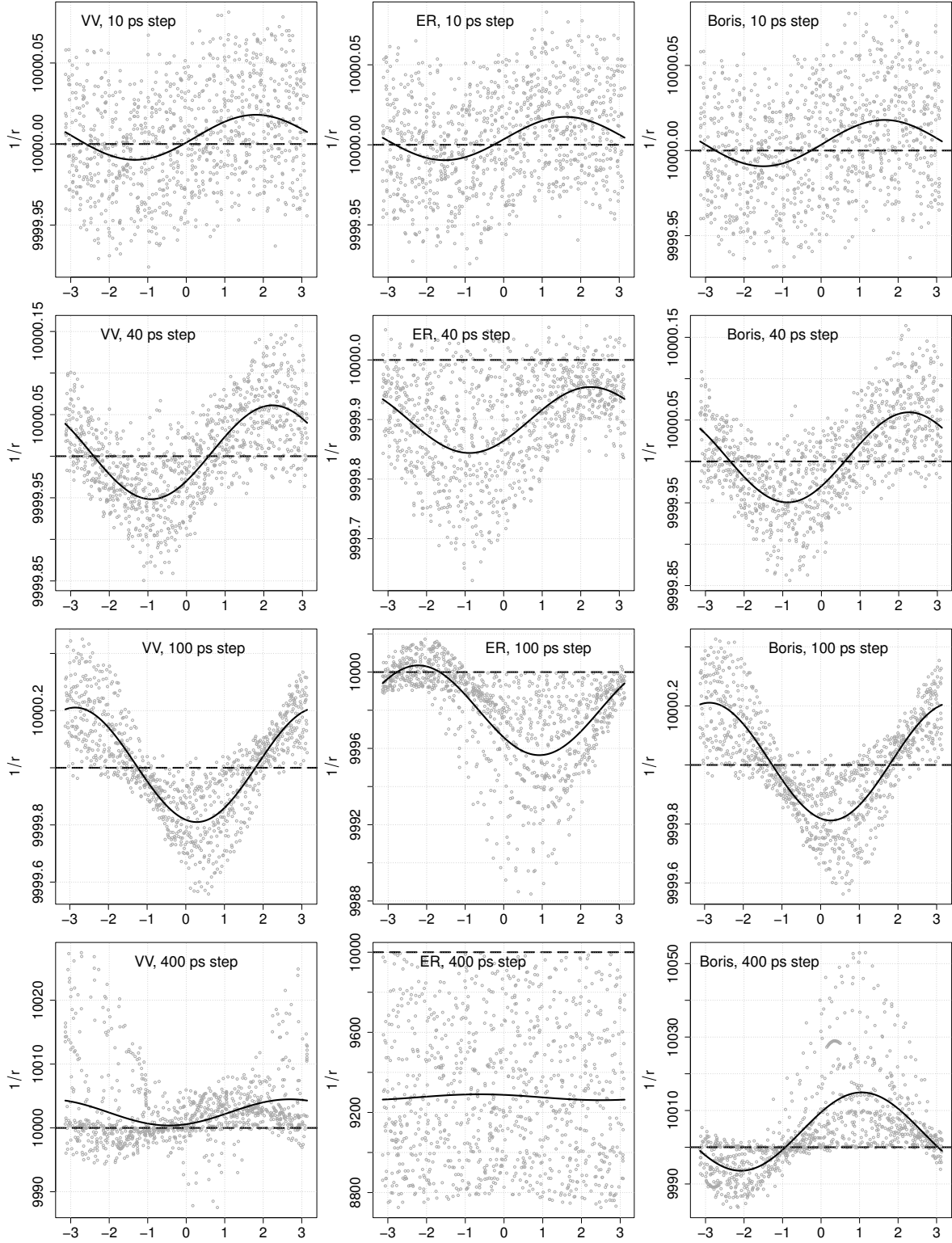


Figure 5.1: Electron positions during circular-Kepler-orbit pot test runs, plotted every 10^6 time steps for the first 10^9 time steps. The electron's orbital phase θ_e is on every horizontal axis. Black curves are fits of eq. (5.1); horizontal dashed lines represent the ideal solution $1/r = 10^4$. Notice the different scales of the plots' $1/r$ axes.

integrator	Δt (ps)	$(\mu/h^2 - 10^4) \text{ (m}^{-1})$	$e_K (10^{-6})$	θ_0 (radians)
VV	4	-0.00059 ± 0.00087	0.097 ± 0.11	-1.3 ± 1.4
VV	10	0.00413 ± 0.00091	1.30 ± 0.13	1.806 ± 0.094
VV	40	0.0047 ± 0.0011	5.65 ± 0.17	2.227 ± 0.027
VV	100	0.0104 ± 0.0021	20.04 ± 0.46	-2.861 ± 0.013
VV	400	2.43 ± 0.16	205 ± 17	2.70 ± 0.11
ER	4	-0.00007 ± 0.00091	0.21 ± 0.13	3.14 ± 0.57
ER	10	0.00393 ± 0.00088	1.35 ± 0.12	1.61 ± 0.10
ER	40	-0.1008 ± 0.0023	5.54 ± 0.29	2.25 ± 0.51
ER	100	-2.001 ± 0.052	235.4 ± 7.3	-2.217 ± 0.021
ER	400	-724 ± 11	1576 ± 1700	-0.6 ± 1.0
Boris	4	-0.00148 ± 0.00087	0.06 ± 0.12	-2.2 ± 2.1
Boris	10	0.00437 ± 0.00089	1.36 ± 0.12	1.64 ± 0.96
Boris	40	0.0049 ± 0.0011	5.45 ± 0.18	2.264 ± 0.027
Boris	100	0.0113 ± 0.0022	19.9 ± 0.45	-2.879 ± 0.014
Boris	400	4.26 ± 0.21	1066 ± 40	1.056 ± 0.019

Table 5.1: Fits of eq. (5.1) to the results of circular-Kepler-orbit pot tests of different particle-motion integrators and different Δt .

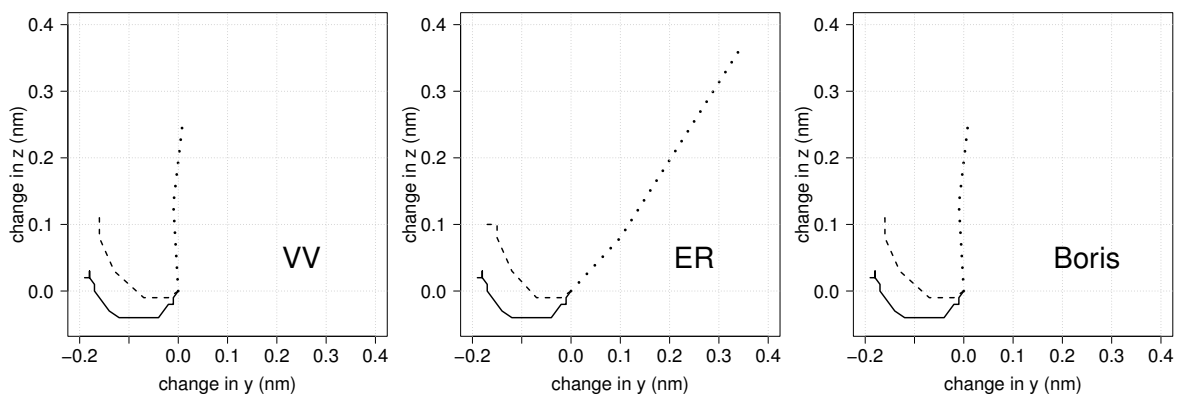


Figure 5.2: Ion trajectories in circular-Kepler-orbit pot tests, recorded every 10^6 time steps over a period of 8 ms of in-simulation time. *Dotted lines:* $\Delta t = 100$ ps. *Dashed lines:* $\Delta t = 40$ ps. *Solid lines:* $\Delta t = 10$ ps.

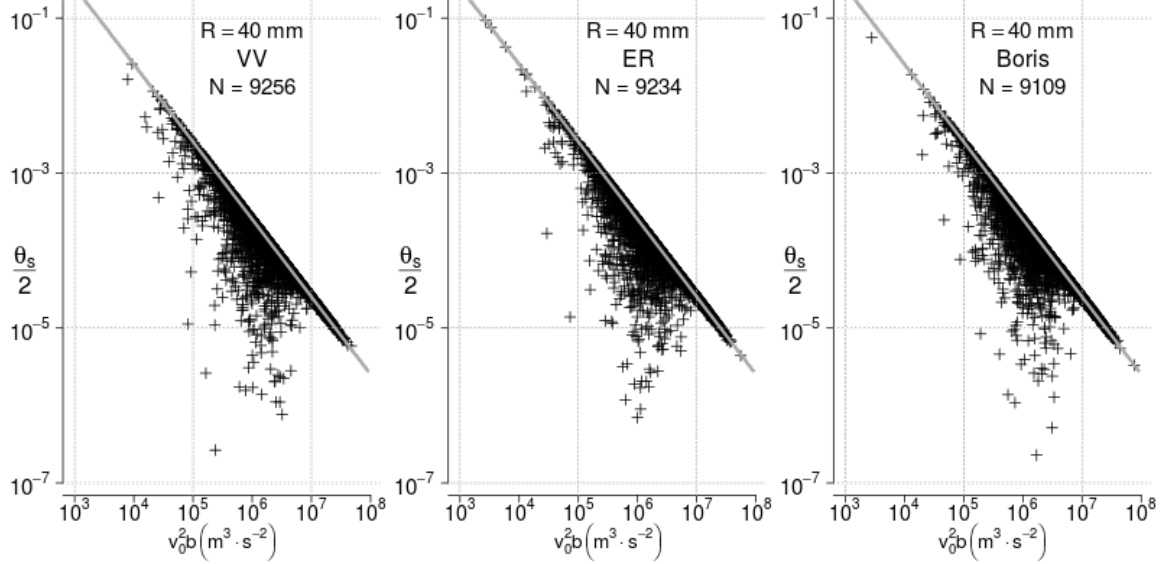


Figure 5.3: The relationship between $v_0^2 b$ and $\theta_s/2$ in the Rutherford-scattering pot tests of different integrators. The straight grey line represents eq. (5.3).

number of time steps multiplied by 10 (by virtue of making Δt 10× smaller) the drift rate fell by more than half. At the lowest Δt value I used, 4 ps, the drift was nearly below the resolution of pot's output, being only ≈ 10 pm in both directions, regardless of the choice of integrator, for an overall drift of about 14 pm in 8 ms.

There was no sign of a systematic error in the ion and electron trajectories which would persist in the $\Delta t \rightarrow 0$ ps limit. pot simulates both the electron and the ion well when the time step is short enough, and pot passes the circular-Kepler-orbit test.

5.1.2 Rutherford scattering

Another two-body process characterized by a single equation is Rutherford scattering. Rutherford developed a model to relate the scattering angle θ_s and impact parameter b of an alpha particle scattering away from a gold nucleus. His model implies

$$b = \frac{2Ze^2}{4\pi\epsilon_0 mv_0^2} \cot \frac{\theta_s}{2} \quad (5.2)$$

where m is the alpha particle's mass, v_0 is the alpha particle's speed infinitely far from the gold nucleus, and Z is the gold nucleus's charge state [160, pp. 43–44].

Under classical physics, the mechanics are no different for an electron scattering around an ion, and Rutherford's equation remains valid once allowance is made for the different charges and masses:

$$b = \frac{Ze^2}{4\pi\epsilon_0 m_e v_0^2} \cot \frac{\theta_s}{2} \iff v_0^2 b = \frac{Ze^2}{4\pi\epsilon_0 m_e} \cot \frac{\theta_s}{2} \quad (5.3)$$

where Z is the ion's charge state. I implemented this classical electron-scattering system as

another pot test: place a singly-charged, heavy ($m_i/m_e = 10^{15}$) ion in the middle of the simulation domain; fire electrons, one at a time, at randomly chosen speeds from the edge of the domain past the ion; and estimate each electron's v_0 , b , and θ_s from the simulated trajectory. Insofar as pot accurately simulated the passage of a charged particle from infinity past another charged particle, each simulated electron's $v_0^2 b$ and θ_s would have been related in the way eq. (5.3) describes. Figure 5.3 tests whether this was so by plotting $\theta_s/2$ against $v_0^2 b$ for Rutherford scattering simulated by the three different integrators with $\Delta t = 4$ ps and a simulation domain radius R of 40 mm.

Evidently the electron tended to be scattered less in the simulation than the Rutherford equation would have dictated: some of the θ_s values emerging from the simulation were too small. Probing more deeply, the relative error in the simulations' θ_s values was always negligible for the electrons with the largest $v_0^2 b$, and consistently small for electrons with the smallest $v_0^2 b$ — only for middling $v_0^2 b$ did pot materially underestimate the scattering, and even there θ_s 's *absolute* error was small.

These facts, and the asymmetry of the error in θ_s , point to the error arising from the finite size of pot's simulation domain, rather than a defect in the program's simulation algorithms. pot computed θ_s as the angle between the electron's bearing when pot initially fired it, and the electron's bearing after the electron passed the ion and returned to the simulation's boundary. As for v_0 and b , pot estimated them as the electron's speed and impact parameter upon initial launch. These were not quite the same as the θ_s , v_0 , and b in the Rutherford equation, because the Rutherford equation assumes that a scattered particle follows an *infinitely long* trajectory around the scattering particle, with θ_s , v_0 and b defined in terms of that infinite trajectory. pot, unable to simulate an infinitely long trajectory, simulated only the finite trajectory the electron traced in the simulation domain, which meant that pot observed less scattering than that implied by the corresponding infinite trajectory, and so systematically underestimated θ_s .

This observation explains why pot underestimated θ_s for certain electrons. High-speed electrons launched with $b \approx R$ traversed only a small fraction of the domain before encountering the simulation boundary, leaving those electrons essentially unscattered and causing pot to vastly (in relative terms) underestimate those electrons' scattering angles.

A ready test of this explanation is to re-plot $\theta_s/2$ against $v_0^2 b$, excluding the minority of electrons with $b \approx R$. I do so in figure 5.4, demonstrating that for the remaining electrons the relationship between $v_0^2 b$ and $\theta_s/2$ is almost exactly as predicted for all three integrators, a striking confirmation that pot's deviation from the Rutherford equation is a finite-size effect, not a symptom of a defect in the code. Were it not for the simulation being finite in size, there would be minimal systematic error in pot's Rutherford scattering results. pot passes the scattering test.

5.1.3 Gases of non-interacting electrons and protons

After finishing the fundamental two-body tests, I set pot the task of simulating many-body systems more akin to the sphere-in-plasma systems for which it was designed. The first many-body system I simulated was the simplest: a gas of electrons and protons which did not interact with each other. I simulated two versions of this system, one without a central collecting sphere, then one with a

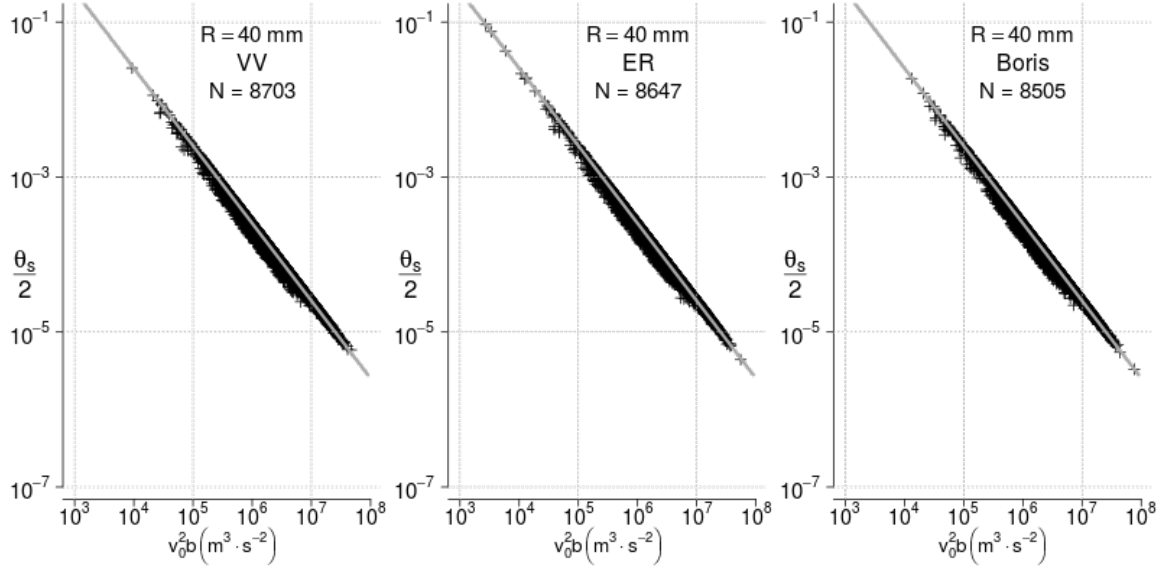


Figure 5.4: The relationship between $v_0^2 b$ and $\theta_s/2$ for electrons with $b < (4/5)R$. The straight grey line represents eq. (5.3).

collecting sphere which produced an electric field in proportion to its collected charge.

To assess whether pot modelled these systems in a reasonable fashion, I checked that the particles' average energy and momentum was approximately conserved during each simulation, and that the equilibrium velocity distributions of the electrons and of the protons were the Maxwell-Boltzmann distributions predicted by theory.

For these test simulations I decided on a standard set of values for pot's parameters, which table 5.2 lists. Holding the parameters constant across the simulations meant that I could eliminate changes in the parameters as reasons why the simulations might give different results. I also kept the particle-motion integrator and reinjection algorithm constant for the simulations by using the Boris integrator and Hutchinson's SCEPTIC reinjection algorithm for all of them. (Keeping to one integrator also reduced the number of simulations I had to run, as I no longer had to re-run every simulation twice with the VV and ER integrators.)

Gas of non-interacting masses without a collecting sphere

I try not to dwell on this test case because it is a relatively lenient one. In a gas of non-interacting electrons and protons without a collecting sphere, the particles coast through the simulation domain in straight lines at constant velocity, and even a low-quality particle-motion integrator can solve for the particles' motion. This scenario is less a test of the integrator and treecode implementation, and more a test of whether pot can run at all when N is large, and of the particle reinjection algorithm.

Conventionally, the first test of a many-particle simulation is whether it suffers from drifts in the total energy as it runs. In this simulation the particles' potential energy was always nil because none of the particles produced an electric field or potential. Less trivially, the particles'

description	flag	name	default value
plasma particle count	-N	N	1.5×10^5
time step	-d	Δt	10^{-12} s
electron temperature	-E	T_e	220 K
ion temperature	-I	T_i	220 K
softening distance	-s	ϵ	2×10^{-8} m
flow/drift speed	-x		$0 \text{ m}\cdot\text{s}^{-1}$
simulation radius	-m	R	4×10^{-4} m
sphere radius	-a	a	2.5×10^{-6} m
settling time	-e		5×10^{-7} s
opening angle parameter		θ	1
ion-to-electron mass ratio		m_i/m_e	1836.15
multipole expansion order			monopole
ion charge state		Z	+1

Table 5.2: pot's default parameter values. The user may supply the first 9 to pot at run-time with the listed command-line flags, but adjusting the last 4 necessitates recompiling the program.

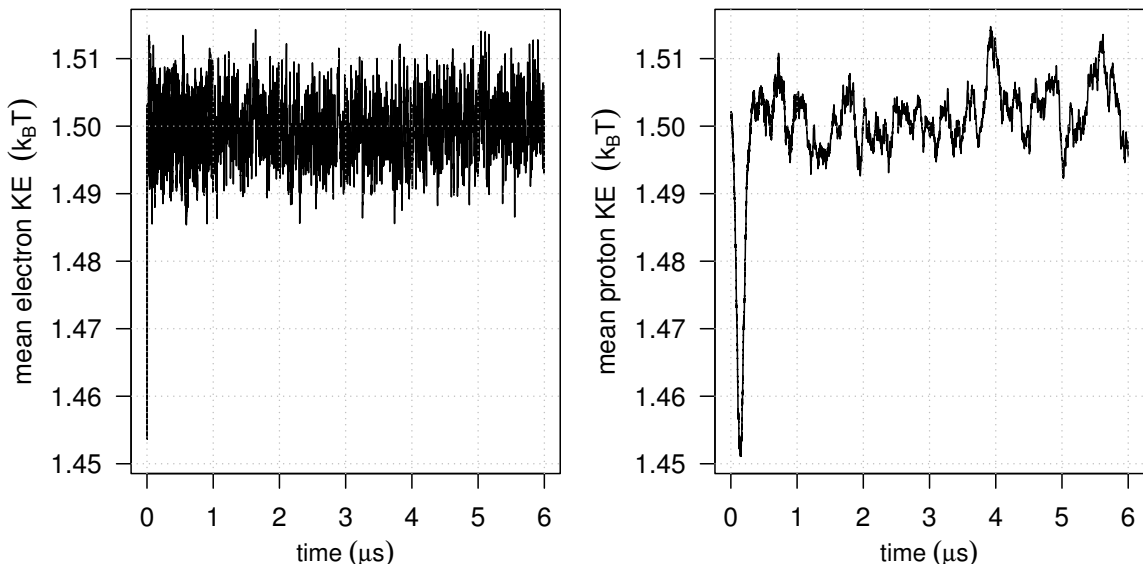


Figure 5.5: Mean kinetic energy of electrons (left) and protons (right) during a pot run without a collecting sphere and without electric fields.

mean kinetic energy was consistently around $(3/2)k_B T$ at equilibrium, with T the fixed background temperature of 220 K for both species. There was no upward or downward drift over millions of time steps (figure 5.5). For both electrons and protons there *was* an initial dip and rebound in the mean kinetic energy of about $0.05k_B T$, but that was a manifestation of the initialization bug which §4.1 described. The gas began with a non-uniform number density throughout space, triggering the immediate, transient dip and rebound in kinetic energy which was part of the gas's relaxation to equilibrium. (The same phenomenon is visible in the more sophisticated simulations to come later in this chapter.)

I also checked for drifts in linear momentum or angular momentum. Plotting each component of the momenta for both species in figure 5.6, there is no obvious tendency for any component to systematically shift away from zero during the simulation. (The grey median-smoothed curves in the electron plots are consistently noisier for the first microsecond of in-simulation time, but that is because I programmed pot to over-sample the macroscopic variables early in the simulation, and because running medians have more noise near the start and end of a time series.)

As an aside, the Maxwell-Boltzmann velocity distribution implies that v_x , v_y , and v_z have Gaussian distributions with a variance of $k_B T/m$ (eq. (2.21)). This further implies that the standard deviation of any linear-momentum component is $\sqrt{mk_B T}$, and the standard deviation of the *sample mean* of a species' linear-momentum component, after normalization by $\sqrt{mk_B T}$, is $(N/2)^{-1/2}$. With $N = 1.5 \times 10^5$, the sample mean's standard deviation here should be 0.004, which indeed matches the spread of the fluctuations in $\langle p_x \rangle$, $\langle p_y \rangle$, and $\langle p_z \rangle$ in figure 5.6.

Finally, I come to the velocity and speed distributions for both species at equilibrium. In figure 5.7 are histograms of v_x , v_y , v_z , and v for both species at the end of the simulation. The histograms adhere to the theoretically predicted distributions, superimposed as black, dashed curves. A (far) sterner test of correctness is to apply a formal statistical test of Gaussianity to each velocity-component distribution for both species. Doing so, all six distributions pass the test with flying colours: an Anderson-Darling test gives a p -value of over 0.5 for every distribution.

In the absence of any sign of problems, I bring forward a less mundane many-body system.

Gas of non-interacting particles around a collecting sphere

Elaborating on the last subsection's system, I ran another simulation, adding a collecting sphere at its centre. The sphere began with a charge of zero, but after the initial settling period the sphere acquired charge by collecting those electrons and protons which collided with it. Once charged the sphere produced a Coulombic electric field, and the electrons and protons accelerated in that field according to the softened Lorentz force law, though the electrons and protons continued not to interact with each other. One would therefore expect the sphere to induce charge separation around itself, but there would be no screening characteristic of a plasma because the electrons and protons had no electric fields of their own in this simulation.

As before I first check the mean particle energies. Because the electrons and protons could now have nonzero potential energy because of the sphere's potential, I plot the mean potential energies beside the mean kinetic energies (fig. 5.8). Both species' kinetic energies again consistently

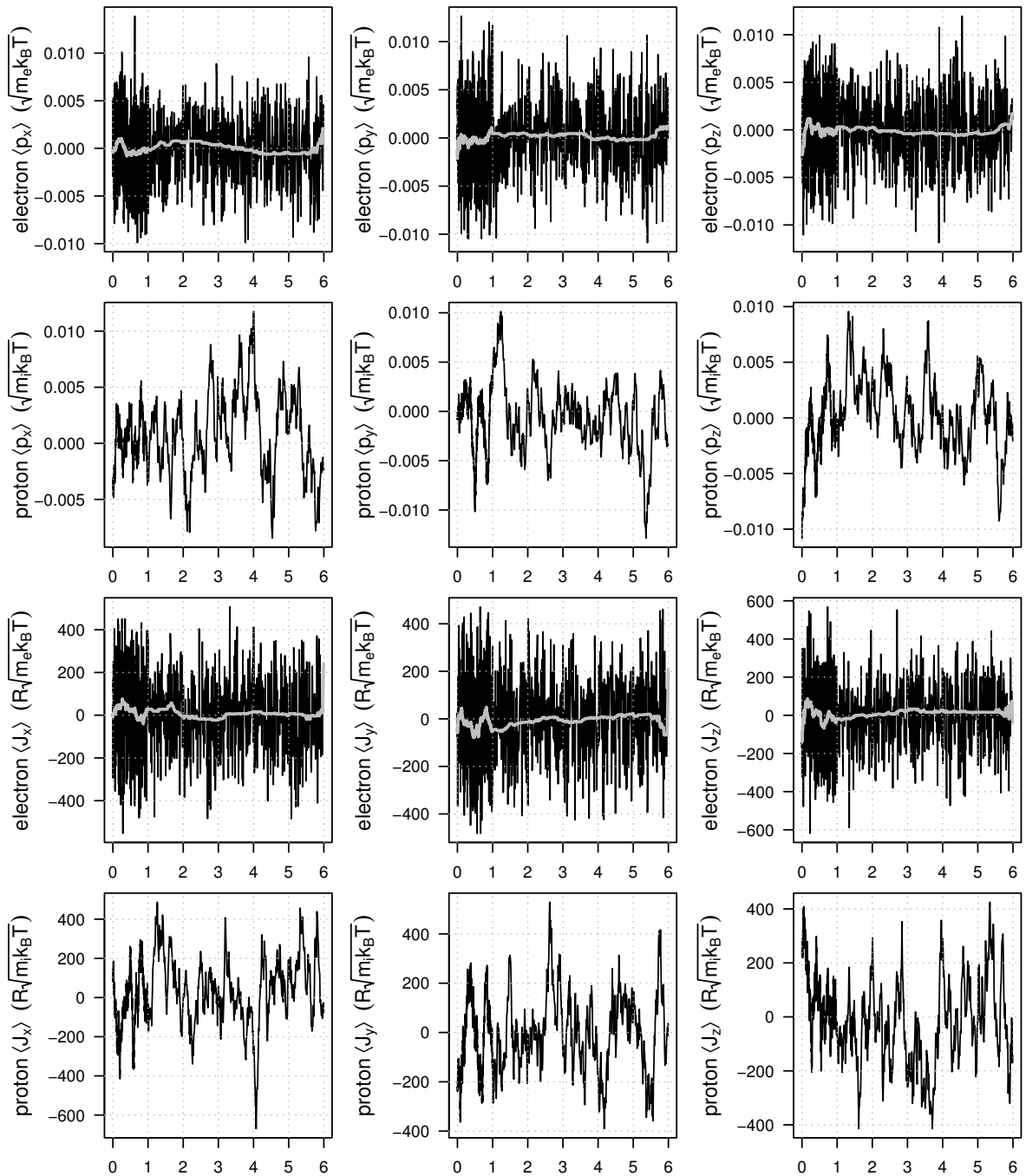


Figure 5.6: Mean linear-momentum and angular-momentum components of electrons and protons during a pot run without a collecting sphere and without electric fields. Horizontal axes represent in-simulation time in μ s. Thick grey lines on the electron plots are running medians to smooth the data and unmask any underlying momentum drifts.

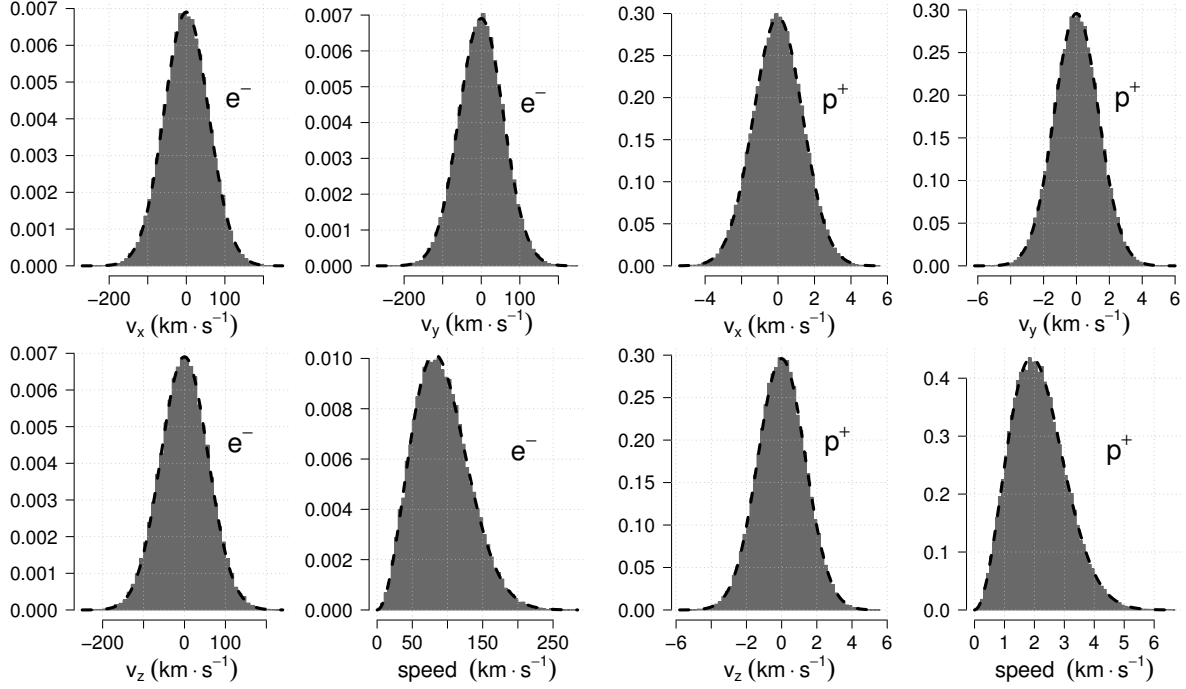


Figure 5.7: Histograms of electrons' and protons' speed and velocity components at equilibrium in a pot test run without a collecting sphere and without any electric fields. Thick, black dashed curves represent the theoretical equilibrium distributions.

averaged about $(3/2)k_B T$. After $t \approx 2 \mu\text{s}$, when the sphere was fully charged, there was no sign of a drift. During the settling time both species' PE (potential energy) was nil, the sphere having no charge with which to generate an electric potential, but once that period ended the electrons had positive PE and the protons had negative PE, an outcome anticipated by the fundamental law of charging: the sphere charged negatively, repelling electrons and attracting ions. The *combined* mean of the electrons' and protons' potential energies was always close to zero (fig. 5.8, bottom right), but became slightly negative as the sphere charged. After the sphere charged the combined mean PE averaged $-3.5 \times 10^{-4} k_B T$; taken as a whole, the plasma was slightly attracted to the central sphere.

The cause of the plasma's net attraction was the protons having a smaller average distance from the sphere than the electrons, making the protons' negative PE slightly higher in magnitude than the electrons' positive PE. Having saved the simulation's microscopic state at the simulation's end, I read out the particles' final positions and calculate their relative number density as a function of distance r from the sphere (fig. 5.9, left). Plotting density separately for the electrons and protons indicates that near the sphere were relatively many protons and relatively few electrons, with more electrons and fewer protons far away. (The specific functions plotted are weighted kernel density estimates of r for both species. I used an Epanechnikov kernel and gave each datum a weight of r^{-2} to transform the unweighted r -space density to a real-space density. The necessarily non-negligible width of the kernel explains the unphysical nonzero density at r values which are slightly less than a or slightly beyond R .)

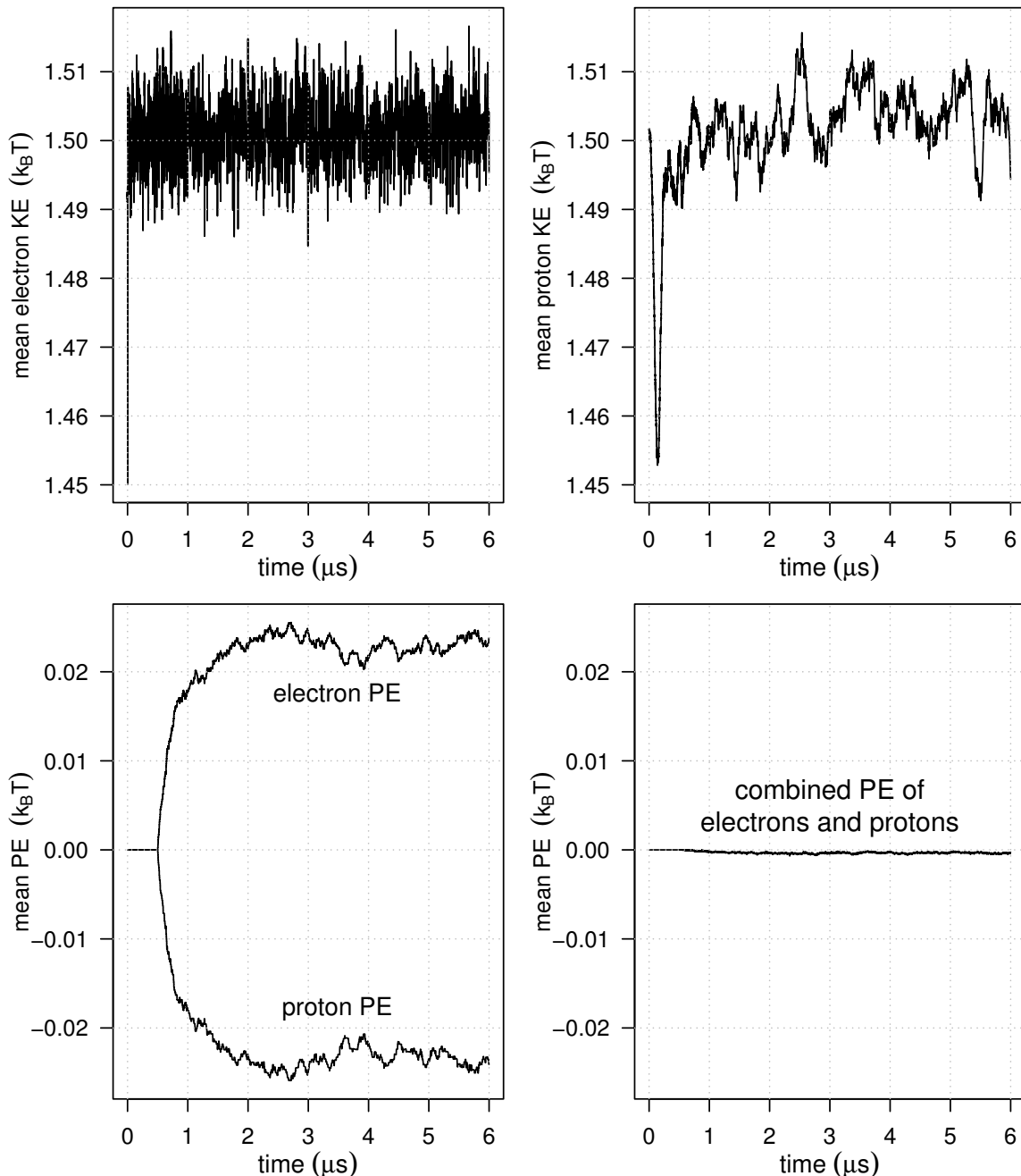


Figure 5.8: Mean kinetic and potential energies of electrons and protons during a pot run with a collecting sphere but no interactions among electrons and protons.

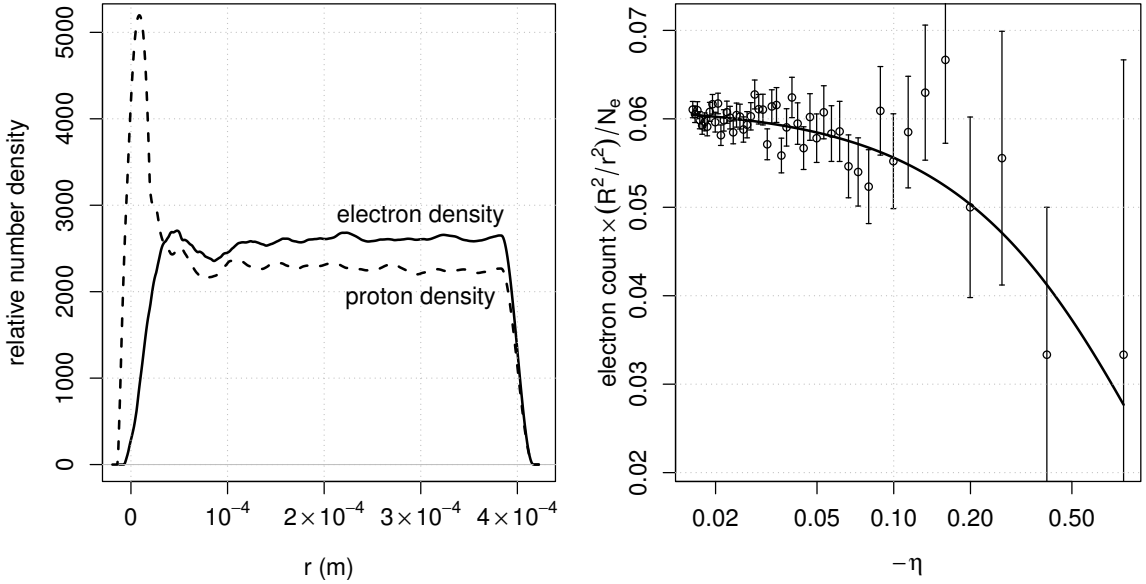


Figure 5.9: *Left*: electron and proton number densities, normalized to have integrals of unity, as a function of r at the end of a pot run with a collecting sphere but no interactions among electrons and protons; the nonzero densities at $r < a$ and $r > R$ are artifacts of the kernel density estimator. *Right*: normalized electron counts, with Poissonian standard error bars, as a function of η across 50 r bins at the end of the same pot run, with a Boltzmann relation fitted as the thick black curve.

pot also recorded $\phi(r)$ at 50 equally spaced radii from the simulation edge inwards at the end of the simulation. Combined with the particle position data this allows one to judge the Boltzmann relation's correspondence to the simulation results. I counted electrons in 49 r bins* centred on the r values where pot sampled $\phi(r)$, rescaled those counts by R^2/r^2 , and plotted the rescaled counts against the normalized electric potential η at each bin's location (fig. 5.9, right). Fitting a Boltzmann relation to the binned results, the two do seem to be statistically consistent — about two-thirds of the data are within a standard error of the Boltzmann relation curve, almost all of the points are within two standard errors of the curve, and the data do not seem to be systematically above or below the curve — though the degree of noise makes this result suggestive, not decisive.

Proceeding to the question of momentum conservation, figure 5.10 plots time series of linear momentum and angular momentum. The dispersion of the momentum components is reassuringly similar to their dispersion for the previous test scenario, the non-interacting gas without a collecting sphere, as is the lack of evidence for steady drifts upward or downward.

Checking the velocity distributions for both species is also reassuring (fig. 5.11). Carrying out Anderson-Darling tests on the six velocity-component distributions, five of the six distributions unambiguously pass (giving p -values of at least 0.17), though the proton v_y distribution now obtains a p -value of 0.022, and the test rejects the hypothesis that the protons' v_y has a Gaussian distribution.

The rejection is almost certainly a statistical coincidence rather than meaningful evidence

*There was no 50th bin because it would have had to extend past the simulation boundary to maintain equal bin widths.

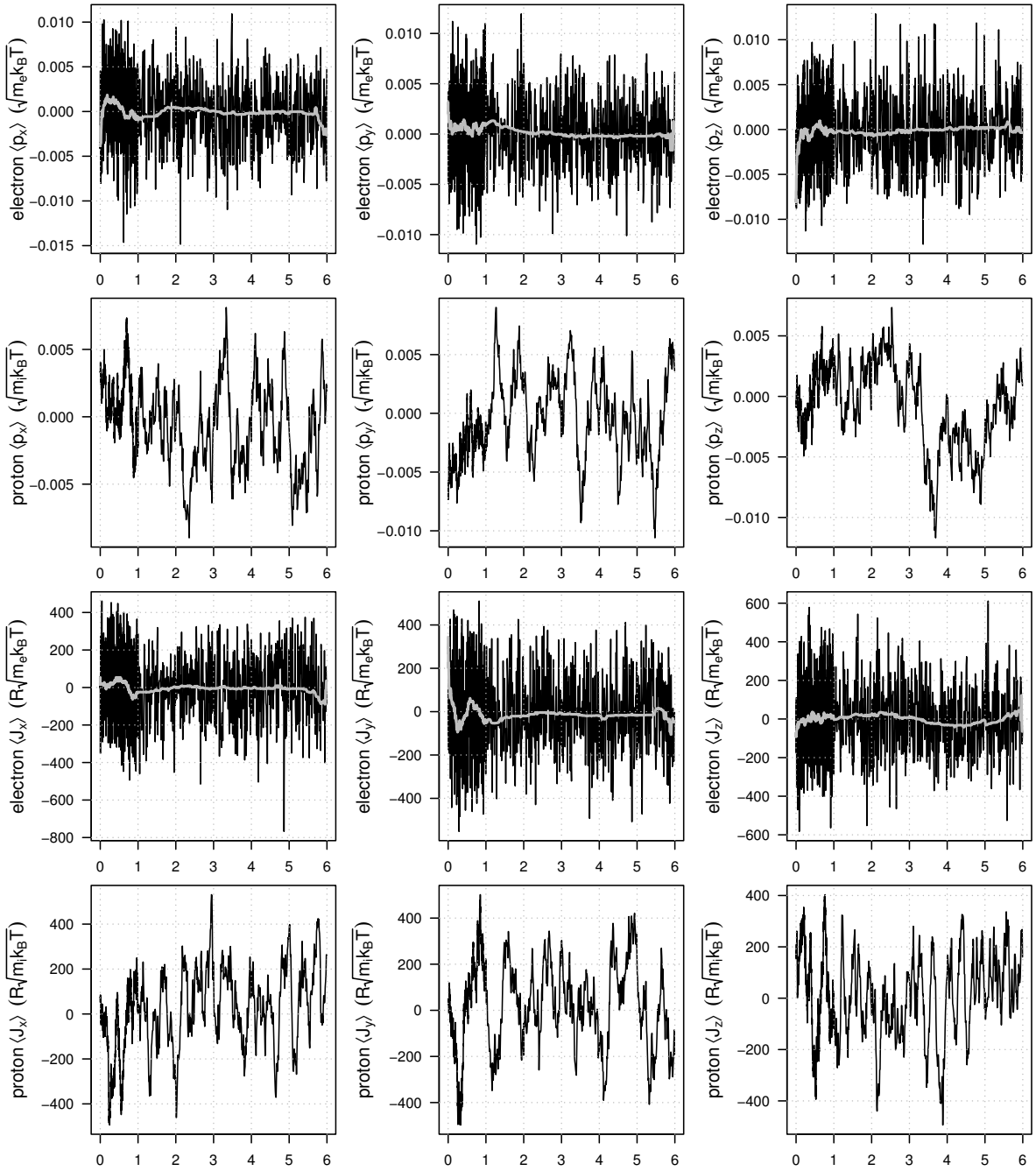


Figure 5.10: Mean linear-momentum and angular-momentum components of electrons and protons during a pot run with a collecting sphere but no interactions among electrons and protons. Horizontal axes represent in-simulation time in μs . Thick grey lines on the electron plots are running medians to smooth the data and reveal any underlying momentum drifts.

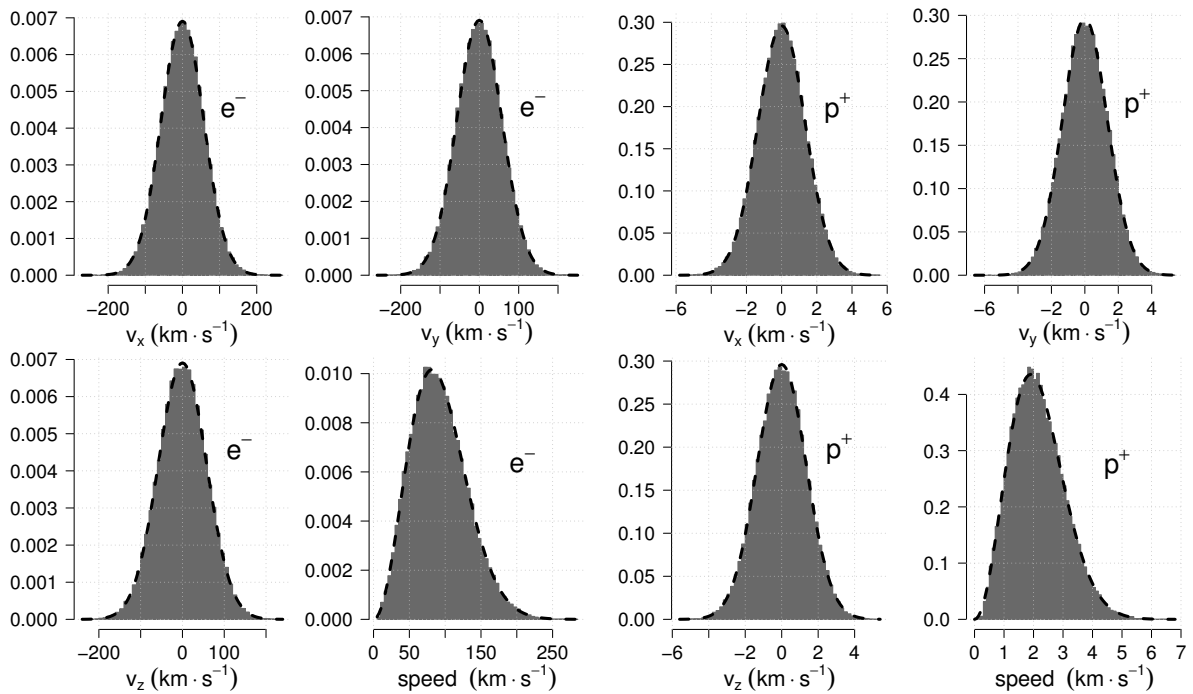


Figure 5.11: Histograms of electrons' and protons' speed and velocity components at equilibrium in a pot test run with a collecting sphere but no interactions among electrons and protons. Thick, black dashed curves represent the theoretical equilibrium distributions.

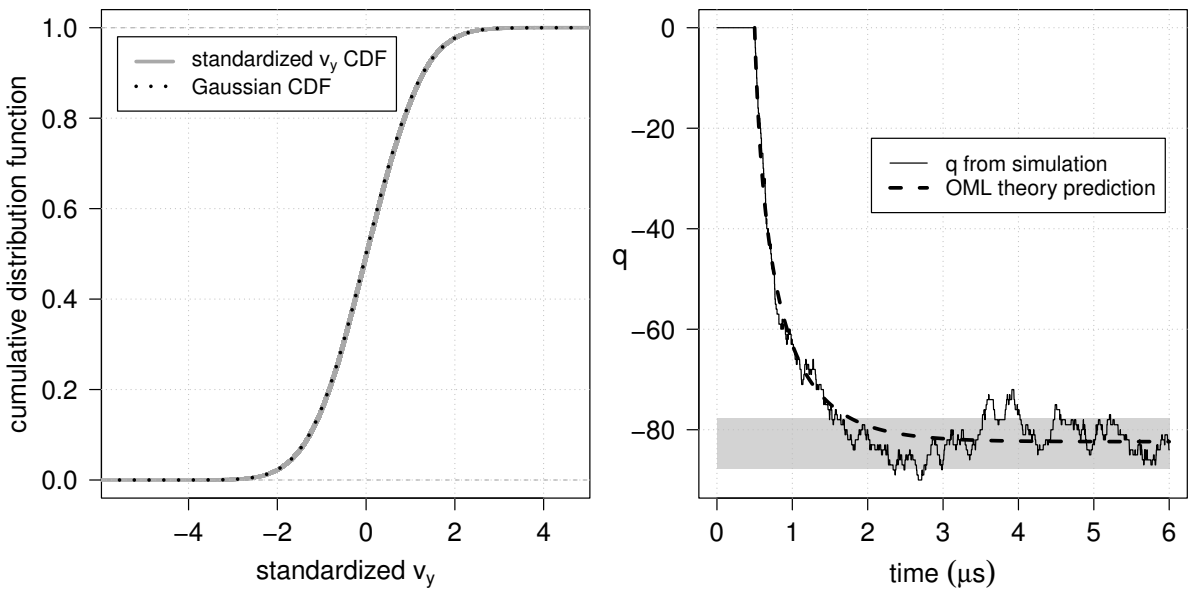


Figure 5.12: In a pot test run with a collecting sphere but no interactions among electrons and protons, the CDF of the standardized v_y among the protons at the run's end (left) and the sphere's charge state q over time (right).

of a faulty reinjection method or integrator. Macroscopically this system should have spherical symmetry, so it would be quite odd for a fault to manifest exclusively in the protons' v_y distribution. Furthermore, there is the statistical issue of multiple testing. A statistical test with a rejection level of 0.05 has a 5% chance of spuriously rejecting its input. Thus far I have tested 12 distributions for Gaussianity, 6 from this simulation and 6 from the previous one, and assuming statistical independence of the tests, the probability of at least one spurious rejection of Gaussianity is $1 - 0.95^{12} \approx 46\%$ — hardly unlikely. Finally, I plotted the cumulative distribution function of the standardized v_y values and overlaid a Gaussian CDF (fig. 5.12, left). No systematic difference between the CDFs was apparent at this scale.

Including a collecting sphere in this simulation meant that the system had the sphere's charge state q as a dependent variable. I compare q 's time evolution in the simulation to the time evolution implied by the OML expressions for the electron and proton currents onto the sphere (fig. 5.12, right). Keeping in mind that q not only converges to its equilibrium value but also fluctuates at equilibrium, I also apply the small-sphere stochastic model of §3 to predict q 's equilibrium standard deviation σ , the expected scale of q 's equilibrium fluctuations. Superimposing a grey 1- σ band around the predicted mean in figure 5.12's q plot, q 's fluctuations not only match the continuous OML-theory curve, but are mostly within the 1- σ band. I therefore have a tripartite consonance between the results of existing theory (the OML model), my own theory (my stochastic model), and my simulation results (from pot).

5.1.4 Pure plasma

The next test system was a pure proton-electron plasma, which was the same as the non-interacting gas system without a collecting sphere, but with the particles now producing electric fields and hence interacting with each other. I continued to use pot's default parameter values (table 5.2) and the Boris integrator, but because these simulations were far more processor-intensive than the earlier test simulations I ran them for less in-simulation time.

With the plasma particles exerting forces on each other, the time series of average kinetic and potential energies were more dramatic (fig. 5.13). Over the first 0.4 μs the mean proton and electron PEs leapt away from zero and then oscillated back towards equilibrium, accompanied by oscillations in the kinetic energies. Looking more closely, the electrons' PE raced away from zero in about 3 ns, then underwent an oscillatory decay to an energy $\approx -0.19k_B T$ over the next 10–15 ns (fig. 5.14, left). It then decayed in an oscillatory fashion towards zero, but over a period ~ 500 ns (fig. 5.14, right). The proton PE did the same but with their mean PE's sign reversed.

These oscillations are a florid expression of §4.1's initialization bug. In the previous subsections' runs, the plasmas' non-equilibrium initial conditions caused a single dip and rebound at the beginning of the simulation, but in the current simulation, where the plasma particles could interact with each other, the initial non-equilibrium conditions triggered longer, Langmuir oscillations in the kinetic and potential energies of both electrons and ions.

To check that the initial conditions caused the oscillations, I re-ran this simulation anew after fixing the non-equilibrium initialization bug. Comparing the new results (thin black curves) to

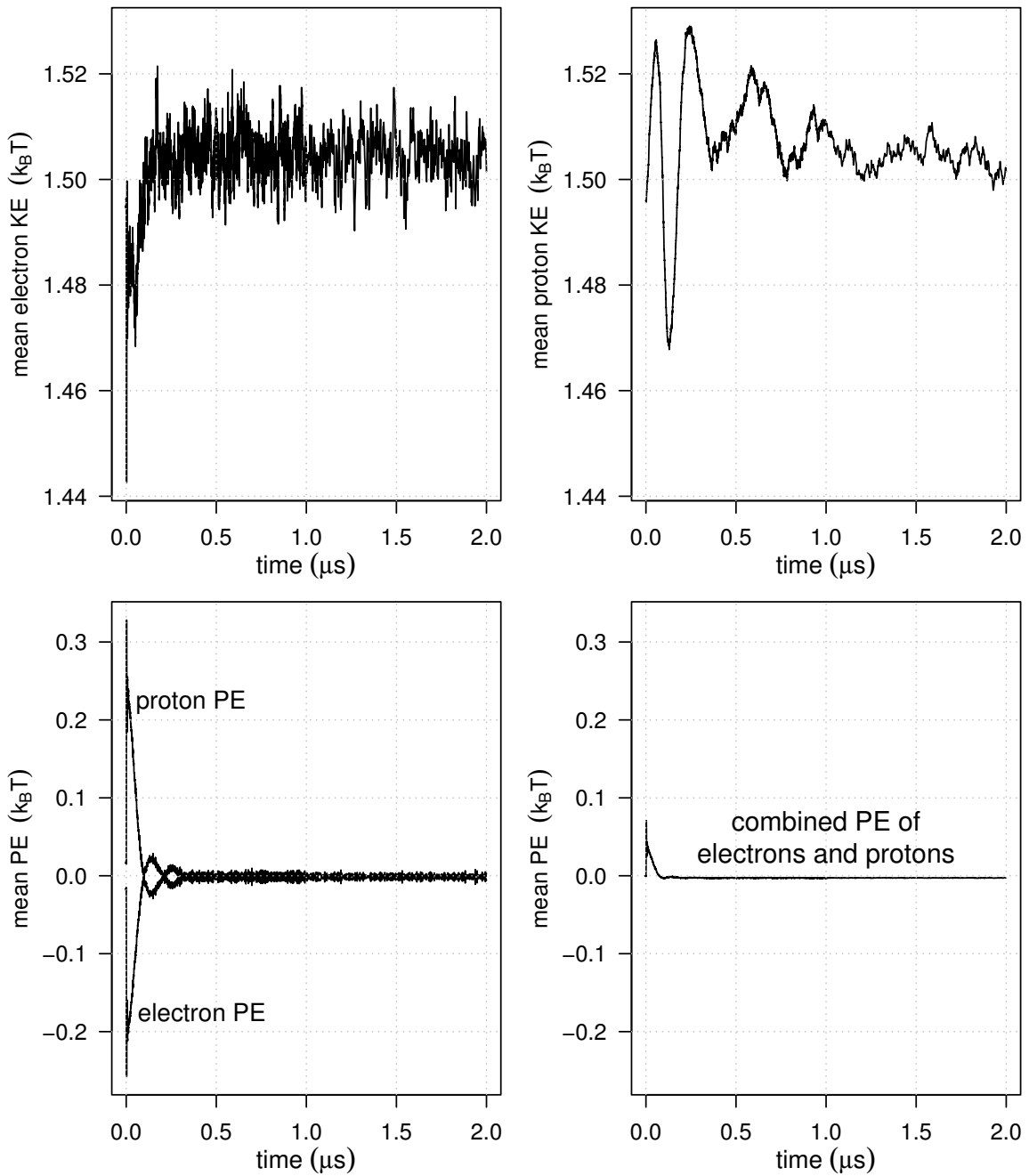


Figure 5.13: Mean kinetic and potential energies of electrons and protons during a pot run with a pure plasma (no collecting sphere).

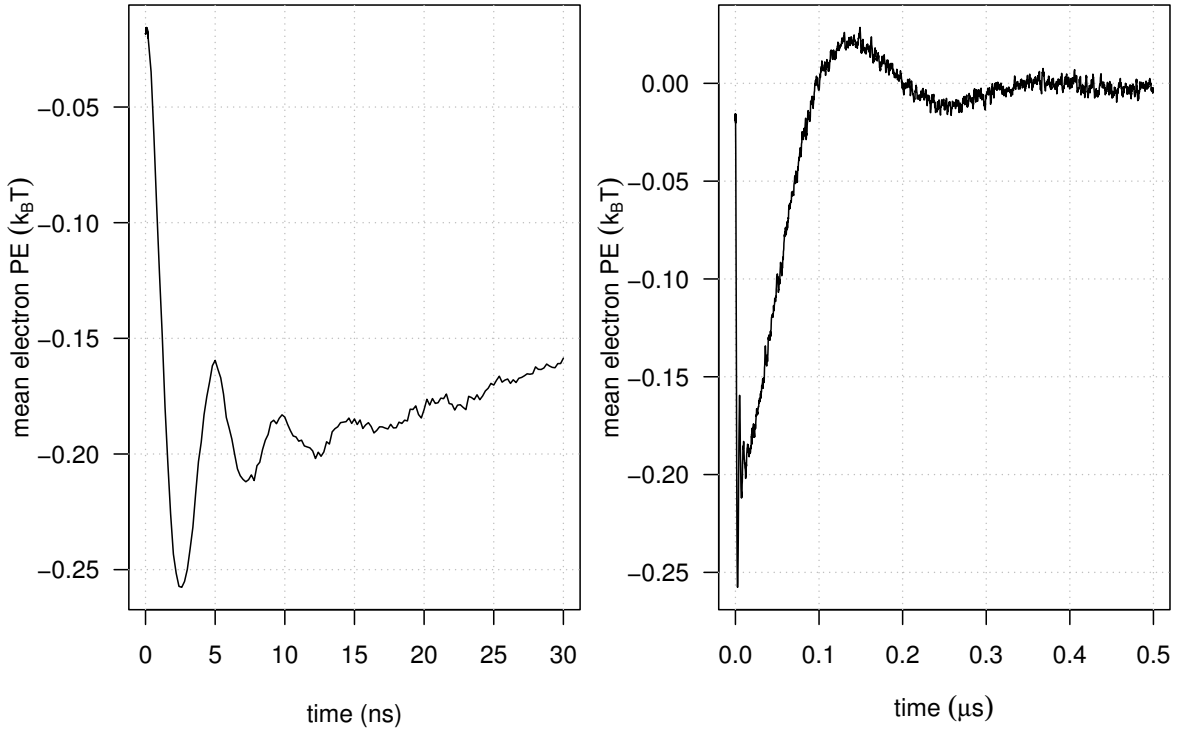


Figure 5.14: Early time evolution of mean electron potential energy in a pure-plasma pot run.

the old (thick grey curves) in fig. 5.15 confirms that the bug fix eradicated the start-of-simulation oscillations.

Turning my attention to the pure-plasma simulation’s momentum time series (fig. 5.16), I see they lack obvious trends, consistent with approximate conservation of momentum over time. The electrons’ and protons’ velocity distributions are also consistent with theoretical expectation (fig. 5.17), and the six velocity-component distributions all pass Anderson-Darling Gaussianness tests with p -values between 0.12 and 0.52, except for the electron v_z distribution, which passes narrowly with a p -value of 0.051. That is almost certainly a false near-positive which is an artifact of multiple testing and statistical noise; the CDF of the standardized v_z differs from a Gaussian CDF only at its uppermost extreme, among the dozen electrons with the highest v_z .

5.1.5 Conclusion

To ensure that pot produced physically sensible results, I used it to simulate several test systems for which I could use known physics as a benchmark. I checked that pot gave a very good approximation to the nearly circular Kepler orbit of an electron around an extremely heavy ion, and that pot’s simulation of electrons scattering around a heavy ion approximately conformed to Rutherford’s scattering equation.

Addressing macroscopic systems, I then ran pot to simulate macroscopic gases (proton and electron masses which did not interact with each other) with and without a collecting sphere, and a pure plasma without a collecting sphere. Simulating these many-body systems, pot produced

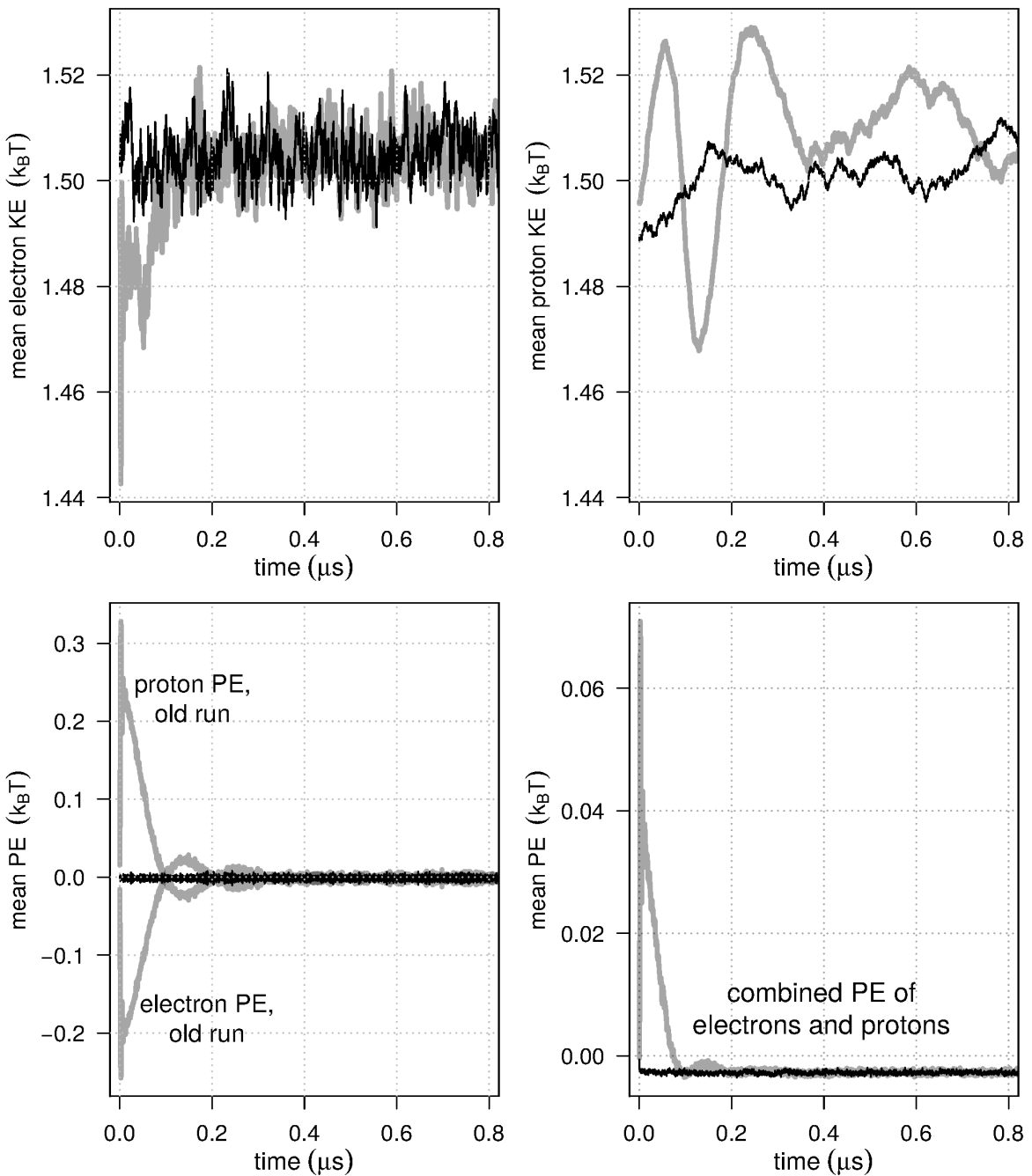


Figure 5.15: Mean kinetic and potential energies of electrons and protons during two pot runs with pure plasmas (no collecting spheres). The first run (thick grey curves) began with a non-uniform spatial plasma distribution; the second (thin black curves) began with a uniform distribution.

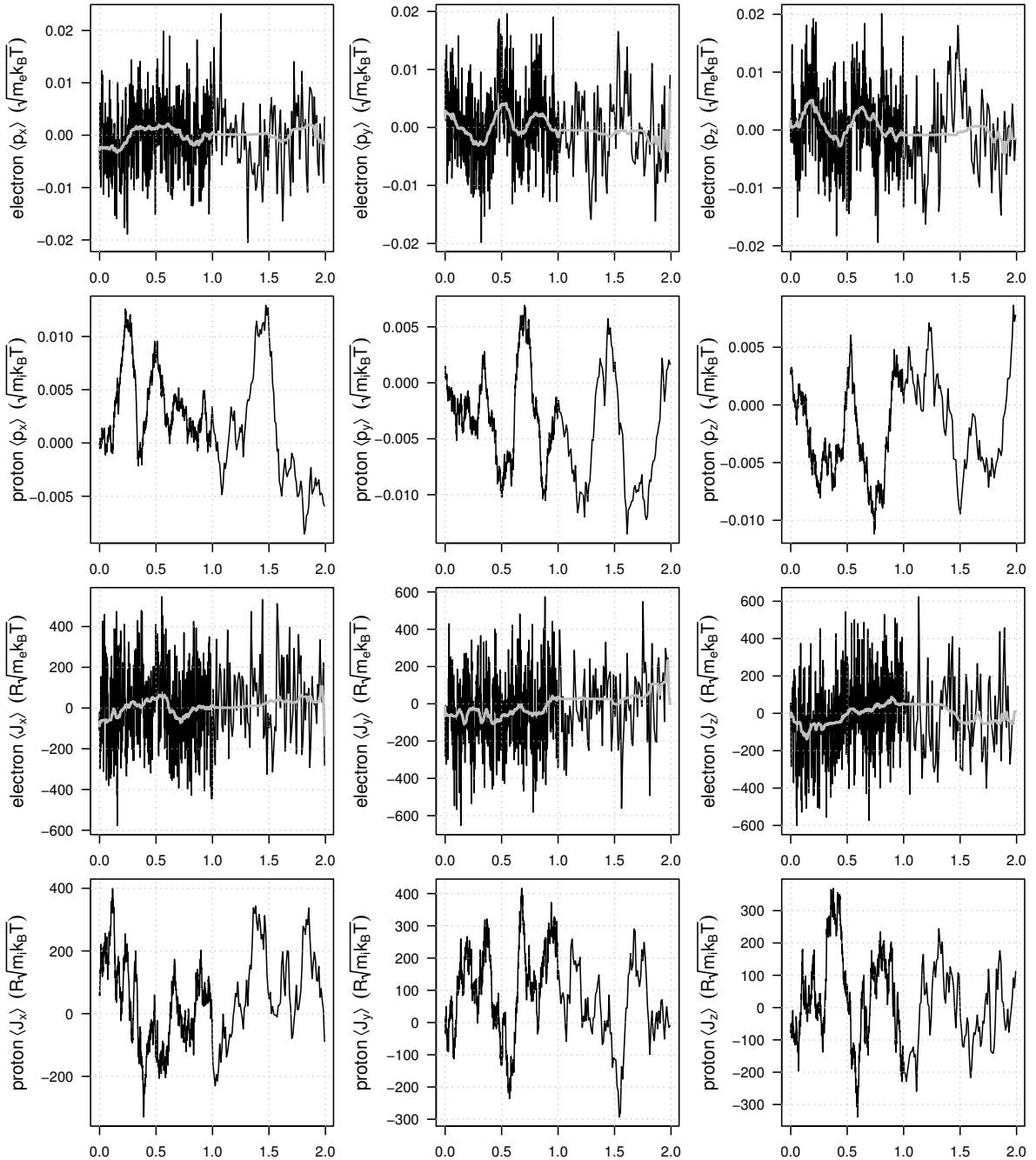


Figure 5.16: Mean linear-momentum and angular-momentum components of electrons and protons during a pot run with interactions among electrons and protons but no collecting sphere. Horizontal axes represent in-simulation time in μs . Thick grey lines on the electron plots are running medians to smooth the data and reveal any underlying momentum drifts.

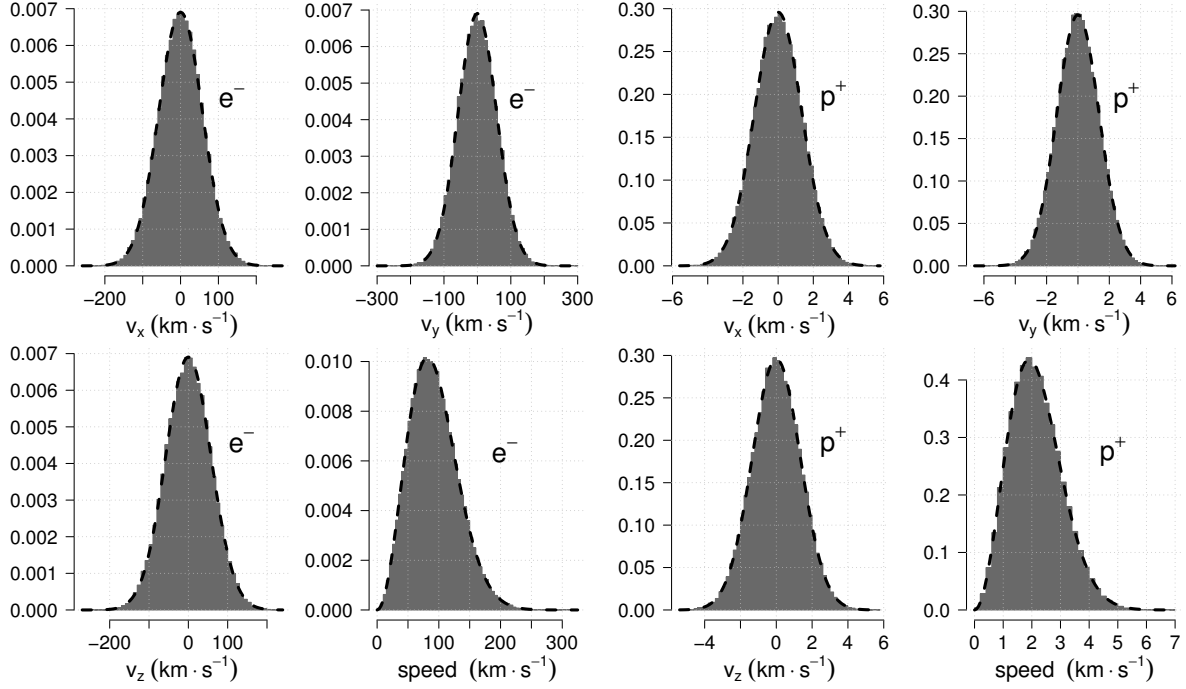


Figure 5.17: Histograms of electrons' and protons' speed and velocity components at equilibrium in a pot test run with interactions among electrons and protons but no collecting sphere. Thick, black dashed curves represent the theoretical equilibrium distributions.

the expected velocity distributions for the particle species, with the particles' average linear and angular momenta stable over time as desired. In the gas-like system with a collecting sphere, the sphere charged in accordance with OML theory, pushing the electron and proton densities to equilibrium spatial distributions consistent with physical expectations (electrons repelled from the sphere in rough agreement with the Boltzmann relation, and ions attracted). All three test systems converged to equilibrium, ending with stable momentum and energy, and with electron- and ion-velocity distributions conforming to the Maxwell-Boltzmann distribution anticipated by theory.

These test runs also indicate how long pot took to run. All of these runs ran on Imperial College's CX1 computing cluster across 16 cores. On that platform, pot needed 44–46 hours to simulate 6 μ s of plasma time evolution for the two runs without particle-particle interactions. For the original pure-plasma simulation which began out of equilibrium, pot took 124.5 hours to simulate 2 μ s of plasma time evolution, and for the newer pure-plasma simulation which started at equilibrium, pot took 99.6 hours to simulate 1.5 μ s of time evolution. Predictably, pot ran far faster (8 or 9 times faster) when it did not compute particle-particle interactions than when it did.

5.2 Comparing sphere-charging results to SOML theory

After pot solved the test cases I arrayed against it, I used it to simulate the first system of actual interest: a sphere collecting particles in the middle of a fully ionized, flowing plasma (q.v.

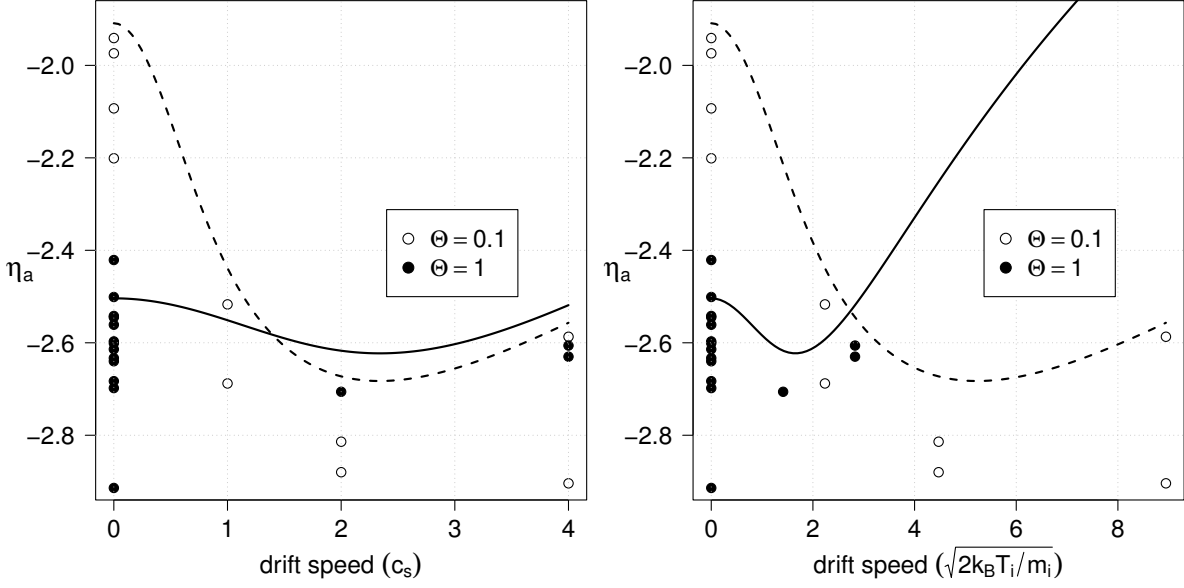


Figure 5.18: pot’s median equilibrium η_a as a function of flow speed with $\Theta = 1$ (closed circles) and $\Theta = 0.1$ (open circles), compared against SOML-theory predictions (solid curve, representing $\Theta = 1$, and dashed curve, representing $\Theta = 0.1$). The panels plot the same data, differing only in the normalization of the drift speed. Some runs with the same drift speed differed in a/λ_D or Δt .

§4.1). This in itself is something of a test case, because SOML theory is available to predict the value of η_a , the relevant dependent variable of the system, and so I can use SOML theory as a benchmark for pot. At the same time, pot’s results are a check on SOML theory and the assumptions the theory makes. In contrast to the most basic, two-body test systems of the previous section, a disagreement between pot and theory here would not necessarily be a reproach to pot — discrepancies might be attributable to a violation of SOML theory’s assumptions, or to an attempt to apply SOML theory where it is invalid.

As noted in §2.2.2 and §2.3, a significant validity condition for the OML and SOML models is that a/λ_D is small. The precise meaning of “small” is Θ -dependent, but for $\Theta \gtrsim 0.1$ a sufficient definition of small a/λ_D is that a/λ_D is less than Θ . I ensured that the pot simulations reported in this section were run with parameters satisfying the $a/\lambda_D < \Theta$ criterion.[†] I experimented with several different a and T_e across different runs, which caused a/λ_D to vary between 0.032 and 0.049 among runs, but as Θ was 0.1 or 1 for each run, a/λ_D was always unambiguously below Θ .

Figure 5.18 directly compares pot’s η_a results to SOML theory’s predictions. Every simulation was of a spherical domain of radius $R = 4 \times 10^{-4}$ m containing 75,000 protons and 75,000 electrons, but there was some heterogeneity in the parameters besides that. I experimented with adjusting Δt between runs, as well as a and T_e , and in some simulations inter-particle interactions were turned off (meaning that the protons and electrons moved in the collecting sphere’s field but did

[†]In pot runs where electrons and ions interact only with the sphere, not with each other, this is more rigour than is necessary, because the $a/\lambda_D < \Theta$ criterion becomes irrelevant; those simulations’ particles do not engage in collective behaviours, and the Debye length is not a characteristic length scale of those systems. For all that, it was more convenient to continue using similar a/λ_D in the no-particle-particle-interaction simulations.

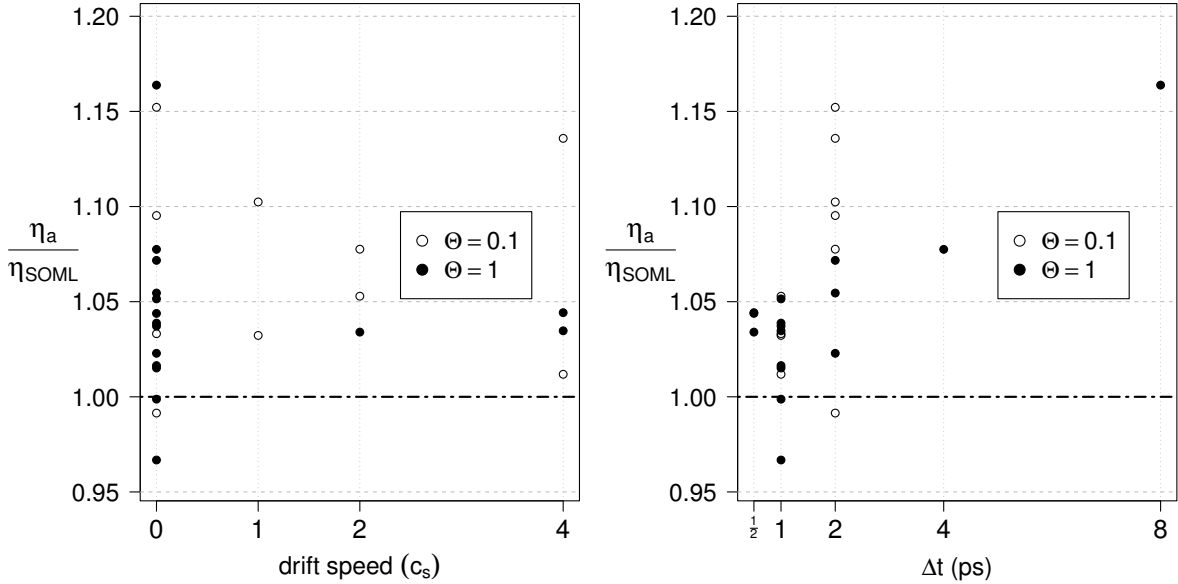


Figure 5.19: The ratio of pot’s η_a estimates to η_{SOML} , the corresponding SOML η_a predictions.

not exert forces on each other). To estimate η_a from the simulations I ran them all to equilibrium, pot periodically recording the sphere’s q , and took the median value of $e^2 q / (4\pi\epsilon_0 k_B T_e a)$ from the equilibrium period (i.e. from $t = 5 \mu\text{s}$ onwards, because the simulations had all equilibrated by then). My main concern was the zero-flow case, but as the plots show I ran further simulations with flow speeds of c_s , $2c_s$, and $4c_s$, where c_s was the Bohm speed.

The plots also show that despite the heterogeneity of the different runs’ parameters, the equilibrium η_a in each run was within 20% of that SOML predicted. To better quantify the closeness between simulation and theory, fig. 5.19 displays the ratio of each simulation’s η_a to η_{SOML} , the corresponding value predicted by SOML. The plot makes obvious that though pot consistently gave results within 20% of the theoretical predictions, pot systematically exaggerated η_a ’s magnitude by 5%–10%.

A too-long Δt explains a good part of the systematic error. The right panel of fig. 5.19 replots $\eta_a/\eta_{\text{SOML}}$ as a function of Δt and reveals that the error tended to become worse at longer Δt . As long as Δt was at most 1 ps, however, pot’s simulation results were within 6% of the SOML predictions, with the systematic error being perhaps 4% (and the choice of 0.5 ps versus 1 ps did not make an obvious difference). This was a dismaying finding. I had expected, and hoped, that a Δt of 2 ps or 4 ps was short enough, not least because those values satisfied the Δt constraints in table 4.1, with the arguable exception of the $\Delta t \ll a/v_{\text{the}}$ requirement: $\Delta t/(a/v_{\text{the}})$ was as high as 0.104, in the simulation with $\Delta t = 4$ ps.

Confining attention to the runs with $\Delta t \leq 1$ ps, the picture improves considerably (fig. 5.20; cf. fig. 5.18). It remained the case that pot exaggerated η_a a little, but the exaggeration was less and the results reflected the general trend of the SOML-theory curves. The eight data points from simulations with $\Theta = 1$, no flow, and $\Delta t \leq 1$ ps give an idea of the systematic and random error in η_a even when the time step is appropriately short; the mean and standard deviation of the eight

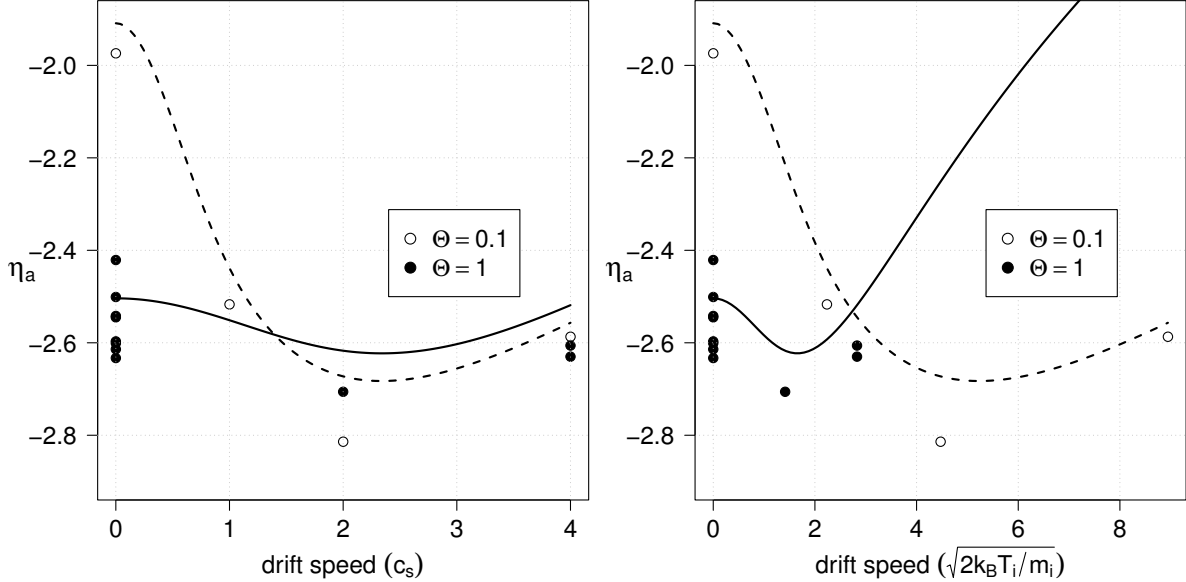


Figure 5.20: pot's median equilibrium η_a (circles) as a function of flow speed compared against SOML-theory predictions (solid curve for $\Theta = 1$, dashed curve for $\Theta = 0.1$), as in fig. 5.18, but only for the subset of runs with $\Delta t \leq 1$ ps.

runs' η_a medians are -2.56 and 0.070 respectively. In the absence of flow, (S)OML theory predicts $\eta_a = -2.50$ in a proton-electron plasma when $\Theta = 1$, implying that pot's systematic and random errors are about 2% and 3% respectively for such short time steps.

As a last note, the fact that SOML theory should approximately match these charging results suggests a second way to estimate η_a from the results, a way which could be more statistically efficient than taking η_a 's equilibrium median. The alternative method is to fit a SOML charging curve directly to the q time series, and infer η_a from the equilibrium q implied by the curve's parameters. To explore this possibility, I wrote the computer program `chafitsoml`, which fits a SOML charging curve to a complete q time series from a pot run — including the initial, non-equilibrium charging period — by maximum likelihood. `chafitsoml` solves the nonlinear likelihood-maximization problem by gradient descent, computing the likelihoods by assuming that electron collection and ion collection are Poisson processes with time-dependent mean collection rates given by the SOML model. The parameter estimates on which `chafitsoml` converges then imply a specific equilibrium q , multiplying which by $e^2/(4\pi\varepsilon_0 a k_B T_e)$ gives an equilibrium η_a estimate.

After each run finished I estimated η_a with this second method. Figure 5.21 compares the η_a values it gave to each run's median equilibrium η_a . The two methods of estimating η_a give very similar results, with a product-moment correlation of 0.992 (whether including all data or only the subset with $\Delta t \leq 1$ ps), and mean absolute differences of 0.033 (all runs) and 0.030 (the runs with $\Delta t \leq 1$ ps).

Part of the difference between the two methods is systematic: the fitted-SOML-curve η_a estimates tend to be more positive than the median-equilibrium estimates, as demonstrated by

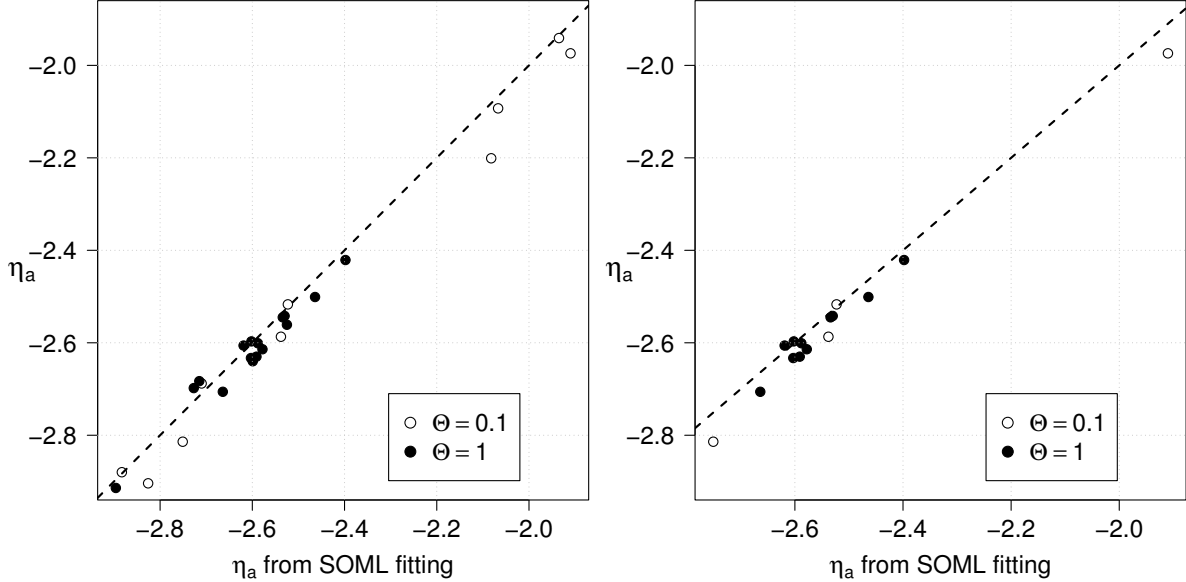


Figure 5.21: Comparing two means of estimating η_a from the same pot runs: median equilibrium η_a versus η_a obtained by fitting SOML charging curves. The left panel plots results from all of the runs already analyzed in this section, the right panel only those with $\Delta t \leq 1$ ps. Dashed lines represent equality of the two estimates.

most of the points in fig. 5.21 lying below the dashed equality line. In the entire data set the fitted-SOML-curve estimates are greater by 0.024 on average; in the subset with $\Delta t \leq 1$ ps they remain greater by 0.026.

It follows that the fitted-SOML-curve η_a estimates might match the SOML model's predictions better than the earlier median equilibrium estimates. Fig. 5.22 explores this possibility by plotting η_a as a function of flow speed, this time using the η_a values from fitting SOML charging curves. The match does in fact improve: one of the $\Theta = 0.1$ data points is now exactly on the SOML prediction curve, and another sits above the curve rather than below it. I conclude that when simulating an unmagnetized plasma with pot, one tends to get better η_a estimates by fitting a SOML charging curve than by estimating η_a directly from q and $T_e a$ alone.

5.3 Comparing sphere-charging results to my stochastic model

Keeping to the statistical theme, I take the opportunity to compare the results of my unmagnetized plasma simulations to the small-sphere stochastic model I developed in chapter 3. Hypothetically this is as effortless as running pot, periodically recording the sphere's q during the run's equilibrium period, counting out a frequency table of q 's values, and comparing it to eq. (3.24), the small-sphere f_q .

This elegant approach, however, is frustrated by the statistical hindrance illustrated in fig. 5.23. At equilibrium, higher-than-average q values tend to be followed by q values which are themselves higher than average, and lower-than-average q values tend to be followed by further

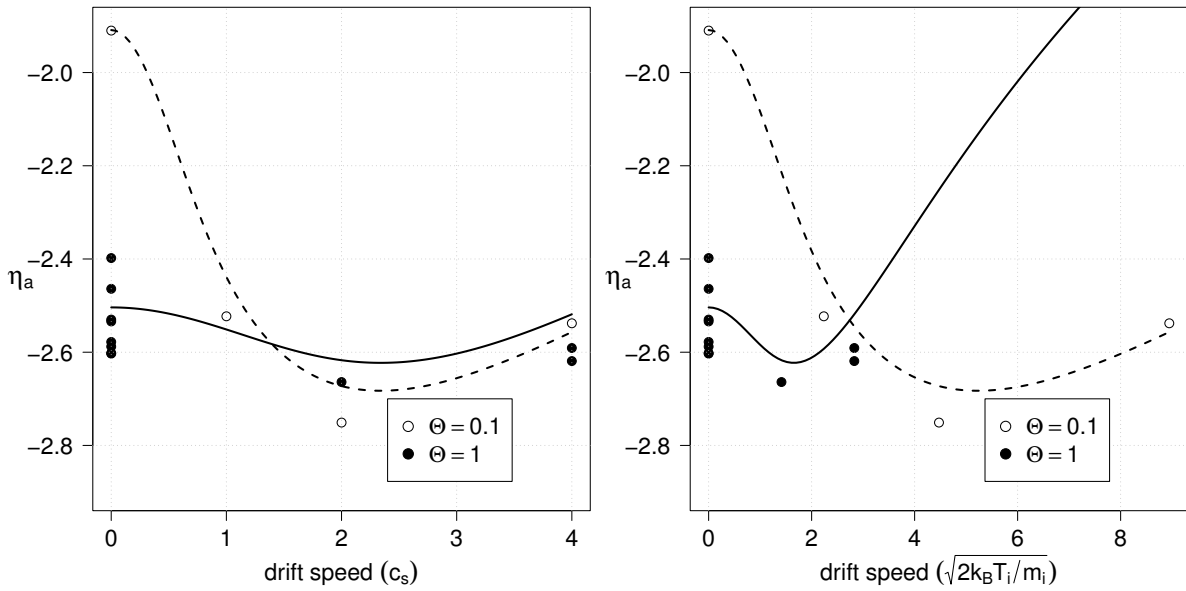


Figure 5.22: Fitted-SOML-curve η_a estimates from pot (circles) as a function of flow speed, compared against SOML-theory predictions (solid curve for $\Theta = 1$, dashed curve for $\Theta = 0.1$), as in fig. 5.18, but only for the subset of runs with $\Delta t \leq 1$ ps.

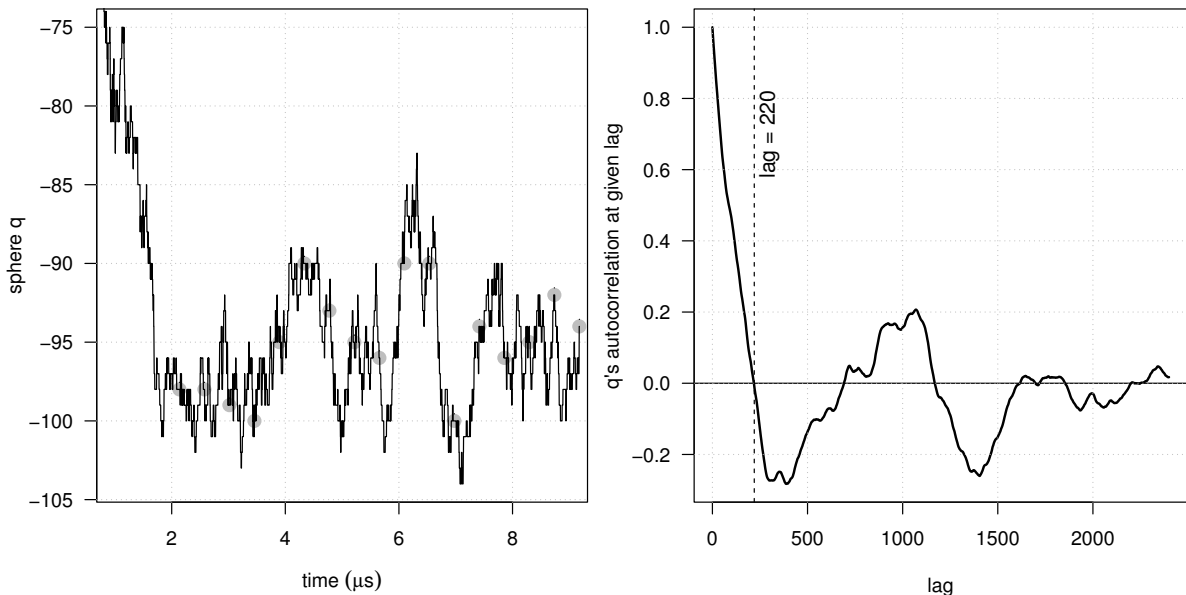


Figure 5.23: A q time series from a pot run, near and at equilibrium (left), and q 's autocorrelation function from $t = 2 \mu\text{s}$ to the end of the simulation (right). Circles filled with grey in the left panel pinpoint values of q at 220-sample intervals; on average such samples are far enough apart to be uncorrelated.

lower-than-average q values: q is *autocorrelated*. Because pot samples q at fine intervals in in-simulation time (at most 200 time steps between measurements) there is a positive autocorrelation not only between adjacent q measurements but between q measurements taken dozens of samples apart. In the specific case plotted in figure 5.23, one must take q values about 220 samples apart (i.e. about 44 ns apart in in-simulation time) for the autocorrelation to vanish.

The persistent autocorrelation in q depresses the effective sample size of a q time series. My record of the run in fig. 5.23 includes q 's value at 9287 different times during the run, 3589 of them at $t \geq 2 \mu\text{s}$. But dividing 3589 by 220 gives a rough, effective sample size of only 16. The equilibrium time series of 3589 q values has about as much statistical information as 16 uncorrelated q values.

Such (effectively) small samples are too puny to justify comparing their distribution to a reference distribution; only grievous deviations from reference distributions would be detectable. Furthermore, such a comparison would be partially redundant, because the previous section has already documented one important deviation between the equilibrium q values pot produces and theoretical predictions: on average, spheres in pot simulations over-charge by several percent. In general the *means* of an observed q distribution systematically differ a little from the theoretical distribution.

Because it is superfluous to compare the observed means to those from my small-sphere stochastic model, and impractical to compare the observed q distribution as a whole to that from my model, I elect to compare the observed *variance* in q in each run to the variance my model predicts. Effective sample sizes on the order of 16 are enough to compare a low-order moment of two probability distributions, and my model predicts that when q 's equilibrium value is large, q 's probability distribution is very nearly Gaussian, so that the mean and variance are the only two moments of real importance.

Table 5.3 compares the observed variances from unmagnetized pot runs with $\Delta t \leq 1 \text{ ps}$ to predictions from my small-sphere stochastic model. For each run, I calculated k , the minimum autocorrelation lag at which q 's autocorrelation was negative. k gave the spacing needed between measurements of q to minimize the correlations between measurements (cf. the circled q values taken 220 samples apart in fig. 5.23; for that run $k = 220$ was the shortest lag for which q 's autocorrelation function crossed zero). Going backwards from the end of the time series, I sampled every k th q value from the time series until reaching a start-of-equilibrium cutoff of $5 \mu\text{s}$. This produced a small subsample of uncorrelated equilibrium q estimates. Table 5.3's "effec." column lists the size N_q of the runs' uncorrelated subsamples. The observed variance of a run's q subsample was then the sample variance[‡] of that subsample, and to obtain a standard error (SE) I multiplied the variance by $\sqrt{2/(N_q - 1)}$.

The model also predicts the observed variance's SE; multiplying the model's prediction of the variance by $\sqrt{2/(N_q - 1)}$ gives the expected SE. Because the model's expected variance generally

[‡]The sample variance is a downwardly biased estimator in the presence of autocorrelation, but a proper correction for the bias would require knowledge of the population autocorrelation function, so I have made no bias corrections to the variances in table 5.3. Unless the autocorrelation is literally perfect, the relative bias is small at sufficiently large sample sizes, and I deem it unlikely to change the conclusions of my analysis.

ID	sample size		variance σ^2 of q				goodness-of-fit check		
	original	effec.	observed		from model		z	cumulative results	
			value	SE	value	SE		X^2	p-value
57	38004	11	9	4	17	8	-1.09	1.20	0.27
58	34874	12	13	6	17	7	-0.53	1.48	0.48
59	38004	18	12	4	17	6	-0.74	2.03	0.57
68	10002	26	9	2	18	5	-1.80	5.28	0.26
69	10002	5	26	18	20	14	0.45	5.48	0.36
70	10002	7	46	27	22	13	1.96	9.31	0.16
71	9949	7	23	13	24	14	-0.06	9.31	0.23
72	9502	8	16	9	30	16	-0.88	10.08	0.26
73	10149	16	20	7	26	9	-0.59	10.44	0.32
74	19003	18	27	9	26	9	0.19	10.47	0.40
75	19003	10	25	12	28	13	-0.24	10.53	0.48
76	19003	9	27	13	30	15	-0.21	10.57	0.57
77	5011	15	22	8	26	10	-0.37	10.71	0.64
78	2089	12	14	6	31	13	-1.27	12.31	0.58
79	6501	17	31	11	31	11	0.01	12.31	0.66

Table 5.3: q 's variance, and the variance's standard error (SE), at equilibrium during unmagnetized pot runs with $\Delta t \leq 1$ ps, compared to the variance (and the variance's SE) predicted by the small-sphere stochastic model. The SE from the model is the model's estimate of the SE of the observed σ^2 ; it is not an error attached to the *model's prediction* of σ^2 .

disagreed with the observed variance, the two estimates of the variance's SE also disagreed.

For the purpose of checking the model's fit to the observations, it is more appropriate to use the SEs given by the model rather than SEs derived from the observed variances. As a systematic goodness-of-fit test of the model, I subtract for each run the model's predicted variance from the observed variance, dividing the difference by the model-derived SE to convert the model-observation discrepancy into a z -score. If the model fits the data, the z -scores are independently distributed with a mean of 0 and a variance of 1, and the sum of the z -scores' squares comes from a distribution extremely similar to a χ^2 distribution, with the number of degrees of freedom being the number of z -scores added together. The last two columns of table 5.3 list X^2 , the cumulative sum of squares of the z -scores, and the p -value returned by a χ^2 test of each X^2 .

At the bottom of the table, the X^2 from all 15 runs is 12.31, which is at the 34th percentile of a χ^2_{15} distribution. The omnibus goodness-of-fit test, using the observed variance from all runs, then has a p -value of 0.66, and the test fails to reject the small-sphere stochastic model as a model of q 's equilibrium variance.

5.4 Equilibrium η_a as a function of magnetic field

My final set of data is the result of investigating how magnetizing a plasma affects the equilibrium η_a of a small sphere in the plasma. I ran pot repeatedly, changing none of the parameters between runs except for the \hat{x} component of the static, homogeneous \mathbf{B} field permeating the plasma; \mathbf{B} 's \hat{y} and \hat{z} components were always zero, making $\mathbf{B} = B\hat{x}$. The simulations all included particle-particle interactions, and used the default parameters (table 5.2), a spherical domain, and the Boris particle-motion integrator.

Patacchini, Hutchinson, and Lapenta (PHL) have already simulated the charging of a sphere in a magnetized, non-flowing plasma using SCEPTIC [161]. They characterized the plasma's magnetization with the dimensionless parameters [161, p. 062111-2]

$$\beta_e \equiv \left\langle \frac{a}{r_{Le}} \right\rangle = a \sqrt{\frac{\pi k_B T_e m_e}{2e^2 B^2}} \quad (5.4)$$

and [161, p. 062111-7]

$$\beta_i = \sqrt{\frac{Z^2 m_e T_e}{m_i T_i}} \beta_e = a \sqrt{\frac{\pi k_B T_i m_i}{2 Z^2 e^2 B^2}} \quad (5.5)$$

PHL gloss β_e as "the ratio of the probe radius over a mean electron gyroradius", giving the unhelpfully misleading impression that β_e 's definition is $a/\langle r_{Le} \rangle$ [161, p. 062111-2]. This is not the same as $\langle a/r_{Le} \rangle$ and as such PHL's verbal description is inconsistent with their algebra; I have used their algebraic definitions.

PHL plotted the values of η_a (" ϕ_f " in their notation) they elicited from SCEPTIC for several β_i between 0 and 0.4 [161, fig. 11]. They also used their findings to check Tsytovich et al.'s simple model of sphere charging in a magnetized plasma [162]. That model made the simplifying assumption that with $\beta_i \ll 1$ and $\beta_e \gg 1$, one could treat the ions as unmagnetized (as if $\beta_i = 0$)

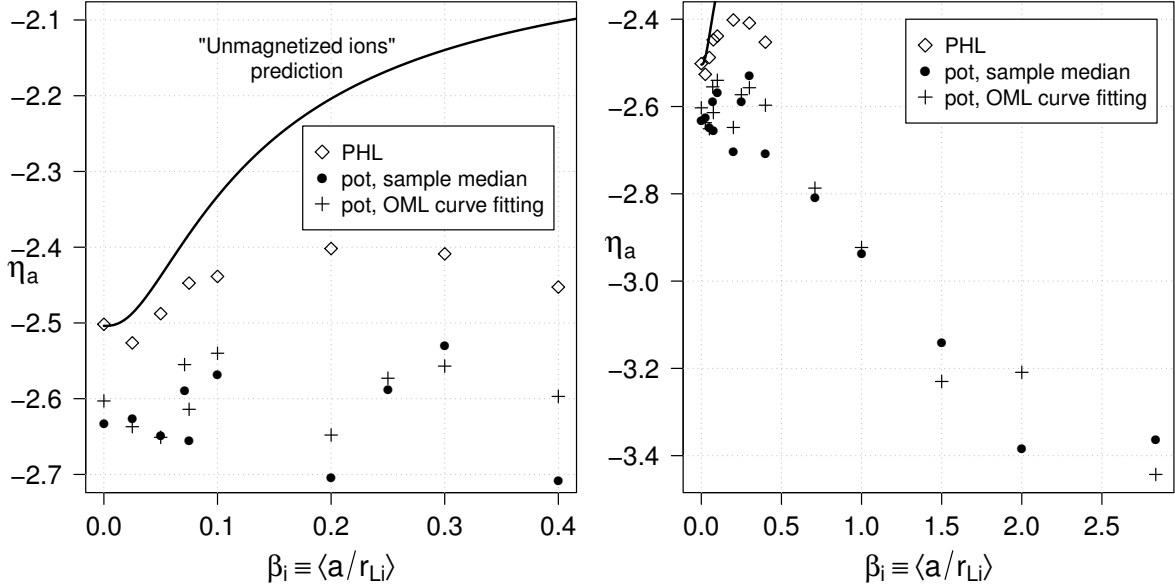


Figure 5.24: η_a as a function of β_i , as estimated by: Patacchini, Hutchinson, and Lapenta (diamonds) using SCEPTIC [161, p. 062111-8]; median equilibrium value in pot runs (circles); fitting OML curves to pot run output (crosses); and from the assumption that ions remain unmagnetized (solid curve) [162].

and the electrons as fully magnetized [161]. To test that model, PHL’s figure included not only the SCEPTIC results but also the η_a implied by Tsytovich et al.’s assumptions.

I ran some of my pot simulations with B selected to match PHL’s β_i values, allowing me to compare my results for proton-electron plasmas to their results. I redraw PHL’s figure, adding my own pot-derived η_a results, in the left panel of figure 5.24. As before I extracted η_a estimates from pot’s raw output in two ways, firstly by taking the median of the η_a values at equilibrium, and then by fitting a maximum-likelihood OML charging curve to the data. With $\beta_i > 0$, fitting OML curves is physically dubious because OML theory does not include the effect of magnetization, but I include the OML-curve-based estimates anyway to observe their deviation from the more robust median estimates.

My first inference is that pot upheld PHL’s conclusion that Tsytovich et al.’s unmagnetized-ion “approximation breaks down at a very small magnetic field” [161, p. 062111-7]. The unmagnetized-ion model predicted steadily increasing η_a with β_i but pot revealed no consistent trend in η_a for $\beta_i \leq 0.4$. One cannot explain the lack of a trend by accusing pot of being insensitive to β_i ’s effect on η_a , because, as fig. 5.24’s right panel proves, pot’s η_a estimates became appreciably more negative at high β_i . Statistical noise in pot’s η_a estimates may have masked a small positive trend in η_a at low β_i , but any such hidden increase could be at most ≈ 0.1 , much less than the increase predicted by the unmagnetized-ion model.

At the same time, over the range of β_i values probed by both pot and SCEPTIC, pot returned consistently more negative η_a estimates. This could have been the same systematic bias as emerged from the SOML pot simulations, but differences between the pot runs and PHL’s SCEPTIC runs

may explain their disagreement instead. PHL ran SCEPTIC to simulate collisionless plasmas, but the pot runs simulated plasmas in which electrons and ions could undergo Coulomb collisions. The difference in collisionality could explain the systematic difference between the pot results and the SCEPTIC results, or at least why the systematic difference here was larger (0.176, or 7%, on average) than the systematic difference of 2% found in §5.2 between pot results and SOML theory.

It is possible that the collisionality in the pot simulations, though not zero, was too low to explain even a 7% difference. In a singly ionized plasma with $\Theta = 1$, electrons and ions share the mean free path [2, p. 14]

$$\lambda_c = \frac{16\pi\varepsilon_0^2(k_B T)^2}{n_0 e^4 \ln \Lambda} = \frac{16\pi}{\ln \Lambda} n_0 \lambda_D^4 \quad (5.6)$$

where $\ln \Lambda$, the “Coulomb logarithm”, is approximately $\ln 9N_D$ [2, p. 12]. Substituting in,

$$\lambda_c \approx 12 \frac{N_D}{\ln 9N_D} \lambda_D \quad (5.7)$$

In every magnetized pot run λ_D was 61 μm and N_D was 269, for a mean free path $\approx 2.5 \times 10^4 \mu\text{m}$. This was much longer than the simulation domain radius of 400 μm ; on average a plasma particle would have had to travel 63 domain radii to experience a large-angle ($> 90^\circ$) collision [2, p. 11]. Such infrequent collisions might not have influenced η_a to a noticeable extent.

There remains another potentially important difference between pot and SCEPTIC. pot simulated individual electrons moving through the simulation, but SCEPTIC did not; it merely assumed the electrons were spatially distributed according to the Boltzmann relation. But that assumption is, in general, false in the vicinity of a collecting sphere, because the Boltzmann relation only models variation in n_e caused by variation in ϕ , not the decrease in n_e from absorption by a surface. In absolute terms the error this causes is small, because near a collecting sphere at equilibrium both $\exp(\eta)$ and n_e/n_0 are small, so their difference is small, but it may be enough to explain why SCEPTIC’s η_a estimates are a few percent smaller in magnitude than pot’s.

My last observation is that the η_a estimates obtained by fitting OML charging curves to pot’s output did not differ systematically from the equilibrium medians. This is somewhat surprising because I had expected the violation of OML theory’s $\beta_i = 0$ assumption to corrupt any attempt to fit OML charging curves for the pot runs where β_i was non-negligible. Apparently OML charging curves were flexible enough to mimic the charging curves produced in these simulations, despite their debatable physical relevance.

5.5 Conclusion

As I developed pot I subjected it to several physical tests with known answers to check that it gave cogent results. pot proved to approximate well the orbit and scattering of individual electrons around a very heavy ion, and reproduced the expected velocity distributions and macroscopic behaviours of gases and plasmas.

Next, I ran pot simulations of small spheres charging in plasmas (with and without inter-particle interactions) flowing at speeds of up to $4c_s$. Comparing the results against the SOML

model, I found that `pot` reliably gave η_a estimates within 20% of the SOML predictions, which estimates I improved by running `pot` with sufficiently short Δt and by developing a special-purpose statistical fitting technique for extracting η_a estimates from `pot`'s raw output. `pot` systematically exaggerated η_a 's negativity by 5%–10%, but cutting Δt brought the systematic and random errors in `pot`'s η_a estimates down to 2% and 3% respectively. Estimating η_a by the special-purpose technique of fitting SOML charging curves to `pot`'s output halved the systematic error again.

Finally, I used `pot` to simulate small spheres charging in plasmas which did not flow, but had a static, uniform magnetic field. To the best of my knowledge these `pot` runs were the first ever simulations of a sphere charging in a magnetized plasma which were fully microscopic and which estimated electric fields without interpolating them from fixed grid points. Their results independently confirm Patacchini, Hutchinson, and Lapenta's conclusion [161] that an unmagnetized-ion model of sphere charging in magnetized plasma breaks down even at low magnetization — and unlike PHL, I reach that conclusion on the basis of simulations which did not assume that plasma electrons were spatially distributed according to the Boltzmann relation. I also ran `pot` in a high-magnetization regime ($\beta_i \gtrsim 1$) not explored in PHL's earlier work, documenting that η_a became significantly more negative at large β_i , despite the lack of a clear dependence on β_i at low β_i .

Chapter 6

Conclusion

'If you do not know where you are going, all roads will lead you there.' So goes a modern saying. [...] We may have some idea of the direction in which we wish to go, but the final destination is bound to be affected by the nature of the journey.

Alec Nove (1983),
The Economics of Feasible Socialism, Part 4, p. 154

6.1 Summary

This dissertation documents the mathematical and computational work I have done during my PhD to model the charging of spherical dust grains in plasmas. Had I written about my work without setting it in physical context, what I wrote might have been intelligible only to myself and my supervisor. To mitigate that risk, chapter 1 began this dissertation not by plunging immediately into a discussion of my work, but by giving a tour of real-life examples of dust in plasmas. Having furnished the reader with the practical context behind my work, chapter 1 defined the central physical variables characterizing dust in plasmas. Those definitions set the scene for the subsequent chapters, which explored the physics of dust in plasmas in an assortment of ways.

Chapter 2 described and re-derived pre-existing models of dust in plasmas, alongside a few original findings, such as my discovery that the normalized surface potential η_a in the ABR model tends to $0.4189 - \ln \mu$ in the $a/\lambda_D \rightarrow \infty$ limit.

Chapter 3 defined and solved my stochastic models of the equilibrium fluctuations of the charge on a spherical grain in a flowing, collisionless plasma. I obtained exact formulae for the equilibrium probability distributions of the charges on such grains, then used the Fokker-Planck approximation to derive Gaussian approximations to those distributions for spherical grains with sufficiently large $\Omega \equiv 4\pi\epsilon_0 k_B T_e a/e^2$. At such large Ω the mean and variance of the equilibrium distributions was of order Ω (and for grains with arbitrarily large a/λ_D the variance converged on Ω itself). I further found that faster plasma flow increases the variance of the charge on small grains, but does not affect the variance of large grains' charges.

Moving from my mathematical modelling to my computational modelling, chapter 4 presented the design of pot, a computer program I wrote to run fully microscopic simulations of a sphere charging in a flowing plasma in a time-independent, homogeneous magnetic field. Chapter 5 then analyzed the results of my test runs of pot, finding that pot's simulations produced physically realistic output, before progressing to the results of fully fledged simulations of spheres charging in proton-electron plasmas.

The first of these were simulations of sphere charging in unmagnetized plasmas with different flow speeds. In line with SOML theory, pot recorded that η_a depended strongly on flow speed when Θ was low (0.1) but not when Θ was higher (1). pot's η_a results aligned well with SOML theory. When run with a sufficiently short time step, pot-derived η_a estimates had a random error of about 3% and differed systematically from the SOML predictions by 1%–2%, depending on which method I used to estimate η_a from pot's output; estimating η_a directly by computing its median value during equilibrium periods of pot runs gave slightly more negative estimates than maximum-likelihood fitting of SOML charging curves to pot output.

Pitting pot against my small-sphere stochastic model, I discovered that the stochastic model's predictions of the variance in the sphere's charge state q at equilibrium were statistically consistent with q 's equilibrium fluctuations in pot runs. The statistical equivalence of these two very different methods of estimating q 's variance is another sign of the methods' soundness.

I also ran pot simulations of spheres charging in non-flowing, magnetized plasmas to investigate how η_a varied with β_i , the dimensionless parameter characterizing a plasma's degree of magnetization. These were, as far as I know, the first simulations of this system which were fully microscopic and which computed electric fields without interpolating them from a fixed grid. At low magnetization ($\beta_i \leq 0.4$) no dependence of η_a on β_i was apparent, although a weak dependence may have been masked by the statistical noise in the pot-derived η_a estimates. pot's illustration that η_a scarcely depended on β_i for $\beta_i \leq 0.4$ refuted the unmagnetized-ion theory's prediction that η_a would rise from -2.5 to -2.1 as β_i increased from zero to 0.4. pot thereby independently confirmed Patacchini, Hutchinson, and Lapenta's earlier simulation-founded conclusion [161] that the unmagnetized-ion theory was substantially incorrect. pot's refutation of the theory was more decisive than that of Patacchini et al. because pot's simulations, unlike Patacchini et al.'s, did not invoke the implausible assumption that plasma electrons everywhere obey the Boltzmann relation. I went beyond Patacchini et al. in another respect, as well: simulating spheres in plasmas with a wider range of β_i values than they used. pot showed that in more vigorously magnetized plasmas β_i 's influence on η_a became obvious, η_a decreasing from -2.7 to -3.4 as β_i grew from 0.4 to ≈ 2.5 .

6.2 What is to be done?

My work is just one incremental contribution to the research programme of modelling the charging of dust in plasmas, and future efforts could build on that contribution by reworking or extending it to model a wider range of dust-in-plasma systems. In the course of this text I have intermittently mentioned possible directions in which one could extend my work, but for convenience I draw them together in this section, with some extra ideas, before I finish.

I am still curious about some theoretical questions pertaining to the ABR model. Numerically solving the model for η_a , I discovered that the model's η_a estimates had predictable asymptotic behaviour in both the $a/\lambda_D \rightarrow 0$ and $a/\lambda_D \rightarrow \infty$ limits. Unfortunately I was unable to rigorously deduce closed-form expressions for the asymptotic limits, simple as the limits seemed to be (proportional to $\mu a/\lambda_D$ for minuscule spheres, and approaching $0.4189 - \ln \mu$ for infinitely large spheres). As a consequence, whether there are proofs of the asymptotic limits is an open question, albeit an enticingly soluble-looking one.

An assumption pervading the physics (both my own and others') presented in this dissertation is that dust grains in plasmas are spherical. In reality this is never perfectly true, although it is often a fair approximation, and unpublished work generalizing the OML model to spheroidal dust grains suggests that modest deviations from sphericity have little effect on η_a [163]. Be that as it may, some forms of real-world dust, like narrow flakes, needle-shaped grains, and grains with highly non-convex shapes, are liable to have an equilibrium η_a very different to that predicted by existing charging theories which assume sphericity. Generalizing those theories to far-from-spherical dust grains would be useful. Modifying pot to simulate a non-spherical collector in a plasma would likewise be useful, though pot's collision detector would have to be rewritten to work efficiently with highly non-spherical shapes, and to maintain physical realism pot would have to allow for the dust grain's Coulomb potential ceasing to be spherically symmetric.

The stochastic models I assembled in §3 are fairly general, accounting for a spherical dust grain's radius and a plasma's T_e , T_i , μ , γ , and flow speed, but the models simultaneously make characteristic assumptions about the sphere and plasma which may not hold. The models assume that the plasma is singly ionized, unmagnetized and collisionless, and that the sphere in the plasma has attained equilibrium, is in the bulk plasma where the ion- and electron-velocity distributions are shifted Maxwellian distributions, and does not engage in secondary charging processes like photoelectric, thermionic, or field emission. These assumptions may limit the models' applicability. As an example, astrophysical dust grains and dust grains in tokamaks are often in non-negligible magnetic fields, fields the stochastic models assume away. Another example is the models' disregard of field-enhanced, thermal electron emission, the secondary (dis)charging process where electrons on a dust grain are hot enough to quantum-mechanically tunnel off the grain, pushed along by the electric field of other electrons. Field-enhanced, thermal electron emission would have a negligible effect in many dust-in-plasma systems but is likely to affect the charge of dust grains and molten droplets in hot tokamaks. It would be instructive to bring phenomena such as these into the models and quantify their effect on the models' predictions.

pot draws on less burdensome assumptions; as is, Coulomb collisions happen automatically between simulated particles as they would in reality, and pot offers the option of magnetizing simulated plasmas. With trivial modifications pot could also include multiple (and multiply ionized) species of ion, and simulated collisions of plasma particles with neutral particles. None of this, of course, means that pot is perfect in its current state. Testing revealed minor bugs in pot's initialization of plasmas. pot initialized plasmas with non-uniform spatial distributions of particles, and refused to initialize simulations with any particles within a of the simulation

domain's centre, even when the simulated plasmas had no collecting spheres. I fixed these lapses but other, more subtle bugs have surely infiltrated the code.

Setting aside patent bugs, there are the relatively easy-to-implement ideas for improving pot I gave in §4.5. Replacing the existing ad-hoc modification in pot's VV integrator with new code designed to incorporate \mathbf{B} properly might make the VV integrator a useable integrator for simulating magnetized plasmas. The Boris algorithm implementation would run more quickly by applying a small-angle approximation to its evaluation of $\arctan(\omega_L \Delta t / 2)$, and one could implement Patacchini and Hutchinson's cyclotronic integrator [154] in pot, which would offer users a fourth option when selecting an integrator, an option which could prove superior to the integrators pot offers already.

A prospect offering more considerable performance gains is re-configuring pot to use macro-particles. Macro-particles are simulated particles with more mass than the real-world particles they represent. Using them is a popular technique in computational physics, because if one scales up the simulated particles' other relevant physical characteristics by the same proportion as their mass, one can sometimes preserve the system's basic physics while having the simulated particles stand in for many more real-world particles. For example, one could recompile pot to use macro-protons with masses of $10m_p$ and charges of $10e$, and macro-electrons with masses of $10m_e$ and charges of $-10e$, to try representing a proton-electron plasma of 1,500,000 particles with only 150,000 simulated particles. I regret that I did not have time to investigate whether macro-particles were suitable for my pot simulations of proton-electron plasmas.

Like all computational physicists, I did not have the processing time and power to ride my code through as much of its parameter space as I would have liked. Running pot with 150,000 particles for long enough to generate adequate charging results took 2–6 days if particle-particle interactions were turned off, and about two months if those interactions were turned on (even with the treecode algorithm calculating those interactions inexactly).

My default set of pot parameters (table 5.2) led to reasonable output in days or weeks, but those parameter values are very unlikely to be optimal for studies, like those in §5, of small spheres charging in plasmas. I suspect, but cannot prove, that raising a to $3\ \mu\text{m}$ or more while keeping it far below λ_D would improve the statistical properties of pot's output by increasing q 's equilibrium average and shrinking q 's coefficient of variation (which determines the relative noise in q and hence η_a estimates). Further pot experiments to ascertain better values of a and the other parameters would be instructive. With better pot parameters one could run pot for shorter periods without degrading the quality of its output, and explore more of its parameter space. Sections 5.2 and 5.4 record how η_a varied with the flow speed and the plasma magnetization. However, in my simulation experiments I altered only one of those two variables at a time, because pot ran too slowly for me to explore the entire two-dimensional joint parameter space of flow speed and magnetization. That means I do not know how flow and β_i interact to influence η_a .

Another informative slice of data could come from programming pot to record where plasma particles land on the collecting sphere. Running pot with that addition would enable an analysis of ion and electron flux densities onto different parts of the sphere as a function of angle and

plasma flow speed. With a high enough particle count it would be possible to try correlating spatial variation in flux densities around the sphere to the angular variation in quantities such as the particles' angular and radial velocity components. Less ambitiously, one could measure flux densities as a function of angle and observe how that function changed with the plasma flow speed, magnetization, and ion-to-electron temperature ratio.

A last comment. Several people have asked me to outline a laboratory experiment which could test my theoretical and computational results. I have hesitated to do so, as I do not claim to be an experimental physicist, and recognize that it is easy to propose a too-clever-by-half experimental design which is unviable in practice. Granting that, I do have an idea for an experiment which, so far as I can tell, could be done but has not been. I propose suspending spherical dust in a plasma by placing the dust in a small vessel through which plasma flows upwards. An experimenter would hold the dust in place by tuning the plasma's flow speed to match the upward ion-drag force on the dust to the force of gravity.

My experimental design does not share the usual flaw of plasma-dust-charging experiments, where the dust stays in place by floating in the electric field of the sheath in front of a wall or electrode. The dust's suspension in the sheath's field in those experiments makes them incomparable to my models, because my models assume there is no substantial, exogenous electric field near the plasma-collecting sphere. The only macroscopic asymmetries my models permit are a uniform \mathbf{B} and plasma flow.

A short calculation indicates that the plasma in my experiment would not need to flow quickly to suspend the dust, a comforting sign that the experiment might be practical. Writing the plasma's (ions') upward flow speed as v_d and the ions' thermal speed as v_{thi} , the upward force of ions colliding with the grain is of order $n_i \pi a^2 v_{\text{thi}} m_i v_d$ under the simplifying assumptions that $v_d \ll v_{\text{thi}}$ and that I may neglect the effect of the dust grains' and ions' electric charges [164, 165]. (The latter assumption implies that my calculation is a conservative one, overestimating the necessary v_d because it leaves out the upward-force-enhancing effect of the negatively charged dust pulling the ions' trajectories sideways.) Gravity's force is $m_d g$, where m_d is the spherical dust grain's mass and g the usual rate of gravitational acceleration near Earth's surface. The flow speed necessary to cancel out gravity is then the v_d satisfying $n_i \pi a^2 v_{\text{thi}} m_i v_d \sim g m_d$, i.e.

$$v_d \sim \frac{g m_d}{n_i \pi a^2 v_{\text{thi}} m_i} = \frac{g (4/3) \pi a^3 \rho_d}{n_i \pi a^2 m_i \times \sqrt{k_B T_i / m_i}} \equiv \frac{(4/3) g a \rho_d}{n_i \sqrt{k_B T_i m_i}} \sim \frac{g a \rho_d}{n_i \sqrt{k_B T_i m_i}} \quad (6.1)$$

where ρ_d is the dust grain's (mass) density. Substituting in the order-of-magnitude estimates $g \sim 10 \text{ m}\cdot\text{s}^{-2}$, $a \sim 10^{-6} \text{ m}$, $\rho_d \sim 10^3 \text{ kg}\cdot\text{m}^{-3}$, $n_i \sim 10^{20} \text{ m}^{-3}$, $k_B T_i \sim 0.1 \text{ eV} \sim 10^{-20} \text{ J}$, and $m_i \sim 10^{-27} \text{ kg}$ gives a gravity-cancelling $v_d \sim 32 \text{ m}\cdot\text{s}^{-1}$, a flow speed consistent with my starting assumption that $v_d \ll v_{\text{thi}}$ and a flow speed realizable in the laboratory. I doubt I will be the person to realize it, but the floor is open to anybody with the space, the time, and the requisite experimental skills. Theory and computation are not the only two frontiers of dusty-plasma physics.

Bibliography

- [1] Imperial College London. Theses for Imperial College research degrees, December 2014. Accessed at <https://workspace.imperial.ac.uk/registry/Public/Current%20Students/Submission%20Checklist%20for%20Imperial%20College%20Degrees-Dec%202014.pdf> on September 30, 2015.
- [2] U. Schumacher. Basics of plasma physics. In Andreas Dinklage, Thomas Klinger, Gerrit Marx, and Lutz Schweikhard, editors, *Plasma Physics: Confinement, Transport and Collective Effects*, volume 670 of *Lecture Notes in Physics*, chapter 1, pages 3–20. Springer Berlin Heidelberg, 2005.
- [3] R. J. Hastie. Plasma particle dynamics. In Richard O. Dendy, editor, *Plasma Physics: An Introductory Course*, chapter 1, pages 5–28. Cambridge University Press, 1993.
- [4] D. G. Swanson. *Plasma waves*. Academic Press Incorporated, 1989.
- [5] R. Merlino and J. Goree. Dusty plasmas in the laboratory, industry, and space. *Physics Today*, 57(7):32–38, 2004.
- [6] D. A. Mendis. Progress in the study of dusty plasmas. *Plasma Sources Science and Technology*, 11(3A):A219–A228, 2002.
- [7] C. M. C. Nairn, B. M. Annaratone, and J. E. Allen. On the theory of spherical probes and dust grains. *Plasma Sources Science and Technology*, 7:478–490, 1998.
- [8] R. V. Kennedy and J. E. Allen. The floating potential of spherical probes and dust grains. Part 1. Radial motion theory. *Journal of Plasma Physics*, 67(4):243–250, 2002.
- [9] R. V. Kennedy and J. E. Allen. The floating potential of spherical probes and dust grains. II: Orbital motion theory. *Journal of Plasma Physics*, 69(6):485–506, 2003.
- [10] Paul Bryant. Floating potential of spherical probes and dust grains in collisional plasmas. *Journal of Physics D: Applied Physics*, 36(22):2859–2868, 2003.
- [11] Percy Williams Bridgman. *The logic of modern physics*. Macmillan, 1927.
- [12] D. A. Mendis and M. Rosenberg. Cosmic dusty plasma. *Annual Review of Astronomy and Astrophysics*, 32:419–463, 1994.

- [13] John Ernest Harry. *Introduction to Plasma Technology: Science, Engineering, and Applications*. Wiley-VCH, 2010.
- [14] Osamu Ishihara. Complex plasma: dusts in plasma. *Journal of Physics D: Applied Physics*, 40(8):R121–R147, 2007.
- [15] Robert L. Merlino. Dusty plasmas and applications in space and industry. In Crockett Grabbe, editor, *Plasma Physics Applied*, chapter 5, pages 73–110. Transworld Research Network, 2006.
- [16] S. Alan Stern. The lunar atmosphere: History, status, current problems, and context. *Reviews of Geophysics*, 37(4):453–491, 1999.
- [17] E. J. Öpik and S. F. Singer. Escape of gases from the Moon. *Journal of Geophysical Research*, 65(10):3065–3070, 1960.
- [18] W. F. Edwards and L. B. Borst. Possible sources of a lunar atmosphere. *Science*, 127(3294):325–328, 1958.
- [19] John Keith Hargreaves. *The solar-terrestrial environment: an introduction to geospace – the science of the terrestrial upper atmosphere, ionosphere and magnetosphere*, volume 5 of *Cambridge Atmospheric and Space Science Series*. Cambridge University Press, 1995.
- [20] Sergey I. Popel and Lev M. Zelenyi. Dusty plasmas over the Moon. *Journal of Plasma Physics*, 80(6):885–893, 2014.
- [21] Eberhard Grün, Mihaly Horanyi, and Zoltan Sternovsky. The lunar dust environment. *Planetary and Space Science*, 59(14):1672–1680, 2011.
- [22] J. J. Rennilson and D. R. Criswell. Surveyor observations of lunar horizon-glow. *The Moon*, 10(2):121–142, 1974.
- [23] A. B. Severny, E. I. Terez, and A. M. Zvereva. The measurements of sky brightness on Lunokhod-2. *The Moon*, 14(1):123–128, 1975.
- [24] Christoph Leinert. Zodiacal light — a measure of the interplanetary environment. *Space Science Reviews*, 18(3):281–339, 1975.
- [25] Herbert A. Zook and James E. McCoy. Large scale lunar horizon glow and a high altitude lunar dust exosphere. *Geophysical Research Letters*, 18(11):2117–2120, 1991.
- [26] Mihály Horányi. Charged dust dynamics in the solar system. *Annual Review of Astronomy and Astrophysics*, 34:383–418, 1996.
- [27] J. E. Colwell, S. Batiste, M. Horányi, S. Robertson, and S. Sture. Lunar surface: Dust dynamics and regolith mechanics. *Reviews of Geophysics*, 45(2), 2007. Paper number 2005RG000184.

- [28] Brian J. O'Brien. Review of measurements of dust movements on the Moon during Apollo. *Planetary and Space Science*, 59(14):1708–1726, 2011.
- [29] Bill Steigerwald. Model helps search for Moon dust fountains. <http://www.nasa.gov/centers/goddard/news/features/2010/lhg.html>, June 2010. Accessed October 21, 2014.
- [30] J. S. Halekas, Y. Saito, G. T. Delory, and W. M. Farrell. New views of the lunar plasma environment. *Planetary and Space Science*, 59(14):1681–1694, 2011.
- [31] NASA. NASA's LADEE mission. http://www.nasa.gov/mission_pages/ladee/main/#.VFQCRIXnhXM, undated. Accessed October 31, 2014.
- [32] W.-H. Ip. Physical studies of the planetary rings. *Space Science Reviews*, 26(1):39–96, 1980.
- [33] C. K. Goertz. Dusty plasmas in the solar system. *Reviews of Geophysics*, 27(2):271–292, 1989.
- [34] Carolyn C. Porco and G. Edward Danielson. The periodic variation of spokes in Saturn's rings. *The Astronomical Journal*, 87(5):826–833, 1982.
- [35] Bradford A. Smith, Laurence Soderblom, Reta Beebe, Joseph Boyce, Geoffrey Briggs, Anne Bunker, Stewart A. Collins, Candice J. Hansen, Torrence V. Johnson, Jim L. Mitchell, Richard J. Terrile, Michael Carr, Allen F. Cook, Jeffrey Cuzzi, James B. Pollack, G. Edward Danielson, Andrew Ingersoll, Merton E. Davies, Garry E. Hunt, Harold Masursky, Eugene Shoemaker, David Morrison, Tobias Owen, Carl Sagan, Joseph Veverka, Robert Strom, and Verner E. Suomi. Encounter with Saturn: Voyager 1 imaging science results. *Science*, 212(4491):163–191, 1981.
- [36] E. C. Stone and E. D. Miner. Voyager 1 encounter with the Saturnian system. *Science*, 212(4491):159–163, 1981.
- [37] Eberhard Grün, Gregor E. Morfill, Richard J. Terrile, Torrence V. Johnson, and Gerhard Schwehm. The evolution of spokes in Saturn's B ring. *Icarus*, 54(2):227–252, 1983.
- [38] T. W. Hartquist, O. Havnes, and G. E. Morfill. The effects of charged dust on Saturn's rings. *Astronomy and Geophysics*, 44(5):5.26–5.30, 2003.
- [39] G. E. Morfill and C. K. Goertz. Plasma clouds in Saturn's rings. *Icarus*, 55(1):111–123, 1983.
- [40] John D. Richardson. A plasma density model for Saturn based on Voyager observations. *Journal of Geophysical Research*, 95(A8):12019–12031, 1990.
- [41] Mihály Horányi, Gregor E. Morfill, and Thomas E. Cravens. Spokes in Saturn's B ring: Could lightning be the cause? *IEEE Transactions on Plasma Science*, 38(4):874–879, 2010.
- [42] G. H. Jones, N. Krupp, H. Krüger, E. Roussos, W.-H. Ip, D. G. Mitchell, S. M. Krimigis, J. Woch, A. Lagg, M. Fränz, M. K. Dougherty, C. S. Arridge, and H. J. McAndrews. Formation

- of saturn's ring spokes by lightning-induced electron beams. *Geophysical Research Letters*, 33(21):L21202, 2006.
- [43] Francis F. Chen. Industrial applications of low-temperature plasma physics. *Physics of Plasmas*, 2(6):2164–2175, 1995.
- [44] Panel on Plasma Processing, Naval Studies Board, US National Research Council. *Plasma Processing and Processing Science*. The National Academies Press, 1995.
- [45] Gary S. Selwyn, J. S. McKillop, Kurt L. Haller, and J. J. Wu. *In situ* plasma contamination measurements by HeNe laser light scattering: A case study. *Journal of Vacuum Science & Technology A*, 8(3):1726–1731, 1990.
- [46] Gary S. Selwyn, John E. Heidenreich, and Kurt L. Haller. Particle trapping phenomena in radio frequency plasmas. *Applied Physics Letters*, 56(18):1876–1878, 1990.
- [47] Integrated Circuit Engineering Corporation. Yield and yield management. In *Cost Effective IC Manufacturing 1998-1999*, chapter 3. Integrated Circuit Engineering Corporation, 1997. Accessed at <http://smithsonianchips.si.edu/ice/cd/CEICM/SECTION3.pdf> on March 2, 2015.
- [48] Gary S. Selwyn. Particulate contamination control in plasma processing: Building-in reliability for semiconductor fabrication. In *1995 International Integrated Reliability Workshop Final Report*, pages 122–129. IEEE, 1995.
- [49] L. Boufendi and A. Bouchoule. Particle nucleation and growth in a low-pressure argon-silane discharge. *Plasma Sources Science and Technology*, 3(3):262–267, 1994.
- [50] Ch. Hollenstein. The physics and chemistry of dusty plasmas. *Plasma Physics and Controlled Fusion*, 42(10):R93–R104, 2000.
- [51] M. A. Childs and Alan Gallagher. Small particle growth in silane radio-frequency discharges. *Journal of Applied Physics*, 87(3):1076–1085, 2000.
- [52] A. A. Fridman, L. Boufendi, T. Hbid, B. V. Potapkin, and A. Bouchoule. Dusty plasma formation: Physics and critical phenomena. theoretical approach. *Journal of Applied Physics*, 79(3):1303–1314, 1996.
- [53] Joseph S. Logan and James J. McGill. Study of particle emission in vacuum from film deposits. *Journal of Vacuum Science & Technology A*, 10(4):1875–1878, 1992.
- [54] Priyamvada Vijayakumar, Vikram B. Suresh, and Sandip Kundu. Lithography aware critical area estimation and yield analysis. In *International Test Conference 2011: Proceedings*, pages 9.2.1–9.2.8. IEEE, 2011.
- [55] Gary S. May and Costas J. Spanos. Process monitoring. In *Fundamentals of Semiconductor Manufacturing and Process Control*, chapter 3, pages 82–121. John Wiley & Sons, Incorporated, 2006.

- [56] Wang Jun-Ping, Hao Yue, and Zhang Jun-Ming. Yield estimation of metallic layers in integrated circuits. *Chinese Physics*, 16(6):1796–1805, 2007.
- [57] Gary S. May and Costas J. Spanos. Introduction to semiconductor manufacturing. In *Fundamentals of Semiconductor Manufacturing and Process Control*, chapter 1, pages 1–24. John Wiley & Sons, Incorporated, 2006.
- [58] Robert Zorich. *Handbook of Quality Integrated Circuit Manufacturing*. Academic Press Incorporated, 1991.
- [59] Matthew P. Bilodeau and W. David Delibac. Equipment maintenance focus in defect density improvements IBM microelectronics, Burlington, Vermont. In *IEEE/SEMI Advanced Semiconductor Manufacturing Conference And Workshop*, pages 22–26. IEEE, 2004.
- [60] Dan Rosso. Global semiconductor industry posts record sales in 2014. Semiconductor Industry Association press release, http://www.semiconductors.org/news/2015/02/02/global_sales_report_2014/global_semiconductor_industry_posts_record_sales_in_2014/, February 2015. Accessed March 12, 2015.
- [61] George Paget Thomson and Moses Blackman. Improvements in or relating to gas discharge apparatus for producing thermonuclear reactions, April 1947. British patent 817,681 (application no. 13963/46).
- [62] John Cockcroft. British research in controlled thermonuclear fusion. *Soviet Atomic Energy*, 14(1):59–62, 1963.
- [63] John Hendry. The scientific origins of controlled fusion technology. *Annals of Science*, 44(2):143–168, 1987.
- [64] M. G. Haines. Fifty years of controlled fusion research. *Plasma Physics and Controlled Fusion*, 38(5):643–656, 1996.
- [65] Mitsuru Kikuchi. Hydrogen fusion: Light nuclei and theory of fusion reactions. In Mitsuru Kikuchi, editor, *Frontiers in Fusion Research: Physics and Fusion*, chapter 2, pages 15–32. Springer London, 2011.
- [66] David J. Rose. Controlled nuclear fusion: Status and outlook. *Science*, 172(3985):797–808, 1971.
- [67] Chris Llewellyn-Smith and David Ward. Fusion power. *European Review*, 13(3):337–359, 2005.
- [68] John Wesson. *Tokamaks*, volume 20 of *Oxford Engineering Science Series*. Oxford University Press, 1987.
- [69] R. C. Isler. Impurities in tokamaks. *Nuclear Fusion*, 24(12):1599–1678, 1984.

- [70] J. Winter. Dust: A new challenge in nuclear fusion research? *Physics of Plasmas*, 7(10):3862–3866, 2000.
- [71] J. P. Sharpe, D. A. Petti, and H.-W. Bartels. A review of dust in fusion devices: Implications for safety and operational performance. *Fusion Engineering and Design*, 63–64:153–163, 2002.
- [72] J. Phillip Sharpe, P. W. Humrickhouse, C. H. Skinner, the NSTX Team, T. Tanabe, K. Masaki, N. Miya, the JT-60U Team, and A. Sagara. Characterization of dust collected from NSTX and JT-60U. *Journal of Nuclear Materials*, 337–339:1000–1004, 2005.
- [73] S. Ratynskaia, C. Castaldo, E. Giovannozzi, D. Rudakov, G. Morfill, M. Horanyi, J. H. Yu, and G. Maddaluno. *In situ* dust detection in fusion devices. *Plasma Physics and Controlled Fusion*, 50(12):124046, 2008.
- [74] R. D. Smirnov, W. P. West, S. E. Krasheninnikov, A. Yu. Pigarov, M. Rosenberg, and B. D. Bray. Laser-dust interaction and dust size distribution measurements on DIII-D. *Physics of Plasmas*, 14(11):112507, 2007.
- [75] William J. Carmack, Kathryn A. McCarthy, David A. Petti, Arnold G. Kellman, and Clement P. C. Wong. Collection and analysis of particulate from the DIII-D tokamak. *Fusion Engineering and Design*, 39–40:477–483, 1998.
- [76] William J. Carmack, Robert A. Anderl, Robert J. Pawelko, Galen R. Smolik, and Kathryn A. McCarthy. Characterization and analysis of dusts produced in three experimental tokamaks: TFTR, DIII-D, and Alcator C-Mod. *Fusion Engineering and Design*, 51–52:477–484, 2000.
- [77] G. Federici, C. H. Skinner, J. N. Brooks, J. P. Coad, C. Grisolia, A. A. Haasz, A. Hassanein, V. Philipps, C. S. Pitcher, J. Roth, W. R. Wampler, and D. G. Whyte. Plasma-material interactions in current tokamaks and their implications for next step fusion reactors. *Nuclear Fusion*, 41(12):1967–2137, 2001.
- [78] J. Winter. Dust in fusion devices—a multi-faceted problem connecting high- and low-temperature plasma physics. *Plasma Physics and Controlled Fusion*, 46(12B):B583–B592, 2004.
- [79] K. A. McCarthy, D. A. Petti, W. J. Carmack, and G. R. Smolik. The safety implications of tokamak dust size and surface area. *Fusion Engineering and Design*, 42(1–4):45–52, 1998.
- [80] Eric Hand. US fusion in budget vice. *Nature*, 487(7408):420, 2012.
- [81] Alexander van Deursen, David Beltran, and Piet van der Laan. Grounding and cabling aspects inside the ITER cryostat. In *2014 XXXIth URSI General Assembly and Scientific Symposium*. IEEE, 2014.
- [82] J. D. Martin, M. Bacharis, M. Coppins, G. F. Counsell, and J. E. Allen. Modelling dust transport in tokamaks. *EPL*, 83(6):65001, 2008.

- [83] Raffi Khatchadourian. A star in a bottle. *The New Yorker*, 90(2), 2014. From the print issue dated March 3, 2014, accessed from <http://www.newyorker.com/magazine/2014/03/03/a-star-in-a-bottle?currentPage=all> on March 26, 2015.
- [84] E. M. Lifshitz and L. P. Pitaevskii. *Physical Kinetics*, volume 10 of *Course of Theoretical Physics*. Butterworth-Heinemann, Elsevier, 2010. Original printing 1981.
- [85] T. J. M. Boyd and J. J. Sanderson. *The Physics of Plasmas*. Cambridge University Press, 2003.
- [86] Paul M. Bellan. *Fundamentals of Plasma Physics*. Cambridge University Press, 2006.
- [87] Benjamin Widom. *Statistical Mechanics: A Concise Introduction for Scientists*. Cambridge University Press, 2002.
- [88] J. A. Bittencourt. *Fundamentals of Plasma Physics*. Springer-Verlag New York Incorporated, 3rd edition, 2004.
- [89] Wikipedia. Maxwell–Boltzmann distribution. https://en.wikipedia.org/w/index.php?title=Maxwell%E2%80%93Boltzmann_distribution&oldid=683263907, September 2015. Accessed October 1, 2015.
- [90] Peter Debye and Erich Hückel. On the theory of electrolytes. I. Freezing point depression and related phenomena. In *The Collected Papers of Peter J. W. Debye*, pages 217–263. Interscience Publishers Incorporated, 1954. Translated from “Zur Theorie der Elektrolyte. I. Gefrierpunktniedrigung und verwandte Erscheinungen”, *Physikalische Zeitschrift*, 24(9), pp. 185–206.
- [91] Francis F. Chen. *Introduction to Plasma Physics and Controlled Fusion*, volume 1. Plenum Press, 2nd edition, May 1990. 4th printing; original printing in January 1984.
- [92] Ian H. Hutchinson. *Principles of Plasma Diagnostics*. Cambridge University Press, 2nd edition, 2002.
- [93] Sture Nordholm. Simple analysis of the thermodynamic properties of the one-component plasma. *Chemical Physics Letters*, 105(3):302–307, 1984.
- [94] T. H. Gronwall. On the determination of the apparent diameters of the ions in the Debye-Hückel theory of strong electrolytes. *Proceedings of the National Academy of Sciences USA*, 13(4):198–202, 1927.
- [95] Victor K. LaMer, T. H. Gronwall, and Lotti J. Greiff. The influence of higher terms of the Debye-Hückel theory in the case of unsymmetric valence type electrolytes. *The Journal of Physical Chemistry*, 35(8):2245–2288, 1931.
- [96] David Bohm. Minimum ionic kinetic energy for a stable sheath. In A. Guthrie and R. K. Wakerling, editors, *The Characteristics of Electrical Discharges in Magnetic Fields*, chapter 3, pages 77–86. McGraw-Hill, 1949.

- [97] K.-U. Riemann. The Bohm criterion and sheath formation. *Journal of Physics D: Applied Physics*, 24:493–518, 1991.
- [98] John E. Allen. Probe measurements. In Brian E. Keen, editor, *Plasma Physics: Lectures from the Culham Plasma Physics Summer School*, volume 20 of *Conference Series*, chapter 5, pages 131–144. Institute of Physics, 1974.
- [99] Michael A. Lieberman and Allan J. Lichtenberg. *Principles of Plasma Discharges and Materials Processing*. John Wiley & Sons, Incorporated, 2nd edition, 2005.
- [100] Boris V. Somov. *Cosmic Plasma Physics*. Springer Science + Business Media, Incorporated, softcover edition, 2000.
- [101] Raoul N. Franklin. *Plasma Phenomena in Gas Discharges*, volume 3 of *Oxford Engineering Science*. Oxford University Press, 1976.
- [102] Hans L. Pécseli. *Waves and Oscillations in Plasmas*. Series in Plasma Physics. CRC Press, Taylor & Francis Group, 2013.
- [103] Raoul N. Franklin. Re: Quasineutrality and Paper II. Personal communication by email, January 3, 2014.
- [104] J. E. Allen, R. L. F. Boyd, and P. Reynolds. The collection of positive ions by a probe immersed in a plasma. *Proceedings of the Physical Society*, B70(3):297–304, 1957.
- [105] R. M. Corless, G. H. Gonnet, D. E. G. Hare, D. J. Jeffrey, and D. E. Knuth. On the Lambert *W* function. *Advances in Computational Mathematics*, 5(1):329–359, 1996.
- [106] Alexander E. Dubinov and Irina D. Dubinova. How can one solve exactly some problems in plasma theory. *Journal of Plasma Physics*, 71(5):715–728, September 2005.
- [107] Harold M. Mott-Smith and Irving Langmuir. The theory of collectors in gaseous discharges. *Physical Review*, 28(4):727–763, 1926.
- [108] Christopher T. N. Willis. *Dust in stationary and flowing plasmas*. PhD thesis, Imperial College London, 2011.
- [109] P. K. Shukla and A. A. Mamun. *Introduction to Dusty Plasma Physics*. Bristol, UK: Institute of Physics Publishing, 2002.
- [110] Elden C. Whipple. Potentials of surfaces in space. *Reports on Progress in Physics*, 44(11):1197–1250, 1981.
- [111] John E. Allen, Beatrice M. Annaratone, and Umberto de Angelis. On the orbital motion limited theory for a small body at floating potential in a Maxwellian plasma. *Journal of Plasma Physics*, 63(4):299–309, 2000.

- [112] Martin Lampe. Limits of validity for orbital-motion-limited theory for a small floating collector. *Journal of Plasma Physics*, 65(3):171–180, 2001.
- [113] Ira B. Bernstein and Irving N. Rabinowitz. Theory of electrostatic probes in a low-density plasma. *Physics of Fluids*, 2(2):112–121, 1959.
- [114] James G. Laframboise. Theory of spherical and cylindrical Langmuir probes in a collisionless, Maxwellian plasma at rest. Technical Report 100, University of Toronto Institute for Aerospace Studies, June 1966.
- [115] C. T. N. Willis, M. Coppins, M. Bacharis, and J. E. Allen. The effect of dust grain size on the floating potential of dust in a collisionless plasma. *Plasma Sources Science and Technology*, 19(6):065022, 2010.
- [116] C. Willis, M. Coppins, M. Bacharis, and J. Allen. Floating potential of large dust grains in a collisionless flowing plasma. *Physical Review E*, 85(3):036403, 2012.
- [117] P. C. Stangeby. Plasma sheath transmission factors for tokamak edge plasmas. *Physics of Fluids*, 27(3):682–690, 1984.
- [118] Wikipedia. Heat capacity ratio. https://en.wikipedia.org/w/index.php?title=Heat_capacity_ratio&oldid=669730184, July 2015. Accessed July 28, 2015.
- [119] J. Michael Shull. Disruption and sputtering of grains in intermediate-velocity interstellar clouds. *The Astrophysical Journal*, 226:858–862, 1978.
- [120] Giovanni Lapenta. Simulation of charging and shielding of dust particles in drifting plasmas. *Physics of Plasmas*, 6(5):11–13, 1999.
- [121] Martha W. Evans, Francis H. Harlow, and Eleazer Bromberg. The particle-in-cell method for hydrodynamic calculations. Technical Report LA-2139, Los Alamos Scientific Laboratory of the University of California, November 1957. Defense Technical Information Center accession number ADA384618.
- [122] C. K. Birdsall and A. B. Langdon. *Plasma physics via computer simulation*. McGraw-Hill, 1985.
- [123] I. H. Hutchinson. Ion collection by a sphere in a flowing plasma: I. Quasineutral. *Plasma Physics and Controlled Fusion*, 44(9):1953–1977, 2002.
- [124] I. H. Hutchinson. Ion collection by a sphere in a flowing plasma: 3. Floating potential and drag force. *Plasma Physics and Controlled Fusion*, 47(1):71–87, 2005.
- [125] I. H. Hutchinson. Ion collection by a sphere in a flowing plasma: 2. non-zero Debye length. *Plasma Physics and Controlled Fusion*, 45(8):1477–1500, 2003.
- [126] I. H. Hutchinson and L. Patacchini. Computation of the effect of neutral collisions on ion current to a floating sphere in a stationary plasma. *Physics of Plasmas*, 14(1):013505, 2007.

- [127] Ian H. Hutchinson. Interaction of flowing plasma with collecting objects. Technical Report NSF/DOE-HUTCH-ER54891, United States Department of Energy and Massachusetts Institute of Technology, October 2013. DOI 10.2172/1127244, report available at <http://www.osti.gov/scitech/servlets/purl/1127244>.
- [128] Leonardo Patacchini and Ian H. Hutchinson. Angular distribution of current to a sphere in a flowing, weakly magnetized plasma with negligible Debye length. *Plasma Physics and Controlled Fusion*, 49(8):1193–1208, August 2007.
- [129] Leonardo Patacchini and Ian H. Hutchinson. Ion-collecting sphere in a stationary, weakly magnetized plasma with finite shielding length. *Plasma Physics and Controlled Fusion*, 49(10):1719–1733, October 2007.
- [130] B. T. Draine and Brian Sutin. Collisional charging of interstellar grains. *The Astrophysical Journal*, 320:803–817, 1987.
- [131] Themis Matsoukas and Marc Russell. Particle charging in low-pressure plasmas. *Journal of Applied Physics*, 77(9):4285–4292, 1995.
- [132] Themis Matsoukas, Marc Russell, and Matthew Smith. Stochastic charge fluctuations in dusty plasmas. *Journal of Vacuum Science & Technology A: Vacuum, Surfaces, and Films*, 14(2):624–630, 1996.
- [133] A. G. Zagorodny, P. P. J. M. Schram, and S. A. Trigger. Stationary velocity and charge distributions of grains in dusty plasmas. *Physical Review Letters*, 84(16):3594–3597, 2000.
- [134] B. Shotorban. Nonstationary stochastic charge fluctuations of a dust particle in plasmas. *Physical Review E*, 83(6):066403, 2011.
- [135] N. G. van Kampen. *Stochastic Processes in Physics and Chemistry*. Elsevier, 2nd edition, 1992.
- [136] Alexander Piel. *Plasma Physics: An Introduction to Laboratory, Space, and Fusion Plasmas*. Springer-Verlag Berlin Heidelberg, June 2010.
- [137] Drew M. Thomas and Michael Coppins. Equilibrium probability distribution of a conductive sphere's floating charge in a collisionless, drifting Maxwellian plasma. *Physical Review E*, 88(2):023110, 2013.
- [138] P. Medgyessy. On the unimodality of discrete distributions. *Periodica Mathematica Hungarica*, 2(1–4):245–257, 1972.
- [139] Themis Matsoukas. Charge distributions in bipolar particle charging. *Journal of Aerosol Science*, 25(4):599–609, 1994.
- [140] Hannes Risken. *The Fokker-Planck Equation: Methods of Solution and Applications*. Springer-Verlag, 1984.

- [141] François Panneton, Pierre L'Ecuyer, and Makoto Matsumoto. Improved long-period generators based on linear recurrences modulo 2. *ACM Transactions on Mathematical Software*, 32(1):1–16, 2006.
- [142] Chris Lomont. Random number generation. http://lomont.org/Math/Papers/2008/Lomont_PRNG_2008.pdf, 2011. Accessed January 10, 2016.
- [143] Josh Barnes and Piet Hut. A hierarchical $O(N \log N)$ force-calculation algorithm. *Nature*, 324(6096):446–449, December 1986.
- [144] Lars Hernquist. Performance characteristics of tree codes. *The Astrophysical Journal Supplement Series*, 64:715–734, 1987.
- [145] Andrew W. Appel. An investigation of galaxy clustering using an asymptotically fast N-body algorithm, April 1981. Undergraduate thesis, Princeton University.
- [146] Andrew W. Appel. An efficient program for many-body simulations. *SIAM Journal on Scientific & Statistical Computing*, 6(1):85–103, January 1985.
- [147] Jack Vanderlinde. *Classical Electromagnetic Theory*. Springer Science + Business Media, Incorporated, 2nd edition, 2005.
- [148] Roger E. Raab and Owen L. de Lange. *Multipole Theory in Electromagnetism: Classical, Quantum, and Symmetry Aspects, with Applications*, volume 128 of *International Series of Monographs on Physics*. Oxford University Press, 2004.
- [149] Tamar Schlick. *Molecular Modeling and Simulation: An Interdisciplinary Guide*. Springer, 2nd edition, 2010.
- [150] Hanno Rein and Scott Tremaine. Symplectic integrators in the shearing sheet. *Monthly Notices of the Royal Astronomical Society*, 415(4):3168–3176, 2011.
- [151] Ian R. Gatland. Numeric integration of Newton's equations including velocity-dependent forces. *American Journal of Physics*, 62(3):259–265, 1994.
- [152] Junchao Xia. *Computer simulations of statistical models of earthquakes*. PhD thesis, Clark University, 2006.
- [153] Hong Qin, Shuangxi Zhang, Jianyuan Xiao, Jian Liu, Yajuan Sun, and William M. Tang. Why is Boris algorithm so good? *Physics of Plasmas*, 20(8):084503, 2013.
- [154] L. Patacchini and I. H. Hutchinson. Explicit time-reversible orbit integration in particle in cell codes with static homogeneous magnetic field. *Journal of Computational Physics*, 228(7):2604–2615, 2009.
- [155] J. P. Boris. Relativistic plasma simulation—optimization of a hybrid code. In Jay P. Boris and Ramy A. Shanny, editors, *Proceedings: Fourth Conference on Numerical Simulation of Plasmas*, pages 3–67. US Naval Research Laboratory, 1970.

- [156] James Gregory. *Exercitationes geometricae*. Guilielmi Godbid & Moses Pitt, 1668. Accessed at <https://archive.org/details/ita-bnc-mag-00001357-002> on September 25, 2015.
- [157] Herman H. Goldstine. *A History of Numerical Analysis from the 16th through the 19th century*, volume 2 of *Studies in the History of Mathematics and Physical Sciences*. Springer, 1977.
- [158] Lewi Tonks and Irving Langmuir. Oscillations in ionized gases. *Physical Review*, 33(2):195–211, 1929.
- [159] David A. Vallado. *Fundamentals of Astrodynamics and Applications*. El Segundo, US: Microcosm Press and Dordrecht, The Netherlands: Kluwer Academic Publishers, 2nd edition, 2004.
- [160] Hermann Haken and Hans Christoph Wolf. *The Physics of Atoms and Quanta: Introduction to Experiments and Theory*. Berlin, Germany: Springer, 7th edition, 2004.
- [161] L. Patacchini, I. H. Hutchinson, and G. Lapenta. Electron collection by a negatively charged sphere in a collisionless magnetoplasma. *Physics of Plasmas*, 14(6):062111, 2007.
- [162] V. N. Tsytovich, N. Sato, and G. E. Morfill. Note on the charging and spinning of dust particles in complex plasmas in a strong magnetic field. *New Journal of Physics*, 5:43.1–43.9, 2003.
- [163] J. T. Holgate and M. Coppins. The charging of non-spherical macroparticles in a plasma. Plasma physics research group, Imperial College London. Typescript, November 13, 2015. Accepted by *Physical Review E*.
- [164] B. T. Draine and E. E. Salpeter. On the physics of dust grains in hot gas. *The Astrophysical Journal*, 231:77–94, 1979.
- [165] S. A. Khrapak, A. V. Ivlev, G. E. Morfill, and H. M. Thomas. Ion drag force in complex plasmas. *Physical Review E*, 66(4):046414, 2002.
- [166] Larry Wasserman. Nonlinear regression. In *All of Nonparametric Statistics*, Springer Texts in Statistics, chapter 5, pages 61–123. Berlin, Germany: Springer, 2006.
- [167] Cosma Shalizi. Extending linear regression: Weighted least squares, heteroskedasticity, local polynomial regression. <http://www.stat.cmu.edu/~cshalizi/350/lectures/18/lecture-18.pdf>. Lecture notes for the class “36-350, Data Mining”. Accessed August 4, 2013.

Appendix A

Symbols and abbreviations

This reference appendix tabulates the meanings of uppercase abbreviations and algebraic symbols featured in the main text. It omits currency and unit symbols, such as “\$” for US dollars and “K” for Kelvin, as well as purely mathematical symbols like Roman letter “d”s to indicate derivatives.

The symbol table lists symbols in alphabetical order, in both senses. The Hebrew “נ” comes first, followed by symbols beginning with a Greek letter, followed by symbols beginning with a Latin letter. A five-pointed star (“★”) marks Ian Hutchinson’s notation from his description of SCEPTIC’s reinjection algorithm [125], and notation directly inspired by Hutchinson’s.

Abbreviation	Full word or phrase
ABR	Allen, Boyd, and Reynolds
BR	Boltzmann relation
CDF	cumulative distribution function
CP	<i>Chinese Physics</i>
DH	Debye-Hückel
ER	Euler-Richardson
FP	Fokker-Planck
IBM	International Business Machines Corporation
ITER	Latin noun “iter”, meaning “the way” (lit. “passage”)
LHS	left-hand side
LLA	linear Laplacian approximation
MOML	modified orbital-motion-limited
MPI	Message Passing Interface
NASA	National Aeronautics and Space Administration
ODE	ordinary differential equation
OM	orbital-motion
OML	orbital-motion-limited
PE	potential energy
PHL	Patacchini, Hutchinson, and Lapenta

PIC	particle-in-cell
RHS	right-hand side
SCEPTIC	specialized-coordinate electrostatic particle and thermals in cell
SE	standard error
SMOML	shifted, modified orbital-motion-limited
SOML	shifted orbital-motion-limited
USSR	Union of Soviet Socialist Republics
UV	ultraviolet
VV	velocity Verlet
WELL512	well equidistributed long-period linear (generator) of degree 512

Symbol	Quantity represented
\mathfrak{x}	§2.2.4: dummy variable for defining the error function
\mathfrak{x}	§3: neutral sphere's electron-collection rate ($4\pi a^2 n_0 \sqrt{k_B T_e / (2\pi m_e)}$)
α	§3: flow-adjusted ion-to-electron temperature ratio ($\Theta s_1(u)/s_2(u)$)
α	★ §4.3.3: angle between \mathbf{u} and particle's entry point into simulation domain
β_e	plasma electron magnetization ($\langle a/r_{Le} \rangle = aeB/\sqrt{\pi k_B T_e m_e/2}$)
β_i	plasma ion magnetization ($\langle a/r_{Li} \rangle = aZeB/\sqrt{\pi k_B T_i m_i/2}$)
Γ_C	plasma's Coulomb coupling parameter ($e^2/(4\pi\epsilon_0\bar{r}k_B T_e)$, if $T_e = T_i$ and $Z = 1$)
γ	heat capacity ratio, a.k.a. adiabatic index
Δt	time step
$\Delta\phi$	characteristic vector of rotation about \mathbf{B}
δ	offset/shift of point about which to compute electric dipole moment
ϵ	softening parameter
ϵ_0	electric constant, a.k.a. permittivity of free space ($8.85 \times 10^{-12} \text{ F}\cdot\text{m}^{-1}$)
ζ	normalized distance (x/λ_D)
ζ	characteristic vector of rotation ($ \hat{\mathbf{u}} \times \hat{\mathbf{z}} \arccos(\hat{\mathbf{u}} \cdot \hat{\mathbf{z}})$)
η	normalized electric potential $e\phi/(k_B T_e)$
η^*	η_a for small spheres; η_s for large spheres
η_a	normalized electric potential at grain's surface
η_s	normalized electric potential at sheath edge
η_{SOML}	SOML prediction of equilibrium, normalized electric potential
$\eta(\zeta)$	normalized electric potential at normalized distance ζ
$\eta(\xi)$	normalized electric potential at normalized radius ξ
$\eta(r)$	normalized electric potential at radius r
$\eta(x)$	normalized electric potential at distance x
θ	§2: zenith angle in spherical coordinates
θ	§4 & §5: treecode algorithm's opening angle parameter

θ_0	constant phase factor of electron's Kepler orbit
θ_e	phase (polar angle) of electron's Kepler orbit
θ_s	Rutherford scattering angle
Θ	ion-to-electron temperature ratio in plasma (T_i/T_e)
Λ	operand of Coulomb logarithm ($\approx 9N_D$)
λ_c	mean free path of plasma particles ($16\pi n_0 \lambda_D^4 / \ln \Lambda$ when $T_i = T_e$ and $Z = 1$)
λ_D	passim: (electron) Debye length (characteristic screening length in a plasma)
λ_{De}	§2.3: electron Debye length divided by a (Ian Hutchinson's notation [124])
μ	passim: square root of ion-to-electron mass ratio ($\sqrt{m_i/m_e}$)
μ/h^2	§5.1.1: Kepler orbital radius
ν	positive convenience parameter for the ABR model ($(a/\lambda_D)^2 \mu / \sqrt{4\pi}$)
ν_{pe}	electron oscillation frequency ($\sqrt{n_0 e^2 / (\epsilon_0 m_e)} / (2\pi)$)
ν_{pi}	ion oscillation frequency ($\sqrt{n_i Z^2 e^2 / (\epsilon_0 m_i)} / (2\pi)$)
ξ	normalized radius (r/λ_D)
ξ_0	normalized sheath-edge location (r_0/λ_D)
ξ_b	normalized radius at which to apply quasi-neutral, ABR boundary condition
ρ_d	(mass) density of dust grain
ρ_f	net (free) space-charge density
σ	§2.2.2: cross-section grain presents to ions (with v_∞ dependence left implicit)
σ	§3 & §5: standard deviation of q 's equilibrium probability distribution
σ^2	§3 & §5: variance of q 's equilibrium probability distribution
$\sigma(v_\infty)$	§2.2.2: effective cross-section grain presents to ions with speed v_∞ at infinity
τ_c	collecting sphere's characteristic charging time in plasma
τ_d	oscillation decay time
τ_s	time scale of quadratic trend
ϕ	electric potential
ϕ_a	electric potential at grain's surface
ϕ_s	electric potential at sheath edge
$\phi(\mathbf{R})$	electric potential from charge cluster at \mathbf{R}
$\phi(\mathbf{r})$	electric potential at \mathbf{r}
$\phi(r)$	electric potential at radius r
$\phi(x)$	electric potential at distance x
χ	★ §4: normalized electric potential
χ^2	§5.3: chi-squared statistic
χ_b	★ normalized electric potential at simulation boundary ($qe\phi(r_b)/(k_B T)$)
$\chi(r_b/r)$	★ normalized electric potential at radius r
ψ	azimuthal angle in spherical coordinates
Ω	characteristic charging parameter for sphere in plasma ($4\pi\epsilon_0 k_B T_e a / e^2$)
ω_L	angular Larmor frequency (qeB/m)
ω_p	undamped, angular frequency of plasma oscillation of particle species

ω_{pe}	undamped, angular frequency of electron plasma oscillation
ω_{pi}	undamped, angular frequency of ion plasma oscillation
A	body's surface area
a	grain radius
a_U	dust albedo for UV light
a_V	dust albedo for visible light
\mathbf{B}	magnetic field, a.k.a. magnetic flux density
B	magnitude of magnetic field
b	impact parameter
b_0	impact parameter of ions with finite radial speed when striking sphere
b_1	impact parameter of absorbed ion in OML theory
b_2	impact parameter of scattered ion in OML theory
b_{crit}	critical impact parameter of grazing ion in OML theory
b_{\max}	★ maximum initial impact parameter of particle entering simulation domain
C	normalization constant for probability density function
C_1	arbitrary constant in an ODE's general solution
C_2	arbitrary constant in an ODE's general solution
c	★ cosine of angle between \mathbf{u} and \mathbf{U}
c_s	ion sound speed, a.k.a. Bohm speed ($\sqrt{k_B T_e / m_i}$)
D	number of spatial dimensions of simulation domain
d	distance between particle and treecode cell's centre of charge
\mathbf{E}	electric field
E	total energy of a physical state
$\mathbf{E}(\mathbf{r})$	electric field at \mathbf{r}
$\mathbf{E}(\mathbf{r}(t), t)$	electric field at time t and position \mathbf{r}
$\mathbf{E}(\mathbf{R})$	electric field from charge cluster at \mathbf{R}
e	elementary charge (1.602×10^{-19} C)
e_K	Kepler orbit's eccentricity
\mathbf{F}	Lorentz force on particle
$\mathbf{F}(\mathbf{r}(t), t)$	Lorentz force on particle at time t and position $\mathbf{r}(t)$
$f(r)$	ansatz/placeholder function in DH derivation
$f(\mathbf{v})$	probability density function of particle species' velocities
$f(v_\infty)$	probability density function of ions' v_∞
$f(v_j)$	probability density function of particle species' velocity component
f_q	q 's probability mass function
g	§3: g_q for large spheres
g	§6.2: gravitational acceleration near Earth's surface ($9.8 \text{ m}\cdot\text{s}^{-2}$)
g^*	normalized ion-collection rate for large spheres (g/\aleph)
g_q	ion-collection rate (probability per unit time of transition from q to $q + 1$)
I	particle species' electrical current onto a body in plasma

I_e	collected electron current onto a body in plasma
$I_e(q)$	collected electron current onto a body in plasma as a function of body's q
I_i	collected ion current onto a body in plasma
$I_i(q)$	collected ion current onto a body in plasma as a function of body's q
$K(\mathbf{v})$	kinetic energy as a function of \mathbf{v}
k	minimum autocorrelation lag for which q has negative autocorrelation
k_B	Boltzmann's constant ($1.38 \times 10^{-23} \text{ J}\cdot\text{K}^{-1}$)
L	plasma simulation's size
l	treecode cell's size
M	sphere's modal charge state
m	particle mass
m_d	dust grain mass
m_e	electron mass ($9.11 \times 10^{-31} \text{ kg}$)
m_i	ion mass
m_p	proton mass ($1.67 \times 10^{-27} \text{ kg}$)
N	total number of plasma particles
N_D	Debye number, a.k.a. the plasma parameter ($4\pi\lambda_D^3 n_e/3$)
N_q	size of pot run's subsample of uncorrelated q values
n	particle species' number density
$n(\phi(\mathbf{r}))$	particle species' number density where electric potential equals $\phi(\mathbf{r})$
$n(\mathbf{r})$	particle species' number density at \mathbf{r}
n_0	reference number density (usually of electrons, hence n_e where $\phi = 0$)
n_e	electron number density
$n_e(q)$	electron number density at body's surface as function of body's q
n_i	ion number density
$n_i(q)$	ion number density at body's surface as function of body's q
$n_i(\zeta)$	ion number density at normalized distance ζ
$n_i(\xi)$	ion number density at normalized radius ξ
$P(\mathbf{r})$	particle species' pressure at \mathbf{r}
\mathbf{p}	electric dipole moment of treecode cell
$\mathbf{p}(\mathbf{s})$	electric dipole moment about \mathbf{s} of treecode cell
p	extremity probability of observed test statistic under null hypothesis
$\langle p_x \rangle$	$\hat{\mathbf{x}}$ component of particle species' mean linear momentum
$\langle p_y \rangle$	$\hat{\mathbf{y}}$ component of particle species' mean linear momentum
$\langle p_z \rangle$	$\hat{\mathbf{z}}$ component of particle species' mean linear momentum
Q	body's net charge in coulombs
Q_j	charge of j th plasma particle
q	charge state (net charge in units of $+e$) of a body or plasma particle
q^*	example value of q
q_0	body's equilibrium charge state

q_1	greater postulated equilibrium q
q_2	lesser postulated equilibrium q
\mathbf{R}	position relative to treecode cell's centre of charge
$\mathbf{R}_{\Delta\phi}$	rotation operator with characteristic vector $\Delta\phi$
R	spherical simulation domain's radius
\mathbf{r}	position
$\mathbf{r}(t)$	position at time t
r	radius, or radial distance
\bar{r}	average distance between plasma electrons $((4\pi n_e/3)^{-1/3})$
r_0	sheath edge location
r_A	absorption radius for ions approaching grain
r_b	★ spherical simulation domain's radius
\mathbf{r}_j	position of j th plasma particle
r_q	electron-collection rate (probability per unit time of transition from q to $q - 1$)
\mathbf{s}	§4: point about which electric dipole moment computed
\mathbf{s}'	alternative choice of point about which to compute electric dipole moment
s	§3: relative probability current between charge states
$s_1(u)$	auxiliary SOML function $(\sqrt{\pi}((1 + 2u^2)\operatorname{erf}(u)/(4u)) + \exp(-u^2)/2)$
$s_2(u)$	auxiliary SOML function $(\sqrt{\pi}\operatorname{erf}(u)/(2u))$
SiH_4	silane
t	time
t_0	initial/starting time
T	particle species' temperature
T_e	electron temperature in plasma
T_i	ion temperature in plasma
$T(\mathbf{r})$	particle species' temperature at \mathbf{r}
\mathbf{U}	★ plasma's flow/drift velocity infinitely far from simulation domain
U	★ plasma's flow/drift speed infinitely far from simulation domain
$\langle U \rangle_A$	amplitude of oscillation of potential energy
$\langle U \rangle(t)$	mean potential energy as a function of time t
$U(r)$	joint potential energy of two particles separated by a distance r
\mathbf{u}	★ particle's velocity infinitely far from simulation domain
u	§2 & §3: normalized plasma flow/drift speed $(\mathbf{v}_d /\sqrt{2k_B T_i/m_i})$
u	★ §4.3.3: particle's speed infinitely far from simulation domain
\mathbf{v}	velocity
\mathbf{v}_d	plasma flow/drift velocity
$\mathbf{v}(t)$	velocity at time t
v	speed
v_0	§2.1.7: ion speed at sheath edge
v_0	§5.1.2: alpha particle's speed infinitely far from gold nucleus

v_∞	ion's speed infinitely far from grain
v_θ	zenith velocity component
v_ϕ	azimuthal velocity component
v_a	speed of ion grazing sphere's surface
v_d	plasma flow/drift speed
v_{in}	radially inward velocity component of particles approaching body
$v_{\text{in},e}$	radially inward velocity component of electrons approaching body
$v_{\text{in},i}$	radially inward velocity component of ions approaching body
v_r	radial velocity component
v_t	tangential velocity component
v_{the}	electron thermal speed ($\sqrt{k_B T_e/m_e}$)
v_{thi}	ion thermal speed ($\sqrt{k_B T_i/m_i}$)
v_x	velocity's \hat{x} component
v_y	velocity's \hat{y} component
v_z	velocity's \hat{z} component
$\mathbf{v}(\mathbf{r})$	velocity at \mathbf{r}
$W_0(z)$	principal branch of Lambert W special function of z
X^2	total discrepancy between observations and model ($\sum z^2$)
\hat{x}	basis vector in Cartesian coordinates
x	§2: distance
x	§4: spatial Cartesian coordinate
x_0	sheath edge location
\hat{y}	basis vector in Cartesian coordinates
y'_0	derivative of $y(q)$ with respect to q , evaluated at $q = q_0$
y	§4: spatial Cartesian coordinate
$y(q)$	§3: derivative of $\ln f_q$ with respect to q
Z	ion charge state (charge in units of e)
\hat{z}	basis vector in Cartesian coordinates
z	passim: spatial Cartesian coordinate
z	§5.3: standardized discrepancy between observation and model

Appendix B

Better boundary conditions for ABR theory from a linear-Laplacian approximation

Section 2.2.1 defines the ABR model, the core equation of which is eq. (2.84), a dimensionless version of Poisson's electrostatic equation. To save the reader the effort of looking back at that section, the relevant equation is

$$\tilde{\nabla}^2 \eta = \frac{d}{d\xi} \left(\xi^2 \frac{d\eta}{d\xi} \right) = \xi^2 \exp(\eta) - \frac{\nu \exp(\eta_a)}{\sqrt{-\eta}} \quad (\text{B.1})$$

where $\tilde{\nabla}^2$ is the Laplacian operator in normalized coordinates. This equation has no closed-form solution, so it must be solved by numerical integration. That integration requires two boundary conditions, and Kennedy and Allen observed that the conditions may be deduced at a ξ large enough that $\tilde{\nabla}^2 \eta$ is much smaller than either of the right-hand side's terms. At such ξ , one may make the quasi-neutral approximation of taking $\tilde{\nabla}^2 \eta \approx 0$, which gives an explicit solution of eq. (B.1) for ξ^2 and hence for η as a function of ξ . This quasi-neutral solution for η (q.v. eq. (2.88)) may serve as the first boundary condition, and its derivative

$$\frac{d\eta}{d\xi} \approx \frac{-4\eta}{(1+2\eta)\xi} \quad (\text{B.2})$$

as the second. Two boundary conditions are enough, so it is not necessary to differentiate again for $d^2\eta/d\xi^2$, not least because one can obtain that derivative by rearranging Poisson's equation:

$$\frac{d^2\eta}{d\xi^2} = \exp(\eta) - \frac{\nu \exp(\eta_a)}{\xi^2 \sqrt{-\eta}} - \frac{2}{\xi} \frac{d\eta}{d\xi} \quad (\text{B.3})$$

However, with the floating-point arithmetic of a computer, calculating $d^2\eta/d\xi^2$ in this way gives suboptimal results at large ξ , because there the first two terms on the right-hand side become nearly equal in magnitude, and taking their difference when computing $d^2\eta/d\xi^2$ can therefore

produce nontrivial floating-point error. To avoid this problem, one may instead differentiate eq. (B.2) to obtain $d^2\eta/d\xi^2$ as

$$\frac{d^2\eta}{d\xi^2} \approx \frac{4\eta(5 + 4\eta(1 + \eta))}{(1 + 2\eta)^3 \xi^2} \quad (\text{B.4})$$

which does not require subtracting two nearly equal numbers.

However, another numerical accuracy problem remains even after circumventing the floating-point difference issue. Eq. (B.4) is approximately correct for small η , but it is inaccurate enough to trigger spurious numerical oscillations in $d^2\eta/d\xi^2$ if a numerical solver abruptly switches from using eq. (B.4) to using eq. (B.3) to evaluate the second derivative. (My solver does this once it has integrated to a ξ where quasi-neutrality stops being a good approximation, at which point eq. (B.4) starts to become substantially wrong but eq. (B.3) becomes amenable to evaluation with floating-point arithmetic.)

One intuitive way to eliminate this problem might be to estimate $d^2\eta/d\xi^2$ as a weighted average of eqs. (B.3) and (B.4), putting gradually increasing weight on the former as ξ shrinks. However, although this idea is conceptually simple, the precise weighting to use is not obvious, and the idea's motivation (trading off the first equation's floating-point error against the second equation's systematic error), although pragmatic, is ad hoc and lacks a firm mathematical grounding.

In my judgement a better approach is to return to eq. (B.1), approximate it in a less blunt fashion, and hence deduce more exact solutions for η and its derivatives. The quasi-neutral solutions come from taking $\tilde{\nabla}^2\eta = 0$, but once the quasi-neutral solution is in hand one no longer has to make such a blunt approximation; one can bootstrap a better one from eq. (B.2), which gives

$$\tilde{\nabla}^2\eta = \frac{d}{d\xi} \left(\xi^2 \frac{d\eta}{d\xi} \right) \approx \frac{d}{d\xi} \left(\frac{-4\eta\xi}{1 + 2\eta} \right) \approx \frac{-4\eta(-3 + 4\eta(1 + \eta))}{(1 + 2\eta)^3} \quad (\text{B.5})$$

a more plausible estimate of $\tilde{\nabla}^2\eta$ than assuming it to be zero. Expanding it to get

$$\tilde{\nabla}^2\eta \approx \frac{12\eta - 16\eta^2 - 16\eta^3}{(1 + 2\eta)^3} \equiv (12\eta - \mathcal{O}(\eta^2))(1 - 6\eta + \mathcal{O}(\eta^2)) \equiv 12\eta - \mathcal{O}(\eta^2) \quad (\text{B.6})$$

suggests approximating $\tilde{\nabla}^2\eta$ as 12η , which is more convenient than employing eq. (B.5) and presumably more accurate than assuming $\tilde{\nabla}^2\eta = 0$. Certainly 12η is a better estimate than zero of the rightmost side of eq. (B.5): for $-1/2 < \eta \leq 0$, the range of η values for which both the quasi-neutral solution and eq. (B.5) have well-defined values, 12η is always between zero and the rightmost side of eq. (B.5). (Notice that this is no guarantee that 12η is a better estimate of $\tilde{\nabla}^2\eta$ than zero, merely encouraging evidence, because eq. (B.5)'s rightmost side itself only approximates $\tilde{\nabla}^2\eta$.)

I therefore replace the quasi-neutral approximation that $\tilde{\nabla}^2\eta = 0$ with the linear-Laplacian approximation (LLA) that $\tilde{\nabla}^2\eta = 12\eta$. Substituting into eq. (B.1),

$$12\eta \approx \xi^2 \exp(\eta) - \frac{\nu \exp(\eta_a)}{\sqrt{-\eta}} \quad (\text{B.7})$$

which has the implicit solution

$$\xi^2 \approx \frac{\exp(-\eta)}{\sqrt{-\eta}} (12\eta\sqrt{-\eta} + v \exp(\eta_a)) \quad (\text{B.8})$$

but unlike in the quasi-neutral case, an explicit solution for η is unavailable. This is no real obstacle, however, because one can solve eq. (B.8) numerically for η , and exploit implicit differentiation to uncover closed-form formulae for η 's spatial derivatives in terms of η . Differentiating eq. (B.8) and simplifying,

$$\frac{d\xi}{d\eta} \approx \frac{6\exp(-\eta)}{\xi} + \frac{v\exp(\eta_a - \eta)\sqrt{-\eta}}{4\eta^2\xi} - \frac{\xi}{2} \quad (\text{B.9})$$

combining which with eq. (B.7) implies

$$\frac{d\xi}{d\eta} \approx \frac{3 + 6\exp(-\eta)}{\xi} - \frac{(1 + 2\eta)\xi}{4\eta} \quad (\text{B.10})$$

Taking reciprocals,

$$\frac{d\eta}{d\xi} \approx \frac{-4\eta\exp(\eta)\xi}{\exp(\eta)(\xi^2 + 2\eta(\xi^2 - 6)) - 24\eta} \quad (\text{B.11})$$

which converges on the quasi-neutral derivative (eq. (B.2)) as $\xi \rightarrow \infty$ and $\eta \rightarrow 0$, confirming that this LLA derivative has sensible limiting behaviour. Differentiating the LLA derivative and rewriting the result in terms of η and ξ alone results in a long-winded expression for $d^2\eta/d\xi^2$, but simplifying it with the further approximation that $\exp(\eta) \approx \exp(2\eta) \approx 1$ leads to

$$\frac{d^2\eta}{d\xi^2} \approx \frac{4\eta(5\xi^4 + 4\eta\xi^4 + 4\eta^2(\xi^4 - 24\xi^2 - 324))}{(\xi^2 + 2\eta(\xi^2 - 18))^3} \equiv \frac{4\eta\left(5 + 4\eta\left(1 + \eta\left(1 - \frac{24}{\xi^2} - \frac{324}{\xi^4}\right)\right)\right)}{\left(1 + 2\eta\left(1 - \frac{18}{\xi^2}\right)\right)^3\xi^2} \quad (\text{B.12})$$

where the rightmost rearrangement makes clear that this second derivative likewise tends to the quasi-neutral second derivative as $\xi \rightarrow \infty$.

Eqs. (B.8), (B.11) and (B.12) together define an implicit solution for η and explicit solutions for its first two derivatives, under an approximation (the LLA) superior to the quasi-neutral approximation. The LLA solutions reduce to the quasi-neutral solutions as $\xi \rightarrow \infty$, but are more exact than the quasi-neutral solutions. The LLA is also closer to self-consistency than the quasi-neutral approximation. The quasi-neutral approximation assumes $\tilde{\nabla}^2\eta = 0$, but its implied solution gives $\tilde{\nabla}^2\eta \approx 12\eta$. Meanwhile, the LLA assumes $\tilde{\nabla}^2\eta = 12\eta$, and (albeit after tedious algebraic manipulation) its implied solution gives

$$\tilde{\nabla}^2\eta \approx 12\eta + \left(\frac{1872}{\xi^2} - 88\right)\eta^2 + \mathcal{O}(\eta^3) \quad (\text{B.13})$$

which is the same as the assumed $\tilde{\nabla}^2\eta$ to first order, a reassuring property not shared by the quasi-neutral approximation.

Practically, for $a/\lambda_D \gtrsim 10^{-1}$ the LLA solutions greatly lessen the spurious oscillations in $d^2\eta/d\xi^2$ which appear when my numerical integrator switches from the approximate, analytic solution to

eq. (B.3). The new approximation thereby boosts the reliability of the numerical solutions and allows them to be found in fewer integration steps.

The LLA solution does sometimes cause slightly *worse* numerical oscillations than the quasi-neutral solution when $\mu = 1$ (corresponding to an electron-positron plasma) and $a/\lambda_D \sim 10^{-2}$, though not when a/λ_D is far smaller or far larger. Eq. (B.13) promises some insight into this otherwise puzzling peccadillo. The quasi-neutral approximation is better than the LLA when $\tilde{\nabla}^2\eta$ is closer to zero than to 12η . Thus an algebraic criterion for the LLA's superiority is $\tilde{\nabla}^2\eta < 6\eta$ (recall that $\eta < 0$). Given $|\eta| \ll 1$ and eq. (B.13) the criterion becomes

$$12\eta + \left(\frac{1872}{\xi^2} - 88 \right) \eta^2 \lesssim 6\eta \quad (\text{B.14})$$

i.e.

$$\left(\frac{1872}{\xi^2} - 88 \right) \eta \gtrsim -6 \quad (\text{B.15})$$

If $\xi \geq \sqrt{1872/88} \approx 4.6$, this inequality is always satisfied because the parenthetical term is then non-positive and so its product with η is always at least zero. However, if ξ is less than $\sqrt{1872/88}$, the parenthetical term is positive and a sufficiently negative η may then violate the inequality.

Not too much weight should be put on the specific numbers in this analysis because they emerge from an array of approximations, but the analysis does suggest why the LLA solution may perform more poorly when $a/\lambda_D \sim 10^{-2}$ and only then. For $a/\lambda_D \gg 10^{-2}$ the solver applies the LLA solution only at $\xi > 4.6$, where inequality (B.15) is sure to be satisfied, while for $a/\lambda_D \rightarrow 0$, $\eta \rightarrow 0$ everywhere and so inequality (B.15) is typically satisfied. (Moreover, as $a/\lambda_D \rightarrow 0$, violations of the inequality cease to matter, because as $\eta \rightarrow 0$ the LLA solution converges on the quasi-neutral solution anyway.) The only remaining circumstances where the LLA superiority criterion may go unsatisfied are those where a/λ_D is small but not negligible.

Appendix C

Proof of f_q 's unimodality

Here is an elementary demonstration that f_q , as defined in chapter 3, is unimodal in the sense of Medgyessy [138], i.e. that the sequence

$$\dots, (f_0 - f_1), (f_{-1} - f_0), (f_{-2} - f_{-1}), \dots \quad (\text{C.1})$$

has exactly one change of sign after discarding zero terms. In intuitive terms, this asserts that f_q has only one peak, though that peak may spread across multiple adjacent abscissae with the same maximal ordinate.

As chapter 3's stochastic models assume $q \leq 0$ a priori, $f_q = 0$ for all $q > 0$. Hence the term $f_0 - f_1 = f_0$ in sequence (C.1), and the terms before it are zero and dispensable. Therefore I need only show that

$$f_0, (f_{-1} - f_0), (f_{-2} - f_{-1}), \dots \quad (\text{C.2})$$

has one change of sign after discarding zero terms. I prove this explicitly for small spheres; the same basic logic applies for large spheres.

Consider f_{q-1}/f_q , given in eq. (3.18). Because $\Omega > 0$, $\exp(q/\Omega)$ strictly increases in q . Similarly, because $s_1(u)$, $s_2(u)$, and Ω are always positive, the product of the denominators on eq. (3.18)'s right-hand side strictly decreases in q . As that product must always be non-negative, eq. (3.18) as a whole is strictly increasing in q for $q \leq 0$. Because f_{q-1}/f_q strictly increases in q for $q \leq 0$, $f_{q-1}/f_q - 1$ and hence $f_{q-1} - f_q$ can change sign at most once for $q \leq 0$. From the second term onwards, then, sequence (C.2) has at most one sign change.

Suppose there were such a sign change. This requires that $f_{q-1}/f_q - 1$ changes sign as q becomes more negative, which means f_{q-1}/f_q must go from being more than 1 to being less than 1, because f_{q-1}/f_q decreases as q becomes more negative. This implies that $f_{-1}/f_0 > 1$, implying $f_{-1} - f_0 > 0$, which in turn implies no sign change in sequence (C.2)'s first two terms (because $f_0 > 0$). As such, if sequence (C.2) has a sign change after the second term, it is the only sign change.

Suppose there were instead *no* sign change after the second term. Then either $f_{q-1}/f_q > 1$ for $q \leq 0$, or $f_{q-1}/f_q < 1$ for $q \leq 0$. The former is impossible, because it asserts that f_q becomes ever larger as $q \rightarrow -\infty$, which would render f_q unnormalizable. The latter implies $f_{-1} < f_0$, and so a

sign change between sequence (C.2)'s first two terms. Thus, were there no sign change after the sequence's second term, there would have to be a sign change between the first two terms.

The last two paragraphs mean that sequence (C.2) has exactly one sign change, completing the proof that f_q is unimodal.

Appendix D

Curve-fitting analysis of the Kepler-orbit test simulations

One of my two-body tests of pot's accuracy was simulation of an electron circularly orbiting a heavy ion. Part of the test involved checking that the electron's orbit obeyed the orbit equation

$$u \equiv \frac{1}{r} = \frac{\mu}{h^2} (1 + e_K \cos(\theta - \theta_0)) \quad (\text{D.1})$$

which has the three parameters μ/h^2 , e_K , and θ_0 . Given my test simulation's initial conditions the first two parameters should have had values of 10^4 and zero respectively. (θ_0 was an irrelevant phase factor and its particular value was of no real concern.) I fitted this equation to the u and θ values generated by my simulation to check it fitted the data reasonably well and gave the expected parameter values.

The usual method of fitting an equation like this to a dataset is least squares regression: one finds the parameter values that best predict u as a function of θ , where the best prediction is defined as the one that minimizes the sum of the squares of the residuals. In this case there were two obstacles that I had to circumvent before I could fit the curve by regression.

The first obstacle was u 's complicated nonlinear dependence on θ , which called for the use of nonlinear regression. (One can often use linear regression to fit a nonlinear model, but it requires transforming the nonlinear model into a linear one, which can hinder interpretation of the parameter estimates' standard errors. The standard errors apply to the parameters in the *transformed* model, not to the untransformed parameters in the original nonlinear model.) However, nonlinear regression requires an approximate starting estimate for each parameter; regression software needs initial guesses to iteratively hone.

To calculate approximate parameter estimates, I rewrote the orbit equation as a linear combination of functions of θ ,

$$u = \frac{\mu}{h^2} + \frac{\mu}{h^2} e_K \cos \theta_0 \cos \theta - \frac{\mu}{h^2} e_K \sin \theta_0 \sin \theta \quad (\text{D.2})$$

and fitted the linear model

$$u = \alpha + \beta_1 \cos \theta + \beta_2 \sin \theta \quad (\text{D.3})$$

by running a linear regression of u on $\cos \theta$ and $\sin \theta$, with pot test results as the dataset. I transformed the regression's α , β_1 , and β_2 estimates into estimates of the desired parameters by observing that

$$\frac{\mu}{h^2} = \alpha \quad (\text{D.4})$$

$$e_K = \frac{\sqrt{\beta_1^2 + \beta_2^2}}{\alpha} \quad (\text{D.5})$$

$$\theta_0 = \arctan\left(\frac{\beta_2}{\beta_1}\right) \quad (\text{D.6})$$

which follows from matching terms in eqs. (D.2) and (D.3). I could then hone these initial parameter estimates by using them as a starting point for nonlinear regression. At this stage I encountered the second, less obvious obstacle. Ordinary least squares regression assumes that the data points have constant dispersion (variance) about the fitted curve. This was visibly not true of some of my test results. The constant-dispersion assumption held for results obtained with $\Delta t \leq 10$ ps, but tended to be increasingly violated as Δt lengthened (figure 5.1).

When the constant variance assumption is broken, the parameters' standard error estimates can be systematically biased. Fortunately, a generalization of ordinary least squares regression known as *weighted* least squares (WLS) can accommodate varying dispersion by weighting the less dispersed data points more heavily. To eliminate the bias one performs a WLS regression with each data point weighted by $1/\sigma_i^2$, where σ_i^2 is the i th data point's variance. However, applying this method does require knowledge of σ_i^2 for every data point.

I estimated σ_i^2 for each datum with Larry Wasserman's nonparametric method [166, p. 87–88]. Once I had σ_i^2 estimates I could redo the nonlinear regression with $1/\sigma_i^2$ weights, which was likely to give better standard error estimates than the unweighted nonlinear regression. (Cosma Shalizi [167] offers concise notes on this method.)

Hence, all in all, my curve fitting procedure had three steps. I first used ordinary, unweighted linear regression to fit the transformed linear model, and transformed its estimates back into initial estimates of μ/h^2 , e_K , and θ . Using those initial estimates I ran an unweighted nonlinear regression to fit the orbit equation directly. Finally, I estimated σ_i^2 for each data point using the residuals from the second regression, and used the reciprocals of σ_i^2 as weights for a final, weighted nonlinear regression.